AD-A225 562

DTIC FILE COPY

STRENGTHENING BY SUBSTITUTIONAL
SOLUTES AND THE TEMPERATURE
DEPENDENCE OF THE FLOW STRESS IN Ni$_3$Al

DENNIS M. DIMIDUK
Processing and High Temperature
    Materials Branch
Metals and Ceramics Division

26 May 1989

Final Report for Period July 1984 - January 1989

DTIC
ELECTE
AUG 2 3 1990
D

Approved for public release; distribution unlimited

**BEST
AVAILABLE COPY**

90 08 22 077

NOTICE

When Government drawings, specifications, or other data are used for any purpose other than in connection with a definitely Government-related procurement, the United States Government incurs no responsibility or any obligation whatsoever. The fact that the government may have formulated or in any way supplied the said drawings, specifications, or other data, is not to be regarded by implication, or otherwise in any manner construed, as licensing the holder, or any other person or corporation; or as conveying any rights or permission to manufacture, use, or sell any patented invention that may in any way be related thereto.

This report is releasable to the National Technical Information Service (NTIS). At NTIS, it will be available to the general public, including foreign nations.

This technical report has been reviewed and is approved for publication.

DENNIS M. DIMIDUK
Project Engineer

FOR THE COMMANDER

NORMAN M. GEYER
Acting Chief
Processing & High Temperature
  Materials Branch
Metals & Ceramics Division

If your address has changed, if you wish to be removed from our mailing list, or if the addressee is no longer employed by your organization please notify WRDC/MLLM, WPAFB, OH 45433-6533 to help us maintain a current mailing list.

Copies of this report should not be returned unless return is required by security considerations, contractual obligations, or notice on a specific document.

REPORT DOCUMENTATION PAGE
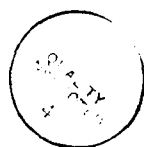
Form Approved
OMB No. 0704-0188

1a. REPORT SECURITY CLASSIFICATION	1b. RESTRICTIVE MARKINGS
Unclassified	

2a. SECURITY CLASSIFICATION AUTHORITY	3. DISTRIBUTION/AVAILABILITY OF REPORT
2b. DECLASSIFICATION/DOWNGRADING SCHEDULE	Approved for Public Release; Distribution is unlimited.

4. PERFORMING ORGANIZATION REPORT NUMBER(S)	5. MONITORING ORGANIZATION REPORT NUMBER(S)
WRDC-TR-89-4106	

6a. NAME OF PERFORMING ORGANIZATION	6b. OFFICE SYMBOL (If applicable)	7a. NAME OF MONITORING ORGANIZATION
WRDC Materials Laboratory	WRDC/MLLM	

6c. ADDRESS (City, State, and ZIP Code)	7b. ADDRESS (City, State, and ZIP Code)
Wright Patterson AFB, OH 45433-6533	

8a. NAME OF FUNDING/SPONSORING ORGANIZATION	8b. OFFICE SYMBOL (If applicable)	9. PROCUREMENT INSTRUMENT IDENTIFICATION NUMBER

8c. ADDRESS (City, State, and ZIP Code)	10. SOURCE OF FUNDING NUMBERS			
	PROGRAM ELEMENT NO.	PROJECT NO.	TASK NO.	WORK UNIT ACCESSION NO.
	61102F	2306	P1	06

11. TITLE (Include Security Classification)
Strengthening By Substitutional Solutes and The Temperature Dependence of the Flow Stress in Ni$_3$Al

12. PERSONAL AUTHOR(S)
Dennis M. Dimiduk

13a. TYPE OF REPORT	13b. TIME COVERED	14. DATE OF REPORT (Year, Month, Day)	15. PAGE COUNT
Final	FROM Jul 84 TO Jan 89	1989 May 26	250

16. SUPPLEMENTARY NOTATION

17. COSATI CODES			18. SUBJECT TERMS (Continue on reverse if necessary and identify by block number)
FIELD	GROUP	SUB-GROUP	Nickel Aluminide, Ni$_3$Al, solution hardening, intermetallics single crystals, antiphase boundaries. flow stress dislocation structures .
11	6	5	
20	2	1	

19. ABSTRACT (Continue on reverse if necessary and identify by block number)

Investigations have been performed to establish the mechanisms by which ternary solute additions to Ni$_3$Al, influence the flow stress as a function of temperature in the region of increasing flow stress. Consideration has been given to the validity of applying the classical theories for solution hardening of disordered metals to ordered alloys. Likewise, a test of the qualitative concept of rationalizing the effects of ternary-solute additions on the basis of their expected influence upon the stability of the L1$_2$ structure has been performed. Ternary additions of Sn and V were made to single-crystal Ni$_3$Al, and the Ni/Al ratio of binary single crystals was varied. The crystals were deformed in compression at an orientation near the (001) direction over the temperature range - 196 to 700°C. The APB energy and the APB-energy anisotropy have been quantified as a function of composition using weak-beam transmission electron microscopy. The dislocation structure has been characterized after deformation at low temperatures.

(Over)

20. DISTRIBUTION/AVAILABILITY OF ABSTRACT	21. ABSTRACT SECURITY CLASSIFICATION
☒ UNCLASSIFIED/UNLIMITED ☐ SAME AS RPT. ☐ DTIC USERS	Unclassified

22a. NAME OF RESPONSIBLE INDIVIDUAL	22b. TELEPHONE (Include Area Code)	22c. OFFICE SYMBOL
Dennis M. Dimiduk	513-255-9839	WRDC/MLLM

DD Form 1473, JUN 86   Previous editions are obsolete.   SECURITY CLASSIFICATION OF THIS PAGE

Block 19 (continued)

Results from the deformation experiments suggest that the mechanism governing the increase in flow stress with temperature is operative at temperatures as low as -196°C. Examination of the dislocation structures provided evidence to suggest that screw dislocations retain significant mobility, even in the Kear-Wilsdorf "lock" configuration. This evidence further suggests that the Kear-Wilsdorf configurations contribute to flow stress only through their influence upon the work hardening rate. These findings indicate a lack of correlation between the APB-energy anisotropy ratio and the strength of the alloy, which suggests that the primary role of solutes is to alter the activation barrier to dislocation-core transformations. These results are inconsistent with expectations from current phase-stability concepts for solute effects.

A-1

FOREWORD

TABLE OF CONTENTS

LIST OF FIGURES

LIST OF TABLES

CHAPTER 1

INTRODUCTION

In 1970, Westbrook made the statement, "A major structural application of a single-phase intermetallic compound lies still in the future..."; he further commented, "Not one structural alloy family of importance has been developed with the prior intent of arriving at an appropriate microstructure containing a pre-selected intermetallic."[1] In 1979, not even ten years later, the structural suitability of ordered alloys based on the the Ti-Al system was acknowledged with the production of a metallurgically sound rolled-sheet product of a two-phase alloy consisting of ordered phases.[2] In the ensuing four years, two different turbine-engine components were produced by superplastically forming and diffusion bonding that sheet.[3] Those components and three others produced from ring rolled stock have been successfully engine tested. Early in 1989, the first rotating turbine-engine components underwent successful engine testing. Furthermore, alloy-development programs are frequently directed toward exploiting ordered phases as the majority phase or even the matrix constituent in a variety of alloy systems and composites. Today, intermetallic compounds form one of the most important alloy classes on the high-temperature engineering-materials horizon.

Of the ordered alloys under consideration for structural applications, the aluminides of Fe, Ni, and Ti have afforded the greatest level of success. In 1979, Aoki and Izumi[4] reported that polycrystalline Ni_3Al exhibited high tensile ductility when alloyed with a few hundred parts per million of boron; and as a result, Ni_3Al has been the subject of major research efforts at several national and industrial laboratories for the last ten years. Four recent reviews of the development of Ni_3Al and the properties of structural intermetallic materials have been conducted;[5-8] consequently, only a brief description of the general

1

mechanical behavior of Ni_3Al will be given here in order to establish a basis for the discussion of solid-solut'.i strengthening. The terms intermetallic compound, ordered alloy, and ordered material are used interchangeably throughout this dissertation. This absence of distinction is in accord with common usage of the terms and at least one accepted theory of ordering.[9]

The binary compound Ni_3Al exists over the composition range 23 to 27.5 atomic p..c. : (a/o) aluminum at room temperature.[10] The compound solidifies peritectically and transforms into a long-range-ordered structure at a temperature near the peritectic temperature. Ni_3Al has the $L1_2$ (Cu_3Au, cP4) fcc derivative structure (Fig. 1.1) and exhibits a long-range-order parameter greater than 0.93, which is nearly constant over the temperature range 25 to 1000 °C.[11-13] Ordered alloys having the $L1_2$ structure have been intriguing for a number of years. At least eighteen of these materials are known to exhibit an anomalous temperature-dependent yield stress in that the yield stress increases by up to a factor of five with increasing temperature over some interval in the range -196 to 800 °C.[14,15] The anomalous flow regime (Region II), where $d\tau/dT > 0$, is illustrated schematically in Fig. 1.2 (from Yoo *et al.*[16]). Polycrystalline Ni_3Al exhibits a yield strength of about 210 MPa at room temperature and about 560 MPa at 600 °C. These values may be significantly altered by deviations from the stoichiometric composition, grain-size variations, and alloying. In addition to anomalous flow behavior, many of these compounds do not obey Schmid's law in octahedral slip. The magnitude of the resolved shear stress in single crystals is found to depend on both the orientation and the sense (tension vs. compression) of the applied stress as illustrated by the data from Ezz, Pope, and Paidar[17] shown in Fig. 1.3. The prominent theories which have emerged to explain these anomalies are described in detail in Chapter 2. Clearly, any theory which is put forth to account for the anomalous flow behavior of materials having the $L1_2$ structure must
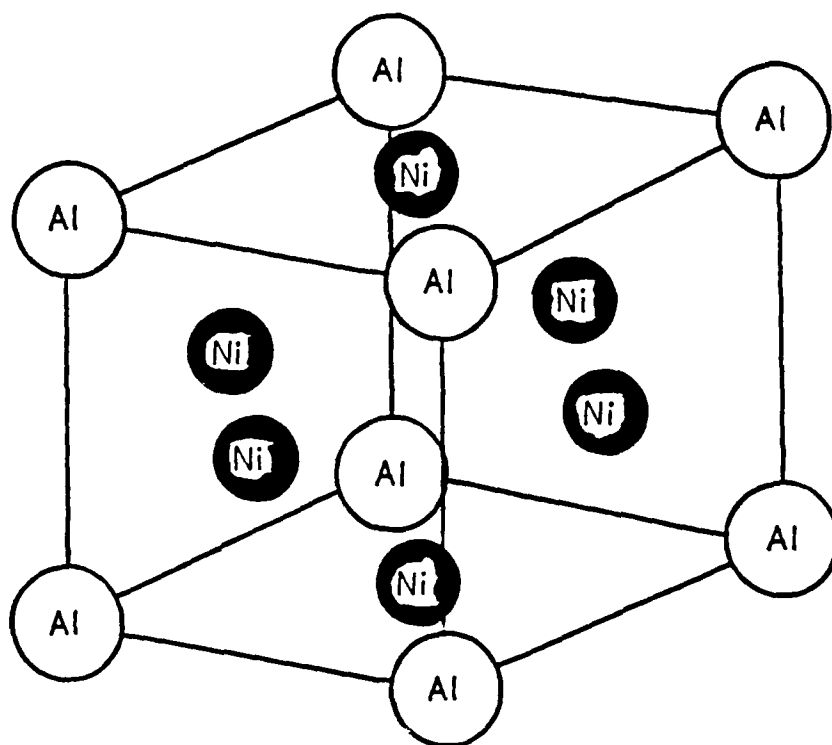
Fig. 1.1   L1$_2$ unit cell of Ni$_3$Al structure.
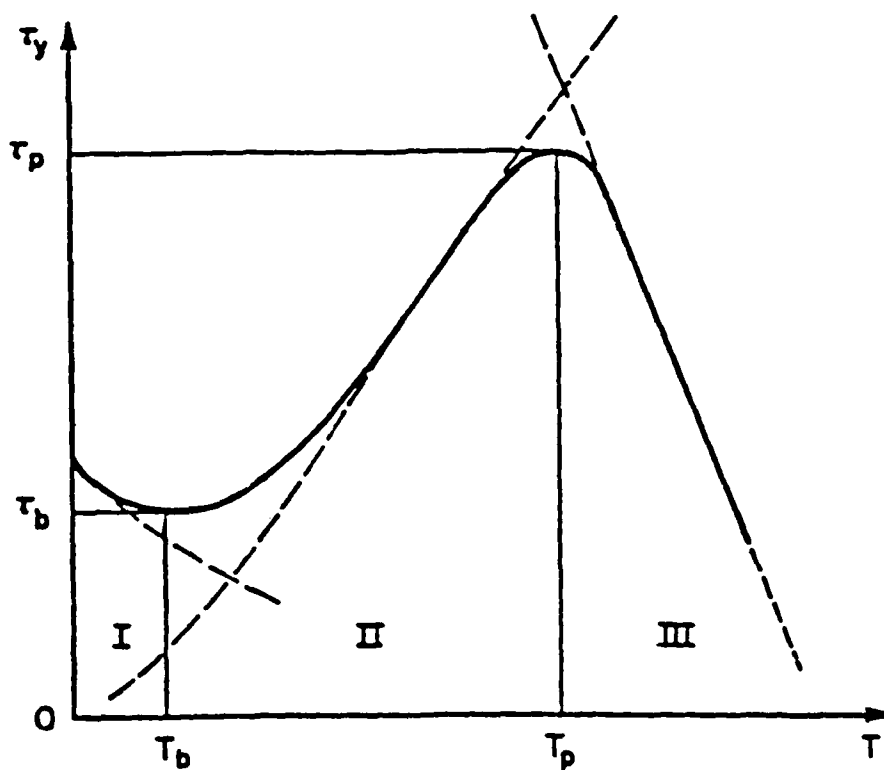
Fig. 1.2   Three characteristic regions of temperature dependence of flow stress in Ni$_3$Al alloys. Schematic after Yoo, et al.[16]

3
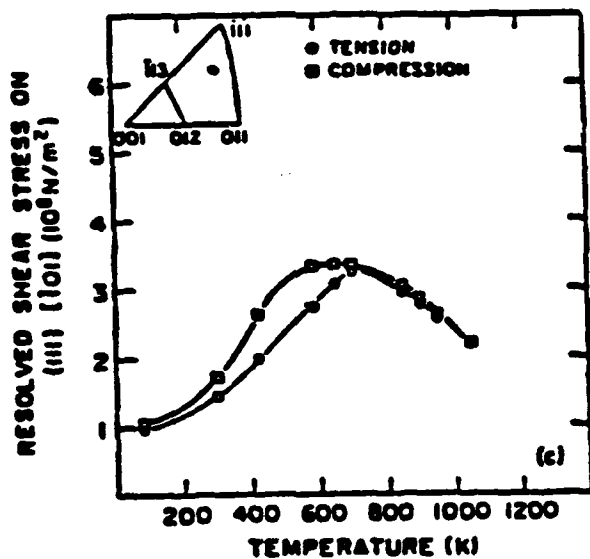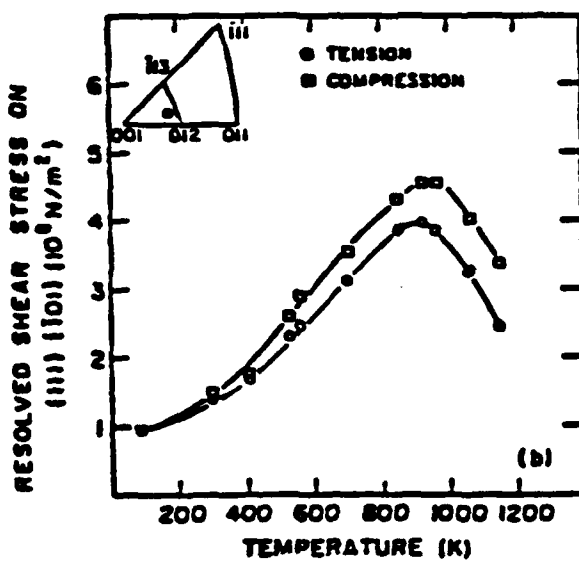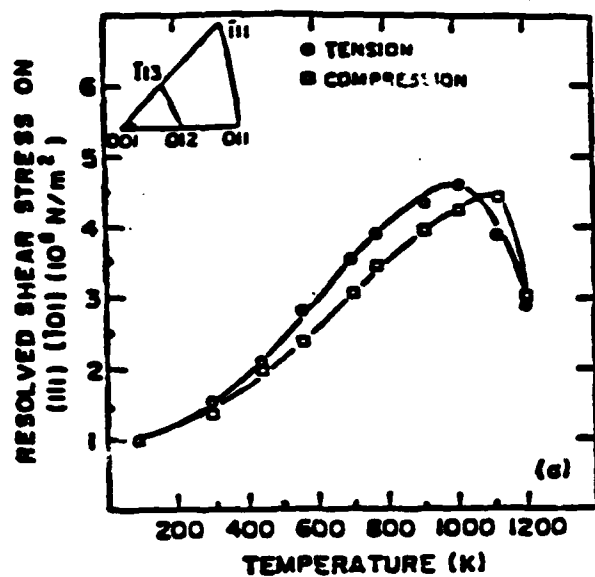
Fig. 1.3 Data from Ezz, Pope and Paidar[17] showing both tension-compression asymmetry and Schmid's-law violation in $Ni_3(Al,Nb)$ single crystals.

4

include some basis for the more than sixteen compounds with the $L1_2$ structure which are known to have a "normal" temperature-dependent flow stress.[14,15]

Despite abundant phenomenological evidence to support the essential aspects of several theories of the anomalous flow behavior in $L1_2$ alloys, there is a distinct lack of established, direct mechanistic evidence (such as direct observation of dislocation configurations during or after deformation, studies of the dislocation dynamics and mobility, and experimental quantification of parameters in the models) to support the models. Only in the last four years has such evidence appeared in the literature. A certain lack of tenability persists, however, in many of the specific dislocation mechanisms proposed to govern the flow behavior.

The effects of alloying on the mechanical behavior of Ni_3Al include both those due to deviations from the stoichiometric composition and those due to ternary element effects. As the discussion in Chapter 2 reveals, two distinct approaches toward describing the alloying behavior of Ni_3Al have appeared in the literature. One approach involves applying the classical concepts of solution hardening based on descriptions of the interactions which can occur between a single solute atom and a lattice dislocation subjected to an applied stress.[18-22] Statistical models relate these discrete interactions to a composition-dependent strengthening increment, $d\tau/dc$, by describing the frequency of their occurrence and the effectiveness of the interactions in inhibiting slip. The interactions of the elastic strain field of the solute atom and either an edge or screw dislocation are usually the most important in disordered solutions. In all classical solid-solution-hardening theories, a fundamental attribute is provision of a relationship for the variation of flow stress with temperature, $d\tau/dT$, which is on the same scale as the variation of the shear modulus with temperature, $d\mu/dT$.

The pronounced anomalous flow behavior in Ni_3Al provides a clear phenomenological indication that a mechanism(s) beyond classical elastic interactions dominates the deformation behavior of this material. A more recent approach to understanding solute behavior in ordered materials has been to apply the concept of phase stability, as measured by relative fault energies in an ordered system, and to derive from this a description of the expected potency of hardening of a given element based on the chemistry of that element, that is, based on its position in the periodic table.[23] While this general concept is only qualitative to date, it implicitly includes the possibility of affecting the mechanism(s) of the anomalous flow behavior by solute additions. Despite the many interesting correlations which have emerged from numerous studies, neither classical solid-solution-strengthening theory nor the phase-stability concept has resulted in a self-consistent description of solution hardening integrated with the theories of the anomalous flow behavior.

The known phenomenology and the various descriptions of solute behavior in the literature gave impetus to the present investigation of the mechanisms of solid-solution strengthening in Ni_3Al-based alloys. Specifically, this effort was designed to determine whether the effects of solutes could be established within the framework of classical solution-strengthening theory and the state-of-the-art descriptions of the mechanism(s) governing the anomalous flow stress versus temperature relationship in these alloys. A critical aspect of this study was to seek a basis for solute effects not only within the mechanical-behavior phenomenology but also within observations of the dislocation substructure.

CHAPTER 2

BACKGROUND

2.1 DEFORMATION OF L1$_2$ SUPERLATTICE STRUCTURES

The background section of this dissertation assumes that the reader is familiar with the basic metallurgical concepts of a superlattice structure, a superdislocation and its partials, and the various shear faults which occur by the motion of superlattice partial dislocations (commonly referred to as superpartials). Aspects of these concepts relevant to the L1$_2$ structure are reviewed here. Throughout this dissertation the terms dislocation core, core structure, and core dissociation are meant to encompass all superlattice partials and adjoining faults making up the total superlattice dislocation. The nomenclature required to distinguish further detail within the core will be given as additional concepts are introduced.

The L1$_2$ structure of Ni$_3$Al was shown schematically in Fig. 1.1. When the prospects for slip in any structure are being considered, lattice-translation vectors having the smallest magnitude are typically examined first since they provide the minimum dislocation energy through the first-order Frank criterion (b^2, where b is the magnitude of the Burgers vector, **b**). For the L1$_2$ structure these vectors are the <001> directions of the primitive lattice. However, after consideration of other criteria such as pre _rred s..p along the closest packed directions and minimization of the total energy of the dislocation after possible core dissociations, it becomes apparent that several geometric possibilities exist for dissociations in the octahedral planes. In particular, dislocations with total Burgers vector, **b** = a_0<10$\bar{1}$>, become important. Reactions of these dislocations have been reviewed by Pope and Ezz[5] and are shown schematically in Fig.   .

7

a. APB on (111)

$$\perp \overset{\text{APB}}{\underset{////////////}{}} \perp$$

$[\bar{1}\,0\,1] = 1/2[\bar{1}\,0\,1] + 1/2[\bar{1}\,0\,1]$

b. APB + CSF on (111)

$$\rfloor \overset{\text{CSF}}{\underset{\text{xxxx}}{}} \llcorner \overset{\text{APB}}{\underset{////////////}{}} \rfloor \overset{\text{CSF}}{\underset{\text{xxxx}}{}} \llcorner$$

$[\bar{1}\,0\,1] = 1/6[\bar{1}\,\bar{1}\,2] + 1/6[\bar{2}\,1\,1] + 1/6[\bar{1}\,\bar{1}\,2] + 1/6[\bar{2}\,1\,1]$

c. SISF on (111)

$$\perp \overline{\text{SISF}} \perp$$

$[\bar{1}\,0\,1] = 1/3[\bar{2}\,1\,1] + 1/3[\bar{1}\,\bar{1}\,2]$

d. APB, CSF & SISF on (111)

$$\rfloor \overset{\text{CSF}}{\underset{\text{xxxx}}{}} \llcorner \overset{\text{APB}}{\underset{//////}{}} \perp \overline{\text{SISF}} \perp \overset{\text{APB}}{\underset{//////}{}} \rfloor \overset{\text{CSF}}{\underset{\text{xxxx}}{}} \llcorner$$

$[\bar{1}\,0\,1] = 1/6[\bar{1}\,\bar{1}\,2] + 1/6[\bar{2}\,1\,1] + 1/6[\bar{1}\,2\,\bar{1}] + 1/6[1\,\bar{2}\,1] + 1/6[\bar{1}\,\bar{1}\,2] + 1/6[\bar{2}\,1\,1]$

e. SISF & SESF on (111)

$$\perp \overline{\text{SISF}} \rfloor \text{SESF} \perp$$
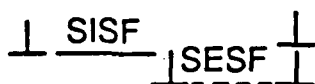
$[\bar{2}\,1\,1] = 1/3[\bar{1}\,2\,\bar{1}] + 1/3[\bar{1}\,\bar{1}\,2] + 1/3[\bar{2}\,1\,1] + 1/3[\bar{2}\,1\,1]$

Fig. 2.1   Possible octahedral dislocation-core dissociations in L1$_2$ structure. Notation
described in text.

8

Kear *et al*.[24-26] have considered each of these possible dislocation reactions with regard to the deformation behavior of Ni-base superalloys. The fault produced by an $a_0/6<11\bar{2}>$ dislocation (the Shockley partial in disordered fcc) is commonly referred to as the complex stacking fault or CSF. In the $L1_2$ structure, such a fault is produced by core dissociations as in Figs. 2.1(b) and (d) which show the dissociation of each of the superpartials of type $a_0/2<10\bar{1}>$ of Fig. 2.1(a). Consequently, the formation of a CSF is referred to hereafter as a superpartial core dissociation or superpartial core. Likewise, in the ordered-fcc-derivative $L1_2$ structure, a fault vector equivalent to a Shockley partial of the ordered lattice, $a_0/3<11\bar{2}>$, produces a shear fault referred to as a superlattice intrinsic stacking fault or SISF, as shown in Fig. 2.1(c). These faults occur simultaneously in the dissociation scheme depicted in Fig. 2.1(d). Finally, an intrinsic-extrinsic stacking-fault pair, with Burgers vectors of the superlattice, is depicted in Fig. 2.1(e). This configuration has been reported only after creep deformation of superalloys.[24,27]

Yamaguchi and co-workers[28-30] considered the stability of these configurations using pair potentials. The configuration in Fig. 2.1(c) was shown to be stable in all cases on the basis of symmetry conditions alone, while all other core configurations were dependent upon the magnitude and sign of the CSF and the antiphase-boundary (APB) energies, as given by variations in the specific interatomic force descriptions used. The configuration of Fig. 2.1(b) was found to exist with the CSF being spread in either the (111) or the (1$\bar{1}$1) plane with essentially equal energy, the importance of which will be shown later. As the CSF energy was increased to the point of instability of this fault, each superlattice partial dislocation was found to be dissociated in (111) and (1$\bar{1}$1) simultaneously.

Another critical point to consider with respect to formation of alloys having the $L1_2$ structure is the APB energy variation with boundary plane. Flinn[31] was the first to

consider this aspect of simple superlattice structures. He specifically addressed the $L1_2$ structure and the energy of the APB produced by the planar dissociation of an $a_0[110]$ dislocation core into two $a_0/2[110]$ superpartials. By taking into account only nearest-neighbor bond violations in a pair-wise interaction model, Flinn's calculations show a smooth variation and a high degree of anisotropy in the APB energy for an $a_0/2[110]$ fault vector as a function of the boundary plane containing the APB. Several crystal planes (most notably the cube plane in the zone of the fault vector) should have an APB energy which is significantly less than that on the octahedral slip planes. For the $a_0/2[110]$ fault vector, the (001) plane has a particularly low APB energy since no first near-neighbor bond violations are created with this fault. Flinn's analysis also considered the formation of a nonconservative APB or an APB described by a displacement vector which is noncoplanar with the fault plane. For the fault vector $a_0/2[110]$, several nonconservative APB planes of lower energy exist in addition to the conservative (001). Refinements by Paidar[32] have included higher neighbor interactions and have shown that the variation in energy is neither smooth nor continuous and that discrete, low-energy nonconservative orientations exist for planes of type $(10n)$. Recently, Beauchamp *et al.*[33] and Douin *et al.*[34] have reconsidered this analysis using atomistic simulation methods for examining the effects of atomic relaxation in the vicinity of the APB and have suggested that these earlier analyses may not be valid in general.

The two aspects of the $L1_2$ structure which have been reviewed above (namely, the core configurations and the anisotropy of the APB energy) form the basis for the models available for describing the anomalous variation of flow stress with temperature in Ni_3Al. In the following subsections, the origin of these models is reviewed following the chronology of their development.

2.2 ANOMALOUS FLOW BEHAVIOR IN Ni₃Al

2.2.1 INITIAL CONCEPTS

Flinn[31] was the first to consider the effects of temperature on flow stress during deformation of superlattice structures. His calculations revealed that, in general, the lowest energy configuration for a dissociated dislocation pair connected by an APB is not in the glide plane. For a pair of pure-screw $a_0/2[110]$ dislocations, the minimum occurs for a common dislocation plane of (001), as noted earlier. Calculations, within isotropic elasticity, of the total energy of two parallel edge superpartial dislocations along [11$\bar{2}$] connected by an APB ribbon revealed that the separation of these dislocations in the (111) glide plane is actually a metastable configuration due to the high elastic energy of the interaction between the edges on (111). The absolute minimum would occur with the edges dissociated in the ($\bar{1}$10) plane. Flinn argued that during deformation at high temperatures, thermal activation allows the superlattice dislocations to lower their self-energy by climb processes which extend the APB on the low-energy planes, leaving them in sessile configurations and giving rise to an increase in the flow stress. These dissociated segments remain sessile either until the applied stress is raised sufficiently to allow the separated superlattice partials to move on parallel glide planes, forming APB tubes in their wake, or until the thermal energy is increased sufficiently to allow the APB to move with the superlattice partials by a diffusive mechanism. In addition, Flinn provided the first experimental evidence that the flow stress of an ordered L1₂ Ni₃Al-Fe alloy increases with increasing temperature

Critics of Flinn's model point out that the anomalous flow-stress change is evident at temperatures typically considered insufficient to support significant climb and, further, that the model does not specifically take into account the breakdown of Schmid's law. Also, as first pointed out by Davies and Stoloff,[35] such diffusion-controlled processes

should cause a high strain-rate sensitivity of the flow stress; however, no strain-rate sensitivity is observed in Ni_3Al. Flinn apparently failed to observe the ease with which screw dislocations can cross-slip into sessile configurations.

In two very important early studies, Davies and Stoloff[35,36] examined both polycrystalline and single-crystal Ni_3Al. Through both low- and high-temperature pre-straining, aging, and re-straining experiments, they demonstrated that the flow stress of Ni_3Al is a function of temperature alone and that neither strain aging nor climb events affect the flow stress. This point was further demonstrated by quenching samples from several high temperatures and testing them at room temperature; the flow stress was found to be independent of quench temperature. From this demonstrated reversibility they concluded that the flow stress was governed by an intrinsic increase in the lattice resistance to slip. They also demonstrated that the Stage II work-hardening rate is reversible with tempera-ture—a point which is often overlooked.

To explain the high strain-hardening rate of Ni_3Al, Copley and Kear[37] adopted a cross-slip model originally introduced by Kear and Wilsdorf[38,39] to describe the unusually high strain-hardening rate in ordered Cu_3Au. Their model adopts Flinn's theoretical treatment of APB energy in suggesting that screw dislocations become immobi-lized due to thermally activated cross-slip (rather than climb dissociation) from the octahe-dral planes of high APB energy to the cube planes where the APB creates no nearest-neighbor bond violations (a configuration commonly referred to as a Kear-Wilsdorf or K-W lock). The adaptation of the model was a direct result of evidence from Kear and Hornbecker[40] revealing that the dislocation configurations in Ni_3Al were similar to those in Cu_3Au. They suggested that constriction of the CSFs as the temperature is raised would be sufficient within a Peierls model (a model where lattice-friction stress varies directly with dislocation-core width) to cause the lattice intrinsic hardening required by Davies and Stoloff.[35] However, they could provide neither a quantitative expression for yielding

12

within this model nor evidence to support their view of the temperature dependence of the CSF energy. As will be shown, these important papers laid the groundwork for what is now known as the "cross-slip pinning" model for anomalous flow-stress behavior in Ni_3Al.

In 1970 Thornton, Davies, and Johnston[41] (hereafter referred to as TD&J) reported the results of a comprehensive study of the deformation behavior of alloyed single crystals of Ni_3Al. They observed and discussed virtually every critical aspect of the now-common descriptions of the flow-stress variation with temperature relationship of this material and included electron-microscopic evidence in support of some of their conclusions. First, they observed that flow stress as a function of temperature was essentially athermal when measured in the microstrain (10^{-5}) regime. Through strain-rate-change tests, they measured an activation volume for the thermally activated component of the flow stress of 25 - 300 b^3, where b is the magnitude of the the total dislocation Burgers vector **b**. Cube slip ($\{001\}<1\bar{1}0>$) was observed in specimens deformed in the <144> orientation at temperatures above 400 °C. On the basis of electron microscopy which revealed long, straight screw dislocations at all temperatures and loop debris at high temperatures, they concluded that debris hardening due to an increased propensity for cube slip with increasing temperature governs the flow stress at high temperatures. The anomalous flow stress is viewed as a continuous transition from Stage I easy-glide at low temperatures to entirely Stage II flow with a very high strain-hardening rate at high temperatures. The mechanism of strain hardening is K-W lock formation. TD&J argued that low temperature flow is governed by exhaustion of edge dislocations which glide relatively easily (as noted by their absence) at low temperatures. These conclusions were based on observations of the dislocation structure after straining to 4% nominal strain. The "reversibility" of the flow stress and the strain-hardening rate reported earlier by Davies and

Stoloff[35,36] was largely ignored. However, TD&J simply stated that the reported mechanisms should provide for both reversibility and low strain-rate sensitivity.

Several major inconsistencies exist in the TD&J view of flow-stress behavior. First, criticism of the TD&J concept was readily apparent from the observation made by Copley and Kear[37] that the flow stress exhibits the anomalous effect even in the <001> orientation. For this orientation the Schmid factors on the {001}<110> systems are zero, making cube slip difficult. Thornton[42] offered an explanation for this based on dislocation-dislocation interactions in a pile-up on the slip plane causing a net shear stress on the cube planes. This isotropic elastic analysis does not provide a mechanism, however, for the formation of strong dislocation pile-ups in single crystals.

Perhaps the single greatest criticism of the TD&J concept of anomalous strengthening is the lack of explanation for the "reversibility" of flow stress and Stage II strain-hardening rate with temperature. In order for debris hardening to be reversible with temperature, a mechanism must be proposed by which the "forest" dislocations (formed from loop debris by local glide on {001}) recover when the stress is removed and the temperature lowered. Thornton et al.[41] propose no such mechanism. Therefore, one must offer an explanation for the ability of edge components, believed to dominate flow at low temperatures, to "cut" the "forest debris" existing at high temperatures without creating an increase in the flow stress at low temperatures. Furthermore, TD&J offer no explanation for the activation volume in Ni_3Al being lower than that in Cu, that is, they offer no explanation for the "forest" being easier to defeat in Ni_3Al. Thornton et al. report an activation volume in Ni_3Al which is two to twelve times smaller than that for Stage III recovery or "forest cutting" in pure Cu. However, if the Burgers vector, b/2, of the superlattice partial dislocation is used (that is, if the two superpartials act "independently") to redefine the measured activation volumes, the new volumes will be directly comparable to Stage III flow in Cu (200 to 2500 b^3 in Ni_3Al vs. 2000 b^3 in Cu). With this realization

14

it is likely that the strain-rate-change tests of TD&J are a measure of "forest cutting" volumes in Ni_3Al, which vary due to total strain level at which the measurement is made in this rapidly hardening material rather than the activation volume for the critical event governing the anomalous flow behavior. Without clearly defining a specific mechanism for the thermally activated event, it is impossible to determine which Burgers-vector magnitude is appropriate.

Finally, TD&J argued that the microstrain behavior, exhibiting only a modest increase with temperature (being "athermal" below 10^{-5} strain), is an indication that dislocations are mobile at low stresses at all temperatures, ruling out an increase in the lattice-friction stress with temperature. They apparently failed to recognize, as reported later by Mulford and Pope,[43] that only a comparatively few dislocations must move to produce a strain of 10^{-5} and that such strains may be achieved entirely by motion of mobile edge segments. Mulford and Pope observed that the dislocation substructure of Ni_3Al-W single crystals contains many mixed and near-edge-dislocation tangles after deformation at -196 °C. These investigators confirmed the "athermal" behavior of the microstrain and, based on electron microscopy, concluded that mobile edge components govern the microstrain at all temperatures. They observed that the flow stress at temperatures below -196 °C increases with decreasing temperature as in fcc metals and that edge and screw dislocations dominate the flow stress at liquid-helium temperature where both dislocation types are equally mobile.

2.2.2 TAKEUCHI AND KURAMOTO MODEL

Takeuchi and Kuramoto[44] (T&K) offered the first treatment of the anomalous flow-stress behavior of $L1_2$ materials in terms of a thermally activated cross-slip process. Through studies of Ni_3Ga single crystals, which exhibit the same three regions of flow variation with temperature as depicted in Fig. 1.2, T&K demonstrated that the critical

15

resolved shear stress (CRSS) on the primary {111}<110> system is orientation dependent or that Schmid's law does not hold. A model was proposed which described the flow stress in terms of a drag stress (and velocity change) produced by portions of screw dislocations cross-slipping into the K-W configuration. T&K envisioned the flow stress as a Friedel[45] percolation problem, wherein a critical line-tension-dependent bowing angle must be achieved on a long screw-dislocation segment in order for the dislocation to defeat a pinning point and traverse laterally to the next obstacle. They treated the major temperature-dependent component of the flow stress, τ^*, in terms of the frequency of obstacle formation. This frequency is viewed as a thermally activated process which is dependent upon the resolved shear stress on the {010} cross-slip plane as well as temperature; thus,

$$\tau = \tau_0 + \tau^* \qquad [2.1]$$

where

$$\tau^* \propto \exp\left(-\frac{H - V^*\tau_{(010)}}{3kT}\right) \qquad [2.2]$$

and τ_0 is the "athermal" flow stress given by the flow stress at -196 °C. In Eq. [2.2], H is the activation enthalpy for obstacle formation, V^* the activation volume and $\tau_{(010)}$ the resolved shear stress on the cube cross-slip plane; k and T have their usual meaning. The model directly takes into account the breakdown of Schmid's law through the $\tau_{(010)}$ parameter; however, the tension-compression asymmetry was neither recognized nor accounted for in their model. By determining the slopes of the $\tau_{(010)}/kT$ versus $\log(\tau)$ plots, the activation volume was estimated to be 6 b^3, where b = |b|/2 and b is the total Burgers vector. Note that an activation volume of this magnitude scales readily to the area swept by forming a constricted Shockley partial node on a dissociated $a_0/2<110>$ superpartial dislocation. When V^* is taken to have the usual definition,[46] or

16

$$V^* = bdl \qquad [2.3]$$

where d is the critical activation distance or displacement, b the magnitude of the Burgers vector, and l a characteristic length of the activated configuration, then an activation volume of magnitude corresponding to that reported by T&K would yield a characteristic activation length of only 0.5 nm. Clearly, such an activation volume suggests physical events which are significant only on the scale of a few atomic spacings, just as the superpartial core dissociation in Ni_3Al is estimated to be.[47,48]

The next critical factor believed to govern the flow stress of anomalous Ll_2 compounds was suggested by Lall and co-workers.[49] Their studies of $Ni_3(Al,Nb)$ single crystals uncovered an effect of orientation upon the measured CRSS for {111}<110> slip which was inconsistent with that analyzed by T&K. The behavior of these crystals was rationalized by considering the fact that dissociation of the superpartial cores into $a_0/6$<112> components must occur in a sequence which results in mirror symmetry about the <110> direction, yielding antiparallel edge components of magnitude $a_0/12$<112>. Consequently, the shear-stress component acting on these cores will tend to either constrict or expand them in the glide plane. This tendency reverses upon reversal of the sense of the applied stress. Lall *et al.* described the flow stress by modifying the exponential term in the relationship for τ^* developed previously by T&K (Eq. [2.2]). The new relationship was given as

$$\tau^* \propto \exp\left(-\frac{H + V_1\tau_1 + V_2\tau_2 + ...}{3kT}\right) \qquad [2.4]$$

where the term $V_1\tau_1$ takes into account the resolved stress on the cube cross-slip plane and the term $V_2\tau_2$ was added to account for the resolved stress on the edge components of the Shockley partials which act either to extend or constrict them. Lall *et al.* recognized that

17

any number of effects might be taken into account by modifying the exponential term within the basic T&K cross-slip concept.

Ezz, Pope, and Paidar[17] verified the findings of Lall *et al.* and specifically demonstrated in tests on the same specimen that the CRSS is dependent upon the sense of the applied stress (a tension-compression asymmetry exists). More importantly, however, Ezz *et al.* found the flow stress of $Ni_3(Al,Nb)$ single crystals to be dependent not only upon the resolved stress which acts to constrict or expand the $a_0/2<110>$ superpartial cores (with screw orientation) on the primary glide plane, (111), but also upon the applied stress which acts to constrict or expand them on the octahedral cross-slip plane, $(1\bar{1}1)$. This dependence was interpreted within the Stroh-Friedel-Escaig model[50-55] for cross-slip in ordinary fcc metals wherein the stresses acting upon the octahedral cross-slip plane alter the driving force for cross-slip by tending to favor or retard the extension of double kinks on the cross-slip plane. These findings, like those of Lall *et al.* were viewed as an extension of the T&K concept of the mechanism of the anomalous flow stress.

2.2.3 PAIDAR, POPE, AND VITEK MODEL

The state-of-the-art in phenomenological understanding of the anomalous flow stress in materials having the $L1_2$ structure is embodied in the model developed by Paidar, Pope, and Vitek[56] (hereafter referred to as PP&V). Their model is based on the following critical concepts developed in the review above: i) the analysis by Flinn[31] (and the refinements thereof) which suggests that the cube-plane APB energy is significantly lower than that for the octahedral planes, ii) the atomic simulations by Yamaguchi *et al.*[28-30] which show that the dissociated components of the superpartial-dislocation cores are not, in general, contained within the octahedral glide plane, iii) the development by Escaig[54] and by Ezz *et al.*[17] which suggests that the sense of the stress on the superpartial dislocation cores acts to vary the orientation dependence of the flow stress, and iv) the early qualitative

18

model by T&K which suggests that the flow stress is governed by local pinning points creating a drag stress and the concomitant velocity reduction in gliding screw dislocations. The PP&V model is developed from the concepts of constriction of superpartial cores in (111), cross-slip into (010), double-kink extension on (010), and re-dissociation of the superpartial cores in either (111) or $(1\bar{1}1)$, as depicted in the sequence of Fig. 2.2. This schematic diagram shows the steps in the specific mechanism for the local pinning points along screw dislocations called out in the T&K model. Here the important scaling parameters, such as the resolved stress components and the kink dimensions, are shown for double-kink extension in the (010) plane. The critical concept introduced in this model is that of the cross-slip-segment dimensions being small, both in length and width, when compared to the expected APB width on (111). By viewing this mechanism as a thermally activated process, PP&V developed a specific form for the activation enthalpy. The driving force and activation barrier for locally transforming a glissile dislocation core into a sessile configuration are shown schematically in Fig. 2.3. The activation barrier is proportional to the CSF energy since the increase in line energy, as well as the interaction energy between constricted Shockley partials, is a function of their initial separation width. The driving force for cross-slip within the PP&V model is dependent only upon the reduction in dislocation energy obtained by having the APB between two superpartials reside on a lower energy (010) plane.

Paidar et al.[56] use the same form as T&K for the temperature depen 1e: c of the flow stress

$$\tau^* \propto A \exp\left(-\frac{H}{3kT}\right)$$

[2.5]

19
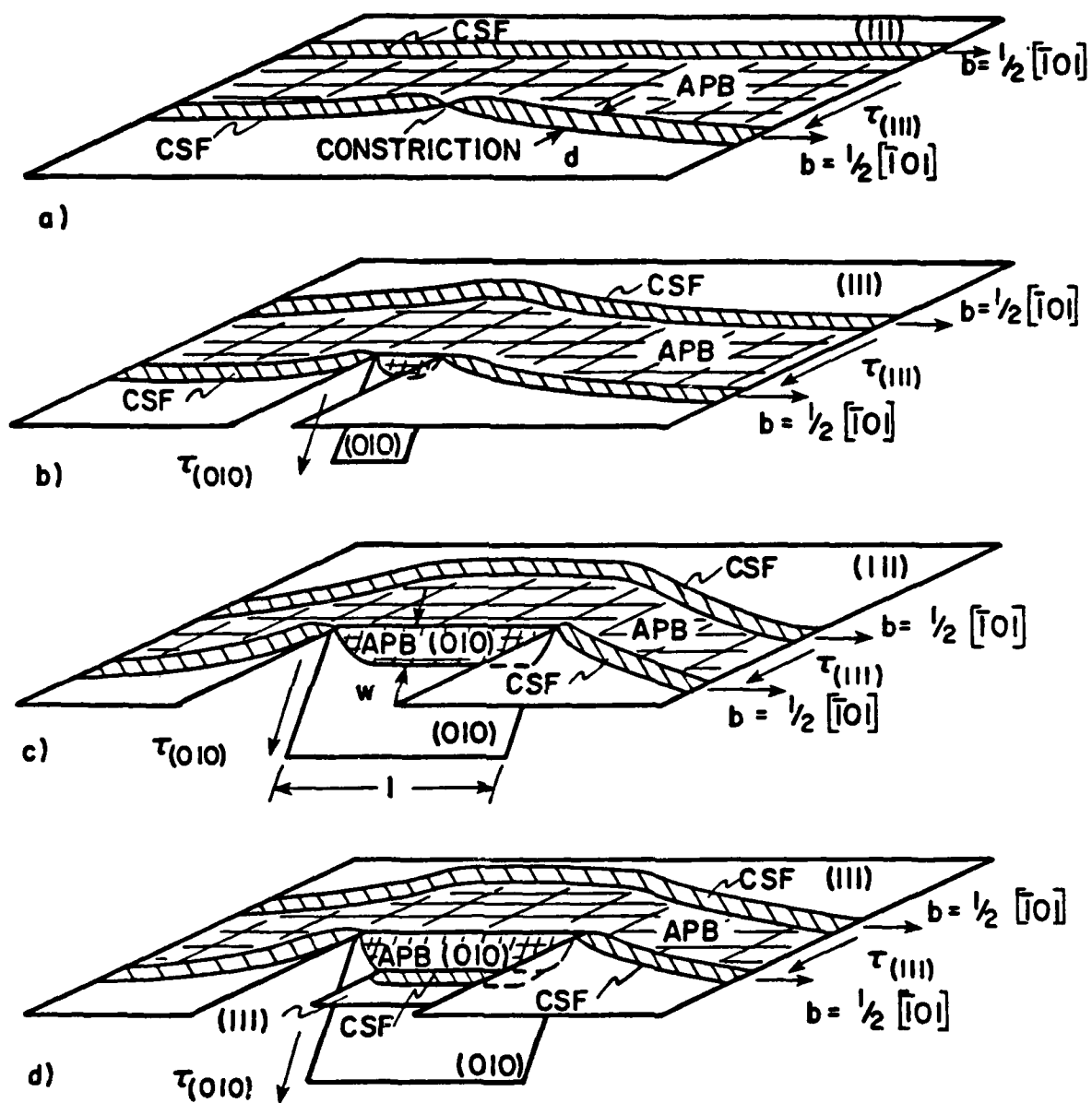
Fig. 2.2   Pictorial description of cross-slip process described by Paidar, Pope, and Vitek
model; a) constriction of leading superpartial core, b) bowing out on cube
cross-slip plane, c) critical stable width and length of double kink formed on
cube cross-slip plane, and d) re-dissociation of leading superpartial core into
octahedral plane.
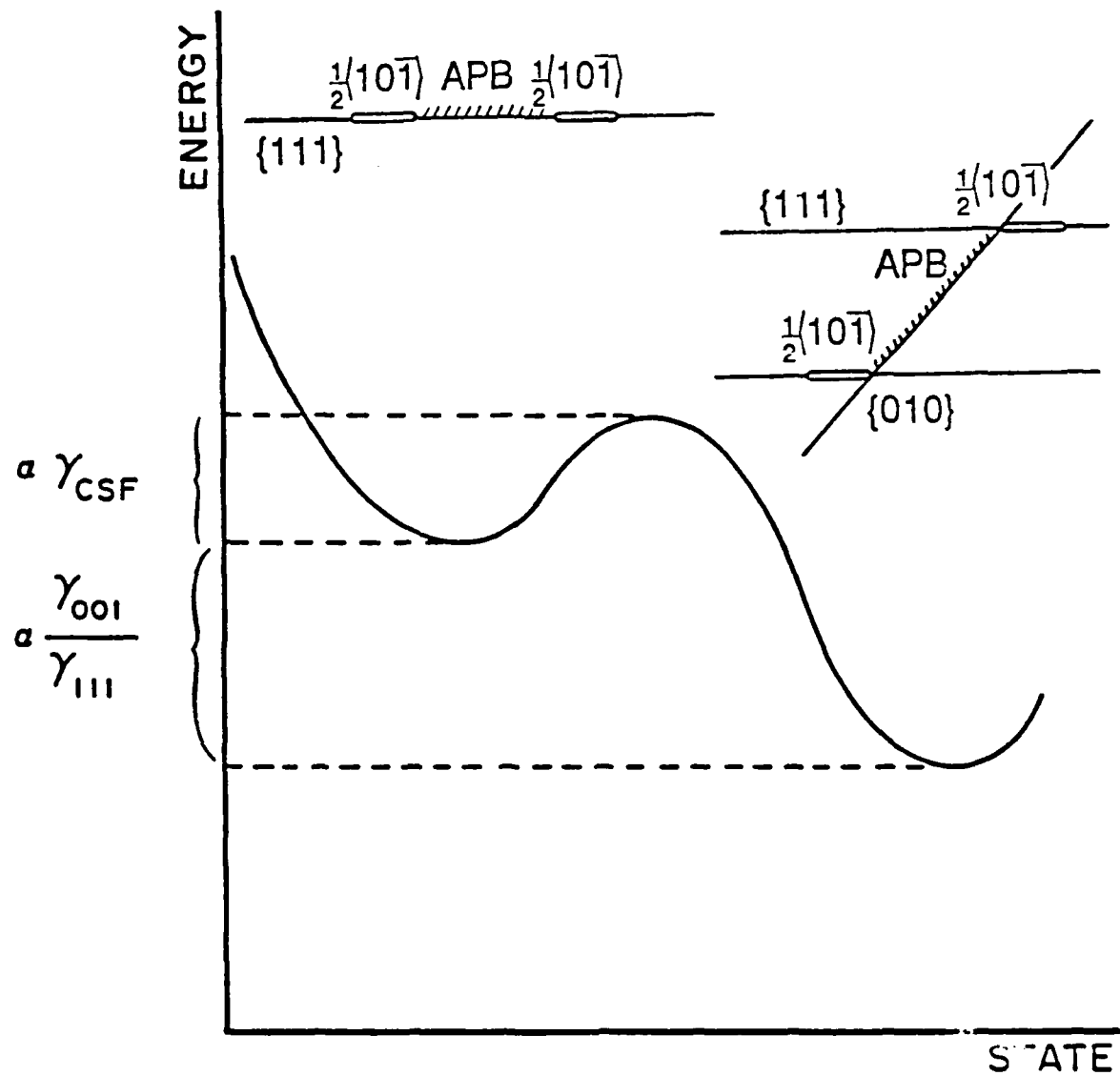
Fig. 2.3 Schematic representation of energetics for core transformation from glissile configuration to "sessile" Kear-Wilsdorf configuration.

where A is a constant of proportionality. The specific form for the activation enthalpy, H, which they developed within the double-kink model, is quite complicated and contains specific terms for the appropriate resolved stress components (normalized to the APB energy over the Burgers vector) as well as the possible jump directions for double-kink formation. However, the enthalpy term for the most favored cross-slip event (Eq. 23 of PP&V[56]) may be expressed in the following reduced form:

$$H = A + \frac{Mb}{2}K\kappa\tau_{(1\bar{1}1)} - \left[C + B\tau_{(010)}\right]^{\frac{1}{2}}$$

[2.6]

where A, C, and B are material-dependent constants which include specific parameters in the Escaig analysis[53] for the resolved-shear-stress components on the cross-slip plane, the CSF energy, and the APB energy on both the (111) and (010) planes; $M = \mu b^2/2\pi$; K is a function of the Schmid-factor ratios N and Q (as defined by Lall et al.[49]); κ is from the Escaig analysis;[53,56] and $\tau_{(1\bar{1}1)}$ and $\tau_{(010)}$ are the resolved-stress components on the primary (111) and cube cross-slip planes, respectively. The critical aspect of the PP&V model for the cross-slip activation enthalpy is that the second term on the right-hand side of Eq. [2.6] directly takes into account the tension-compression asymmetry, while the last term addresses the breakdown of Schmid's law or the orientation of the applied stress (although, as described above, the two effects cannot be completely separated). The original PP&V form of the term in square brackets in Eq. [2.6] above contains the specific form of the driving force for cross-slip, which is given as

$$\Delta E = M\left(\frac{1}{\sqrt{3}} - \frac{\gamma_{010}}{\gamma_{111}}\right)\frac{w}{R}$$

[2.7]

where ΔE is the energy gain by cross-slip; γ_{010} and γ_{111} are the APB energies on the cube cross-slip and primary octahedral glide planes, respectively; w is the double-kink width

22

(about 3b); and R is the stress-free spacing of the $a_0/2<110>$ superlattice-partial dislocations before cross-slip. This form of the driving force yields a limiting condition— the ratio of the APB energy on (111) to that on (010) must be of greater magnitude than $\sqrt{3}$ for cross-slip to be favored. Later, Yoo[57-59] made an important modification to the driving force for cross-slip used by PP&V by including a term for the elastic-interaction stresses between the superpartial dislocations. Following the formalism of Foreman[60] and Stroh,[61] Yoo showed that an out-of-plane interaction stress exists that arises from the anisotropic elastic behavior of the material, and that it can be as large as 60% of the in-plane or radial interaction stress between superlattice partials in Ni_3Al. Yoo's modification of the driving force for cross-slip will not be discussed here—but in Chapter 5 since the specific research results presented in this dissertation deal directly with the role of this new term.

2.3   ELECTRON MICROSCOPY AND ANOMALOUS FLOW BEHAVIOR

Prior to 1984, several transmission-electron-microscopy (TEM) investigations of the deformation substructure of Ni_3Al were conducted by a number of investigators, primarily under bright-field imaging conditions.[40,41,43,62-66] These studies established that in Ni_3Al and alloys thereof, the low-temperature (room temperature and below) deformation substructure consists primarily of wavy dipole dislocation lines of mixed and edge character. As the temperature of deformation is raised, the substructure in Region II becomes dominated by extended, straight screw dislocations aligned in the <110> directions. Oblak and Rand[67] and Staton-Bevan and Rawlings[63] provided weak-beam dark-field and detailed bright-field images, respectively, indicating that the extended, straight screw dislocations are in a Kear-Wilsdorf cross-slipped configuration (K-W locks). Most of these studies, with one notable exception,[63] have also reported the existence of SISF-coupled dislocations in the substructure which are likewise aligned in the

23

<110> directions and are either antiparallel $a_0/3<112>$ or dissociated $a_0/3<112>$ super-lattice partial dislocations.[66] Without a clear basis (again, with the Staton-Bevan and Rawlings study being an exception), these studies concluded that the deformation behavior of Ni_3Al-based alloys is governed by the motion of $a_0<110>$ superlattice dislocations, even though the SISF-coupled dislocations are often observed. These investigators further concluded that SISF-coupled dislocations play no role in the anomalous flow behavior of Ni_3Al.

While the studies cited above have identified a few common features in the deformation substructure of Ni_3Al, they have provided little or no insight into the mechanism(s) governing the anomalous flow behavior of Ll_2 alloys. For example, only the study by Oblak and Rand[67] reports a value for the APB energy in Ni_3Al, and this value is only for the (010) plane. The critical parameters in the T&K/PP&V model for anomalous flow remain unaddressed in these early studies. The studies reviewed in the remainder of this section appeared in the literature over the time period when the research reported in this dissertation was being conducted. Several of the studies reviewed below have raised new critical questions which directly challenge the T&K/PP&V model regarding the mechanism of anomalous-flow-stress behavior in Ni_3Al. In this section, the results of these studies are cited without critical review. Such review is reserved for the discussion section of this dissertation (Chapter 5).

The climb-dissociation mechanism postulated by Flinn[31] was reconsidered by Veyssière et al.[68,69] in recent weak-beam dark-field studies which included analysis of dislocation cores formed during high-temperature deformation of Ni_3Al. Clear evidence of both cube-plane glide and dislocation cores dissociated by climb processes was found in polycrystalline samples deformed at 800 °C. Dislocation segments of mixed character were often found to be dissociated by climb, with the adjoining APB residing on an {013} plane. Furthermore, no evidence indicating K-W cross-slip could be found. While these

results do not eliminate the K-W mechanism from consideration, they do suggest that Flinn's analysis should not have been discounted so readily, particularly in cases of deformation at temperatures near the peak temperature. Veyssière *et al.* conclude that some cross-slip mechanism must dominate the low-temperature behavior even in Region II since diffusive processes do not occur readily over most of the Region II temperature range.

In a separate study, Veyssière *et al.*[70] treated the formation of SISF dissociations, again in polycrystalline Ni$_3$Al deformed over the range of Region II flow. They concluded that although the dislocation reactions

$$a_o<1\overline{1}0> \rightarrow a_o/2<1\overline{1}0> + a_o/2<1\overline{1}0> \rightarrow a_o/2<1\overline{1}0> + a_o/6<11\overline{2}> + a_o/3<1\overline{2}1> \quad [2.8]$$

should not be favored according to line-energy arguments, they may be favored due to elastic interactions between superlattice partials; in fact, they do occur over the temperature range 350 to 650 °C. Also in this study, Veyssière *et al.* report a value for the SISF energy which ranges from 5 to 15 mJm^{-2} and values for the {111} APB and {010} APB energies of 180 mJm^{-2} and 140 mJm^{-2}, respectively. These values yield an APB-energy ratio of 1.28, which is less than the critical value of 1.73 required in the cross-slip model of PP&V. Douin, Veyssière, and Beauchamp[71] later suggested a change in these fault-energy values after making the correction for the anisotropic elastic properties of Ni$_3$Al. The new values for the {111} and the {010} APB energies were 111 ± 1⁵ mJm^{-2} and 90 ± 5 mJm^{-2}, respectively, yielding a new APB-energy ratio of 1.23, which still falls short of the critical value in the PP&V model.

In 1988 Korner[72] reported the results of a weak-beam electron-microscopy investigation of deformed single crystals of Ni$_3$(Al,Ti). He found that crystals having an orientation near [$\overline{1}$11], with a maximum resolved shear stress on (001), which were deformed in compression at room temperature contained truncated dislocation loops

extended on the cube cross-slip plane, (010). He further reported that the APB energies on the {001} and {111} planes were equivalent, having a value of 250 ± 30 mJm^{-2}. Korner interpreted these results as being in conflict with the concept of cross-slip pinning proposed by T&K. Rather, he adopted the concept introduced by Thornton et al.[41] wherein the increased propensity for cube slip with increasing temperature provides an increased frequency of pinning points on dislocations and, hence, an increase in flow stress with temperature.

Sun and Hazzledine[73] made a highly relevant observation concerning the nature of a_o<110> dislocations within the gamma-prime phase of a superalloy having a high volume fraction of Ni$_3$Al precipitates. They noted, through weak-beam dark-field TEM studies, that dislocations in K-W lock configurations are not, in general, perfectly straight; rather they contain many small kink segments extending parallel to the screw-oriented dislocation line, defined by Sun and Hazzledine as "superkinks." Furthermore, they observed two distinct types of kinks—those whose a width is less than the APB width and those whose width is significantly greater than the APB width. The most important observation by Sun and Hazzledine, however, is that these kinks should have glissile edge segments joining them to the K-W lock dislocation line and that under an applied stress, the kinks are free to move along the screw line and propagate it through the crystal. These authors were the first to suggest that the K-W lock configuration is not really a "lock" at all—the configuration remains mobile by double-kink formation, just as screw dislocations remain mobile by thermal activation of double kinks in bcc metals.

Mills et al.[74] recently reported similar observations to those of Korner[72] and Sun and Hazzledine[73] and concluded that edge segments, limited by the frequency of K-W locking, control the flow stress of Ni$_3$Al rather than the percolation of screw segments as proposed by T&K.[44] Veyssière[75] reviewed many of these recent observations and discussed them in conjunction with observations in other intermetallic materials. He

reached the conclusion that the cube cross-slip concept proposed by TD&J is well supported by recent TEM studies and provides the most consistent explanation for the source of pinning points which are thought to be necessary for limiting screw-dislocation mobility (K-W "lock" mobility) and controlling the anomalous increase in flow strength with temperature in Ni_3Al.

The most recent TEM observations, which are relevant to the mechanism governing the flow stress of Ni_3Al, are the weak-beam dark-field results of Caillard *et al.*[76] which were recorded under *in situ* deformation conditions. Their observations suggest that screw-oriented $a_0<10\bar{1}>$ dislocations readily change the plane containing the <u>APB</u>, *back and forth*, from the (111) primary glide plane to the (1$\bar{1}$1) cross-slip plane to the (010) cube cross-slip plane. This evidence is interpreted as an indication that K-W locks are weak obstacles to glide (a point discussed in greater detail in Chapter 5). The $a_0<10\bar{1}>$ core transitions are reported to have an intermediate sessile configuration wherein the $a_0/2<10\bar{1}>$ superpartial cores (CSF-coupled dislocations) are split on (1$\bar{1}$1) with the APB residing on (111). While this configuration is not explicitly observed with the resolution of weak-beam dark-field microscopy, the core structure of the sessile configuration is inferred from the observed existence of a waiting time between sessile and glissile configurations (jerky glide). In all cases the transition, from a K-W sessile configuration with the APB spread on (010) to a glissile (gliding) configuration with APB on (111), has the intermediate sessile configuration with APB on (111).

Caillard *et al.* have interpreted the K-W/T&K/PP&V cross-slip model as one requiring "irreversible" locking events, a requirement which is considered to be inconsistent with their dynamic observations. They conclude from their observations that the most stable core configuration is one with the CSFs on (1$\bar{1}$1) and the APB on (111). As the temperature of deformation is raised, the CSF$_r$ *widen on* (1$\bar{1}$1) *which creates a* "continuous increase of the lattice resistance..."[76] The flow stress is then governed by

27

defeating these increasingly potent obstacles with the help of thermal activation. The specific implications of this model will be treated in greater detail in Chapter 5; however, it is important to note here that the observations made under *in situ* deformation conditions of thin-foil specimens are subject to possible artifacts. The specific studies reported by Caillard *et al.* did not address these possibilities. One very important consideration which may effect their direct observations of APB-plane transformations is the action of surface-nucleated kinks. Atomic relaxations at the free surfaces will likely provide an "infinite" source of thermal kinks which could account for the rapid transformations observed over the entire dislocation line.

2.4 SUBSTITUTIONAL SOLUTES IN Ni$_3$Al

In ordered alloys, any model of solid-solution strengthening must include effects due to deviations from the stoichiometric composition. Figure 2.4, taken from the work of Noguchi *et al.*[77] on polycrystalline Ni$_3$Al and Ni$_3$Ga, shows that the effects on yield stress can be strong and are not necessarily equivalent for hypo- and hyper-stoichiometric deviations. In considering the framework of classical solid-solution hardening theory, the solute-dislocation interaction energies must be redefined for superlattice dislocations. In disordered metals the elastic interaction of a dislocation with a solute atom is proportional to b^2. The Burgers vectors of the ordered lattice are typically of greater magnitude (doubled in Ni$_3$Al) than those of the disordered lattice and, therefore, should have greater elastic interaction (not necessarily doubled) energies with solute atoms. New descriptions of the interaction energies must take into account not only the interchange between the solute-atom strain field and the superlattice partials but also the influence of the solute atom upon the APB and other fault energies associated with superdislocation cores. The fact that Ni$_3$Al is known to be elastically anisotropic does not make the problem of modeling solute-
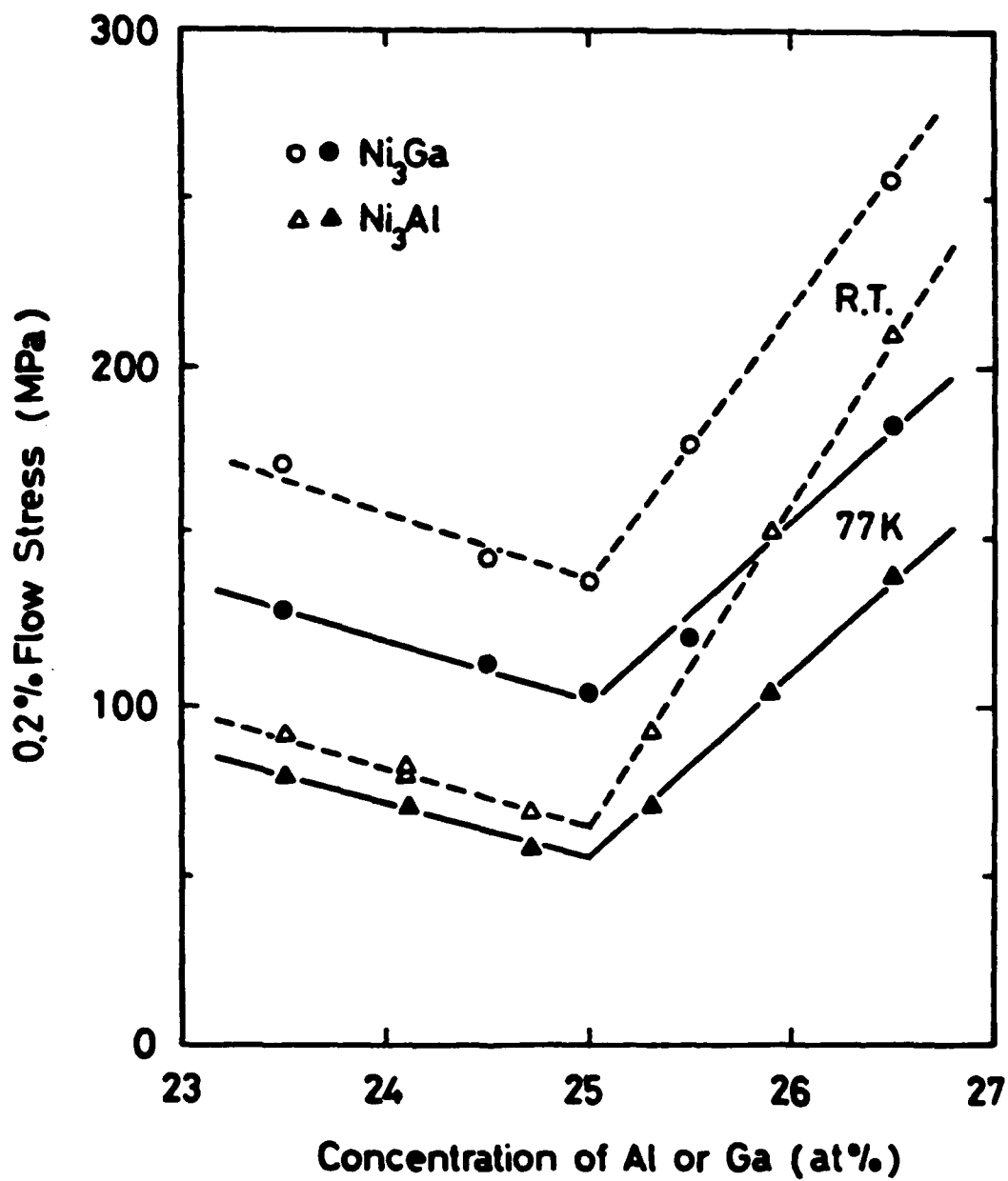
Fig. 2.4   Data from Noguchi, et al.,[77] showing asymmetric solid-solution strengthening about the stoichiometric composition in polycrystalline Ni_3Al and Ni_3Ga.

dislocation interactions more tractable. Once the individual elastic interactions are solved, the statistical nature of the interactions between dislocations and solutes may have to be reconsidered. In ordered materials the leading and trailing superlattice dislocations do not necessarily exhibit symmetrical behavior; in general, a larger, nonuniform interaction volume may be expected due to the expanded strain field of the paired dislocations. Therefore, the statistics of solute-dislocation interactions treated in classical solution-hardening theory may deviate from the Friedel and Labusch limits typically considered in disordered metals. Despite these possible limitations associated with directly applying the theory for disordered metals to ordered systems, an elasticity-based point-obstacle theory must provide a variation of flow stress with temperature which is less than zero ($d\tau/dT < 0$). For the $L1_2$ alloys which exhibit anomalous flow behavior, $d\tau/dT$ becomes greater than zero near room temperature. For this reason, solution-hardening theories based on elastic interactions between dislocations and solutes should be applicable only for a given temperature range and solute type which causes a decrease in the magnitude of $d\tau/dT$ and may not be relevant even in this case. For temperatures even slightly above room temperature, the effect of the mechanism(s) governing the anomalous increase in flow stress appear to dwarf any possible "classical" effects.

A review of experimental studies of solid-solution effects in Ni_3Al is given in the following two subsections. Those studies describing the behavior of Ni_3Al within the framework of classical solid-solution hardening for disordered metals are treated first, after citing observations from the TD&J study discussed above. Several of these studies are restricted to low temperature and have not addressed the mechanism(s) governing anomalous flow behavior. The second subsection is a review of the treatment of solution hardening as a change in crystal-structure stability.

2.4.1 CLASSICAL SOLUTION STRENGHTENING

The earliest significant evaluation of alloying effects in Ni_3Al was performed by Guard and Westbrook.[78] The most important contributions of this work involve the observation of anomalous flow-strength behavior through measurements of hardness change with temperature and data indicating that ternary additions affect anomalous behavior. Ternary-element substitutions for Ni and Al sites (or both simultaneously) were considered; however, elements substituting for Al were found to provide the most potent hardening increment (dh/dc). This increment could not be related specifically to atom-size effects as revealed by lattice-parameter change (da_0/dc), and no systematic study of modulus, electronic, or chemical factors was performed. The anomaly in the temperature dependence of hardness was attributed to strain aging since interstitials were observed to have an effect on hardness. However, later work by Davies and Stoloff[35] demonstrated that strain aging is insignificant in Ni_3Al; therefore, the work of Guard and Westbrook serves primarily as a data base of the solid-solution hardening effects of some of the more important alloying elements in Ni_3Al.

In an attempt to understand the temperature dependence of flow stress in Ni-base superalloys, Thornton et al.[41] investigated Ni_3Al with additions of Cr, Ti, and Nb. In addition to important contributions toward understanding the mechanism of the flow-stress anomaly, their work shows that Ti not only increases the flow strength at all temperatures but also accentuates the anomalous behavior by changing the rate of increase in flow strength with temperature and shifting the peak temperature. While Nb was found to provide a uniform shift of the flow-strength-versus-temperature curve to higher stresses, Cr caused an increase in peak temperature with little or no strengthening. These investigators concluded that the factors which control trends in flow stress are probably the

31

same for all alloys; consequently, they made no attempt to evaluate the differences in strength observed in terms of solution-hardening models.

Lopez and Hancock[79] made what appears to be the first systematic attempt to understand the effects of deviations from the stoichiometric composition and of Ti additions to Ni_3Al. Below the peak temperature, both Ni- and Al-rich compositions were found to be stronger than a near-stoichiometric alloy, with Al-rich deviations providing the greatest incremental strengthening. At temperatures greater than the peak temperature, the stoichiometric alloy proved to be strongest. Despite earlier work of Guard and Westbrook and their reference to an internal study at Pratt and Whitney, both of which suggested that Al-rich Ni_3Al contained excess Ni vacancies, Lopez and Hancock discounted vacancy-defect hardening as the prominent strengthening mechanism and argued that Al substitution on Ni sites was sufficient and appropriate to account for the strengthening. Later work showed Lopez and Hancock to be correct.

Two other important contributions from the work of Lopez and Hancock must be noted. First, in order to lay to rest suggestions that grain-boundary hardening was the source of strengthening in Al-rich compositions, they made microhardness traverses across grain boundaries. No evidence for boundary hardening was found. Secondly, with regard to Ti additions, they noted that Ti was a potent solid-solution strengthener, that it lowered the peak temperature, and that it promoted the onset of cube slip at lower temperatures. The inconsistency between these data and those of Thornton *et al.*[41] on the effects of Ti has been discussed in detail by Pope and Ezz.[5] The onset of cube slip at lower temperatures in Ti-containing material is an important aspect of using the cross-slip model to explain flow behavior. Within the cross-slip model, significant strengthening should occur at lower temperatures if more cross-slip to cube planes is promoted at these lower temperatures. While Lopez and Hancock provided interesting results which showed the sensitivity of Ni_3Al to alloying, they made no attempt to analyze their results within the

framework of Fleischer's theory of solution strengthening which was well developed for disordered solutions at that time.

The first clear attempt at understanding the yield behavior and solution hardening of Ni_3Al in terms of the theory for disordered metals is contained in the Ph.D. dissertation of Curwick.[80] He studied the effects of five ternary elements (Mo, Nb, Ta, Ti, and W) on flow behavior as a function of temperature in Ni_3Al. All of these elements are known to substitute predominantly on the Al sites. His data showed these additions to provide an increase in the CRSS for {111}<110> slip and a decrease in the CRSS for {001}<110> slip. He attempted to correlate the strength changes with changes in the Voight integrated shear modulus; however, no clear relationship could be found. A qualitative correlation between lattice-parameter increase and increase in the CRSS for {111}<110> slip was evident, but no similar comparison for the CRSS on {001}<110> could be made. In an attempt to explain the alloying effects within Fleischer's solution-hardening theory, Curwick showed the incremental increase in the CRSS for {111}<110> slip at room temperature to be a direct function of concentration, c, rather than $c^{1/2}$ or $c^{2/3}$. At higher temperatures no direct function was claimed. Finally, a pronounced temperature dependence of the {111}<110> strengthening increment which paralleled the temperature dependence of the flow strength led Curwick to the conclusion that alloying directly affects the mechanism controlling anomalous flow behavior. He concluded that the effects of alloying on the {111} and {001} APB energies account only for "minor inconsistencies" in the flow-behavior model. Current understanding of the cross-slip pinning model suggests inconsistencies in his arguments.

Curwick's studies provided an important set of data on the variation of the single-crystal elastic constants (C_{ij}'s) with ternary solute content. While his measured values for these constants in binary alloys do not compare well with those reported by either Ono and Stern[81] or Dickson, Wachtman, and Copley,[82] they are in excellent agreement with

those from the recent careful study by Kayser and Stassis.[83] On this basis, one gains confidence in the reliability of the ternary-alloy constants from Curwick. Little comfort is derived, however, in further recognizing that the values reported by these four independent sources do not compare favorably with each other. A difficulty with the Curwick data is that the reported values of lattice-parameter change with ternary-element concentration do not obey a linear relationship (even at low concentrations) as do those reported by Guard and Westbrook.[78] Furthermore, the Debeye-Scherrer x-ray powder-diffraction patterns for his high Ta and Nb alloys show extraneous diffraction lines which cannot be indexed as an $L1_2$ structure. These difficulties suggest that Curwick's data must not be accepted unequivocally.

Rawlings and Staton-Bevan[84] studied the effects of elements substituting individually for Al and Ni and substituting for both Al and Ni on the flow stress of polycrystalline Ni_3Al. The strength increment derived from each addition was determined and expressed in terms of the shear modulus, μ, as determined from the Ono and Stern[81] elastic constants. The hardening (or softening) increment, $d\sigma/dc$, was determined to range from $-\mu/72$ to $+\mu/4$ for a wide variety of solutes. Rawlings and Staton-Bevan tabulated their results along with those of previous investigators, and made at the following generalizations:

- All elements substituted produced strengthening typical of the gradual hardening of spherically symmetrical defects.

- Elements substituting for Al and Al-rich deviations from the stoichiometric composition provide significant strengthening, while other substitutions very often result in softening.

- At least two different hardening mechanisms (only one of which is discussed) appear to exist, depending on the substitution site of the ternary element.

In order to analyze the hardening in terms of the Fleischer elastic interaction of solute atoms and dislocations, Rawlings and Staton-Bevan plotted the hardening increment as a function of a size-misfit parameter derived from the difference in atomic radii between the solute atom and the atom for which it substitutes. A rather poor fit to a linear relation was obtained for the room-temperature data; no attempt at a fit is reported for elevated-temperature data. The observed effect of composition in binary alloys was discussed in detail. Rawlings and Staton-Bevan observed that hardening due to compositional variation in binary alloys is only effective at temperatures below the peak temperature. The rationale for this is the cross-slip model for flow-stress behavior which indicates that at temperatures greater than the peak temperature, deformation is accomplished by cube slip. Below the peak temperature, octahedral slip is dominant as well as compositional-dependent hardening. Therefore, the mechanism of composition-dependent hardening in binary alloys operates only on the octahedral planes. Stacking-fault (CSF as defined previously) effects are suggested to control this variation in octahedral slip since the dislocations cannot dissociate into $a_0/6<112>$ type partials on the cube planes and, hence, would be ineffective above the peak temperature. Rawlings and Staton-Bevan do not discuss in detail how the CSF energy is expected to change with composition, nor do they furnish direct evidence to indicate that it actually does. They refer only to an observation reported by Lopez and Hancock[79] that the number density of annealing twins changes when Ti is added; therefore, a concomitant change in CSF energy can be inferred.

While Rawlings and Staton-Bevan provide an analysis of their data within Fleischer's theory, they have used only a single elastic parameter—the atomic radius difference (rather than da_0/dc). No consideration is given to a modulus effect which is likely to be more important in directly altering dislocation processes in anisotropic media. Neither these investigators nor any others who have reported their results in the literature have given consideration to Fleischer-type solute-dislocation interactions being appropriate

when superlattice dislocations are controlling flow. As stated previously, one can speculate that the specific descriptions of these interactions must be modified for ordered materials.

In a series of papers, Aoki and Izumi[12,85,86] provide the next major clarification of the effects of alloying and deviations from the stoichiometric composition upon the mechanical behavior of Ni_3Al. In their first paper[12] through lattice parameter measurements, density determinations, and both calculated and measured long-range-order parameters, they clearly show the nature of the non-stoichiometric structure of Ni_3Al. These results lay to rest speculation concerning the defect structure by showing that on both sides of the stoichiometric composition, the excess atoms substitute directly on the "wrong" sublattice without introduction of constitutional vacancies. Furthermore, they state that since the long-range-order parameter is always near its maximum theoretical value (0.9 from 23 to 27 a/o Al) and varies symmetrically about the stoichiometric composition and since the flow strength is asymmetric about the stoichiometric composition, the compositional dependence of the order parameter cannot account for the compositional dependence of strength.

In a study of Cu, Ti, and Ta ternary additions to Ni_3Al and of binary alloys in the range 23 to 27 a/o Al, Aoki and Izumi[85] determined the hardening increment derived from each of these elements. Since constitutional vacancies are not introduced by alloying, the influence of composition in the binary alloys was treated in an analogous fashion to ternary additions. A notable part of their findings is that Al is a more potent hardener, in terms of $d\sigma/dc$, than Ta which is generally considered to be one of the most potent hardeners. In fact, $d\sigma/dc$ for Al is $\mu/6$ which is similar to $d\sigma/dc$ for Hf, the most potent substitutional-strengthening solute. While not as effective as Al, excess Ni was shown to be at least as effective as Ti in strengthening Ni_3Al.

Aoki and Izumi[86] performed a complete analysis of their data from Cu, Ti, Al, and Ni additions to Ni_3Al within the framework of Fleischer's theoretical treatment, again without regard to the question of the appropriateness of his parameters. They measured the change in lattice parameter with concentration, da_0/dc, and used this along with a modulus parameter (the details of which are unreported) to identify the "mechanism" of elastic hardening. With a reasonably good fit to their data, they conclude that the modulus effect on screw dislocations dominates strengthening even for Ni and Al additions—an observation not previously reported. The Aoki and Izumi results are, like those previously reported, only applicable in the temperature regime up to room temperature where the flow stress is largely athermal.

While the work of Aoki and Izumi suggests that the hardening produced by ternary additions to Ni_3Al can be described by classical solution-hardening theory—at least at room temperature—the appropriateness of doing so within the current theoretical development of solution hardening is questionable; this was a prime driving force for the investigation reported herein. Pope and Ezz[5] have rejected classical descriptions on the basis of their understanding of the cross-slip model for flow strength and suggest instead that the effect of alloying on the {111} and {001} APB energies is the prime factor in ternary effects. A change in the APB-energy anisotropy with alloying was initially proposed by Lall, Chin, and Pope[49] and has been more widely developed for $L1_2$ compounds, in general, through investigations by Suzuki et al.[14,15,23,77,87-91] The semi-quantitative ...odels of these studies as described below were the basis for the alloy selections for this research effort.

2.4.2 PHASE STABILITY AND STRENGTHENING

Wee and Suzuki[14,15] examined the temperature dependence of hardness in more than thirty binary $L1_2$ alloys. Considered were alloys composed of transition metals and Group IIIA or IVA elements as well as those formed between transition metals only. They

observed alloys having the $L1_2$ structure both with and without an anomalous thermal dependence of hardness and concluded that a certain correlation exists between the mechanical behavior of these alloys and the position in the periodic table of the elements making up the compound. Additionally, Wee and Suzuki, like Lall et al.[49] were careful to note that if the K-W cross-slip mechanism controls the mechanical behavior of a compound, then the difference in APB energy between the {111} and {001} planes becomes the primary factor influencing the temperature dependence of yield stress. They further suggest that factors related to phase stability (structure stability) should govern APB-energy anisotropy and, therefore, anomalous flow behavior. That is, since many of the geometrically close-packed (GCP) structures can be related by a periodic placement of structural faults (such as APBs and intrinsic stacking faults), the stability of the $L1_2$ structure relative to other GCP structures should provide insight into the relative fault energies in $L1_2$ compounds. Wee and Suzuki use the electron-to-atom ratio, e/a, and an atomic-size parameter as indicators of phase stability.

The size parameter, defined here as ΔR and given by

$$\Delta R = (R_B - R_A) / R_A \qquad [2.5]$$

where R_B and R_A are the atomic radii of the elements which make up an A_3B compound, may be computed from Hume-Rothery atomic radii and experimental determinations of lattice-parameter change with ternary additions. One of the chief difficulties with using these parameters is that they do not fit directly into a structural model. That is, while they provide some level of qualitative trends in structural stability, they cannot be entered directly into a thermodynamic solution model or a statistical model of ordering. This difficulty becomes more apparent through further review.

In order to establish the effect of ternary additions to $L1_2$ alloys in a more rigorous fashion, Suzuki et al.[87] selected the Ni_3Ge-Fe_3Ge pseudo-binary system for a series of solid-solution alloys. From their previous studies,[77] they knew that Ni_3Ge exhibits anomalous flow behavior, while Fe_3Ge does not. A series of tests demonstrated that an alloy of $(Ni,Fe)_3Ge$ containing about 28 a/o Fe has a flow stress which is essentially athermal to 500 °C. From Liang and Pope[92] the flow stress was assumed to consist of an athermal part where the temperature dependence is proportional only to that of the shear modulus and a temperature-dependent part which contains the activation energy for the anomalous flow. The apparent activation energy was determined empirically from an Arrhenius relationship and was suggested to represent the change in Shockley partial separation. A continuous change in the activation energy from a relatively low value in pure Ni_3Ge to an essentially infinite value in Fe contents greater than 28 a/o was taken to indicate a steady change in APB and CSF energy and to imply a change in stability of the $L1_2$ structure. While these implications could be made, no direct evidence for a change in fault energies was provided.

Wee et al.[89] measured the flow stress in eleven binary $L1_2$ compounds and determined the apparent activation energy for each. A modified flow-stress equation was used to account for the fact that many of these Pt-based $L1_2$ alloys exhibited a negative temperature dependence of flow between -196 °C and some higher temperature, T_b, and then displayed an anomalous positive temperature dependence for temperatures greater than T_b. These apparent activation energies were plotted as a function of the size parameter, ΔR, of the compound in order to show a dependence of activation energy upon phase stability. Wee et al. argue that alloys with negative ΔR are highly stabilized $L1_2$ alloys and, therefore, normal in their flow behavior, while those with ΔR values of about 0.05 are destabilized in a maximum way and exhibit anomalous behavior. An ideal $L1_2$ material

should have a ΔR value of zero. Interesting as they may be, these arguments are clearly qualitative, being proposed from, but not proven by, the data.

To further support th. ~ nase-stability concept of alloying effects in compounds exhibiting anomalous flow behavior, Yodogawa et al.[88] alloyed Cu_3Au with Ni and observed a change in the thermal APB morphology from an anisotropic to an isotropic shape. Within the framework of the Clapp and Moss[93-95] and Richards and Cahn[9] pairwise interaction parameters, V_i, Morinaga[96] demonstrated that Cu_3Au is near the boundary of $L1_2/DO_{22}$ stability. Yodogawa et al.[88] used this to suggest that Ni additions to Cu_3Au further stabilize the $L1_2$ structure, as evidenced by the change in thermal APB morphology. The difficulty with these results lies in the fact that Cu_3Au exhibits nearly normal flow-strength behavior without Ni additions. Wee and Suzuki,[89] however, point out that the order parameter of Cu_3Au decreases rapidly with temperature and that this overrides the anisotropic APB-energy effect. A better test would be to enhance the anisotropy of Cu_3Au through alloying and demonstrate anomalous flow behavior.

Recognizing that the flow strength of many binary $L1_2$ alloys is very sensitive to composition, Noguchi, Oya, and Suzuki[77] made a systematic attempt to apply the phase-stability concept to the effects of compositional deviation from the stoichiometric alloy in polycrystalline Ni_3Al and Ni_3Ga. The activation energy for anomalous flow in Ni_3Al was shown to decrease with increasing Al content up to the stoichiometric composition where a discontinuity exists and then to continue to decrease at a faster rate with further Al addition. A similar result was obtained for Ni_3Ga; at the stoichiometric composition, both compounds displayed a strength minimum for temperatures below the peak. Noguchi et al. could only provide indirect evidence to explain these results.

The work of Suzuki and Oya[90] on $L1_2$ alloys in the Pt and Pd groups shows that with an increase in the minority element, many of the compounds exhibit a transition to

another GCP phase. While no similar observation can be made in either of the Ni systems studied by Noguchi et al.,[77] parallel arguments are used. They note that the DO_{22} and $L1_2$ structures have identical near-neighbor configurations; therefore, the first near-neighbor interaction parameter, V_1, alone cannot account for the compositional effect. In accord with Richards and Cahn,[9] they suggest that the second-near-neighbor interaction parameter, V_2, must become less negative as the minority-element concentration is increased. Some difficulties arise with this line of reasoning in that when the composition deviates from the stoichiometric composition, the DO_{22} and $L1_2$ structures do not necessarily have identical first-near-neighbor configurations. For a B-rich deviation from the stoichiometric composition, the $L1_2$ structure will have a nearest-neighbor configuration where the excess B atoms have at least four B nearest neighbors arranged on a plane and eight A-atom nearest neighbors, rather than the usual twelve. In the DO_{22} structure, this same B-rich deviation results in four wrong nearest neighbors to the excess B atom, as in $L1_2$ structure; however, the new B-B bonds may be arranged with either planer symmetry as in $L1_2$ or with tetrahedral symmetry, depending on the site of the substitution. Further, the second-near-neighbor configuration to the excess B atom may also change from that in a B-rich $L1_2$ alloy, both structures having either six A-atom next near neighbors to the excess B atom or a more complex arrangement. The effects of these bonding arrangements on APB-energy anisotropy require further study.

Noguchi et al.[77] associate the discontinuity in the mechanical behavior and the apparent activation energy with the occurrence of triangular arrangements of B atoms as first near neighbors which form with APBs on {111} planes in a B-rich alloy. They suggest that these arrangements increase the {111} APB energy in a stepwise fashion but, again, do not arrive at this from an APB-energy model or from direct evidence. Clearly, for these additional B-B interactions to result in a stepwise change in phase stability (APB energy), the change should be evident in experimentally determined APB energies. Such

changes have not been demonstrated to date; however, they have been considered in the current research. As a final point in applying the phase-stability concept to binary alloys, it is interesting to note that the size parameter, ΔR, does not have the same relationship with the activation energy as in ternary alloys. The data of Noguchi et al.[77] show a change in the apparent activation energy from 0.145 eV/atom in a 23 a/o Al alloy to 0.062 eV/atom in a 27 a/o Al alloy. The change in size parameter over this same composition range is virtually undetectable. In the ternary systems discussed previously, a change in activation energy over a similar range occurred with a factor-of-ten change in size parameter. Perhaps this last point best illustrates the difficulties which arise in applying Hume-Rothery-type phase-stability concepts to ordered systems.

In some of their most recent work, Suzuki et al.[91] provide a summary of results from their previous studies. The following four conclusions are drawn:

1. An $L1_2$ compound exhibiting the anomalous temperature dependence of strength has lower structural stability with respect to the DO_{22} structure. In other words, the anomalous alloy lies near the stability boundary between the $L1_2$ and DO_{22} structures.

2. Consequently, in the anomalous $L1_2$ compound, the contribution of the nearest-neighbor interaction is predominant in reducing the {001} APB energy.

3. As one of the components is partially or entirely substituted to increase the electron-to-atom ratio or the atomic-radius ratio of the components, the structural stability is reduced and, thus, the anomalous temperature response is strengthened.

4. Increasing the content of the minority component from A-rich to B-rich deviations beyond A_3B stoichiometric composition progressively strengthens the anomalous flow-stress behavior.

42

The first of these conclusions amounts to a reiteration of the thesis set forth by Wee and Suzuki.[89] While this thesis may be sound, the parameters used thus far by Suzuki and co-workers are not sufficiently quantitative to provide validation of the thesis. In some cases, however, correlations which are consistent with the phase-stability concept have been observed.

The second conclusion is perhaps more significant in that it is aimed directly at one of the specific factors which must be incorporated into a hardening model, namely, the APB energy and its anisotropy. The conclusion that the magnitude of V_1 must be large (relative to the magnitude of V_2) for anomalous flow behavior to occur is reached on the basis of the Richards and Cahn phase-stability model, coupled with the concept of low phase stability resulting in high APB-energy anisotropy. The Richards and Cahn model requires the value of V_2/V_1 to be negative and near zero in order for the $L1_2$ structure to have low stability. In order to arrive at their second conclusion, Suzuki et al. assumed that their thesis was valid and that the Richards and Cahn stability theory was applicable. Clearly, a key parameter to consider in the solution strengthening of Ni_3Al is the anisotropy of the APB energy and the effects of composition upon anisotropy. The relative structural stability may or may not be a necessary consideration in this regard. Recent quantum-mechanical calculations by Freeman et al.[97] have shown that the calculated {001} APB energy of stoichiometric Ni_3Al may not be obtained by treating the DO_{22} structure as a periodically faulted $L1_2$ structure. The {001}-plane APB energy calculated for a DO_{22} structure with Ni_3Al composition (that is, from two APB interfaces separated by a monolayer antiphase domain) was determined to be greater than that calculated for a single APB interface by more than a factor of three. This result suggests that the phase-stability analysis of strengthening is a concept which currently lacks clear theoretical definition, is difficult to parameterize quantitatively in non-ideal systems, and is more general than the issue of alloying effects on the mechanical behavior of Ni_3Al. The anisotropy of the

equilibrium APB energy, on the other hand, should be directly measurable in alloys and has been the subject of these investigations.

The last two conclusions of Suzuki *et al.* are not self-consistent within binary alloys. While their data[23,77] show that B-rich deviations from the stoichiometric composition result in significant hardening, these data do not indicate that the electron-to-atom ratio decreases (rather than increases) with an increase in the B-atom content. At the same time, the size factor, ΔR, first decreases and then increases over the composition range 23 to 27 a/o Al in Ni_3Al. These results are inconsistent with Conclusion 3 above.

2.5   RESEARCH OBJECTIVES

Based on the above review, the single most important factor limiting the understanding of ternary-element effects is the variation in fault energies with composition. Neither the early TEM studies of these alloys nor the more recent weak-beam microscopy investigations reviewed above have evaluated this parameter with variations in ternary composition or with variation in the Ni/Al ratio of the binary compound. This glaring deficiency exists despite nearly 30 years of theoretical development which has hinged on the estimated anisotropy of the APB energy. The research described herein was aimed at quantifying the variation in APB energy within both binary alloys and select ternary alloys designed within the concepts of phase stability and hardening. The primary objective of the investigations was to establish a relationship between the anisotropy of the APB energy, the amount of solute, the mechanical behavior in Regions I and II, and the dislocation structure within both binary and ternary single-crystal alloys.

Solute additions of Sn and V were chosen on the basis of expected variation in fault energies within the phase-stability models of alloying. Additions of V were expected to

44

destabilize the $L1_2$ structure relative to DO_{22} (and, hence, to lower the {001} APB energy) since the binary DO_{22} compound Ni_3V is in equilibrium with Ni_3Al in the Ni-Al-V ternary system.[91] Similarly, it was reasoned that Sn additions destabilize the $L1_2$ structure relative to the DO_{19} structure since the binary compound Ni_3Sn has the DO_{19} structure. Destabilization toward the DO_{19} structure is expected to reduce the SISF and CSF energies from the point of view that the DO_{19} structure is an $L1_2$ structure with periodic SISFs on the octahedral planes. On these bases alone the additions are expected to destabilize Ni_3Al, although both ternary solutes will result in an increase in the electron-to-atom ratio. Both ternary solutes were expected to substitute for Al based upon the data of Ochiai *et al.*[91] Studies of the effect of the Ni/Al ratio on fault energies and flow stress in binary alloys were included as well, since these were viewed as critical in establishing solute effects in ternary systems.

The objective of establishing the structure-property relationships at the TEM level was addressed by conducting compression tests as a function of temperature for two different solute levels of each ternary addition. Tests were limited to the [001] orientation since the effects of the resolved shear stress on the cube cross-slip system are minimized for this orientation, and the effects of CSF constriction or extension are minimal when compared to orientations in the remainder of the stereographic triangle.[17] Small total strains were examined in order to minimize the possibility of dislocation interactions obscuring the underlying substructure associated with anomalous flow behavior. These TEM investigations were focused on low-temperature deformation behavior in an attempt to prevent both dynamic and static recovery events from influencing the substructure and since events taking place in the transition from Region I to Region II behavior (see Fig. 1.2) were expected to be equivalent to "freezing in" the events governing the late Region II behavior.

CHAPTER 3

EXPERIMENTAL PROCEDURE

3.1 ALLOY SELECTION AND PREPARATION

Binary alloy compositions which span the single-phase region were chosen in order to establish base-line behavior with both Ni-rich and Al-rich deviations from the stoichiometric composition of Ni_3Al. Initially, alloys having nominal compositions of 23, 24, and 27 a/o Al, with the balance being Ni, were chosen for establishing the binary-alloy behavior. One binary alloy which was added late in the study had a composition of 23.4 a/o Al. The ternary-alloy compositions used in this study were selected on the basis of phase-stability arguments, as described in Chapter 2. Two levels of each ternary solute were selected after consideration of the maximum solubility of each solute as reported by Ochiai et al.[91] For Sn substitutions for Al in Ni_3Al, the maximum Sn solubility was reported to be 4 a/o at 1000 °C. Similarly, for V substitutions, the maximum solubility was reported to be greater than 11 a/o at 1000 °C. Consequently, solute levels of 1 and 4 a/o each for Sn and V were chosen in order to provide a direct comparison of the potency of the two solutes at changing the APB energies and the flow stress of the alloys. Four ternary alloys with the following nominal compositions were chosen: i) Ni-24Al-1Sn, ii) Ni-21Al-4Sn, iii) Ni-24Al-1V, and iv) Ni-21Al-4V (all compositions are reported in atomic percent).

Single-crystal and directionally solidified (DS) bars of the selected alloy compositions were supplied by Pratt and Whitney Aircraft in East Hartford, Connecticut. The compositions were solidified by a modified Bridgman growth method. Binary Al-rich crystals were grown for this and a parallel study at Pratt and Whitney;[98] successful

46

growth of such crystals has not been reported previously. The binary-alloy phase diagram shown in Fig. 3.1 suggests that Al-rich compositions should be difficult to grow since beta-phase (β-NiAl) solidifies first in compositions with greater than 24.6 a/o Al. Persistent attempts at crystal growth on the part of Dr.'s C. C. Law, D. P Shah, and J. Lin at Pratt and Whitney apparently resulted in a combination of thermal gradient and growth rate which allowed growth of at least one Al-rich composition. Details of the crystal-growth parameters were not provided.

The 23 a/o Al binary, the 1 and 4 a/o Sn ternary alloys, and the 1 and 4 a/o V ternary alloys were supplied as single-crystal or coarse-grained polycrystalline DS bars having a diameter ranging from 22 to 50 mm and lengths ranging from 100 to 150 mm. The 24 a/o and 27 a/o binary alloys were supplied as arbitrarily shaped pieces cut from the conical bottom end sections of 90 mm-diameter crystals. The crystals were homogenized in vacuum at temperatures ranging from 1100 to 1250 °C for times from 100 to 120 hours, followed by furnace cooling. The 23.4 a/o Al crystal was provided by Prof. D. P. Pope (at the University of Pennsylvania) and tested in the as-received condition which included a homogenization treatment for 1 hour at 1300 °C. The specific homogenization schedule for each specimen set is provided in the top left section of the data sheets in Appendix A.

Binary alloys having compositions with less than 24.2 a/o Al (the eutectic composition shown in the phase diagram of Fig. 3.1) form cored structur᷈ ᷉ with gamma (γ) dendrites which transform upon further cooling to $\gamma + \gamma'$ mixtures and finally to single-phase γ' upon homogenization. An example of the as-cast and homogenized structure of these alloys is shown in Fig. 3.2. The single-crystal alloys which solidify directly as the γ' phase exhibit featureless microstructures in both the as-cast and homogenized conditions. Such structures are not shown but were exemplified by the V-containing ternary alloys.
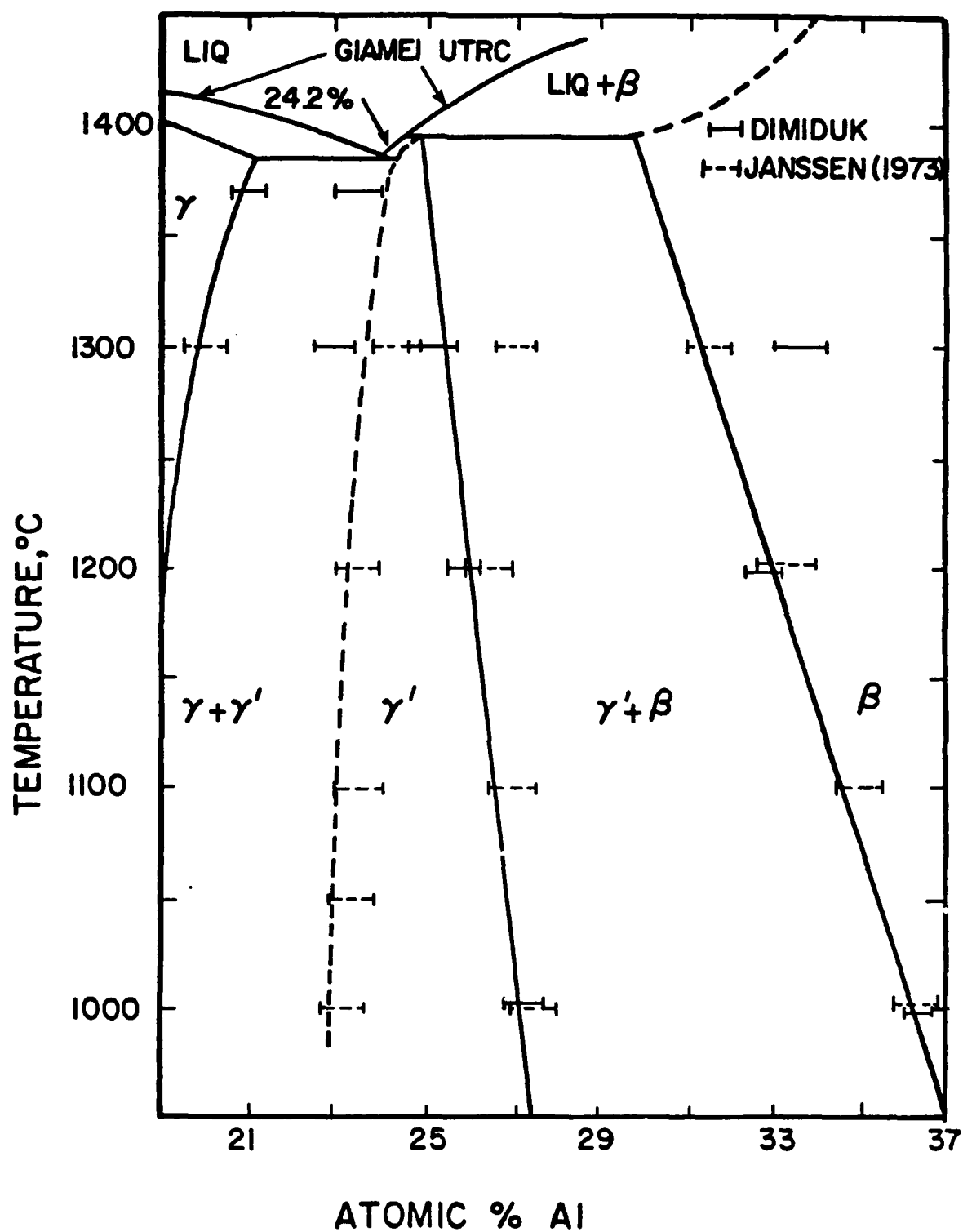
Fig. 3.1 The Ni-Al binary-alloy phase diagram in vacinity of Ni₃Al phase, as verified in present study. Data shown by dashed lines are from Janssen,[99] and the liquidus curves were provided by Pratt and Whitney.

48
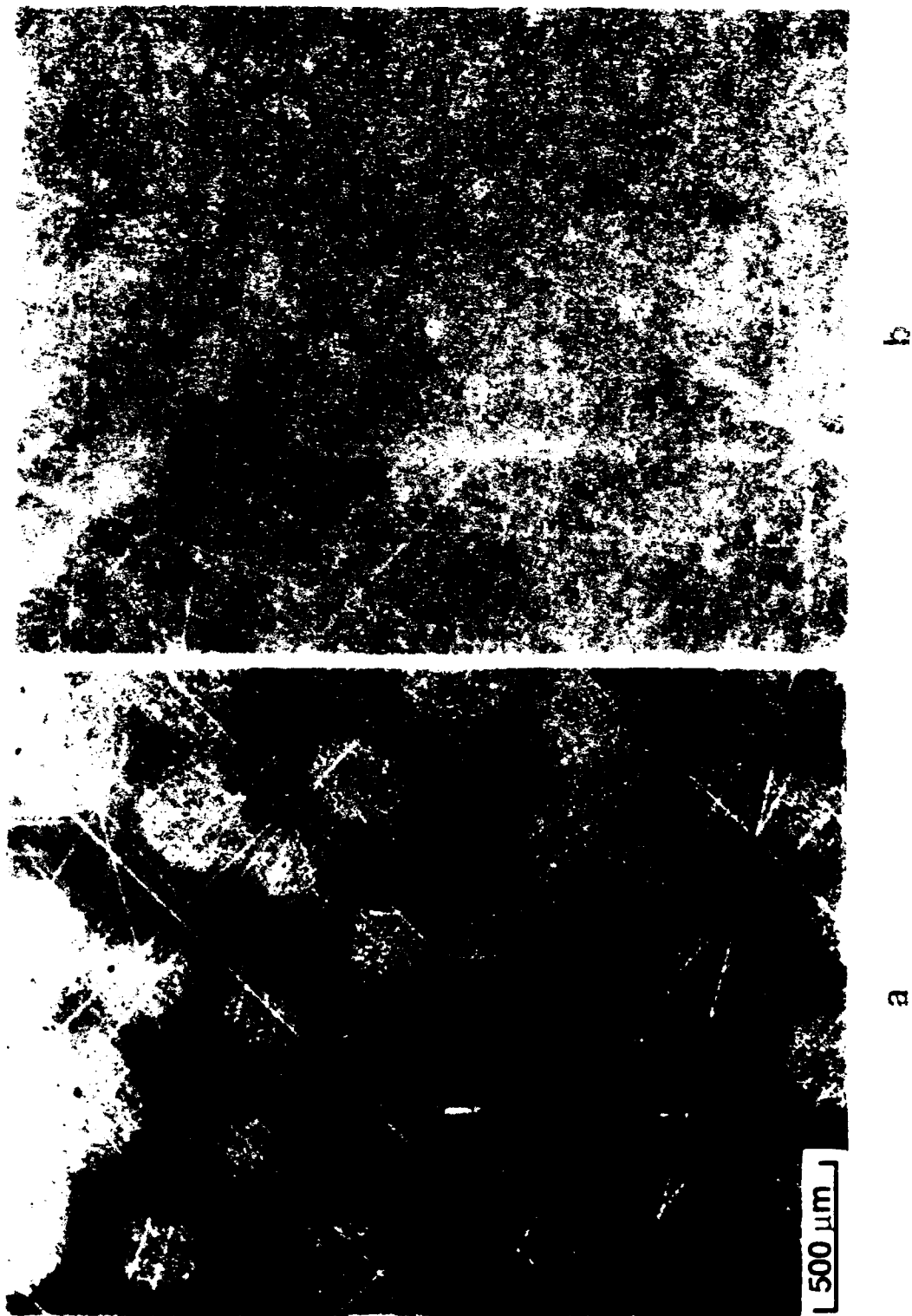
Fig. 3.2 Backscatter scanning electron micrographs of alloy Al 230; a) as-cast, γ'-phase matrix with γ + γ' dendrite cores, and b) after homogenization at 1200 °C / 120 hr / furnace cooled.

500 μm

a

b

Typically Al-rich compositions solidify dendritically, with β-NiAl solidifying first. This dendrite formation inhibits single-crystal growth of Al-rich compositions under most solidification conditions; in the crystals used in the present study, β-phase dendrite cores could not be completely removed by thermal treatment (see Fig. 3.3). The γ'/β phase boundary shown in Fig. 3.1 was determined in the present study and found to fit well with the boundaries reported by Janssen.[99] Polycrystalline material, having an analyzed composition of 27.2 a/o Al, was extruded into 10 mm-diameter rod, homogenized for times ranging from 400 to 500 hours, and analyzed using the electron microprobe in order to determine the phase boundary at 1200 °C and below.

The Sn-containing ternary alloys exhibit an interdendritic polyphase mixture in the as-solidified condition, consisting primarily of Ni_3Sn and Ni_3Al as shown in Fig. 3.4(a). The 1 a/o Sn alloy was readily homogenized into single-phase γ' after heat treating for 100 hours at 1250 °C. However, extended heat treatment of the 4 a/o Sn alloy at 1200 °C and above resulted in the two-phase spherodized structure shown in Fig. 3.4(b). Some specimens were tested in this condition which is hereafter referred to as the "-SH" condition. Heat treatment at 1180 °C for 100 hours, provided a nearly single-phase structure in the high Sn alloy, as shown in Fig. 3.4(c).

3.2   CHEMICAL ANALYSIS

A convenient scheme for identifying the alloys was adopted from that used by Law et al.[98] This method allowed easy identification of the ternary solute and any deviation from the stoichiometric-alloy composition. Each alloy was assigned a designation consisting of the atomic symbol of the ternary-alloy addition, followed by numerical designation of the nominal-Al and ternary-solute content. For example, the
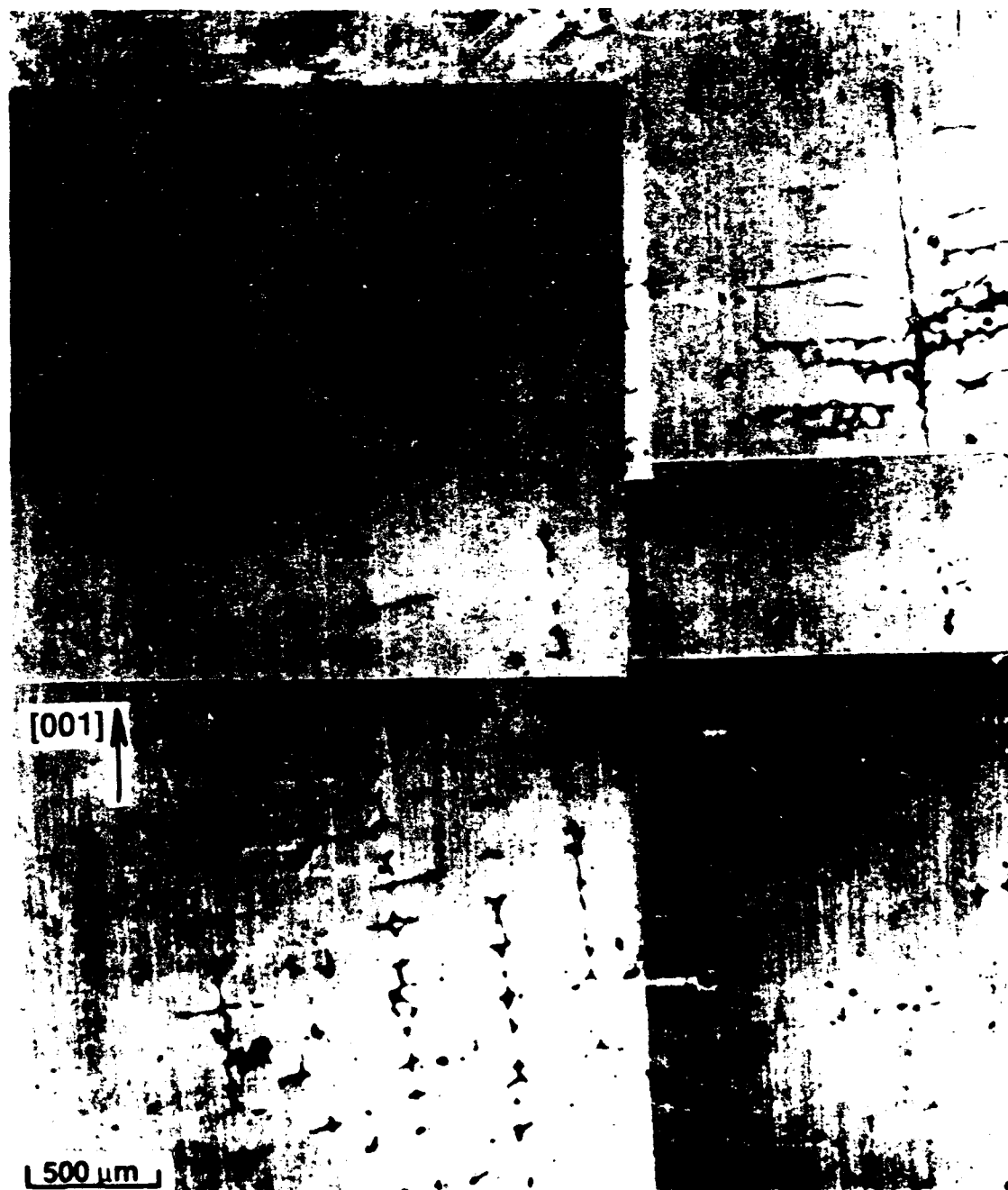
Fig. 3.3   Backscatter scanning electron micrograph of alloy Al 270 after 1100 °C / 120 hr /
furnace cooled. Dark phase is β-NiAl.
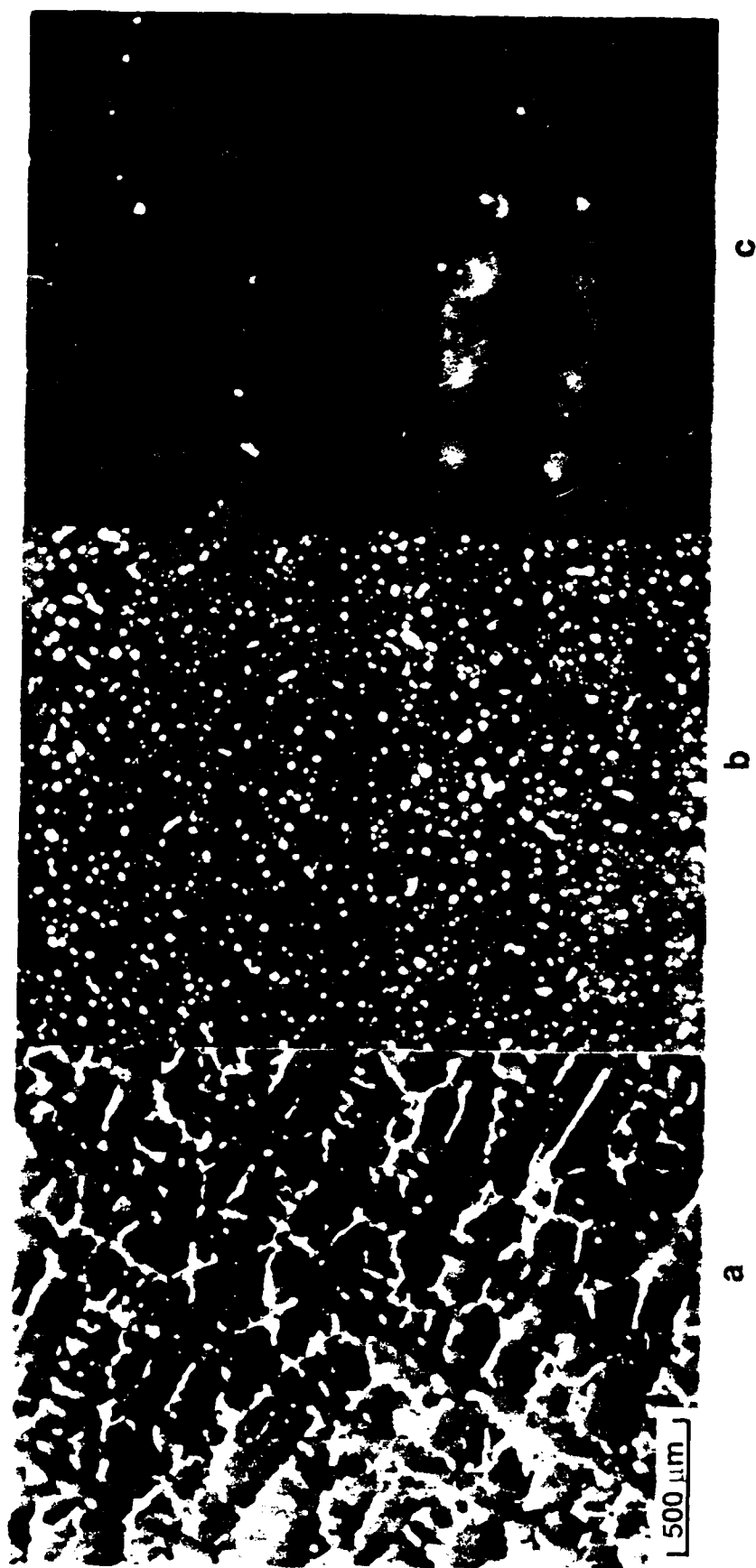
Fig. 3.4   Backscatter scanning electron micrographs of alloy Sn 214: a) as-cast, b) heat treated in the two-phase region above 1200 °C, and c) after 1180 °C / 100 hr / furnace cool. Light regions are Sn-rich consisting primarily of Ni_3Sn.

4 a/o Sn alloy has been designated "Sn 214," indicating a nominal composition of Ni-21Al-4Sn. The binary alloys were labeled similarly; however, all three numbers designate the Al content. For example, the 23.4 a/o Al binary alloy has been designated "Al 234."

The nominal and analyzed compositions for the alloys are given in Table 3.1 (first two lines for each alloy), along with their analyzed major impurity contents. The alloys have been analyzed by both wet-chemical methods and electron-probe microanalysis techniques. In most cases the results compare favorably. The wet-chemical analysis was conducted through the Wright Research and Development Center (WRDC) Materials Laboratory analytical chemistry group. Total interstitial impurity contents were analyzed at less than 100 ppm by weight. Wet-chemical analysis of the 23.4 a/o Al alloy was not conducted at WRDC; the reported analysis was provided by Prof. Pope along with the crystal.

Microprobe analysis of the alloys was conducted using instrumentation in the WRDC Materials Laboratory Materials Characterization Facility, and the results can be found in the line designated "Probe a/o" for each alloy in Table 3.1. The analysis was conducted by first sampling the composition in a local region (8 x 8 μm) nine independent times to establish the statistical error bar; this was followed by sampling in 20 μm steps along a line at least 400 μm in length. The reported compositions are the 99.5% confidence intervals when the calculated error bar of $\pm$ 1.4% of the amount present is used to define the analyzed composition range. The microprobe analysis reported for alloys Al 270 and Sn 214-SH is the measured composition of the γ' phase alone. The compositions reported and discussed throughout the remainder of this dissertation refer to the results of the microprobe analysis, unless otherwise stated.

Table 3.1 Alloy Compositions

Alloy		Ni	Al	Sn	V	Co	Cr	Fe	Mn	Si
Al 230	w/o	87.88	12.12	0.01	<.001	0.05	0.03	0.01	---	0.01
	a/o	76.9	23.1	---	---	---	---	---	---	---
Probe	a/o	77.1	22.9	---	---	---	---	---	---	---
Al 234	w/o	---	---	---	---	---	---	---	---	---
	a/o	76.6	23.4	---	---	---	---	---	---	---
Probe	a/o	76.7	23.3	---	---	---	---	---	---	---
Al 240	w/o	87.12	12.61	---	---	---	---	---	0.03	0.23
	a/o	75.7	23.8	---	---	---	---	---	---	0.4
Probe	a/o	75.8	24.2	---	---	---	---	---	---	---
Al 270	w/o	85.80	13.83	---	---	---	---	---	0.04	0.20
	a/o	73.6	26.0	---	---	---	---	---	0.0	0.4
Probe	a/o	74.1	25.9	---	---	---	---	---	---	---
Sn 241	w/o	85.69	11.86	2.39	<.005	<.005	<.005	0.03	<.001	0.03
	a/o	76.0	22.9	1.1	---	---	---	---	---	---
Probe	a/o	75.0	24.1	0.9	---	---	---	---	---	---
Sn 214	w/o	81.01	10.39	8.49	<.005	0.05	0.03	0.03	<0.01	<0.01
	a/o	75.1	21.0	3.9	---	---	---	---	---	---
Probe	a/o	75.2	21.1	3.7	---	---	---	---	---	---
Probe -SH		75.0	21.8	3.2	---	---	---	---	---	---
V 241	w/o	87.09	12.09	<.005	0.75	<0.01	<0.01	0.05	<.001	0.03
	a/o	76.2	23.0	---	0.8	---	---	---	---	---
Probe	a/o	75.6	23.4	---	1.0	---	---	---	---	---
V 214	w/o	85.96	11.15	<.001	2.86	<.005	<.002	0.02	<.001	0.01
	a/o	75.7	21.4	---	2.9	---	---	---	---	---
Probe	a/o	75.2	20.8	---	4.0	---	---	---	---	---

3.3 DETERMINATION OF MECHANICAL PROPERTIES

3.3.1 SPECIMEN PREPARATION

The large DS grains making up the bulk crystals were separated into single crystals by wire electrodischarge machining (wire EDM). One end of each crystal was trimmed nominally perpendicular to the crystal axis by wire EDM and then electropolished in a solution of 10 volume percent H_2SO_4 in methanol at -10 °C at 13 to 16 V. The Laue back-reflection x-ray diffraction technique was used to orient the polished face perpendicular to an axis located on a great circle in the range 2 to 10 degrees off the [001] crystal direction. The traces of the [010] and [100] crystal directions were marked with scribe lines on the crystal face before the crystal was transferred to a mounting block and vise for further machining.

For the present experiments square-cross-section compression specimens having approximate dimensions ranging from 3 x 3 x 8 mm to 5 x 5 x 15 mm were sectioned from the crystals by wire EDM. The specimens were ground by hand on SiC emery papers to a 600-grit finish in order to remove the EDM re-cast layer and to assure that the sides of the specimens were parallel to within 0.025 mm over the specimen length. These specimens were electropolished using the solution and polishing conditions stated above to remove a minimum of 0.15 mm from the width. Following electropolishing, the specimens were annealed at 1000 °C for 1 hour in vacuum prior to testing. A Laue back-reflection x-ray diffraction pattern was recorded, with the x-ray beam direction being parallel to the specimen axis to permit determination of the final specimen orientation. The ends of each specimen were then lapped flat and parallel to within ± 0.005 mm across the end diagonal on SiC paper, using a fixture which held the specimens perpendicular to their axis. Several circular cross-section specimens were prepared from alloy Al 240 by plunging a tubular electrode through a single-crystal block by EDM. The cylindrical

5 5

specimens were hand finished using SiC papers and a jeweler's lathe, following procedures similar to those described above. The tables in Appendix A contain the final specimen dimensions and some Schmid factors determined from the final Laue patterns for each specimen. Appendix B provides the angles between the specimen axis and the three <001> crystal axes as determined for each specimen. The angles reported have a measurement error range of ± 0.25 degree.

3.3.2 RESOLVED-SHEAR-STRESS MEASUREMENTS

Compression tests were carried out using a screw-type Instron mechanical-testing machine. The specimens were heated in air in a three-zone resistance furnace. Thermocouples were placed near the specimen top, center, and bottom. The specimens were compressed between René 95 push rods, each rod having a removable René 95 platen attached to it. Platens made of TiC were used for test temperatures exceeding 600 °C. The temperature was allowed to equilibrate for at least 30 minutes for each test. Tests were conducted at -196 °C by placing the specimens in a bath of liquid nitrogen contained by a polystyrene bowl. The temperature was allowed to stabilize until the specimen stopped contracting, which typically required about 20 minutes in the liquid nitrogen.

A load-displacement record was made for each specimen using a constant-speed strip-chart recorder to track the cross-head displacement and load cells having a maximum load capacity of either 22 or 44 kN to measure the applied load. A typical chart speed of 2.1 mm/s and a typical cross-head speed of 0.002 mm/s were used to achieve a displacement resolution of ± 0.00025 mm. These conditions provided a nominal strain rate of 2×10^{-4}/s. Through the use of 0.5 or 1.0 kN full-scale ranges (provided by stepped zero suppression) for the load readings, a load resolution (precision) of ± 2.0 N was maintained. Each sample was deformed to an axial engineering strain ranging from 0.25 to 0.45% at a given temperature; then the temperature was raised by 200 °C and each

sample strained again. In this way the entire flow-stress-versus-temperature curve was determined from a single sample. The validity of the technique was verified by straining a sample directly at 600 °C and comparing the measured flow-stress value with the values determined from the same alloy by incremental straining. Typically, three compression samples were tested for each alloy at each temperature, and the average flow-stress and work-hardening-versus-temperature values are reported. By making the assumption that the errors associated with measured specimen dimensions and orientation may be added to those associated with measuring load, the total error associated with measuring flow stress is estimated to be ± 1 MPa.

At least one specimen from each alloy was prepared by mechanically polishing two faces at 90 degree angles to each other before testing and straining to a maximum plastic strain ranging from 0.2 to 0.4% at room temperature and/or -196 °C. After testing, the specimen was examined optically to observe the surface slip traces. These observations revealed that nearly all of the specimens were deformed in the Stage II multi-slip regime. The specimen was restrained to a total plastic strain of 0.7 to 1.3% and then oriented and prepared for viewing in the TEM by a procedure which will be described later. The results for each specimen at each test temperature are given in the tables in Appendix A.

3.3.3 SPECIAL TESTS

Two separate special test procedures were carried out in order to verify the "reversibility" of flow stress with temperature reported earlier by Davies and Stoloff.[35] One cube-oriented specimen of alloy Al 230 was prepared using the procedure described above. The specimen was pre-strained to a nominal plastic strain level of 0.65% at 600 °C, cooled to 24 °C, and additionally strained at the lower temperature to an additional 0.2% nominal plastic strain (see record for specimen Al 230-4 in Appendix A). A second cube-oriented sample, prepared in the same manner, was strained at -196 °C to a nominal

plastic strain of 0.6%, annealed at 600 °C, and additionally strained at -196 °C to a total plastic strain of 1.2%.

3.4 ELECTRON MICROSCOPY

3.4.1 SAMPLE PREPARATION

Following deformation at room temperature, samples were sectioned by EDM into 0.5 mm-thick slices and oriented parallel to the primary slip plane as revealed by two surface slip-trace analyses. The slices were cut into 3 mm-diameter discs by EDM. The discs were thinned by hand grinding on SiC 600-grit emery paper to thicknesses ranging from 0.3 to 0.4 mm. Thin-foil specimens were prepared from the discs by twin-jet electropolishing in a solution of 2% perchloric acid in butyl cellosolve at 10 °C at 75 to 80 V and 10 to 15 mA.

Initially, several specimen discs had been thinned to a thickness of 0.2 mm before final preparation; however, as reported in Appendix C, these specimens were shown to exhibit extended stacking faults as artifacts of the preparation and handling process. When thicker specimen blanks were used for thin-foil preparation, the extended stacking faults were not observed. Additional evidence suggesting that extended stacking faults can be artifacts of damage or deformation of thin-foil specimens was obtained by examining the slip bands occurring in thin-foil specimens prepared from thick discs but damaged in handling after electropolishing. Appendix C contains examples of the two different substructures observed in alloy Sn 241 through the use of two different specimen blank thicknesses as well as the Burgers-vector analysis for one section of a slip band in a damaged sample of Al 230. After observations had been made and the analysis performed

as reported above, all subsequent specimens blanks were maintained at a thickness greater than 0.3 mm.

3.4.2 WEAK-BEAM MICROSCOPY

Most of the TEM observations reported herein were made and recorded under weak-beam kinematical-imaging conditions. The weak-beam technique was originally developed by Cockayne et al.,[100,101] who established the general weak-beam imaging conditions within the column approximation for obtaining optimum contrast and minimum chance of observing artifacts. Recently, Riviere and Cadoz[102] developed a more specific and somewhat less stringent set of imaging conditions including specifications for the magnitude of the deviation vector, s_g, which vary with the character of the dislocation. For the present studies, however, the condition specified by Cockayne et al. (that is, $s_g > 0.2$ nm^{-1}, where s_g is the magnitude of s_g) was used for most of the observations. For dark-field images formed with the reflection g on the optic axis and the reflection ng at the Bragg angle, the value of n which satisfies the condition $s_g > 0.2$ nm^{-1} may be found from the following geometric relationship:[103]

$$s_g \approx g^2 \frac{\lambda}{2} (n - 1)$$

[3.1]

where g is the magnitude of the imaging vector, g, and λ is the wavelength of the electrons. The condition given by Cockayne et al. is both necessary and sufficient for obtaining good weak-beam images with a minimum error (less than about 0.7 nm) between the apparent dislocation position and the actual position. Table 3.2 provides, for several fundamental reflections in Ni$_3$Al, the extinction distances (in nm) for both 100- and 200-kV electrons and the necessary values of n for both 100- and 200-kV electrons, to satisfy the condition $s_g > 0.2$ nm^{-1}.

Table 3.2 Extinction Distances and n Values for Weak-Beam Microscopy of Ni₃Al

g (hkl)	ξ_g (nm) (100 kV)	ξ_g (nm) (200 kV)	n (100 kV)	n (200 kV)
111	40.0	69.6	5.6	7.8
200	48.4	83.1	4.4	6.1
220	70.2	120.5	2.7	3.6
311	87.7	150.4	2.3	2.8

3.4.3 OPERATING CONDITIONS AND CALIBRATION

While early experiments were carried out with a JOEL 100CX analytical electron microscope operating at 100 kV, most of the experiments were performed using a JEOL 2000FX analytical electron microscope, with a LaB_6 filament, operating at 200 kV. Dislocation types were identified by standard two-beam dynamical imaging using ± g conditions to identify dipole dislocation lines. The standard $g \cdot b = 0$ and $g \cdot (b \times u) = 0$ invisibility conditions were employed for determining dislocation Burgers vectors. In order to optimize the image contrast, minimize the effects of inelastic electron scattering, and minimize the film-exposure times required for recording images, several special conditions were fixed in the microscope. A 70 μm condenser aperture was used to minimize beam convergence, and a 20 μm objective aperture was used to minimize the contribution of inelastically scattered electrons. Weak-beam images were recorded using typical exposure times ranging from 16 to 22 seconds. These exposure times were made possible by the use of high-speed electron imaging film (Kodak SO 163) which was processed for 15 minutes (approximately double the manufacturer's recommended time) at 21 °C in Kodak D-19 developer mixed according to the specifications on the label. The

magnification of the microscope was calibrated using a standard, ruled carbon-diffraction grating. The manufacturer's specification for the grating was 2160 lines/mm ± 3.0%, which provided an adequate calibration for magnifications of up to 1×10^5. The diffraction grating was photographed at various fixed-lens currents (chosen such that the shadow image of the selected-area aperture was focused on the bright-field image) which were recorded and used for subsequent experiments. The calibration was found to be stable and repeatable to ± 1.2%.

3.4.4 DISSOCIATION MEASUREMENTS

In order to determine the dissociation plane of the APB-coupled dislocations, trace analysis was performed under weak-beam dark-field conditions (primarily using g-ng {220} with n = 3.5 to 5) by tilting about an axis parallel to the dislocation-line direction, u. Each dislocation pair was analyzed by tilting over an angular range from 55 to 100 degrees and observing the image width at 20 degree intervals. By finding the beam direction for which a given dissociated dislocation pair would exhibit a maximum image width and/or a minimum or edge-on width, the plane of dissociation could be determined unequivocally. The magnification was held constant for all chosen beam directions by setting the lenses to the calibrated lens currents and focusing the image by adjusting the specimen height. Dislocation lines were photographed at direct magnifications ranging from 5 to 8×10^4.

Determination of the dissociation distances of superlattice partial dislocations was made by calibrating 2X to 4X enlarged photographs of dislocation lines (recorded primarily under g·b = 2 weak-beam dark-field conditions) and viewing the lines with a ruled 7X magnifying loupe. The distance between positions of maximum intensity of partial dislocations was used as the dissociation distance for calculating APB energies. Typical dissociation widths in the printed images ranged from 0.4 to 1.5 mm, which corresponded

to actual dissociation distances of 2.0 to 7.0 nm. The individual linewidths for the superpartial dislocations typically ranged from 0.5 to 1.5 nm. Two independent measurements were typically made for a given segment of constant character (edge versus screw) of a dissociated dislocation pair, and 4 to 10 dislocation line pairs (each containing from 1 to 10 measured segments) were characterized from each alloy in a given condition. Segments of constant character and having aspect ratios (dissociated width to length) of less than 5 were avoided due to possible elastic distortion of the separation width under such conditions.

The largest error associated with the measurement technique is in the determination of the maximum-intensity positions for a given line pair. This is an error of constant magnitude whcih occurs when measuring the enlarged micrographs, and has been approximated to be ± 0.05 mm for the narrow magnification range used in these studies. Such an error in measurement of the print typically corresponded to an error of ± 0.25 nm in the actual dissociation distance. A second major error is associated with the precision of reading the ruled loupe for a given measurement. This error, again of constant magnitude, was estimated to be ± 0.025 mm for the measurement, which typically corresponded to an error of ± 0.125 nm in the actual dissociation distance. By adding these errors to the error associated with the calibration of the microscope, a typical error range of ± 8 to ± 12% of the measured spacing is obtained. The actual error will depend upon the specific print magnification; for most of the measurements reported here, the error bar is between the mid-point value and the low end of the error range. For the data presented in the results section of this dissertation, a constant error bar of ± 0.5 nm was assigned.

CHAPTER 4

RESULTS

The results of the present investigation will be presented in four major subsections. The first two contain the findings from binary-alloy evaluations, with the mechanical-behavior phenomenology being treated first, followed by results from the electron-microscopy studies. The last two subsections discuss, in a similar way, the findings from ternary alloys.

4.1 BINARY-ALLOY MECHANICAL BEHAVIOR

4.1.1 EFFECT OF TEMPERATURE AND COMPOSITION

The resolved shear stress at 0.2% plastic engineering strain (defined here as the critical resolved shear stress,τ, or CRSS) for $\{111\}<10\bar{1}>$ octahedral slip was determined in compression for four binary-alloy compositions. The samples having a compression axis oriented near the [001] crystallographic direction, were tested using the incremental straining technique described in Chapter 3. Detailed results from those tests are contained in the tables in Appendix A. Figure 4.1. shows the mean values of the CRSS plotted as a function of temperature for the binary alloys evaluated in this study. In general, a peak temperature for flow stress was not observed because of the limited temperature range studied and the sample orientations being very near the [001] axis which resulted in a low resolved shear stress on the cube-slip systems. The data set marked "25% Al Calc." is the estimated CRSS-versus-temperature curve for stoichiometric Ni_3Al, hereafter referred to as τ_s. Values for this data set were determined by plotting the CRSS variation with Al
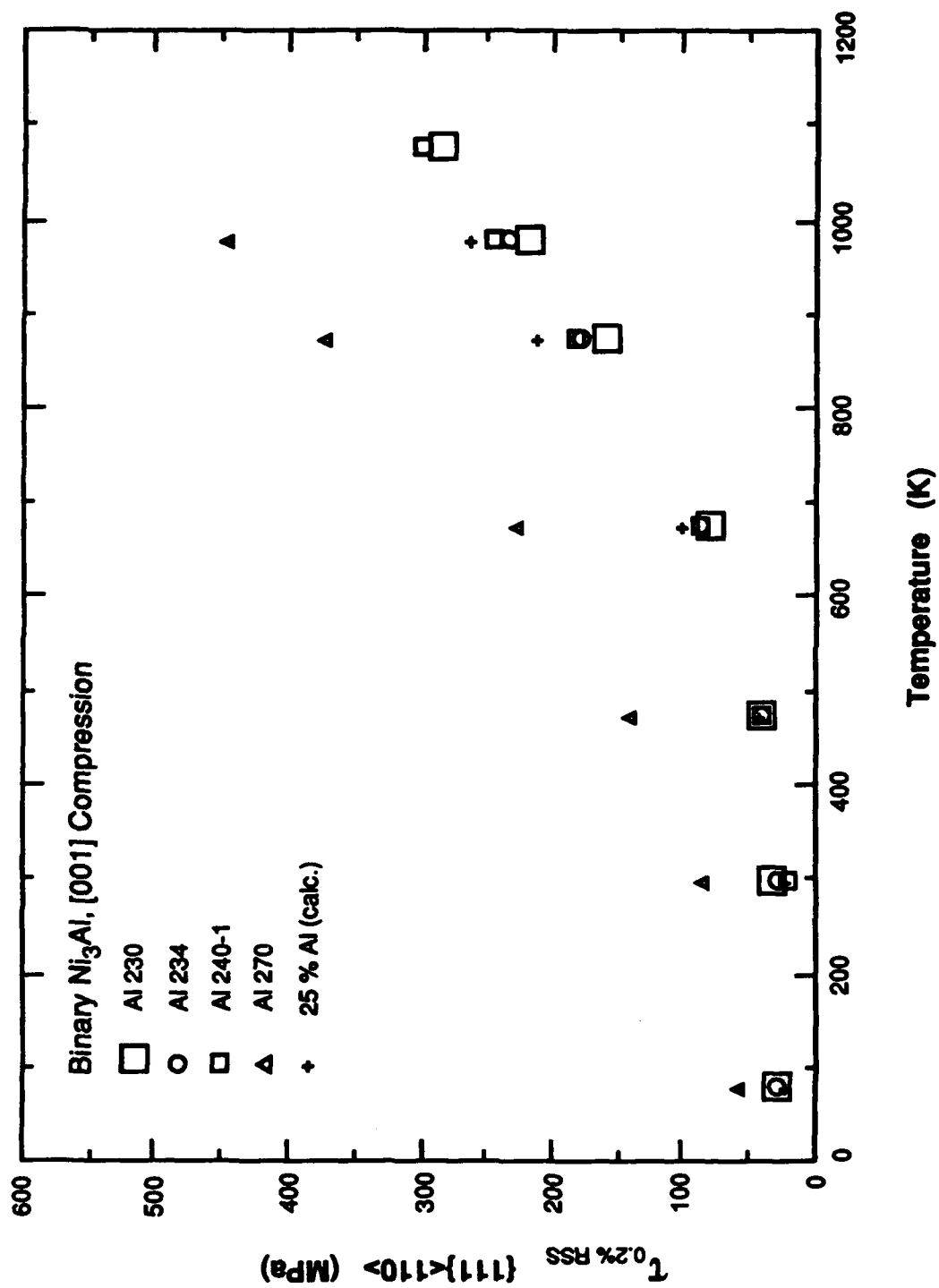
Fig. 4.1 Resolved shear stress versus temperature for binary alloys.

64

concentration for each temperature (as shown in Fig. 4.2) and linearly extrapolating the results to the stoichiometric composition.

Both Figs. 4.1 and 4.2 clearly show that Ni-rich deviations from the stoichiometric composition have little effect upon the strength of Ni_3Al at low temperatures and serve to weaken the material relative to the stoichiometric composition at elevated temperatures. An apparently "athermal" regime extending from -196 to nearly 200 °C exists in the flow-stress-versus-temperature data for the Ni-rich alloys. The slight decrease in flow stress with increasing temperature in this regime is on the same scale as the variation in the shear modulus over this temperature regime $(d\mu/dT)$; however, the data are not sufficiently precise to verify this temperature-dependent decrease. A linear relationship for the flow-stress variation with temperature has been determined using these low-temperature data to fix the y-intercept and assuming proportionality between the variation of flow stress and the shear modulus with temperature or

$$\frac{1}{\tau}\left(\frac{d\tau}{dT}\right) = \frac{1}{\mu}\left(\frac{d\mu}{dT}\right)$$

[4.1].

The temperature-dependent elastic data compiled by Yoo[57] have been used to calculate the right-hand term of Eq. [4.1], and the following linear relationship was determined for the variation of "athermal" flow stress, τ_0, with temperature:

$$\tau_0 = 26.9 - 0.007 \ (T)$$

[4.2]

where τ_0 is in MPa units.

The potent effect of excess Al in the compound is also evident in Figs. 4.1 and 4.2, where the CRSS is shown to increase by nearly 100% at -196 °C, with less than 1 a/o increase in the Al concentration. Excess Al in the compound extends the anomalous flow
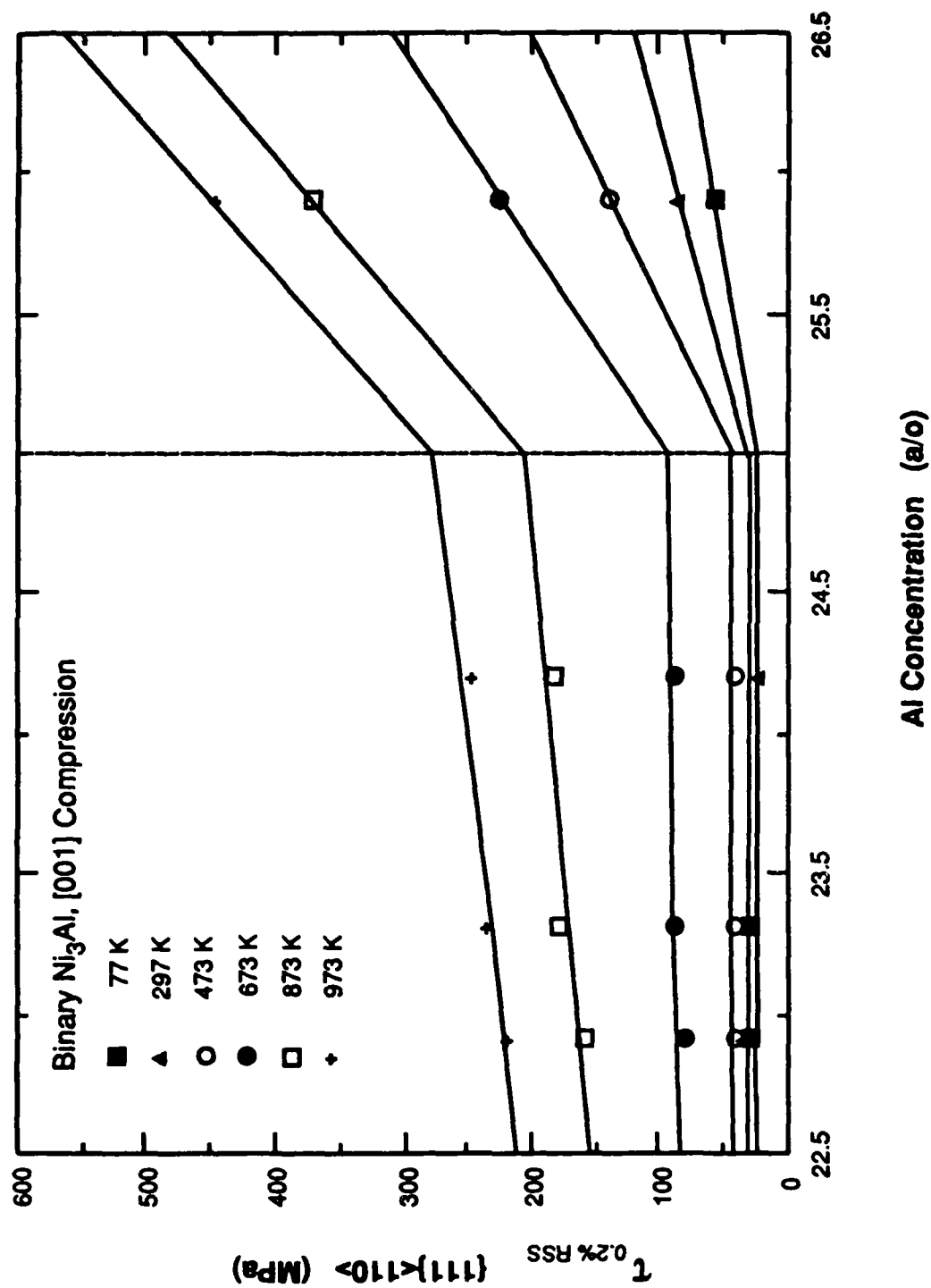
Fig. 4.2 Resolved shear stress versus Al concentration for various temperatures.

66

behavior to -196 °C, eliminating the athermal flow-stress regime and providing a positive slope in the CRSS-versus-temperature curve.

4.1.2 STRAIN HARDENING

With rare exception, all of the samples tested in the present study were deformed in the Stage II strain-hardening regime, with only a few samples exhibiting a small (approximately 0.05%) easy-glide strain. The average Stage II strain-hardening rate, as determined from the nominal stresses and strains ($d\sigma/d\varepsilon$), has been plotted with the variation in temperature and is shown in Fig. 4.3 for both a Ni-rich (Al 230) and an Al-rich (Al 270) binary alloy. Unlike the CRSS, the Stage II work-hardening rate increases with increasing temperature from -196 °C to a temperature near the typical peak temperature for the CRSS, in the case of both Ni-rich and Al-rich alloys. The work-hardening curves for the Al- and Ni-rich compositions have similar slopes but the curve for the Al-rich alloy is shifted toward higher values of strain-hardening rate. This point will be discussed in greater detail in Chapter 5. The slight curvature in the data as plotted is not meaningful since the data contain average error bars of at least ± 250 MPa (not shown for clarity), due to measurements being made on compression samples strained to less than 0.4% plastic engineering strain.

4.1.3 COMPOSITIONAL-STRENGTHENING INCREMENT

The ability of a given element to affect anomalous flow behavior may be observed most readily by examining the difference, $\Delta\tau$, between the flow stress for that alloy at a given temperature, τ, and the flow stress of the stoichiometric compound, τ_s, at that same temperature. This incremental strengthening with temperature has been plotted for the binary alloys and is shown in Fig. 4.4. Again the Ni-rich alloys exhibit essentially no strengthening at low temperature and incremental softening at high temperature. However,
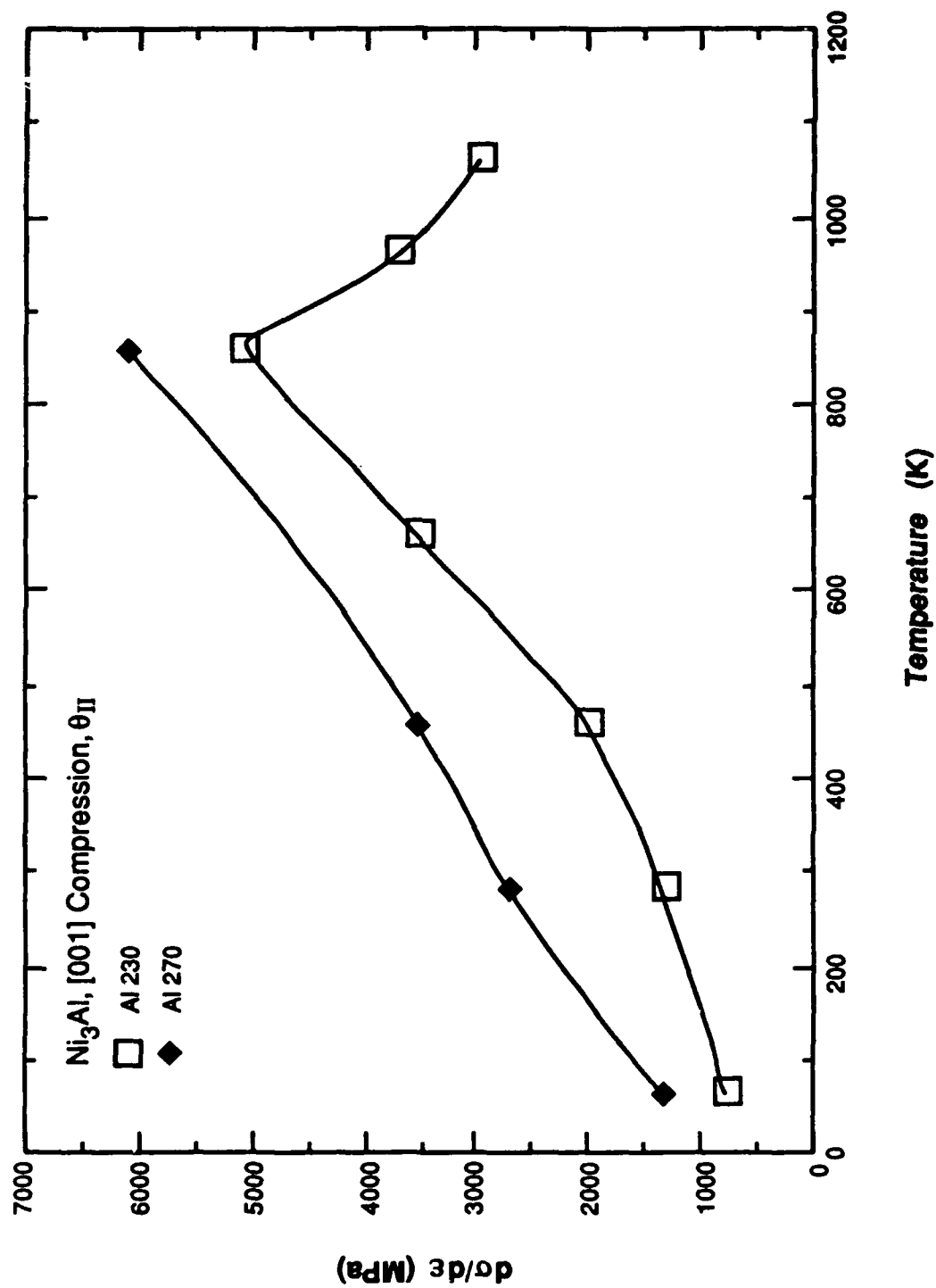
Fig. 4.3 Average Stage II work-hardening rate versus test temperature for two binary alloys.
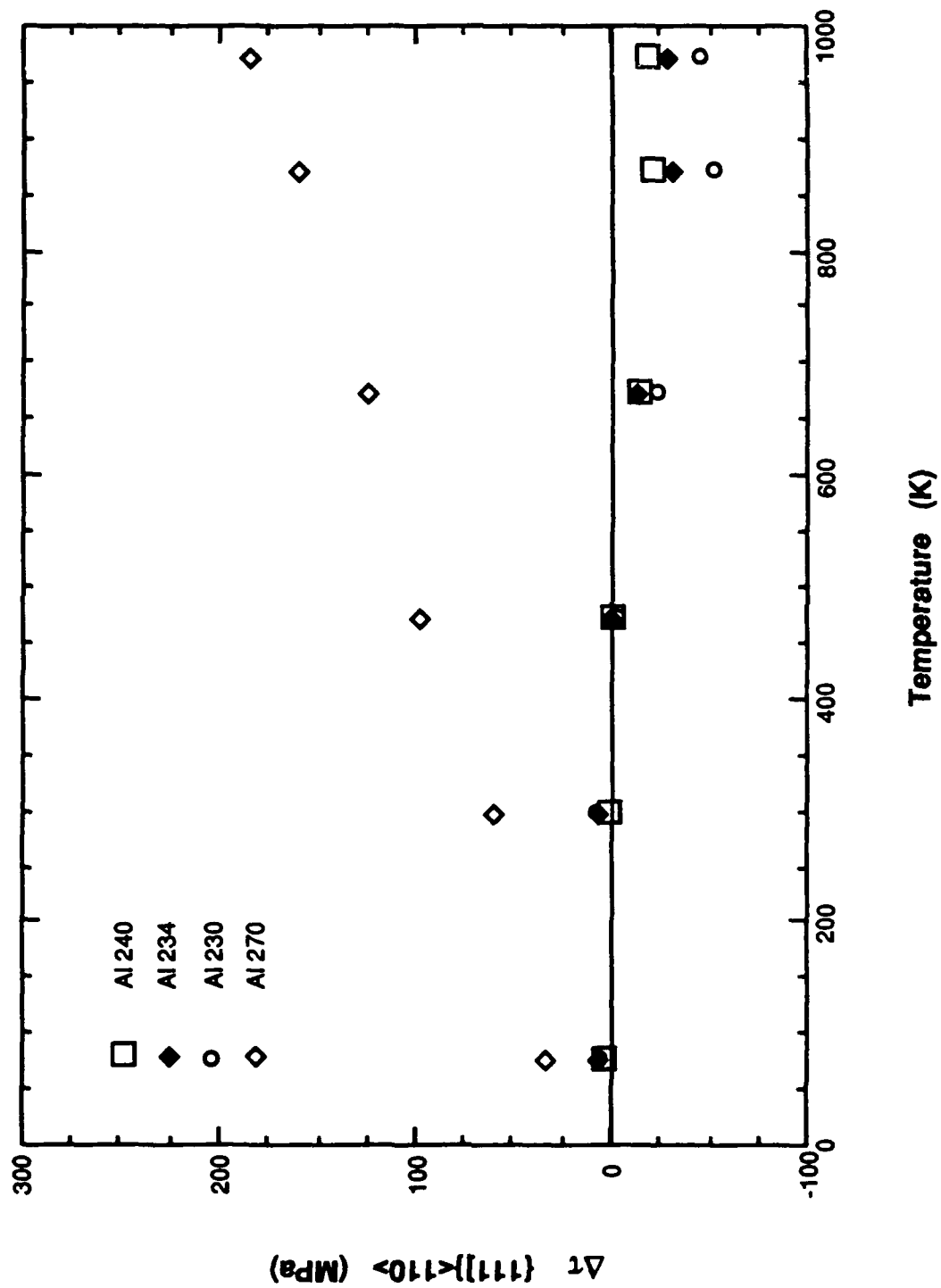
Fig. 4.4 Plot of $\Delta t = \tau - \tau_s$ versus temperature (τ_s from Fig 4.2).

the Al-rich alloy shows an increasing incremental hardening (or divergence of its flow-stress-versus-temperature curve from the calculated curve for the stoichiometric compound) through the highest temperatures studied. This result suggests that adding Al to the alloy is equivalent to raising the temperature of deformation of the stoichiometric compound. A "classical" solute effect (purely elastic) is expected to exhibit a negative slope when the incremental-hardening data are plotted.

An apparent activation enthalpy for the thermally activated process governing the flow-stress-versus-temperature behavior has been computed for the binary alloys by assuming an empirical exponential relationship between flow stress and temperature. The hardening increment due to thermal activation, τ^*, is given by the difference between the flow stress of an alloy at a given temperature, τ, and the effective athermal flow stress at that temperature, given by τ_0, as determined from Eq. [4.2]. The computed values of τ^* were plotted as a function of the reciprocal of temperature in an Arrhenius plot (Fig. 4.5) in order to determine the apparent activation enthalpy. The curve for the Ni-rich alloys is similar to that for the stoichiometric material, having a slope which yields an activation enthalpy of 0.2 eV. Alloy Al 270 exhibits an activation enthalpy of about 0.1 eV which is about half that of the Ni-rich alloys. These values are about one tenth the activation energies for self-diffusion in this system.[99] Clearly, the mechanism(s) governing the anomalous flow strength have been affected by the presence of Al as a solute.

4.1.4 SLIP CHARACTER

Slip character was examined after room-temperature deformation of one sample from each alloy. As shown by other investigations[41,49,64] and confirmed by the present study, the alloys deform by fine planar slip on the primary {111} system when tested with the compression axis oriented along [001]. An example of such slip character in alloy Al 230 is shown in Fig. 4.6. The Al-rich alloy which contained residual β-phase
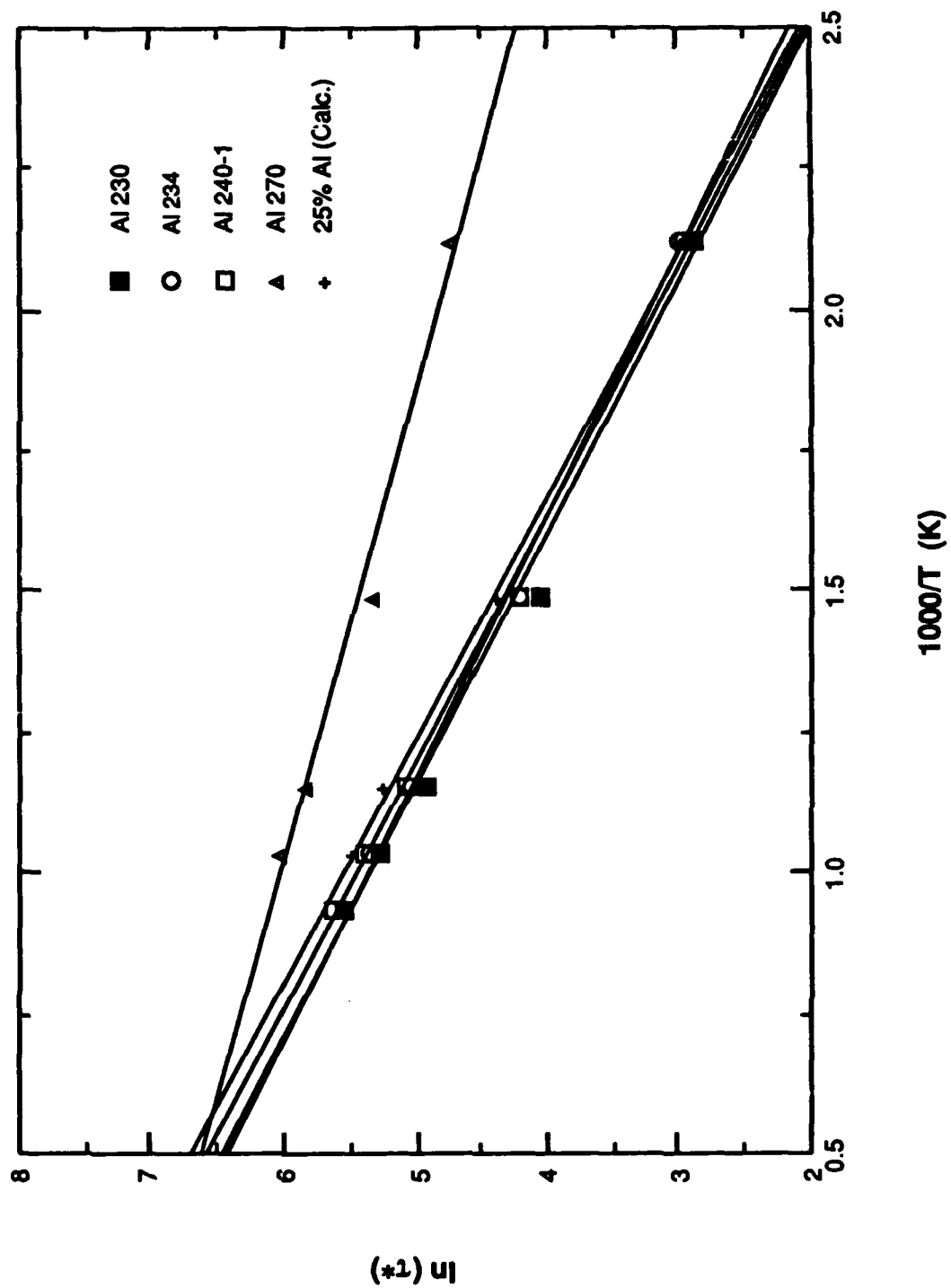
Fig. 4.5 Logarithmic plot of thermally activated stress increment, τ^*, (from Eqs. 4.1 and 4.2) versus reciprocal of temperature.

71
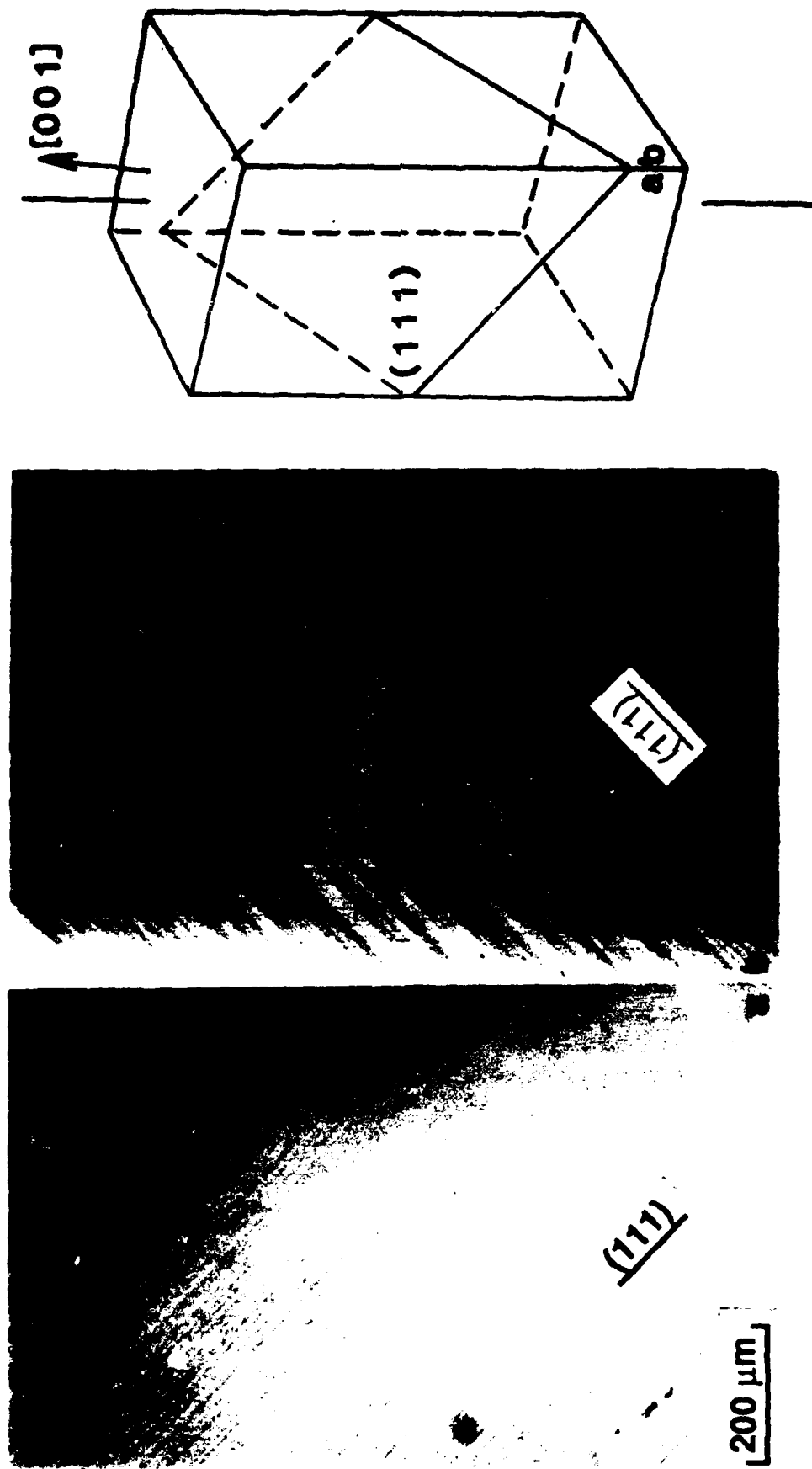
Fig. 4.6 Fine, planar {111} slip in cube-oriented sample of alloy Al 230 deformed at 24 °C.

dendrites also exhibited extensive {111} slip and was relatively unaffected by the β-phase dendrite cores. An example of the slip character of this alloy after room-temperature deformation is shown in Fig. 4.7. At least two different {111} slip systems are clearly operative in this specimen.

4.1.5 PRE-STRAINING EXPERIMENTS

Figure 4.8 shows stress-strain results from an experiment which was carried out in order to demonstrate (in much the same way as the experiments of Davies and Stoloff[35,36]) the "reversibility" of the mechanism(s) governing the flow-stress-versus-temperature relationship in Region II for Ni$_3$Al. A single-crystal specimen of Ni-rich binary alloy (specimen Al 230 4) was pre-strained at 600 °C in compression to a plastic engineering strain level of 0.65%. The same sample was re-strained at 24 °C to achieve an additional plastic strain of 0.25%. The flow-stress values resulting from the two tests of this sample were compared to those of a second sample (Al 230 1) which was strained to the same total-plastic-strain level, entirely at 24 °C. As shown in Fig. 4.8, the high-temperature pre-strained sample had a flow stress at room temperature which was 56% higher (19 MPa increase) than the specimen strained at room temperature alone but did not retain strength levels typical of 600 °C. *The Stage II work-hardening rates revealed no significant difference in the two specimens at room temperature.* The strain-hardening increment between 0.2% and 0.93% plastic strain at 600 °C was shown to be equal to the sum of the strain-hardening increment over the same plastic strain range at 24 °C and that at 24 °C due to prior straining at 600 °C. These results imply that increased flow stress at 24 °C due to pre-straining is attributable to the higher total dislocation density expected from elevated-temperature pre-straining in a higher work-hardening-rate regime. The same point can be made more directly by comparing the effective work-hardening rate at low temperature for the pre-strained sample (slope of the dashed line in Fig. 4.8) with the work-hardening rate

Fig. 4.7   Fine, planar {111} slip on two systems in a cube-oriented sample of alloy
Al 270 deformed at room temperature.
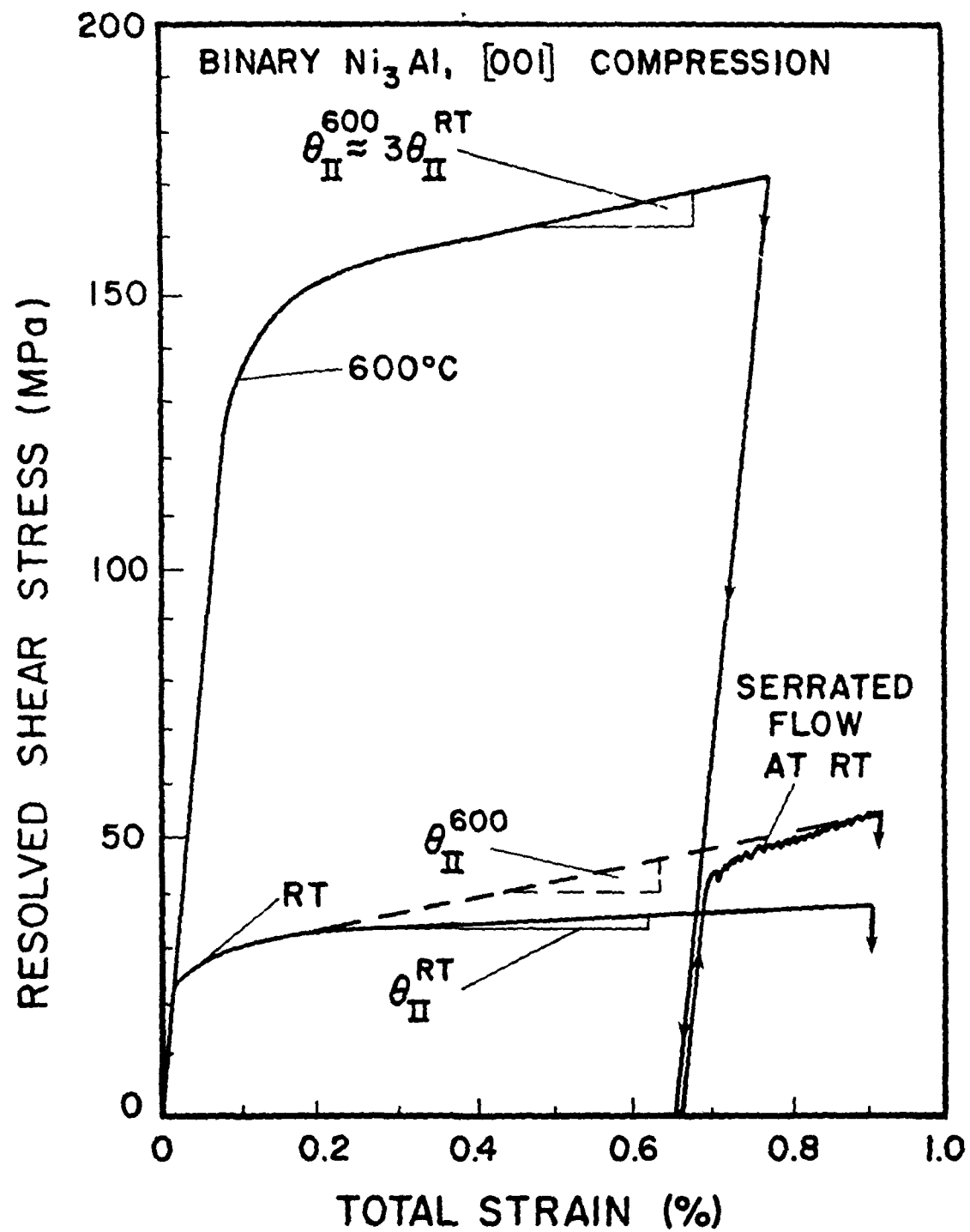
Fig. 4.8 Resolved shear stress versus strain curves for high-temperature prestraining experiment performed with alloy Al 230 samples.

at 600 °C for the same sample. These rates are identical within the range of experimental error. Finally, note that the flow curve of the pre-strained crystal exhibited pronounced serrated flow at room temperature. This behavior was not observed in any other tests.

A second experiment was performed in order to demonstrate the thermal reversibility of the flow stress. A sample of crystal Al 230 was strained at -196 °C to a plastic strain level of 0.55% and then annealed at 600 °C for 1 hour. The crystal was re-strained at -196 °C to an additional plastic strain of 0.7%. As shown in Fig. 4.9, this crystal exhibited no change in flow stress at -196 °C due to the high-temperature anneal. Likewise, *the Stage II work-hardening rate was unaffected by the high temperature anneal.*

4.2 ELECTRON MICROSCOPY OF BINARY ALLOYS

Throughout this and subsequent subsections dealing with electron-microscopy results, many transmission electron micrographs are shown either as single bright-field images or as sets of images, usually recorded under weak-beam conditions. The two-beam imaging vector, g, used for forming these images has been marked by an arrow on the micrograph, with the crystallographic plane which is perpendicular to the vector being indicated numerically. The beam direction is indicated below the image (as in most of the weak-beam image sets), at one of the upper corners, or in the figure caption. The images were recorded from thin-foil specimens having a foil normal which was within 5 degrees of being parallel to the primary slip-plane normal, [111]. These foils were prepared from crystals having a nominal plastic strain ranging from 0.6 to 1.6%. For most of the three- and four-image weak-beam sets, only one image has been marked with an imaging vector. Unless otherwise noted, the reader may correctly assume for these cases that the same vector was used for forming the images having the various other beam directions indicated.
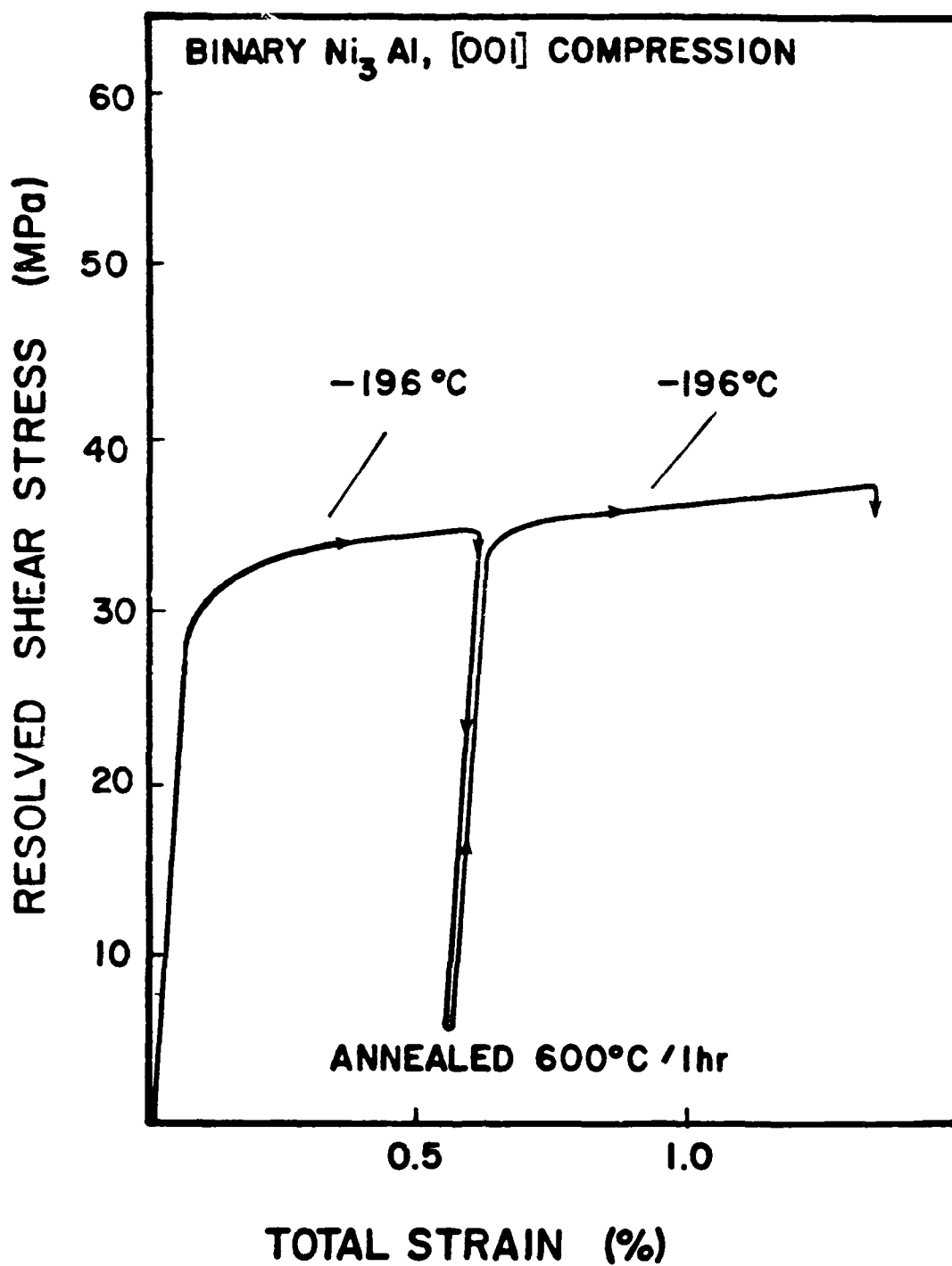
Fig. 4.9   Resolved shear stress versus strain curve for pre-strain, anneal, and re-strain experiment.

Likewise, a single indication of the magnification has been provided for the image sets; however, this indicator may not be precisely correct for every image in the set due to small differences in the photograghic enlargement of the plates. Where dissociation distances are noted, they have been made by precise calibration of the images and are typical examples of measurements used for determining APB energies. The beam directions indicated are typically within 5 degrees of the true crystallographic direction. The resulting small errors (< 0.5%) in dissociation-distance measurements have been ignored in reporting dissociation distances; however, where beam directions other than the one perpendicular to the dissociation plane have been used for determining dislocation spacings, the geometric correction has been made. All images were formed using an operating voltage of 200 kV unless otherwise noted.

Before the deformation structures were examined, a crystal of a Ni-rich binary alloy was sectioned parallel to a {111} plane and prepared for TEM studies of the grown-in dislocation structure. The thin foils from this crystal were essentially featureless. Very few dislocations of any type were observed, and those found were threading through the thin foil rather than lying on the {111} plane parallel to the foil surfaces. Occasionally, low-angle boundaries characterized by well-developed dislocation networks were observed. These featureless foils suggested that the crystals were well annealed and that dislocations contained in deformed samples were very likely due to deformation processes.

4.2.1 DISLOCATION STRUCTURES IN Ni-RICH BINARY ALLOYS

A low-magnification view of the general dislocation structure obtained in a Ni-rich single crystal deformed at room temperature is shown in Fig. 4.10. The most characteristic feature of the dislocation structure is the abundance of dislocation dipole pairs, consisting of dislocations having mixed-character Burgers vectors of $\pm a_0 <10\bar{1}>$; these pairs often occur as tangled groups, such as those at points labeled A in Fig. 4.10. This feature of the

Fig. 4.10 Bright-field image from alloy Al 230 deformed at 24 °C; B[111]. Mixed-character dipoles at A. Kear-Wilsdorf screw dislocations at B. End segments cross-slipped onto ($1\bar{1}1$) at C.

79

dislocation structure is similar to that reported to occur after deformation of $Ni_3(Al,W)$ crystals at -196 °C,[43] and was observed in both Ni-rich binary alloys (Al 230 and Al 240) examined in the present study. A few long, straight screw dislocations (B in Fig. 4.10) were observed. The ends of these dislocations were frequently curved having mixed or edge character in the (111) or ($1\bar{1}1$) plane (as at C in Fig. 4.10). These end segments could frequently be made to move in the thin foil (if located near the foil edges) by converging the illumination in the vicinity of the edge segment. *The edge segment would then glide toward the thicker section of the foil, effectively "unzipping" a portion of the long, straight screw segment.*

The straight screw segments were shown to have $a_0<10\bar{1}>$ total Burgers vectors and to be dissociated into APB-coupled superlattice-partial dislocations according to the scheme discussed in Chapter 2 and depicted in Fig. 2.1(a). Trace analysis of weak-beam dark-field images of these dislocation lines showed them to be in a K-W configuration, with their APB lying in the (010) plane (Figs. 4.11 through 4.13). These screw configurations were extremely straight and uniform on the scale of the resolution of the weak-beam images and were precisely aligned along the $<10\bar{1}>$ directions. Any possible further dissociation into CSF-coupled dislocations could not be resolved in the weak-beam images. The straightness of the dislocation lines was broken only by the formation of large mixed-character kink segments such as the one having a 4.6 nm dissociated width in Fig. 4.11(b) or by joining with end segments which intersected the top and bottom surfaces of the thin foil, as in Figs. 4.12 and 4.13. The large kink segments, hereafter referred to as macrokinks, were shown to be dissociated on the (11ı) glide plane. Occasionally, screw dipole dislocation pairs having the K-W configuration were observed. These K-W dipole pairs appeared edge-on with an <010> beam direction and exhibited an apparent maximum separation, when viewed along the <101> beam direction. One such pair is shown in Fig. 4.14. The straight dislocation segments in the upper center region of

Fig. 4.11 Weak-beam images of Kear-Wilsdorf screw dislocation in alloy Al 230 deformed at 24 °C; g-3.5$g(20\bar{2})$; a) dissociated pair viewed edge-on, b) macrokink segment split in (111), c) pair viewed with $B[121]$, and d) straight segments dissociated in (010).

110   111   112   114
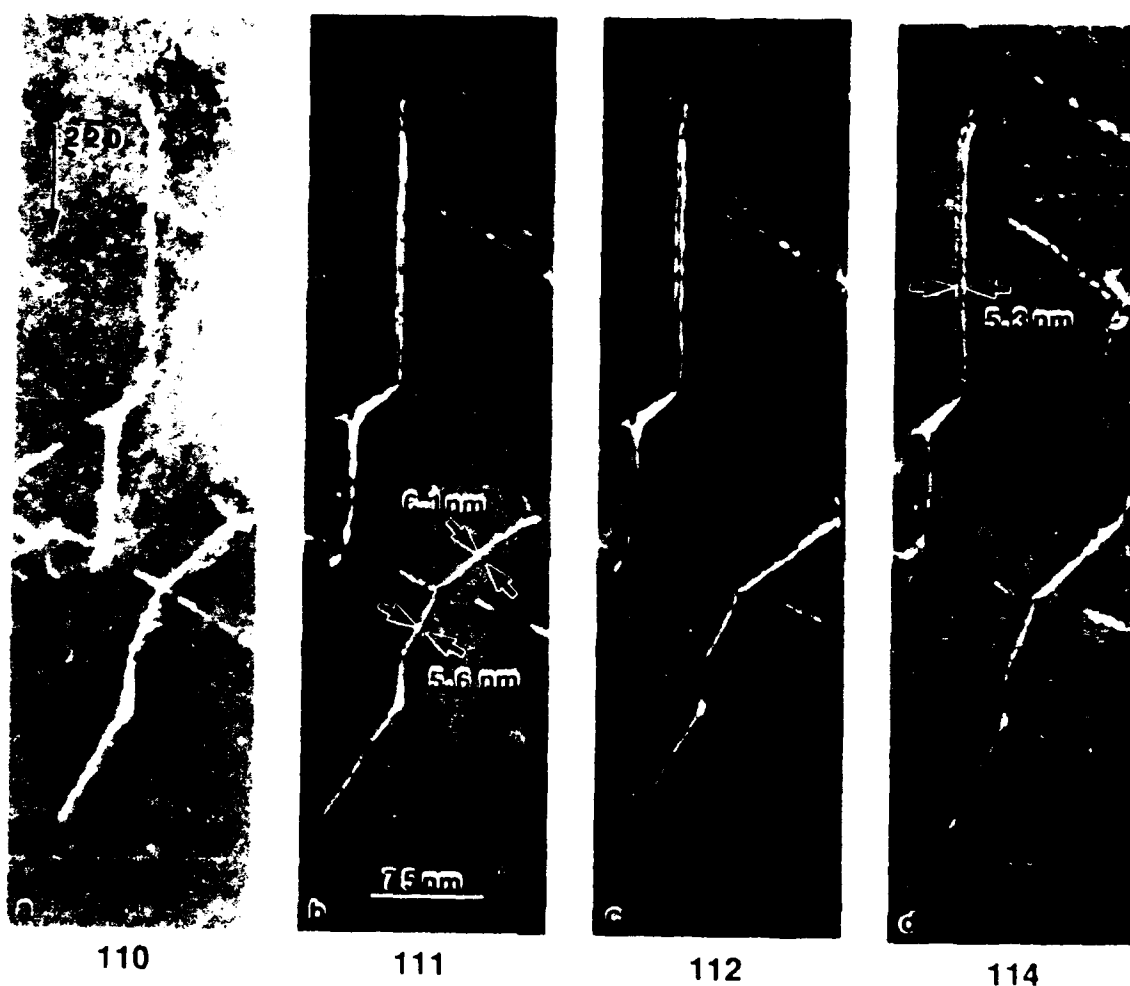
Fig. 4.12 Weak-beam images of Kear-Wilsdorf screw dislocation and mixed-character
           segments with **b** = ±[2$\bar{2}$0] in alloy Al 240 deformed at 24 °C; **g**-4g(2$\bar{2}$0); a)
           dissociated screw pair viewed edge-on, b) mixed-character segments split in
           (111), c) pair viewed with **B**[112], and d) screw segments dissociated in (010)
           viewed with **B**[114].

8 2

Fig. 4.13 Weak-beam dark-field images of screw dislocation in alloy Al 240 deformed at 24 °C; **g**-4g(0$\bar{2}$2).
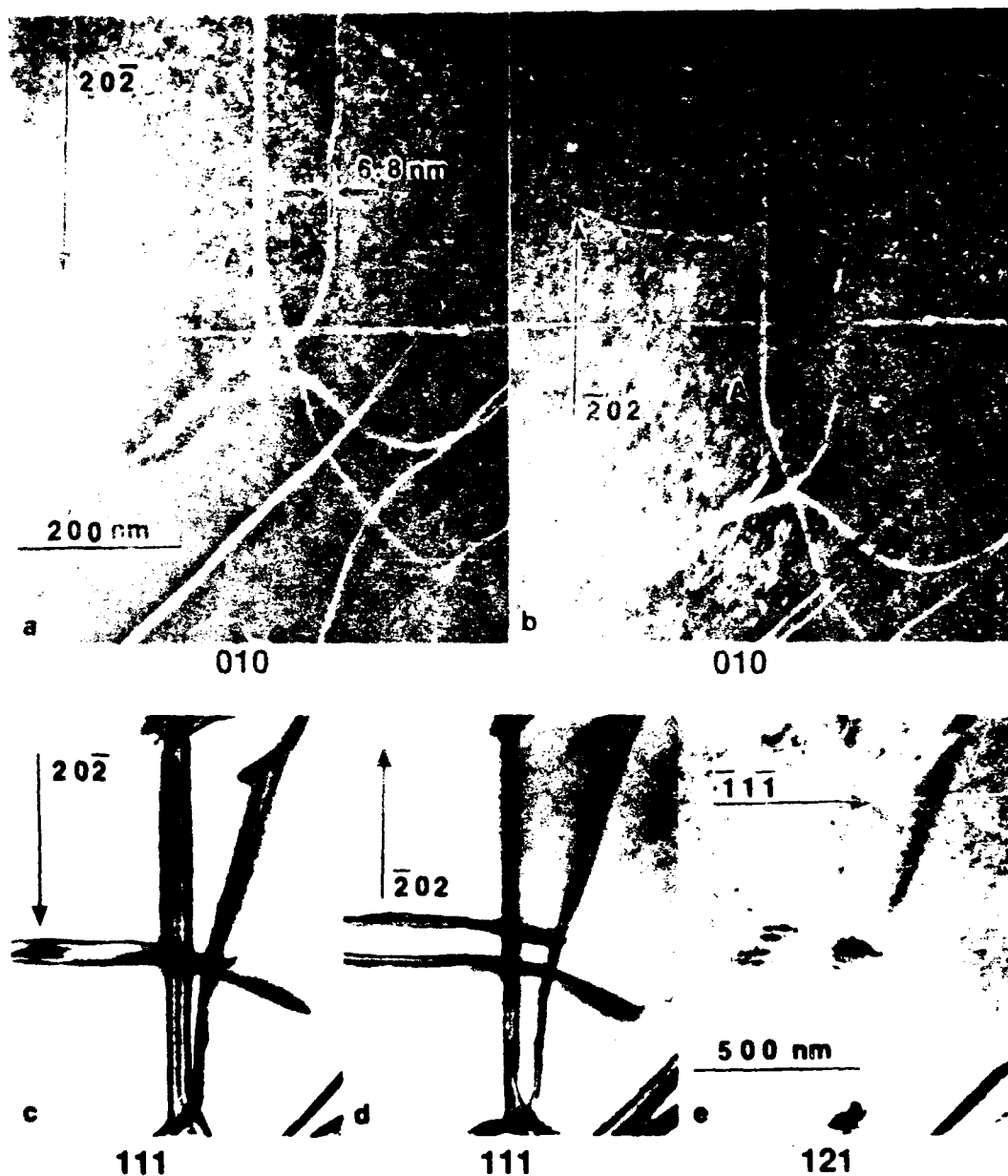
Fig. 4.14 Kear-Wilsdorf screw dipole pair; a) g-3.5g($20\bar{2}$) weak-beam image, b)
g-3.5g($\bar{2}02$) weak-beam image, c) and d) ±g($20\bar{2}$) BF's and e) $\mathbf{g \cdot b} = 0$ for
g($\bar{1}1\bar{1}$). Alloy Al 230 deformed at 24 °C.

Figs. 4.14(a) and 4.14(b) are shown to change their apparent width with a reversal of sign (positive to negative) of the imaging vector **g**. The bright-field images exhibit similar behavior in Figs. 4.14(c) and 4.14(d), while the image of the dislocation line is invisible for **g** perpendicular to the line in Fig. 4.14(e). Occasionally, dislocations having more closely spaced macrokink segments were observed (Fig. 4.15).

Stacking-fault-coupled dislocations were observed only on rare occasions in the Ni-rich binary alloys, either as reactions occurring at dislocation intersections or as dipole loops lying in the slip plane (the latter are treated in greater detail in Subsection 4.4.1). These dislocations were difficult to locate in the thin foil. No cases of pure screw segments dissociated on the primary glide plane could be located. Likewise, *no indications of glide in the cube cross-slip plane were observed.*

4.2.2 DEFORMED AND ANNEALED Ni-RICH SAMPLES

One sample of alloy Al 230 was deformed at room temperature, annealed at 700 °C, and water quenched after deformation. The general dislocation structure of this alloy is shown in Fig. 4.16. The polygonized region at the top of the figure is believed to be an artifact of crystal growth and not a result of the annealing treatment since no similar dislocation networks were observed in other samples prepared from the same crystal. The dislocation-dipole segments, which are characteristic of low-temperature deformation in Ni-rich alloys, are apparent after annealing (see points A). Screw dislocations having the K-W configuration (B in Fig. 4.16) are observed with somewhat greater frequency; however, they are not an prominent feature of the dislocation structure.

The sample of alloy Al 230 which was pre-strained at -196 °C, annealed at 600 °C, and re-deformed at -196 °C was examined in the TEM. This sample revealed a dislocation structure which was strikingly different from that of the samples of the same alloy

Fig. 4.15 Weak-beam images of dislocation with many macrokinks in alloy Al 230 after deformation at 24 °C; g-3.5g(20$\bar{2}$).

Fig. 4.16 Bright-field image of alloy Al 230 deformed at 24 °C, annealed at 700 °C, and water quenched; B[211]. Mixed-character di ule pairs at A. Kear-Wilsdorf screw dislocations at B.

deformed at 24 °C. The dislocation structure consisted almost entirely of crystallographically straight dislocation segments aligned parallel to <10$\bar{1}$> directions (as shown in Fig. 4.17), many of which were shown to be a_0<10$\bar{1}$> screw dislocations having the K-W configuration. *The characteristic dipoles and tangled mixed-character dislocations, which are typical of low-temperature straining, were not observed in this sample although the deformation was carried out at -196 °C.* These results suggest that dislocation structures typically observed after deformation at temperatures above room temperature must be due, in part, to the extension of dislocations along crystallographic directions after some pinning events.

4.2.3 DISLOCATION STRUCTURES IN Al-RICH BINARY ALLOY

The dislocation structure as well as the mechanical behavior of the Al-rich alloy Al 270 was, in general, very different from that observed in the Ni-rich binary alloys. As shown in Fig. 4.18 extended, rather-straight dislocations were observed after deformation at room temperature; however, the dislocations were neither crystallographically straight nor aligned. Rather, the dislocation lines exhibited a high frequency of closely spaced macrokink segments, such as those labeled A in Fig. 4.18, which connected dislocation segments having near-screw character. Relatively few dislocations of wavy, mixed-character-dipole segments, characteristic of the Ni-rich alloys, were observed in the dislocation structure of alloy Al 270. A long, isolated dipole pair is indicated by B in Fig. 4.18.

The structure of the heavily kinked dislocation lines was examined in further detail using the weak-beam dark-field technique. In Fig. 4.19 a pure screw a_0[10$\bar{1}$] segment can be seen which is dissociated in the (010) plane at a distance of 4.1 nm. Such dislocation

Fig. 4.17 Bright-field image of alloy Al 230 deformed at -196 °C, annealed at 600 °C, and re-strained at -196 °C; B[111]. High density of extended screw dislocations having Kear-Wisdorf configuration is present despite low deformation temperature.

Fig. 4.18 Bright-field image of alloy Al 270 deformed at 24 °C; B[111]. Macrokink
segments connecting Kear-Wilsdorf segments at A. Dipole pair of mixed
character at B.

90

101   111   121   010
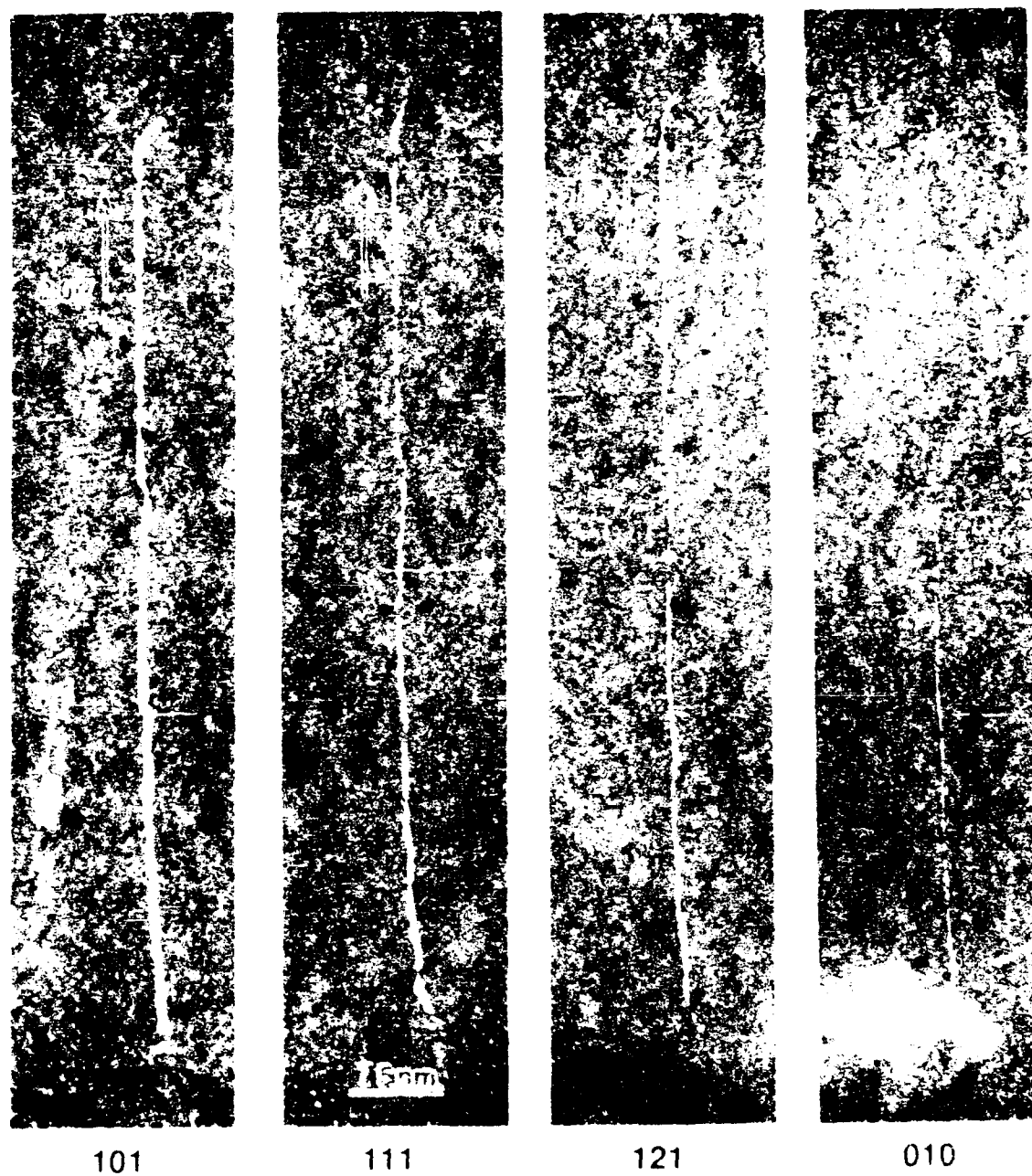
Fig. 4.19 Weak-beam images of screw dislocation in alloy Al 270 after deformation at 24 °C; $\mathbf{g}$-4$\mathbf{g}$(20$\bar{2}$). High density of microkinks may be observed by sighting along dislocation line, nearly parallel to the page.

segments having a rather uniform separation distance over a long length were observed only rarely. The majority of the dislocation lines exhibited an overall deviation from exact screw character and were made up of extremely short segments, having lengths on the order of two to ten times the APB width (aspect ratios of 2:1 to 10:1); those dislocation lines were identified as screw segments in the K-W configuration. These short K-W segments were joined by kink segments of comparable, or even shorter, length. Some of the longer kink segments were shown to be dissociated in the (111) plane, such as in Fig. 4.20(b); however, the majority of the kinks were of a size comparable to the dissociated width of the APB and often appeared as a constriction on the superpartial pair. These small kinks, hereafter referred to as microkinks, resulted in an overall roughness to the appearance of the dislocation lines, which can be most readily observed by sighting along the dislocation lines at an angle of observation nearly parallel to the plane of the micrographs. For most dislocation segments examined in this alloy, the dissociation plane of the dislocation core was difficult to determine, and the possibility exists that the dissociation distances recorded from this alloy are affected by the high density of constrictions and kinks along the dislocation line; in general, the result is an apparent dissociation distance which is less than the equilibrium value, due to the forced curvature of the segment near the constrictions.

One sample of alloy Al 270 was examined in the electron microscope after deformation at -196 °C. An example of the dislocation structure in this sample is shown in Fig. 4.21. The structure has an appearance similar to that of the Ni-rich alloys deformed at 24°C. Many more stacking-fault-coupled $a_0/3<11\bar{2}>$ dipole loops (treated in subsection 4.4.1) which usually emanate from $a_0/2<10\bar{1}>$ mixed-character segments (A in Fig. 4.21) were observed. These dislocations were not observed after room-temperature deformation of this alloy and occurred only rarely in the Ni-rich alloys. The long, wavy dipole pairs which are characteristic of low-temperature deformation are indicated by B in Fig. 4.21.

92

Fig. 4.20 Weak-beam images of screw dislocation with both macrokink and microkink segments; alloy Al 270, $\pm g\text{-}5g(2\bar{2}0)$, deformed at 24 °C.

93

Fig. 4.21 Bright-field image from alloy Al 270 deformed at -196 °C; B[111]. Extended stacking faults bounded by $a_0/3<11\bar{2}>$ dipole dislocation loops at A. Macrokink segments connecting dipole pair of mixed character $a_0<10\bar{1}>$ dislocations at B. Kear-Wilsdorf segments at C.

The segments marked C are examples of straighter, rougher dislocation lines which are similar to those observed after room-temperature deformation. *Although this sample exhibited a dislocation structure which resembled that of the Ni-rich alloys deformed at room temperature or that characteristic of low-temperature deformation of Ni_3Al alloys, the sample had a CRSS of 60 MPa at -196 °C, which is 100% greater than that of the Ni-rich alloys at both -196 and 24 °C.*

4.2.4 DETERMINATION OF APB ENERGIES

The dissociation distances of the $a_0/2<10\bar{1}>$ superpartial dislocations on the (111) plane have been determined as a function of dislocation character and alloy composition. Likewise, the average dissociation distance has been determined for $a_0/2<10\bar{1}>$ dislocations in the pure-screw K-W configuration dissociated on the (010) plane. These dissociation distances are shown for alloys Al 230 and Al 240 in the plots in Figs 4.22 and 4.23, respectively, as determined from samples deformed at room temperature. In each of these figures, the dissociation distance, d, is plotted as a function of the dislocation character as described by the angle θ between the Burgers vector, b, and the line direction, u, measured in the octahedral glide plane. The average spacing of pure screw dislocations dissociated in the cube cross-slip plane is indicated along the ordinate. The individual distance measurements are recorded in Appendix D.

A similar plot of the dissociation distances obtained after heat treatment of alloy Al 230 at 700 °C, followed by water quenching, is shown in Fig. 4.24. Significantly greater variability in the {111}-plane-dissociation distance was observed after heat treatment. The weak-beam micrographs in Figs. 4.25 and 4.26 show that macrokink segments along screw-dislocation lines remained dissociated after heat treatment, as indicated by the large arrow in Fig. 4.25(a). This particular macrokink segment as well as some others appear to have expanded in the {111} plane, giving rise to greater variability in

95
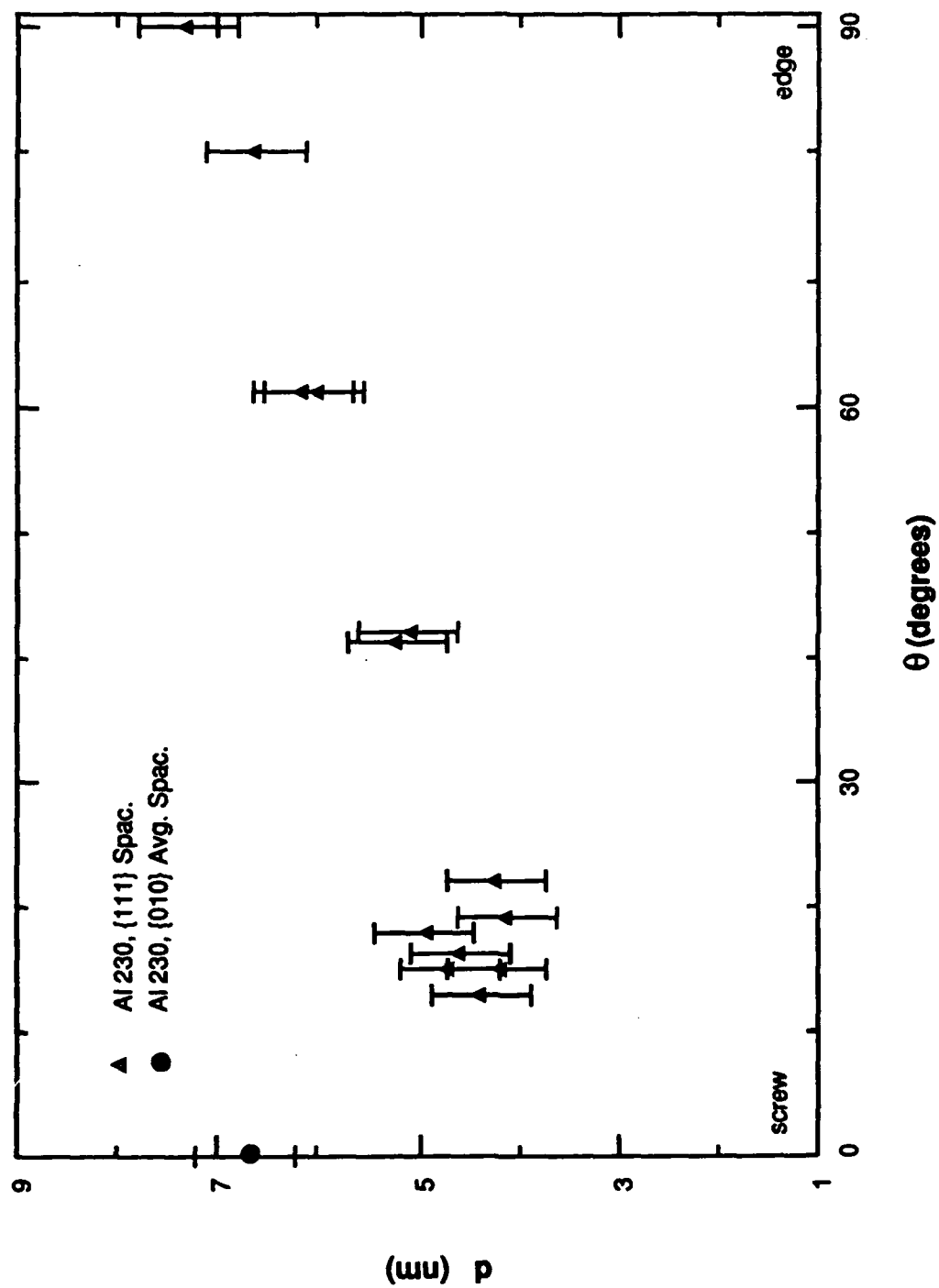
Fig. 4.22 Dissociation distance versus dislocation character, Al 230, as deformed at 24°C.

96
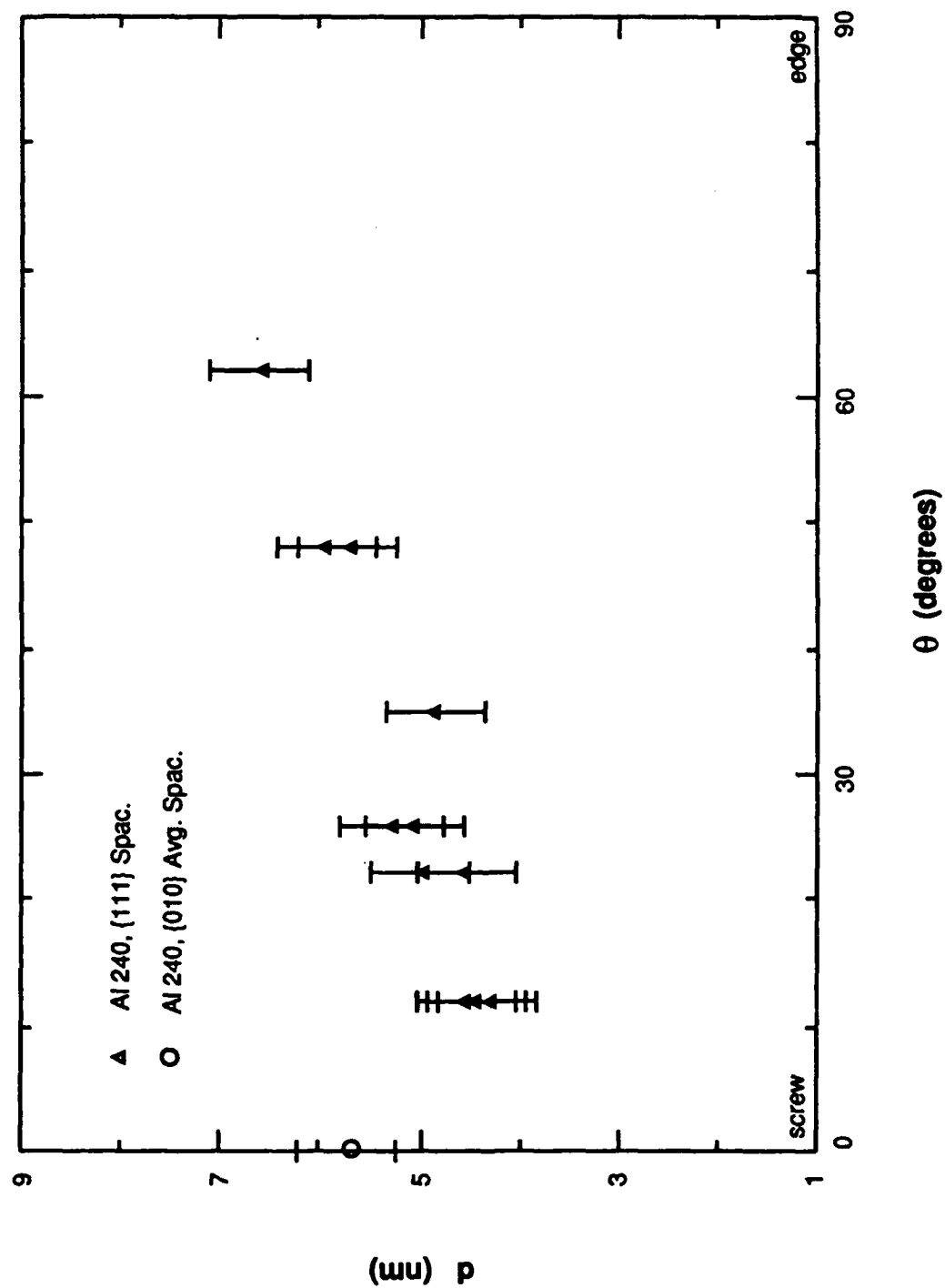
Fig. 4.23 Dissociation distance versus dislocation character, Al 240. as deformed at 24 °C.
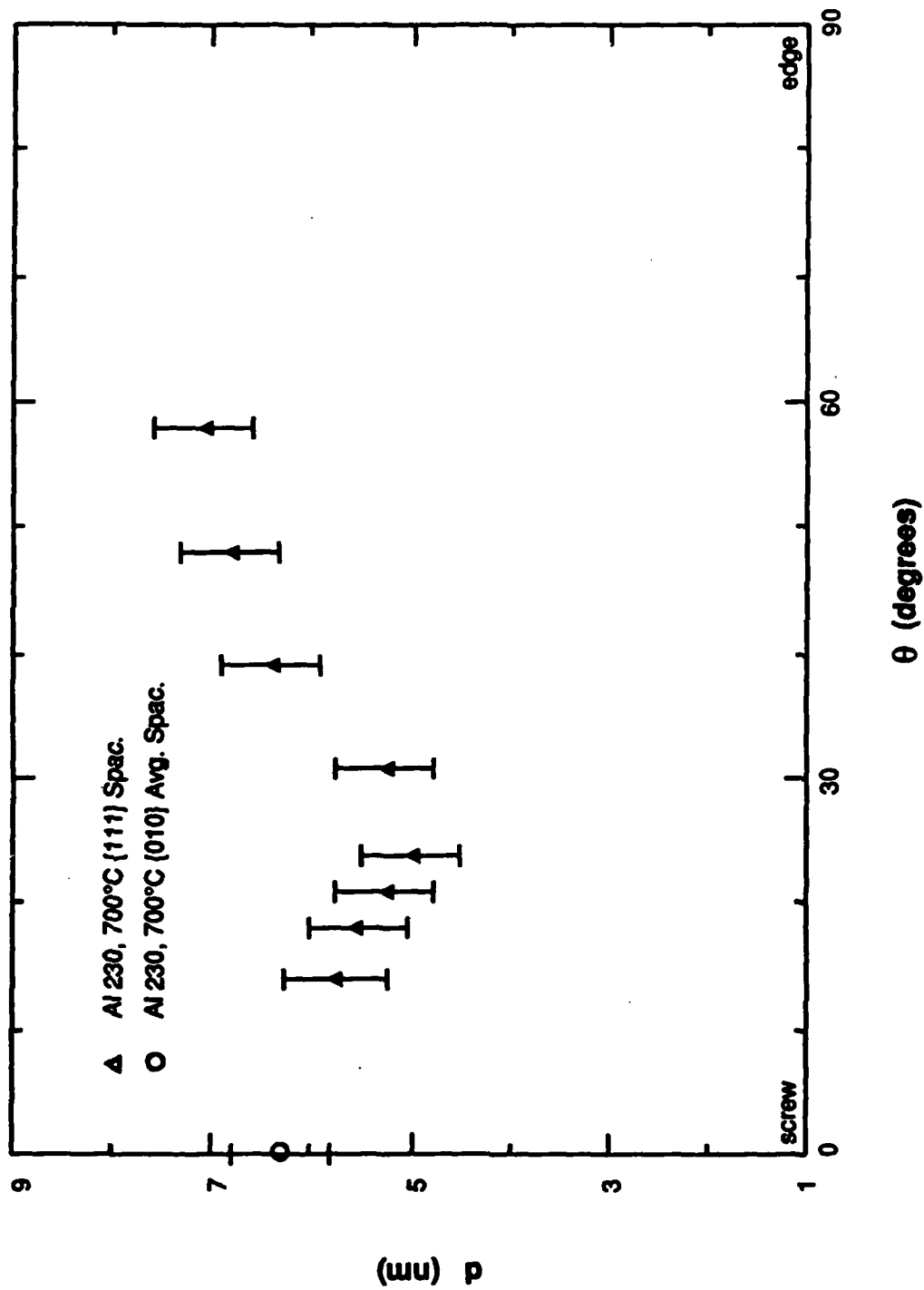
Fig. 4.24 Dissociation distance versus dislocation character, Al 230, deformed at 24 °C, annealed at 700 °C for 1 hr, and water quenched.
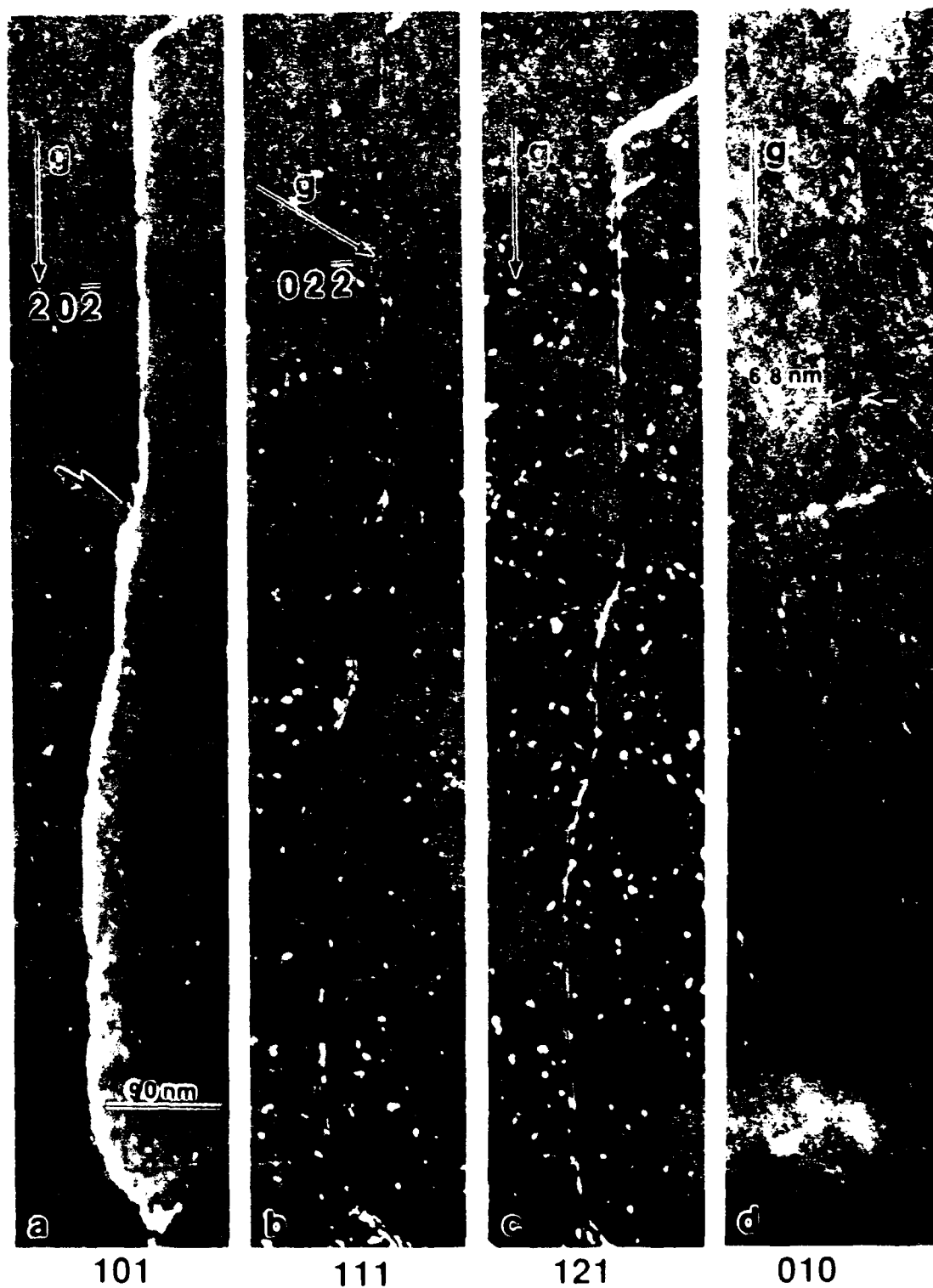
Fig. 4.25 Weak-beam images from alloy Al 230 deformed at 24 °C, annealed at 700 °C, and water quenched: **g**-3.5g(202), 100-kV electrons; a) dissociated pair viewed edge-on with macrokink split in (111) show. at large arrow, b) viewed with **B**[111], c) viewed with **B**[121], and d) screw segments dissociated in (010).

Fig. 4.26 Weak-beam images from alloy Al 230 deformed at 24 °C, annealed at 700 °C, and water quenched; g-4g($2\bar{2}0$); a) dissociated pair viewed edge-on, b) viewed with **B**[111], c) viewed with **B**[114].

the dissociation-distance measurements. An analysis based on the expected anisotropy of the APB energy and the expected mobility of thermally activated kinks suggested that the heat treatment given to these samples should have been sufficient to convert these macrokink segments to large jog segments dissociated in a plane of lower APB energy. This analysis is presented in Appendix E. The APB energy on the {111} plane apparently decreases at high temperature, thereby reducing the driving force for the formation of large jog segments.

The dissociation distances found in the Al-rich alloy Al 270 are shown in Fig. 4.27. Figures. 4.28 and 4.29 contain two additional weak-beam dark-field-image sets showing dislocations in this alloy. As in the heat-treated Ni-rich alloy, a greater variability exists in the measurements made on alloy Al 270. However, this variability is due, in part, to the overall smaller spacings which contain larger percentage errors as well as to the likelihood of the elastic line tension preventing these heavily kinked dislocations from reaching their equilibrium spacing. Line-tension effects are expected to alter the screw-oriented dislocations lying on the cube planes (due to the sessile core configurations of screw-oriented dislocations and, hence, lower mobility) to a greater degree than the kink segments lying on the {111} plane.

The dissociation distances in Appendix D have been used to compute the average APB energy for the {111} and {010} planes as a function of composition. The following standard relationship[104,105] (derived from the total energy of the dissociated core using the framework of anisotropic-elastic theory) which yields the APB energy as a function of the dissociation distance and the elastic-energy coefficient has been used:

$$\gamma = K(\theta) \, b^2/2\pi d \qquad\qquad [4.3]$$
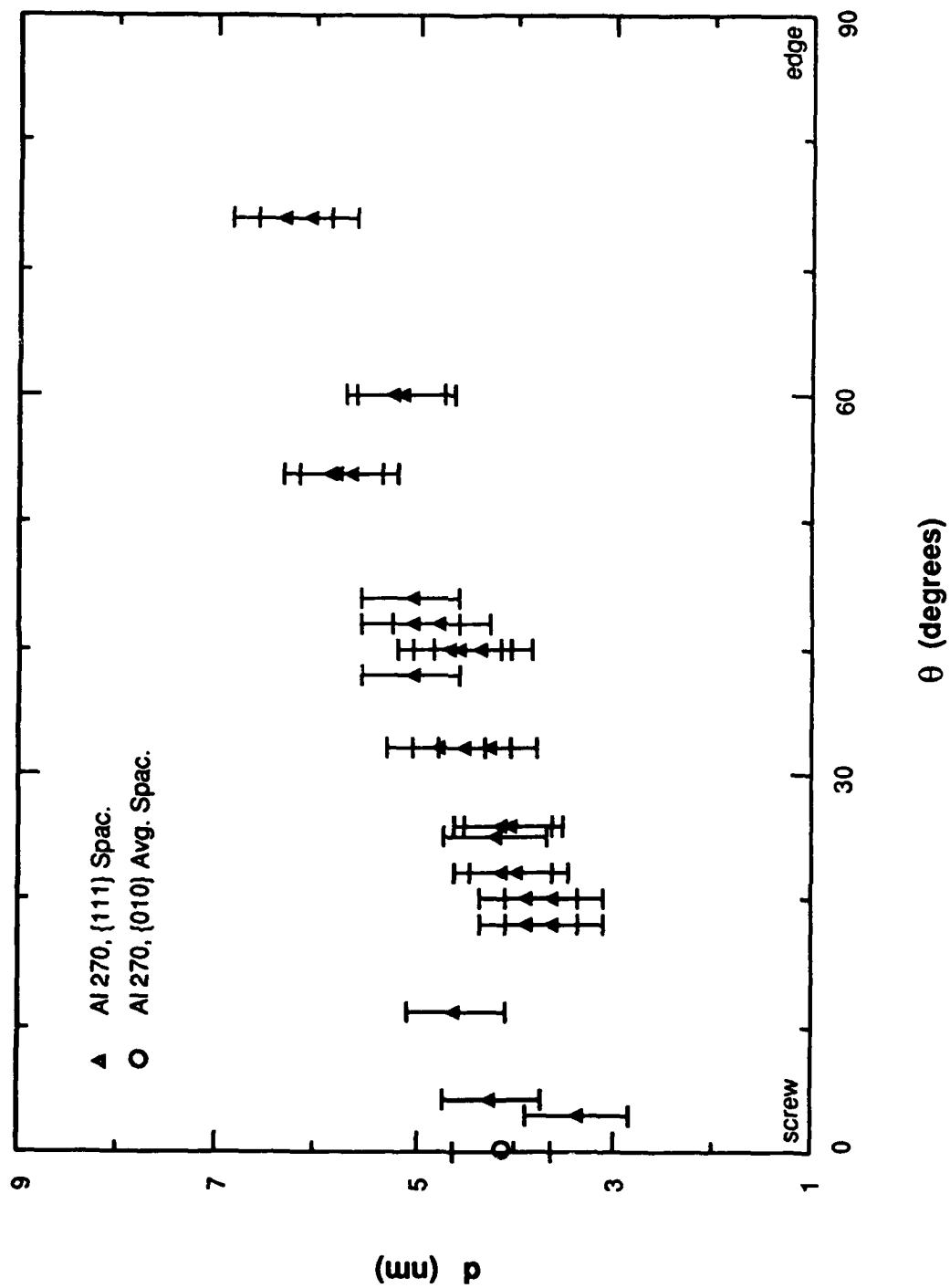
Fig. 4.27 Dissociation distance versus dislocation character; Al 270, as deformed at 24°C.
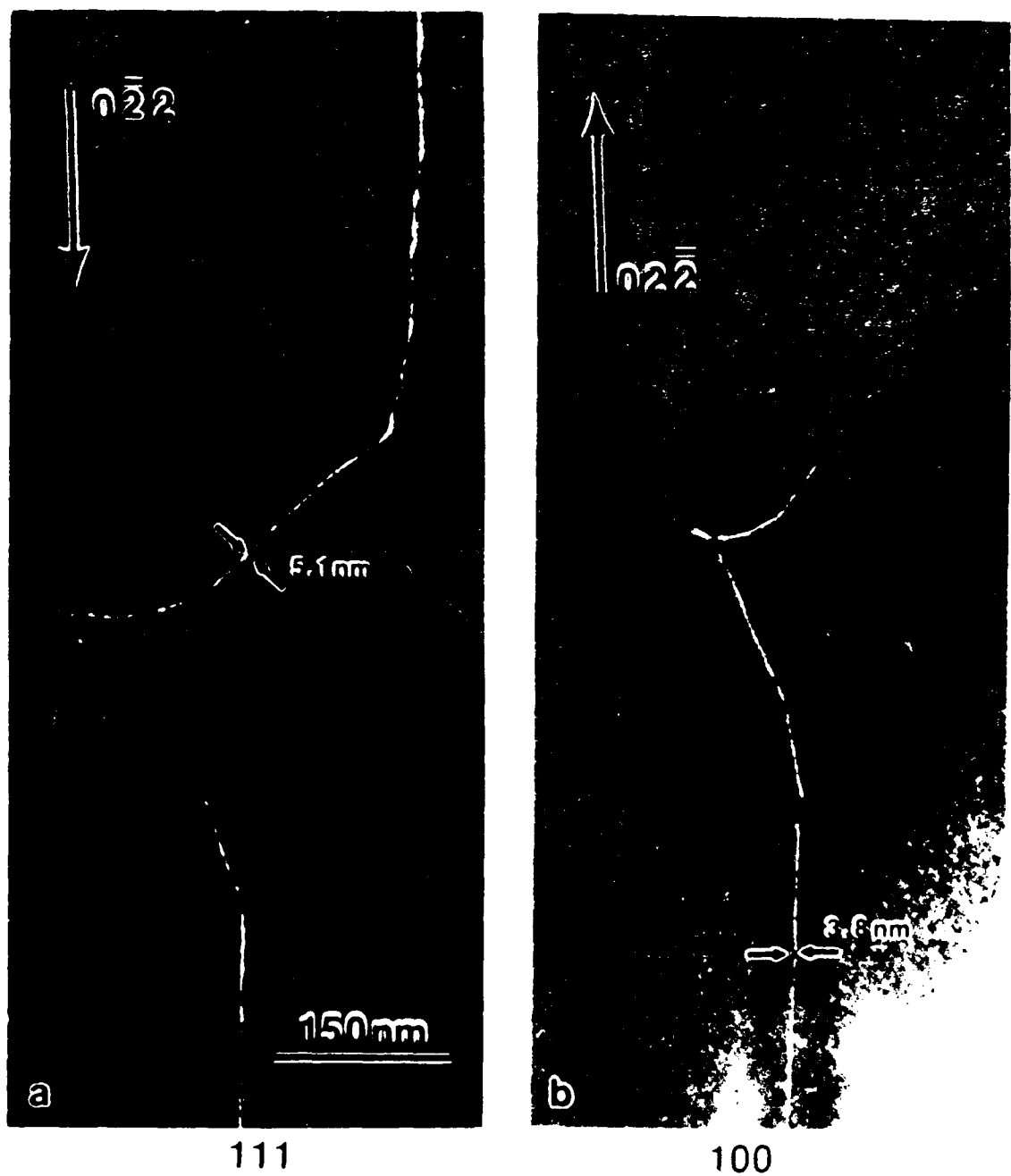
Fig. 4.28   Weak-beam images from alloy Al 270 after deformation at 24 °C; ±g-4g(0$\bar{2}$2).

103
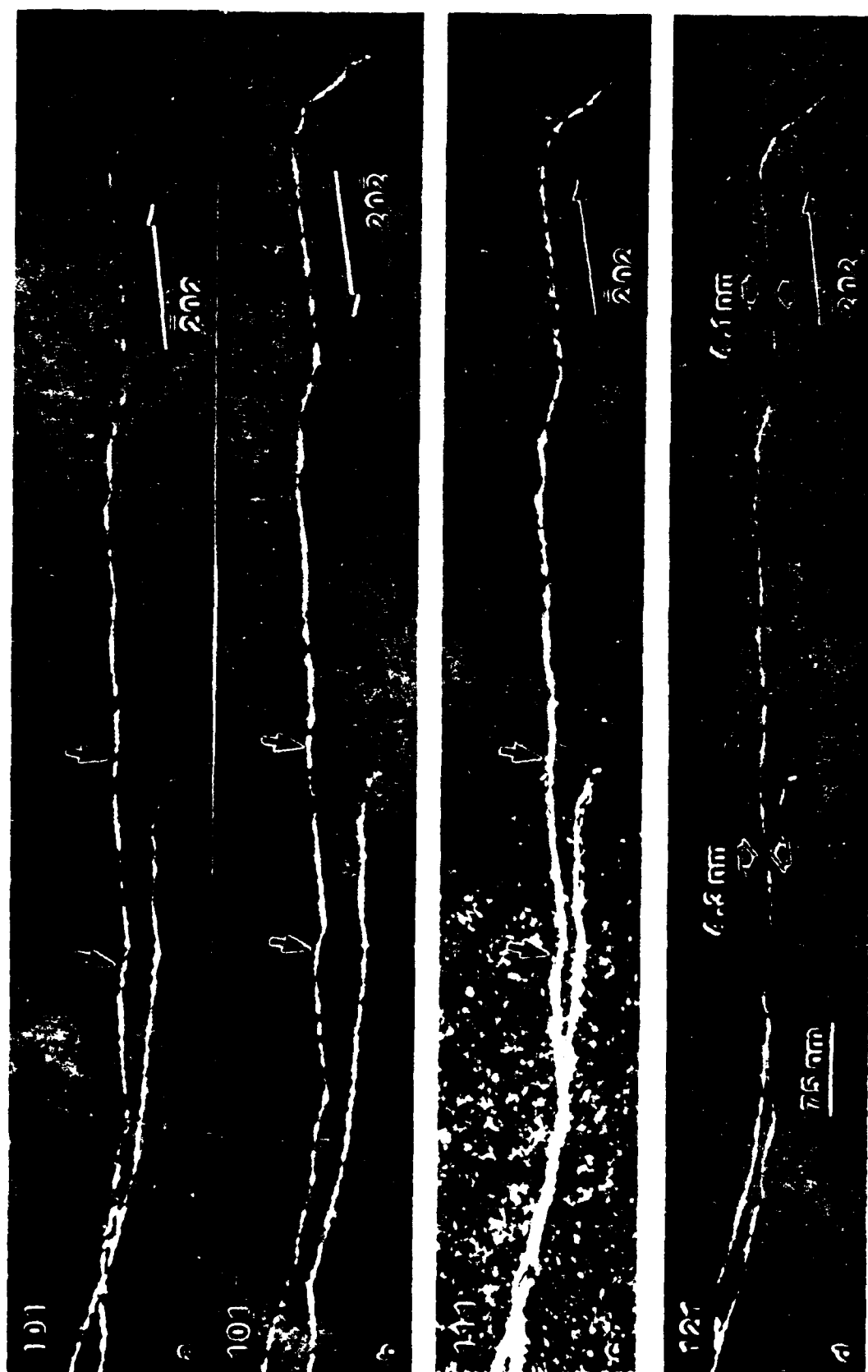
Fig. 4.29 Weak beam images of near-screw-oriented dipole pair from alloy Al 270 after deformation at 24 °C; a) and b) ±g-5g(202), c) g-4g(202), and d) g-4.5g(202). Macrokinks dissociated in (1̄11) at solid arrows.

where γ is the APB energy, $K(\theta)$ the anisotropic elastic-energy coefficient which varies as a function of dislocation character (θ being the angle between the Burgers vector and the line direction), b the magnitude of the Burgers vector, and d the measured dissociation distance. The energy coefficients computed for Ni_3Al as a function of temperature by Yoo[59] have been used in this analysis. The same room-temperature energy coefficient was used for all binary alloys since compositionally dependent corrections are not available. The value employed is given at the top of the tables in Appendix D. The magnitude of the Burgers vector was corrected for each alloy using the data for the lattice-parameter variation, with the composition being given by Ochiai *et a.* [06] The individual Burgers-vector magnitudes can also be found at the top of the tables in Appendix D. Table 4.1 contains the measured average APB energies for the {111} and {010} planes (γ_{111} and γ_{010}, respectively), and the APB-energy ratio, $\gamma_{111} / \gamma_{010}$, for each binary alloy. These data show the effect of increasing the Ni concentration beyond the level for the stoichiometric composition which is a slight lowering of the APB energy on the {010} plane, while the {111}-plane energy remains essentially unaffected. At 700 °C both the {010}- and the {111}-plane APB energies decrease in the Ni-rich alloys. When the Al concentration is increased beyond the level of the stoichiometric compound, the APB energies rise sharply on both the {010} and {111} planes but even more rapidly on the {010} plane, causing the APB energy ratio to decrease to almost unity. *Only the most Ni-rich alloy has an APB energy ratio comparable to the square-root-of-three value required by the PP&V model.*

Table 4.1 Antiphase Boundary Energies for Binary Ni_3Al Alloys

Alloy	Composition (a/o)	γ_{010} (mJm^{-2})	γ_{111} (mJm^{-2})	$\gamma_{111}/\gamma_{010}$
Al 230	Ni-22.9Al	104 ± 8	169 ± 19	1.63
Al 230 *	"	92 ± 8	123 ± 20	1.33
Al 240	Ni-24.2Al	122 ± 11	163 ± 21	1.34
Al 270	Ni-25.9Al	170 ± 21	190 ± 26	1.12

* annealed at 700 °C for 1 hour and water quenched

4.3 TERNARY-ALLOY MECHANICAL BEHAVIOR

4.3.1 EFFECT OF TEMPERATURE AND COMPOSITION

The 0.2% CRSS for $\{111\}<10\bar{1}>$ octahedral slip was determined in compression for two Sn-containing and two V-containing ternary alloys. As with the binary alloys, the compression samples were tested with a compression axis oriented near the [001] crystallographic direction, using the incremental straining technique described in Chapter 3. The detailed specifications and test results from each specimen may be found in Appendix A. Figures 4.30 and 4.31 show the mean values of the CRSS measured as a function of temperature for the ternary alloys. As in the case of the binary alloys, a well-defined peak temperature for the flow stress was not observed since the samples were oriented very near the [001] axis; however, the values of CRSS for the low- and high-concentration V-containing alloys did converge at high temperature, suggesting that the
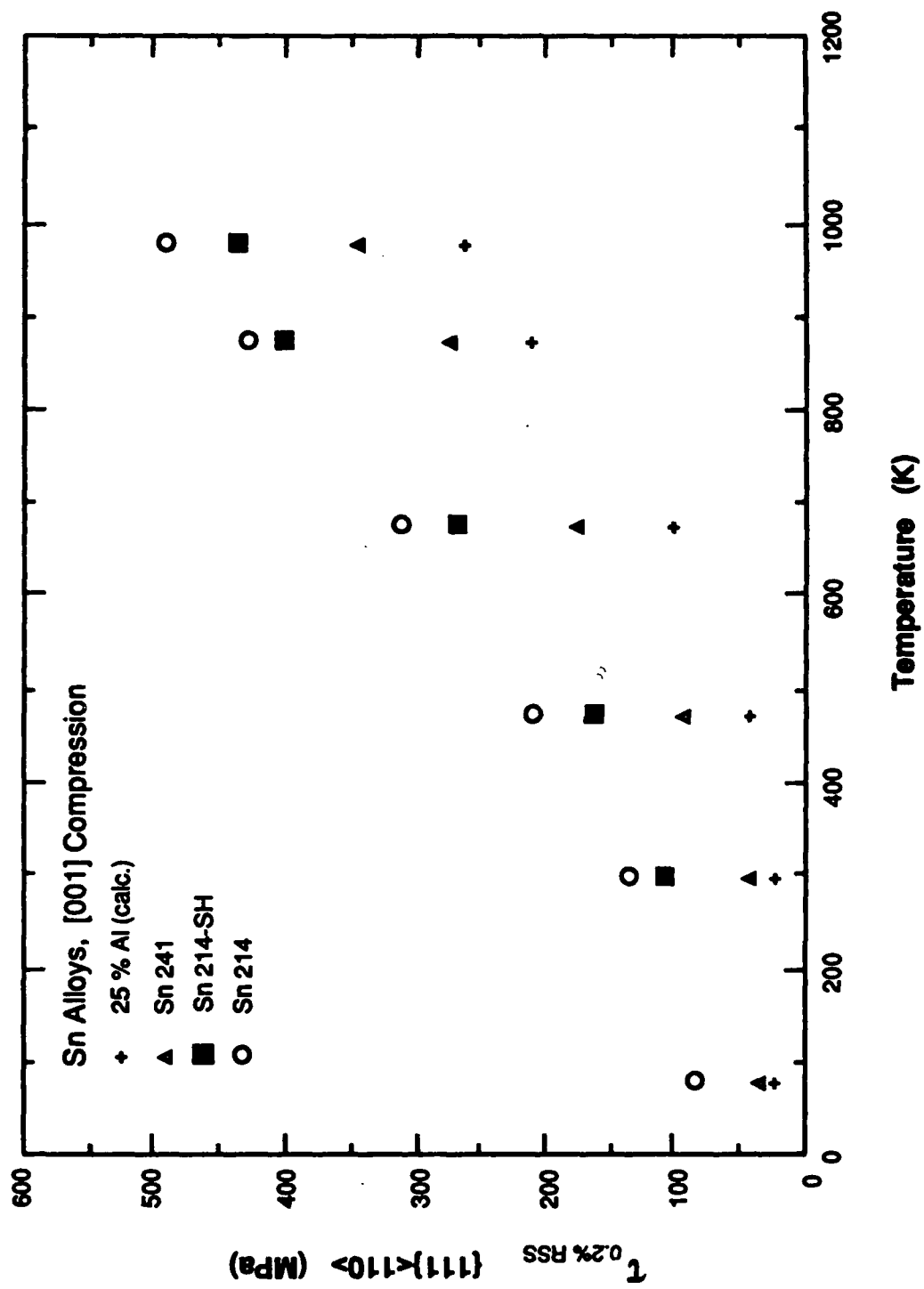
Fig. 4.30 Resolved shear stress versus temperature for alloys containing Sn. Estimated properties for stoichiometric binary Ni₃Al shown for comparison.
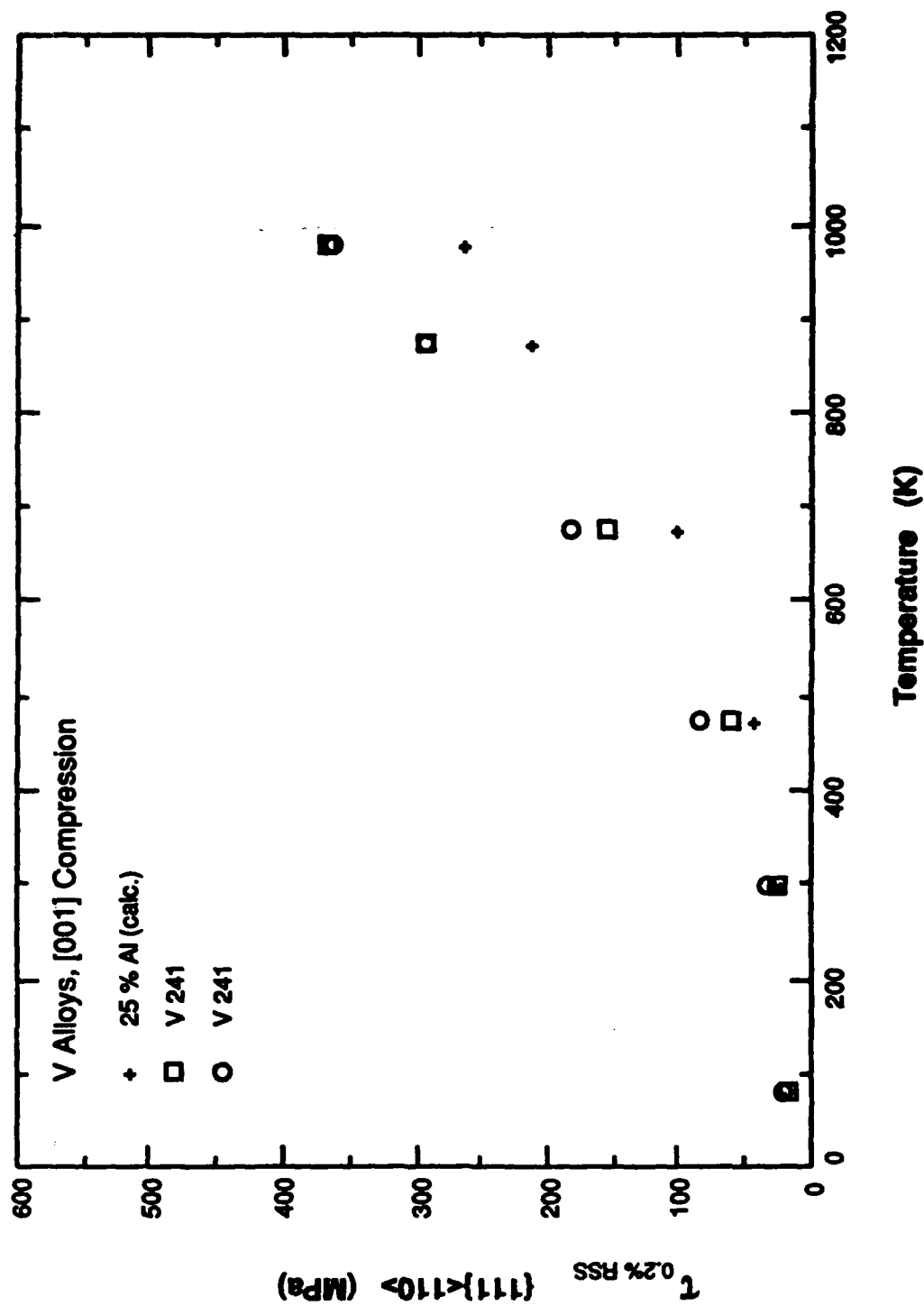
Fig. 4.31 Resolved shear stress versus temperature for alloys containing V. Estimated properties for stoichiometric binary Ni₃Al shown for comparison.

108

effect of V on the flow stress begins to saturate at concentrations well below the solubility limit (greater than 11 a/o V). The computed data set for the stoichiometric compound, τ_s, is shown on each plot (marked "25 % Al Calc.") for comparison purposes.

As in the Ni-rich binary alloys, the low-concentration Sn- and V-containing alloys exhibit a nearly "athermal" flow-stress regime, as does the high-concentration V-containing alloy V 214. However, both the high-concentration Sn-containing alloys (Sn 214 and Sn 214-SH) exhibit significantly higher flow stress than the stoichiometric material, down to the lowest temperatures studied. Unlike the case of excess Ni in the compound, additions of Sn or V did not weaken the material relative to the stoichiometric composition at elevated temperatures. Examination of the CRSS data as a function of the ternary solute concentration for the various temperatures tested shows a nearly linear relationship. These data are shown in Figs. 4.32 and 4.33.

4.3.2 TERNARY-ALLOY STRAIN HARDENING

The average Stage II strain-hardening rate ($d\sigma/d\epsilon$) plotted with the variation in temperature is shown in Fig.4.34 for the Sn-containing alloys and in Fig. 4.35 for the V-containing crystals. Again, the Stage II work-hardening rate increases with increasing temperature from -196 °C upward, just as in the case of the binary alloys. However, the Stage II strain-hardening rate saturates for the ternary alloys at a temperature which decreases as the solute concentration increases. As with the binary-alloy data, these values contain average error bars of at least ± 250 MPa (not shown for the sake of clarity).

4.3.3 COMPOSITIONAL-STRENGTHENING INCREMENT

The incremental strengthening ($\Delta\tau = \tau - \tau_s$) with temperature plotted for the ternary alloys is shown in Figs. 4.36 and 4.37. The Sn-rich alloys exhibit strengthening relative to the stoichiometric compound (positive deviations from zero) which increases

109
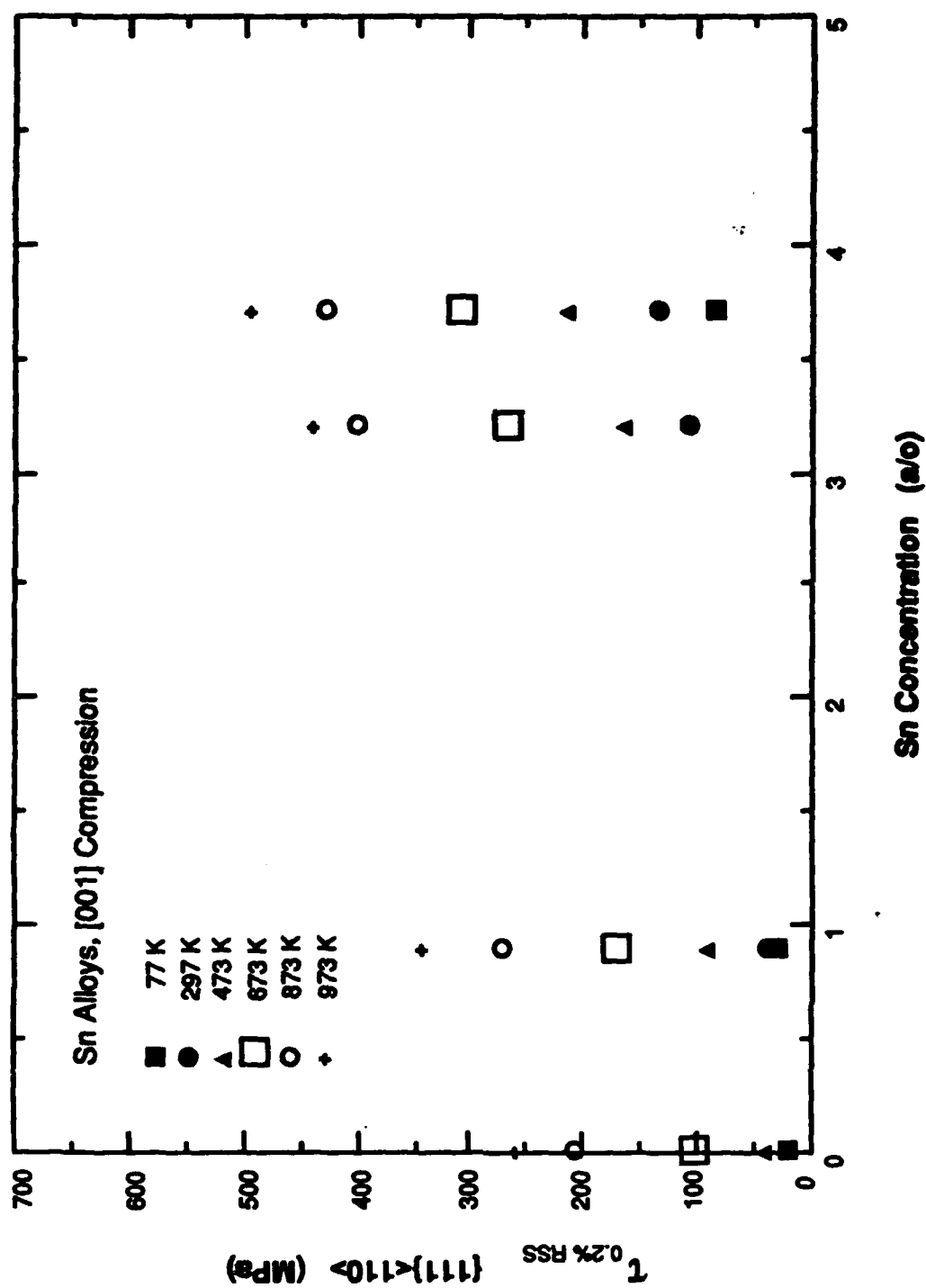
Fig. 4.32 Resolved shear stress versus Sn concentration at given temperatures.
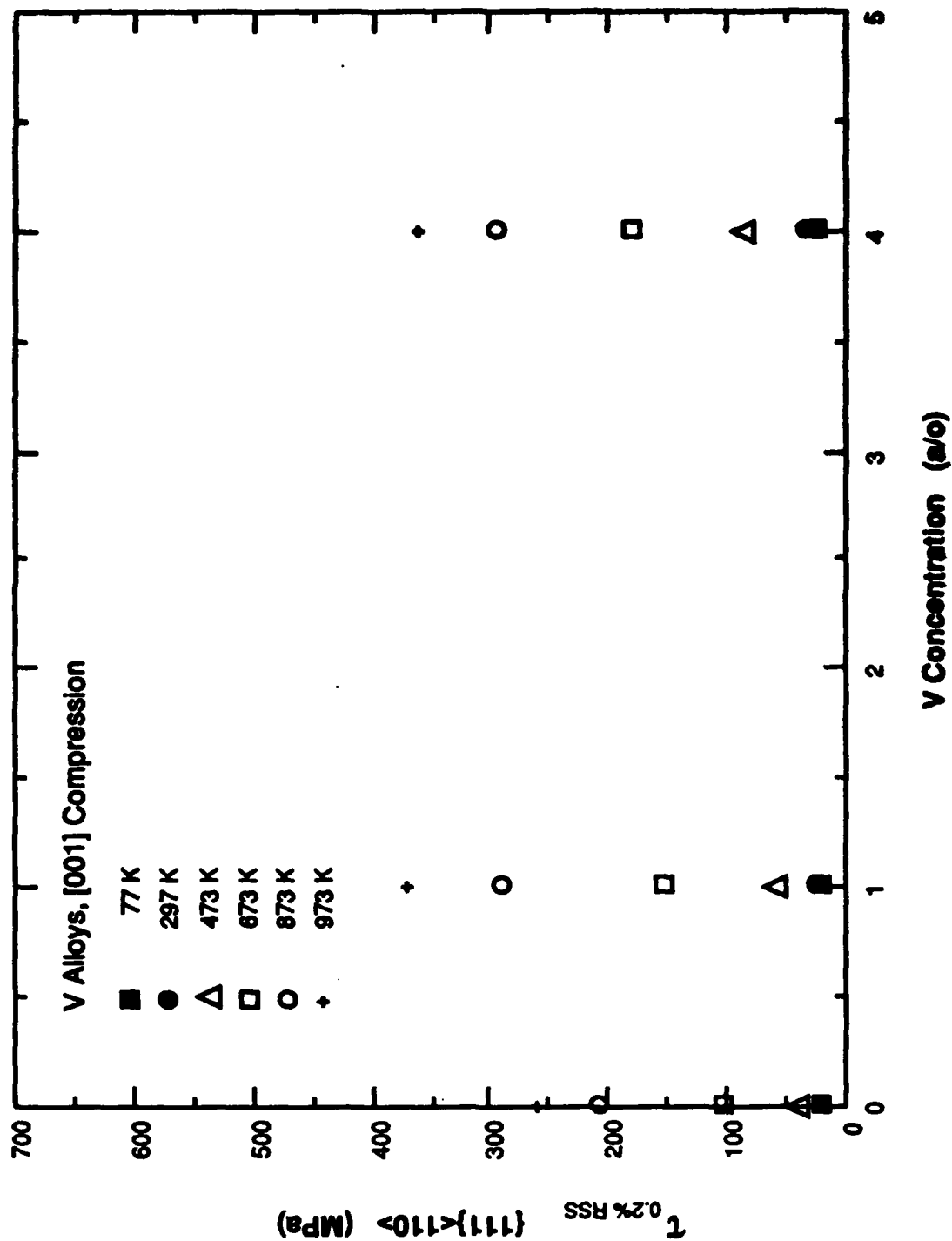
Fig. 4.33 Resolved shear stress versus V concentration at given temperatures.
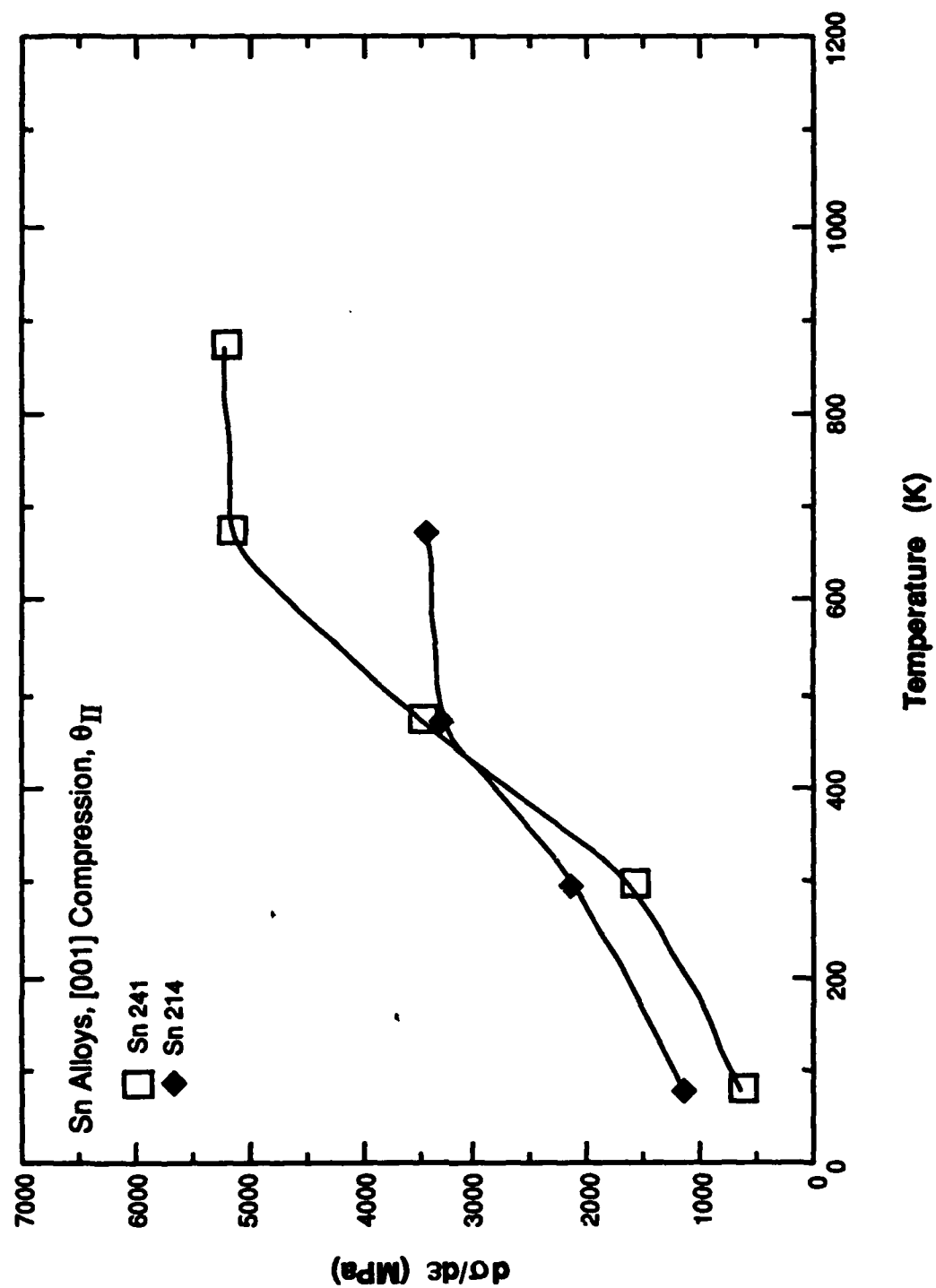
Fig. 4.34 Average Stage II work-hardening rate versus test temperature for two Sn alloys.
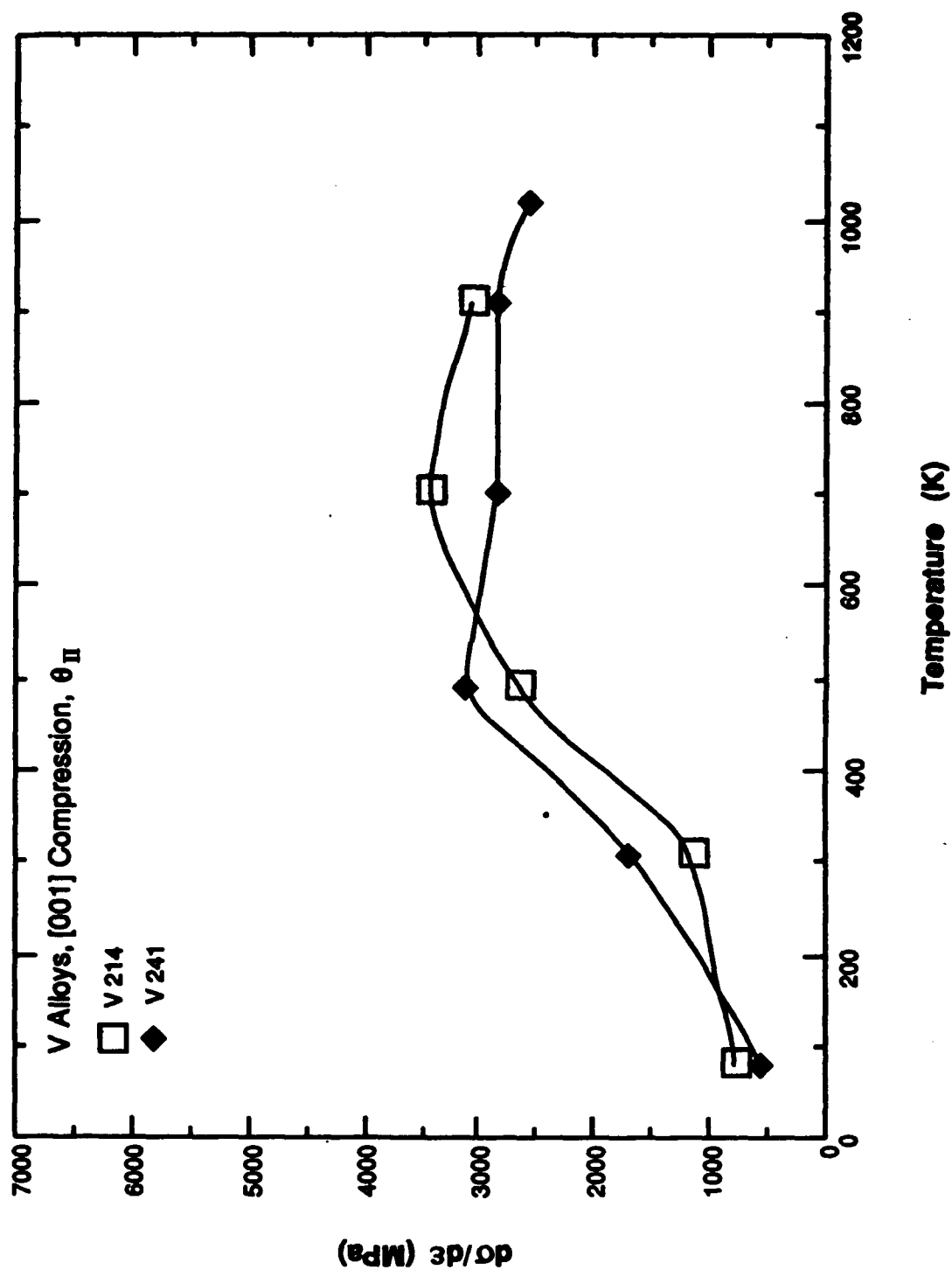
Fig. 4.35 Average stage II work-hardening rate versus test temperature for two V alloys.

113
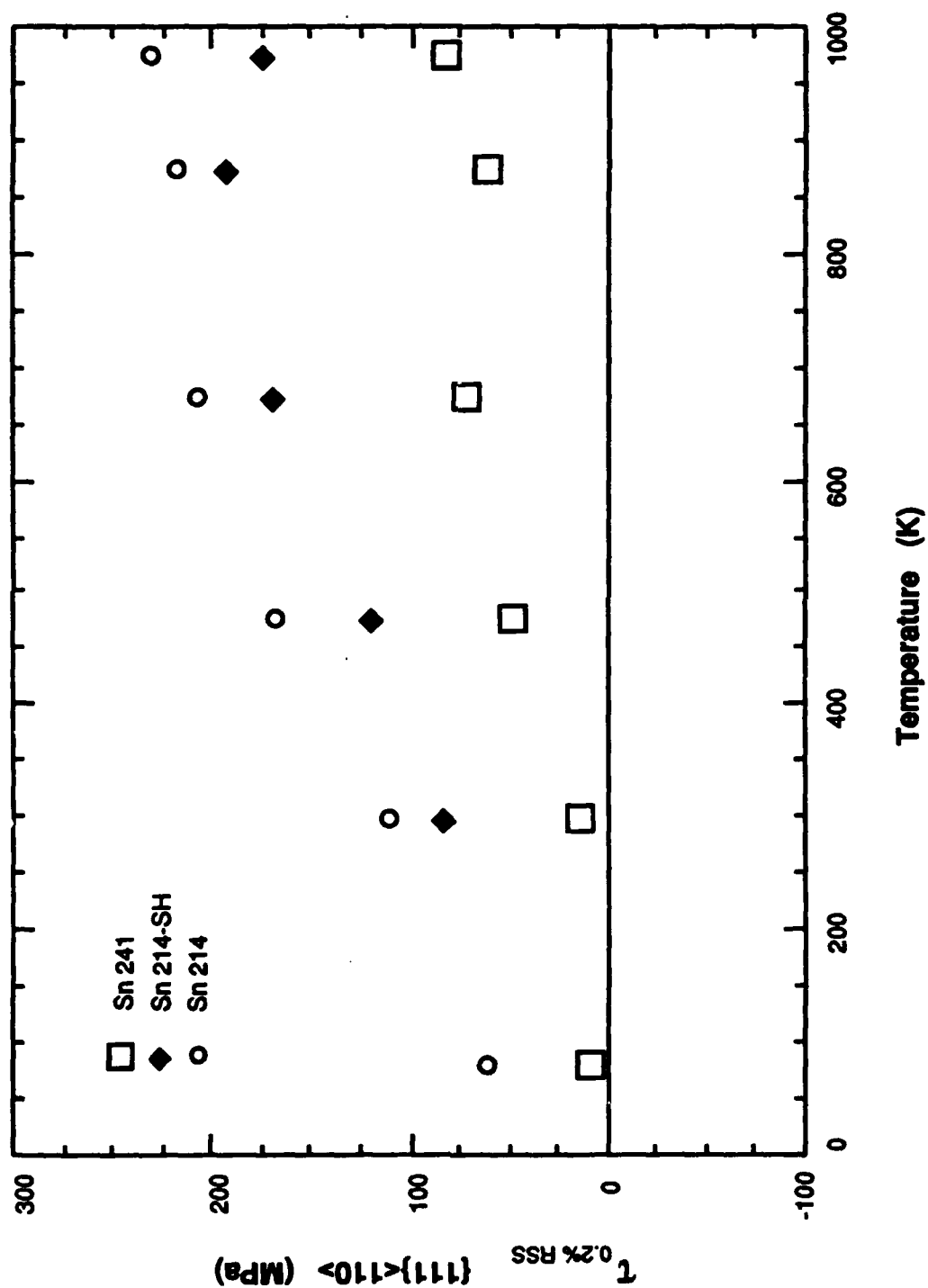
Fig. 4.36 Plot of $\Delta\tau = \tau - \tau_s$ for Sn alloys versus temperature (τ_s from Fig 4.2).

114
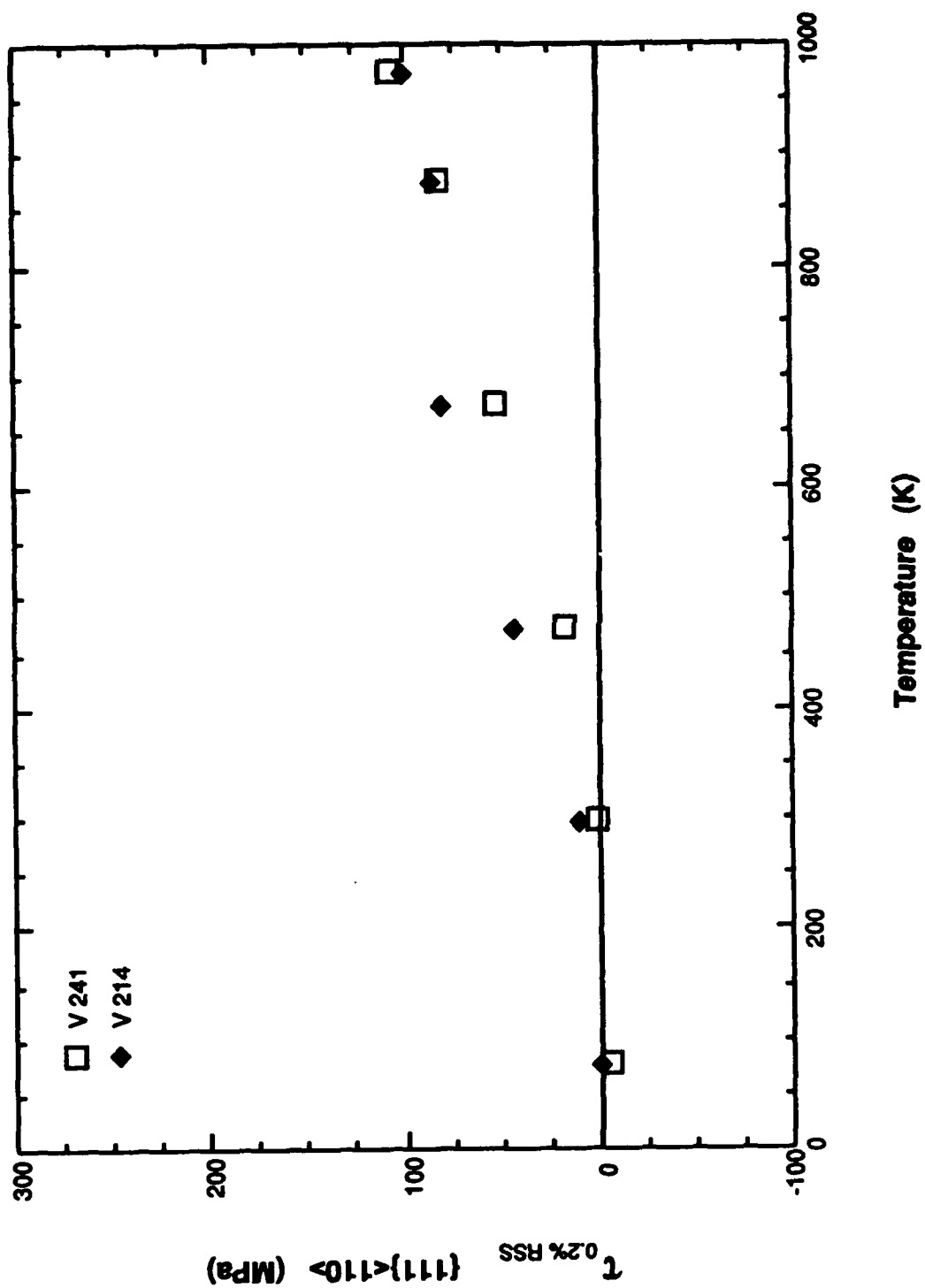
Fig. 4.37 Plot of $\Delta\tau = \tau - \tau_s$ for V alloys versus temperature (τ_s from Fig 4.2).

115

with temperature and begins to saturate above 400 °C. However, the V-rich alloys do not exhibit significant hardening until the temperature is raised above room temperature; then the effect of this solute saturates above 400 °C. Overall, V is a significantly less potent strengthener than Sn or excess Al.

The apparent activation enthalpy for the thermally activated process governing the flow stress anomaly has been computed for the ternary alloys. Logarithmic plots of the hardening increment due to thermal activation, $\tau^* = \tau - \tau_0$, as a function of $1/T$ are shown in Figs. 4.38 and 4.39. The measured activation constants determined from the slopes of the curves range from 0.12 to 0.07 eV for increasing Sn concentration and from 0.18 to 0.13 eV for increasing V concentration. *Note that the lowest activation constant for alloy Sn 214 (0.072 eV) is less than 3 kT at room temperature; above 560 °C, kT exceeds the activation constant, implying that no energy barrier exists and that the thermally activated event must be completely saturated.*

4.3.4 SLIP CHARACTER

The slip character of the ternary alloys was examined after room-temperature deformation. With the single exception of alloy Sn 214-SH, which contained Sn-rich dispersoids, the slip character was indistinguishable from that observed in the binary alloys. An example for the fully homogenized alloy Sn 214 is given in Fig. 4.40, showing that the alloys deform by fine planar slip on the primary {111} system. The alloy Sn 214-SH samples exhibited very fine intersecting slip bands which were not well resolved in the optical microscope. The slip character in this alloy was expected to be dominated by second-phase particles.
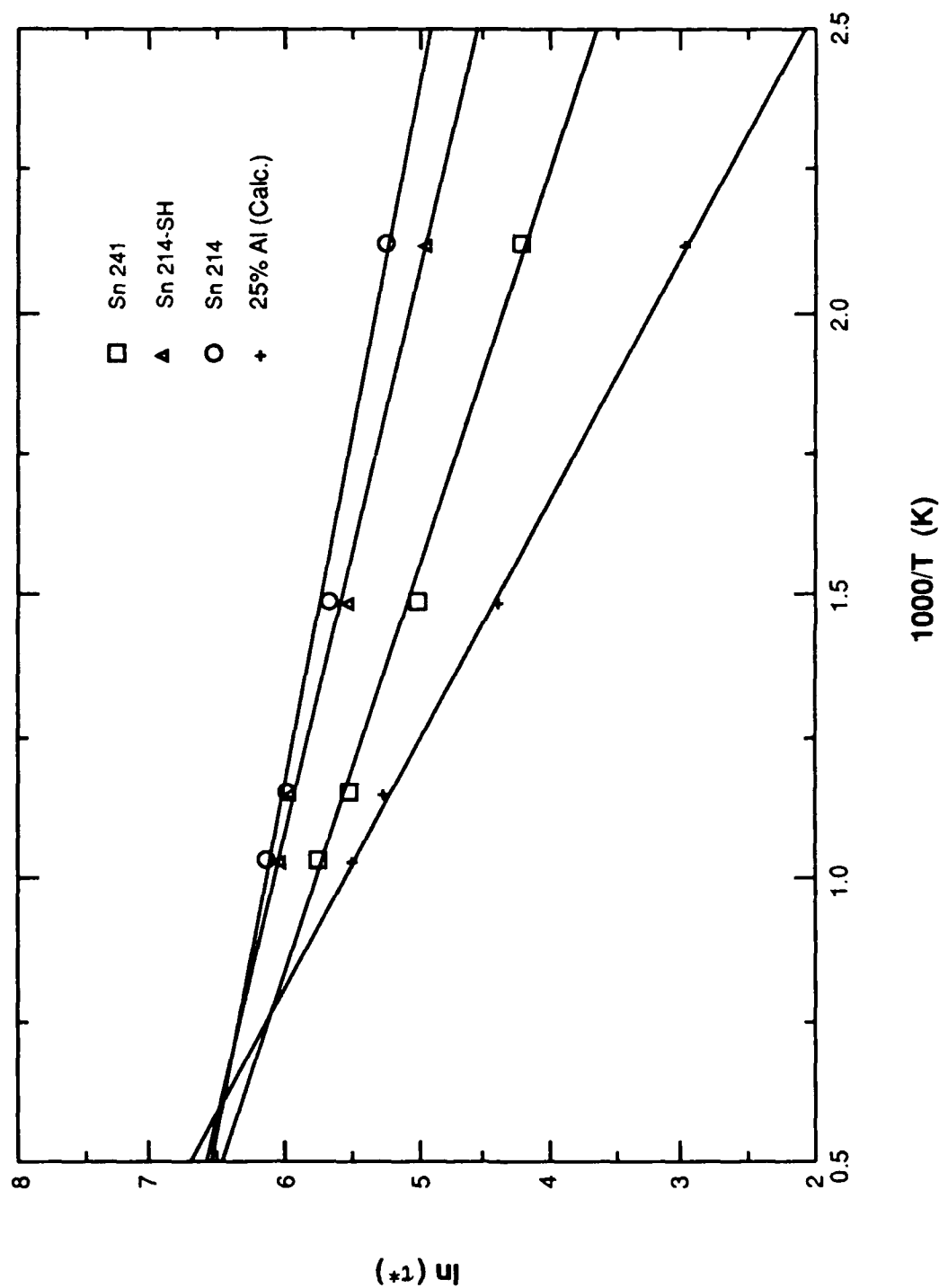
Fig. 4.38 Logarithmic plot of the thermally activated stress increment in Sn alloys, τ* (from Eqs. 4.1 and 4.2) versus the reciprocal of temperature.

117
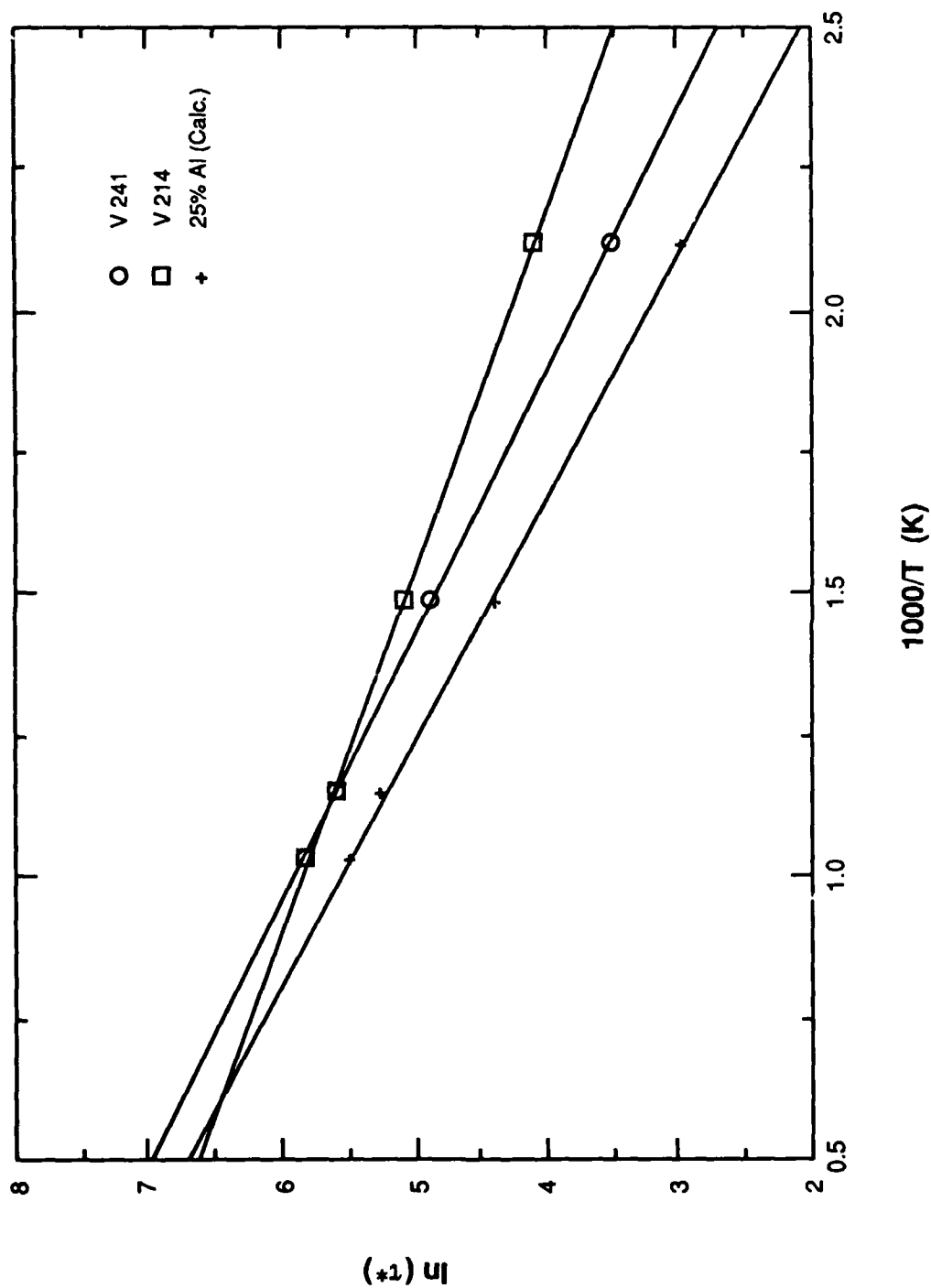
Fig. 4.39 Logarithmic plot of thermally activated stress increment in V alloys, τ^*
(from Eqs. 4.1 and 4.2) versus the reciprocal of temperature.

Fig. 4.40 Fine, planar {111} slip at 24 °C in cube-oriented sample of alloy Sn 214.

119

4.4 ELECTRON MICROSCOPY OF TERNARY ALLOYS

4.4.1 DISLOCATION STRUCTURES IN "ATHERMAL" ALLOYS

In subsection 4.3.1 three of the four ternary alloys studied were reported to exhibit athermal CRSS-versus-temperature behavior. The dislocation structures observed after room-temperature deformation in the two low-concentration alloys (Sn 241 and V 241) were similar to those observed in the Ni-rich binary alloys and could not be distinguished from the Ni-rich alloys by the morphology of the $a_0<10\bar{1}>$ dislocations alone. The general morphology of the $a_0<10\bar{1}>$ dislocations was characterized by tangles of wavy mixed-character dipole pairs. However, as evident from the low-magnification view in Fig. 4.41, the dislocation structure of alloy V 214 contained a slightly different feature. The wavy dipole pairs, which are characteristic of the "athermal" alloys are present, but overall the dislocations are straighter in this alloy. As shown in the series of $g\{111\}$ images in Fig. 4.42, many of these nearly straight dislocations have mixed rather than pure-screw character. For pure-screw dislocations these images would contain very few visible straight lines along directions perpendicular to g. The alignment of these dislocations suggests that either the lattice-friction stress for dislocations of mixed or edge character is quite low or that a "Peierls valley" has developed along $<10\bar{1}>$ directions. In either case, the mechanical-property data suggest little effect on the low-temperature CRSS.

The low-concentration Sn-containing alloy exhibited an additional prominent feature both in the as-deformed condition and in a crystal which was annealed at 700 °C and water quenched after room-temperature deformation. As shown in Fig. 4.43(a), many fault-coupled dislocation loops were observed and shown to be greatly extended along $<10\bar{1}>$ directions. The same area of the sample is shown in Fig. 4.43(b), with g chosen such that the loops are out of contrast. The Burgers vectors of dislocations bounding the loops were determined by standard methods. Figures 4.44 and 4.45 contain an example of the

120

Fig. 4.41 Bright-field image from alloy V 214 deformed at 24 °C; **B**[111]. Mixed-character dipoles are present. Many of the straight dislocations are <u>not</u> Kear-Wilsdorf screw dislocations, but 60° mixed dislocations split in (1 . 1).

121

Fig. 4.42 Bright-field image series using three independent {$\bar{1}11$} **g** vectors. Straight dislocations which are visible, and have line directions perpendicular to **g** are <u>not</u> screw dislocations.

Fig. 4.43 Bright-field image pair from alloy Sn 241 deformed at 24 °C, annealed at
700 °C, and water quenched; a) B[011], $\pm a_o/2[10\bar{1}]$ dislocations invisible, dark
bands are extended stacking fault dipole loops; and b) same area with B[111],
dipole loops are invisible.
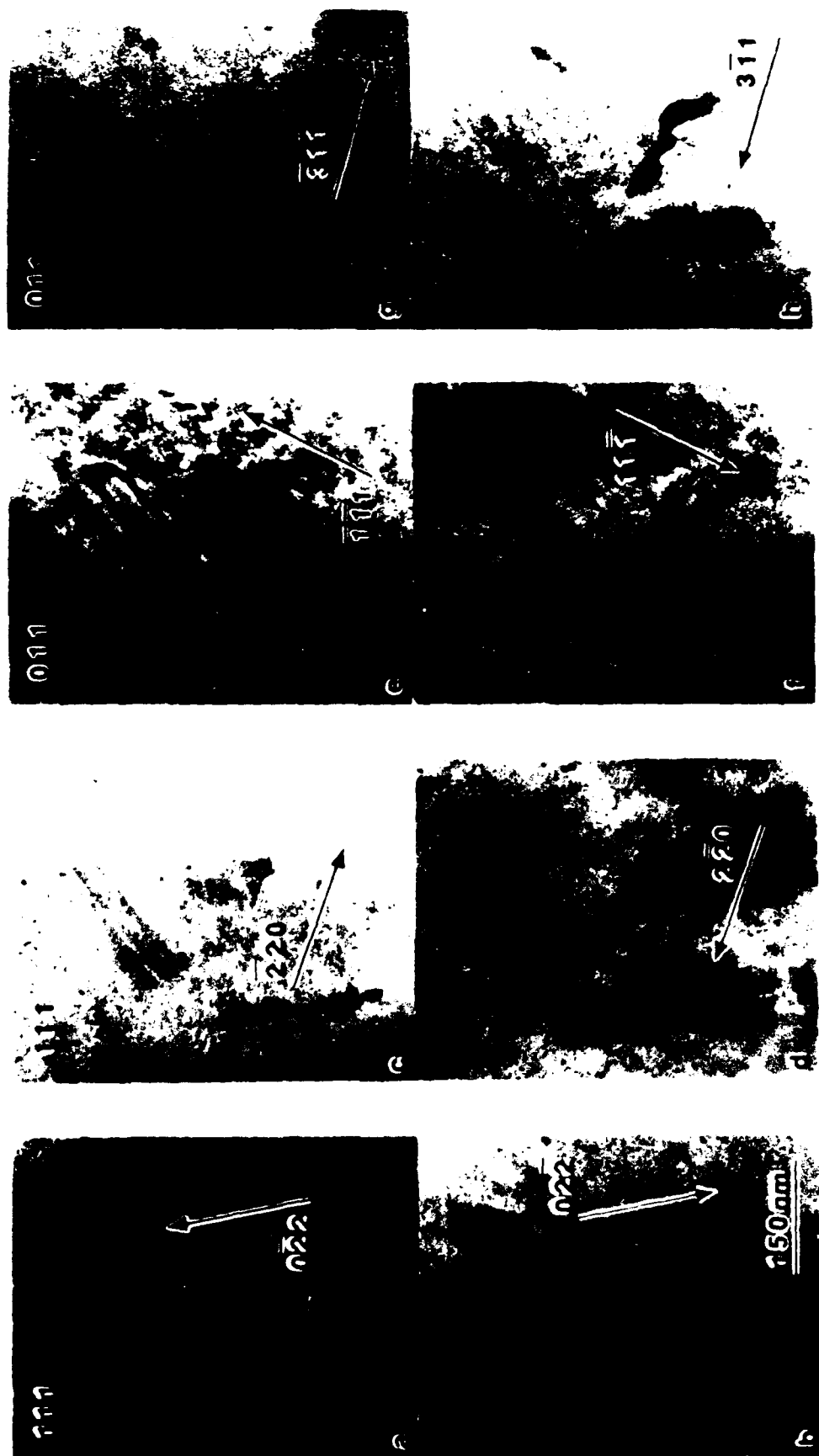
Fig. 4.44 Burgers vector analysis for $\mathbf{b} = a_0/3[11\bar{2}]$ loop in alloy Sn 241. Bright-field images with the following values for $\mathbf{g} \cdot \mathbf{b}$: a) +2, b) -2, c) 0, d) 0, e) -4/3, f) +4/3, g) 0, and h) 0.
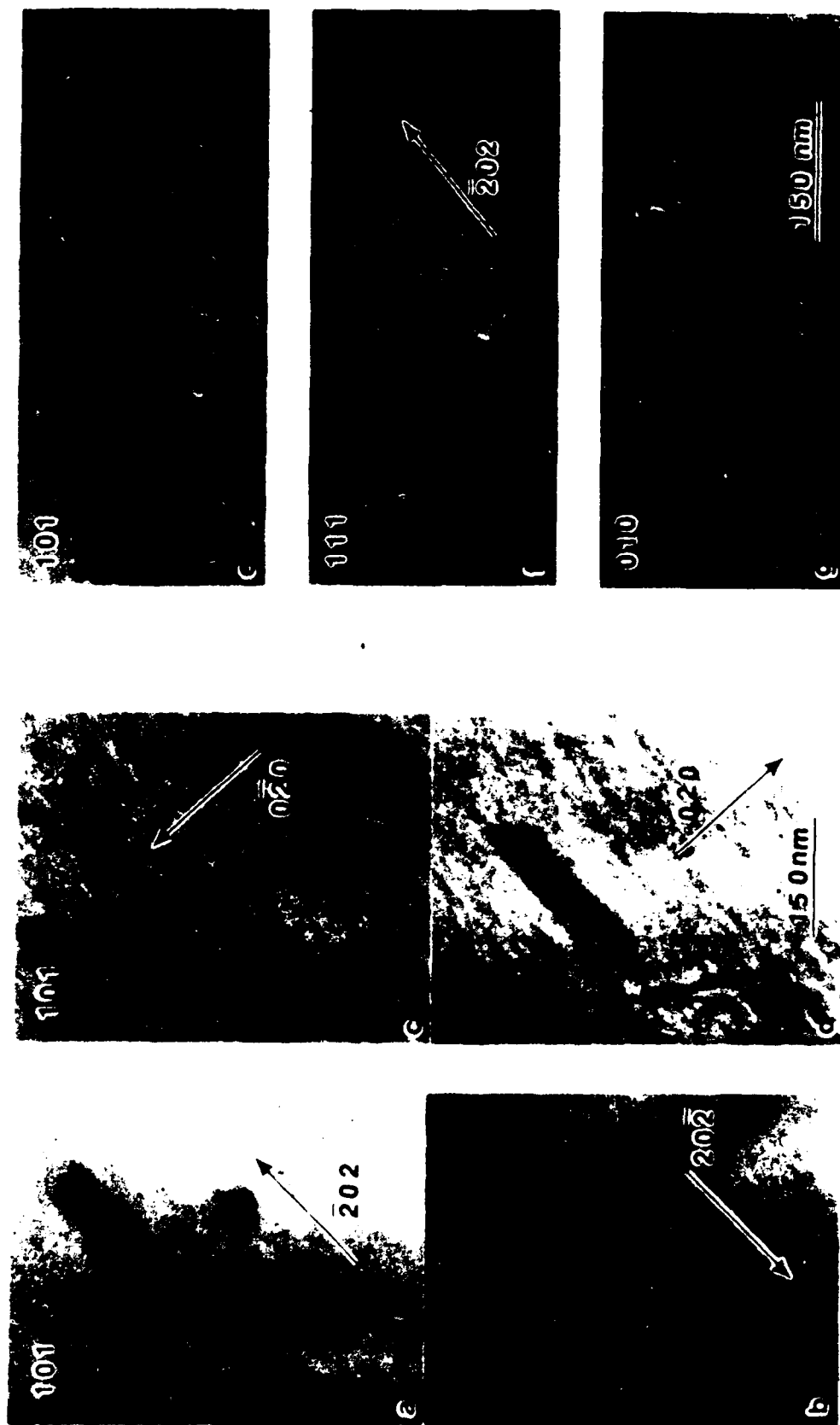
Fig. 4.45 Continuation of Burgers vector analysis for **b** = a$_o$/3[11$\bar{2}$] loop. Bright-field images with values of **g·b** given as: a) -2, b) +2, c) -2/3, and d) +2/3. Images e) through g) are weak-beam dark-field images verifying that the loop is in the plane of the foil.

analysis for a loop completely contained in the plane of the foil. The entire dislocation loop and fault are invisible for $\pm$ g($\bar{2}$20) as in Figs. 4.44(c) and 4.44(d) and for $\pm$ g(3$\bar{1}$1) as in Figs. 4.44(g) and 4.44(h), while only the bounding dislocation is invisible for g(0$\bar{2}$0) shown in Fig. 4.45(c); these observations are consistent with the contrast expected for a Burgers vector of $a_0/3[11\bar{2}]$ and a SISF dipole loop.[66] Frank loops (Burgers vectors of $a_0/3<111>$) would be visible for g{311}.

Examination of these faulted loops under weak-beam dark-field conditions revealed additional detail associated with the dislocation which forms the loop, suggesting that each loop is actually a pair of concentric loops. Figure 4.46 is a high-magnification weak-beam image which shows fine splitting of the $a_0/3[11\bar{2}]$ dislocation, as indicated by the arrows. The splitting distance is less than 1.5 nm except at the ends of the loop. Given the alignment along $<10\bar{1}>$ directions, the most likely nature of the splitting of such loops would be dissociations such as those proposed by Giamei *et al.*,[62] wherein the following reactions take place:

$$a_0/3 <11\bar{2}> \rightarrow a_0/2 <10\bar{1}> + APB_{(010)} + a_0/6 <\bar{1}2\bar{1}> \qquad [4.4]$$

Such reactions are energetically unfavorable by the simple Frank criterion; however, the formation of the loops may be controlled by the dynamics of deformation, as proposed by Pak *et al.*[107] for Ni_3Ge, which allows such reactions to occur. A reaction such as that of Eq. [4.4] would provide a means for stabilizing the loops at their apparent widths of only 20 to 50 nm by having an out-of-plane APB.

Similar loops were observed, although rarely, in the low-concentration V-containing alloy V 241. A contrast analysis of the dislocation loop was carried out using this alloy under weak-beam imaging conditions in order to establish the nature of the fine-scale dissociation of the bounding partials. Portions of that analysis are shown in

126
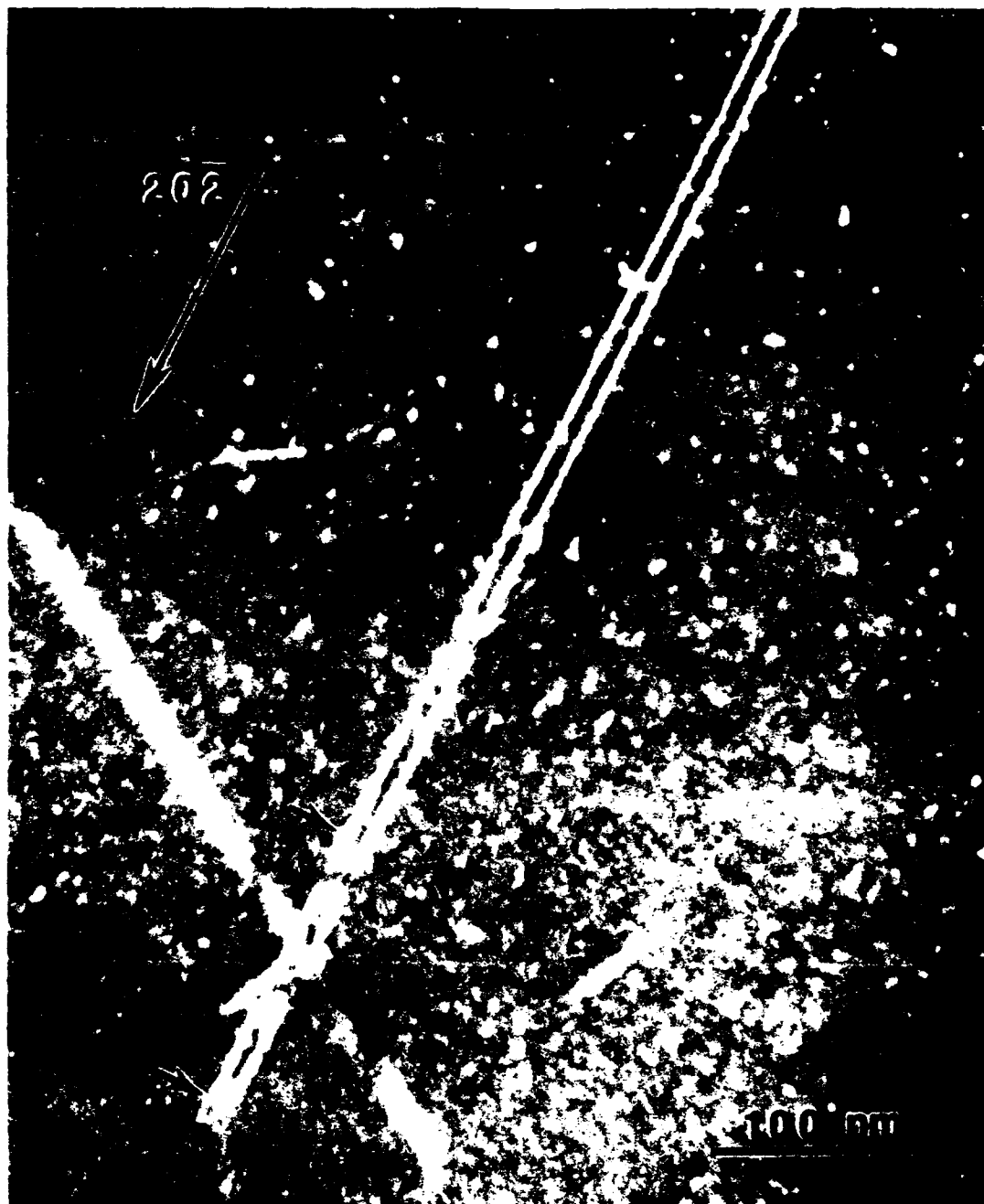
Fig. 4.46 Weak-beam image of stacking fault loop in alloy Sn 241; B[111]. Note fine
dissociated segments at arrows.

127

Figs. 4.47 and 4.48. In Figs. 4.47(a) and 4.47(b), the inner and outer loops alternately have strong and weak intensity with a change in the sign of the imaging vector from $+g$ to $-g$ (note the upper and lower ends of the irregularly shaped loop). Such contrast reversal is typical for $g \cdot u = 2$ images. The loop was invisible for $\pm g(\bar{2}0\bar{2})$ and $\pm g(31\bar{1})$. When g was chosen perpendicular to the long $<10\bar{1}>$ direction ($g \cdot b = 0$ for the $<10\bar{1}>$ components) using either $\pm g\{11\bar{1}\}$ or $\pm g\{200\}$ reflections, a strong fault contrast was evident in the weak-beam image which obscured the image of the bounding dislocations, as shown in Figs. 4.48(a) and 4.48(b). For this reason reactions such as those of Eq. [4.4] have not been specifically shown, and the true nature of the fault loops is not known unequivocally.

The weak-beam dark-field technique was used to determine the dissociation distances for the $a_0<10\bar{1}>$ dislocations, along with the detailed structure of the dislocations having the K-W configuration. Several examples of these results are contained in Figs. 4.49 through 4.55. The weak-beam dark-field series of Fig. 4.49 shows in alloy Sn 241 the very straight nature of the K-W segments (APB on the (010) plane), with an occasional macrokink segment dissociated on the (111) plane. The same structure existed after annealing this alloy at 700 °C and water quenching. The dislocation line shown in Fig. 4.50 from an annealed sample of alloy Sn 241 is clearly dissociated and bowed out in the (010) plane. The line and the curved segment are viewed edge-on in Fig. 4.50(a), while the mixed-character segment which is curved in the (010) plane is indicated by the arrow in Fig. 4.50(d). Dislocation configurations such as these, that is, configurations which indicate extensive glide in the (010) plane, were extremely rare. *Only two such large-scale bowed configurations were observed in the alloys and specimens examined.* Figure 4.51 shows the other dislocation line which was found to be bowed, or in a glide configuration, on the (001) plane in alloy V 214. Note the extremely narrow dissociated width of the superlattice partial dislocations (3.1 nm) in the (001) plane. These examples
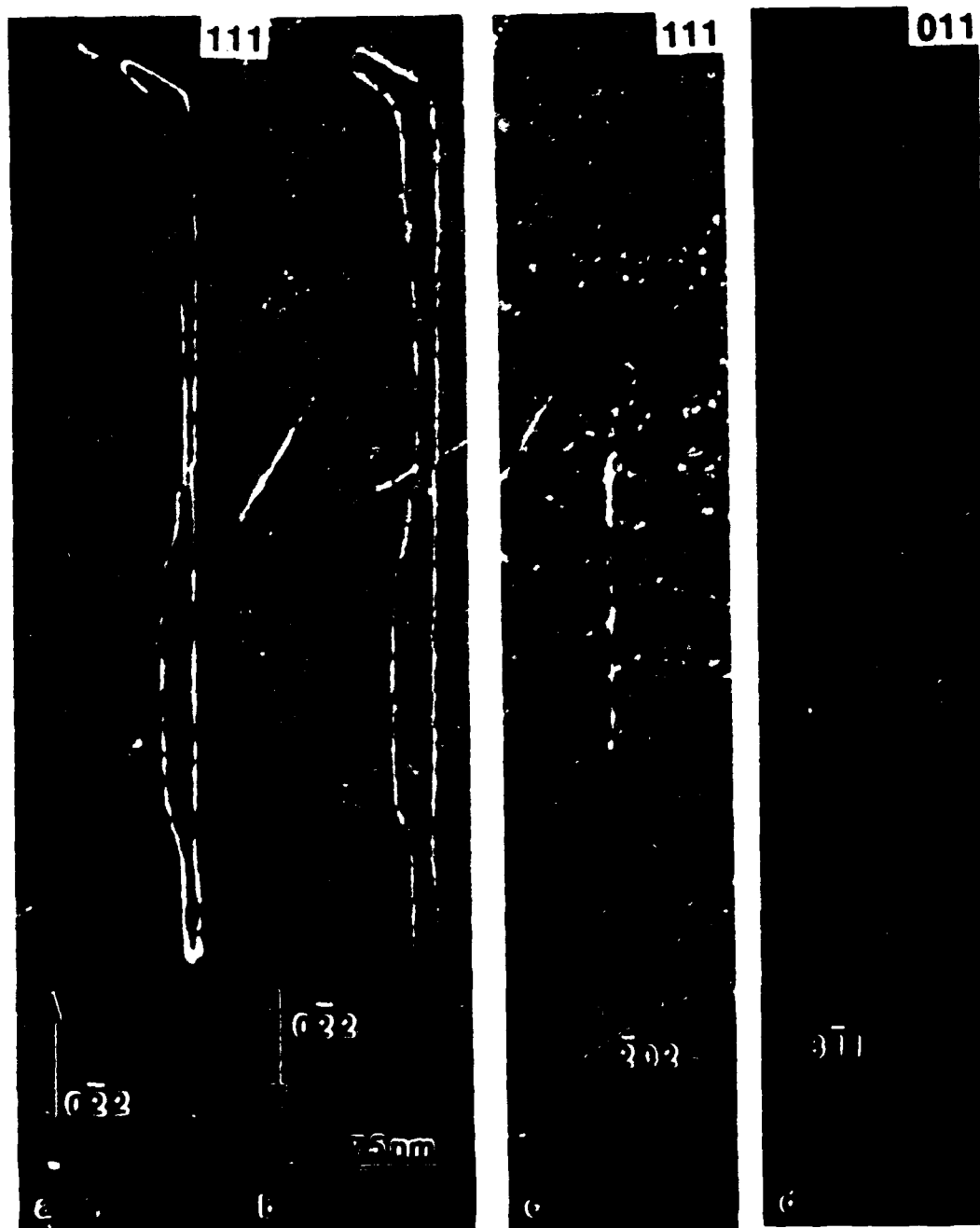
Fig. 4.47 Burgers vector analysis for $b = a_0/3[1\bar{2}1]$ loop in alloy V 241. Weak-beam images with values $g \cdot b$ given as: a) +2, b) -2, c) 0, and d) 2. Loop is invisible in image c).

129

Fig. 4.48 Continuation of Burgers vector analysis for $\mathbf{b} = a_0/3[1\bar{2}1]$ loop in alloy V 241.
Weak-beam images with values $\mathbf{g \cdot b}$ given as: a) +2/3, b) -2/3, c) 0, and d) 0.
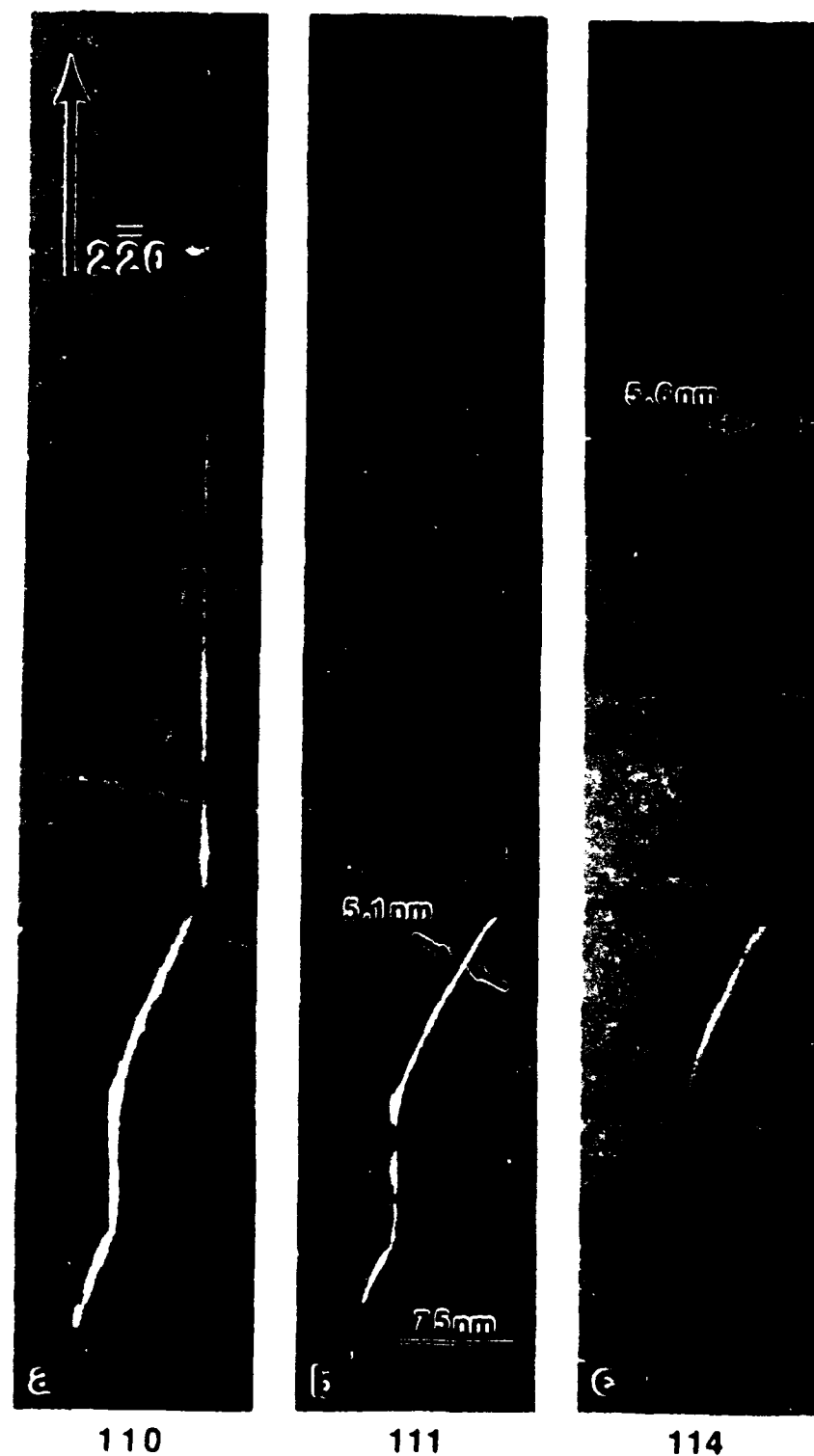
Fig. 4.49 Weak-beam images of Kear-Wilsdorf screw dislocation and mixed-character
macrokink segment with $\mathbf{b} = \pm[2\bar{2}0]$; alloy Sn 241 deformed at 24 °C;
g-4g($2\bar{2}0$); a) dissociated screw pair viewed edge-on, b) macrokink segment
split in (111), c) pair viewed with $\mathbf{B}[114]$. Note very slight bending in (001)
plane just above macrokink in c).

131
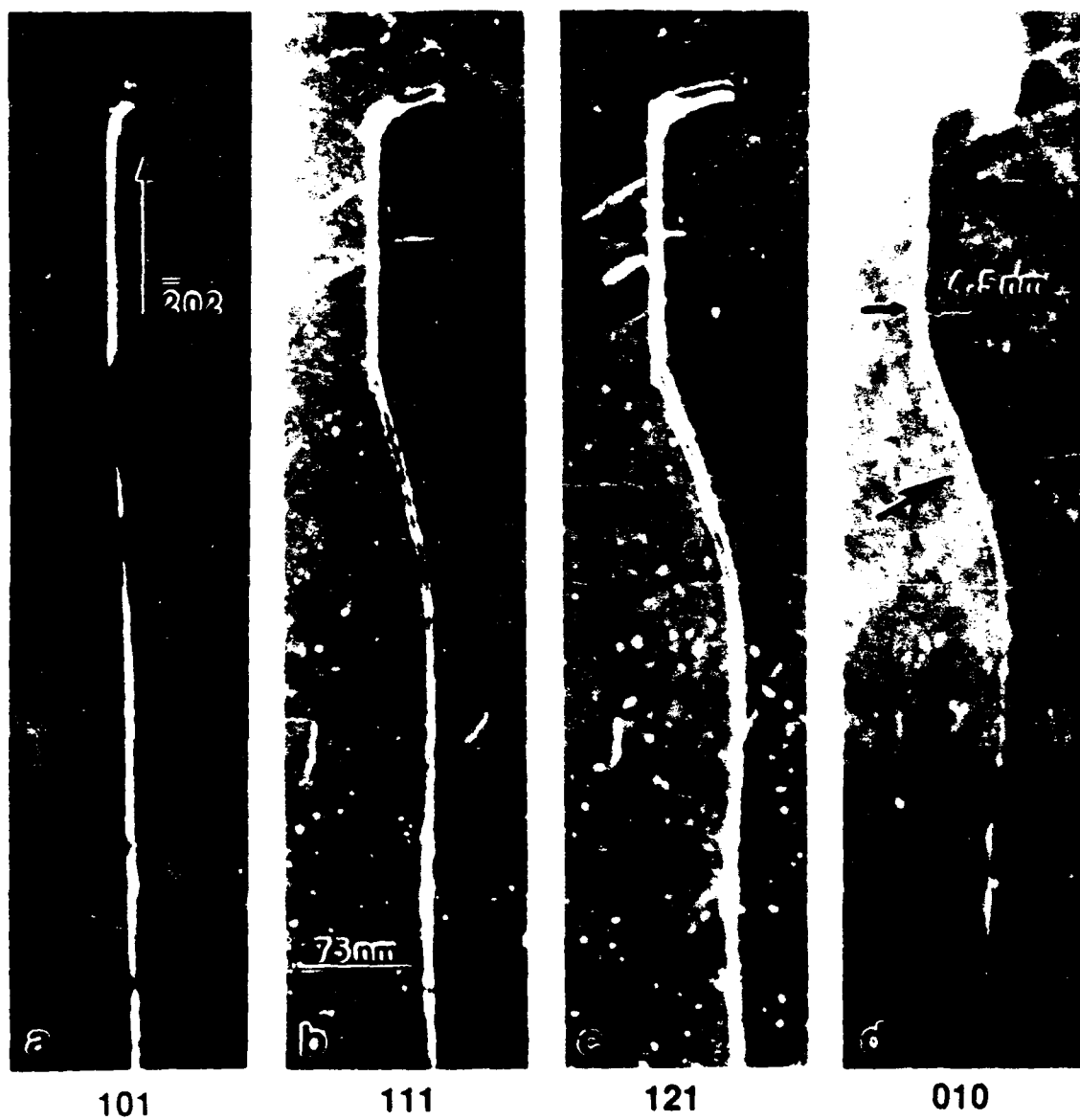
Fig. 4.50 Weak-beam images of screw dislocation and mixed-character segment bowed in (010) plane; alloy Sn 241 deformed at 24 °C, annealed at 700 °C, and water quenched; g-4g($\overline{2}$02); Note segment is bowed in (010) plane in d) and viewed edge-on in a).

132
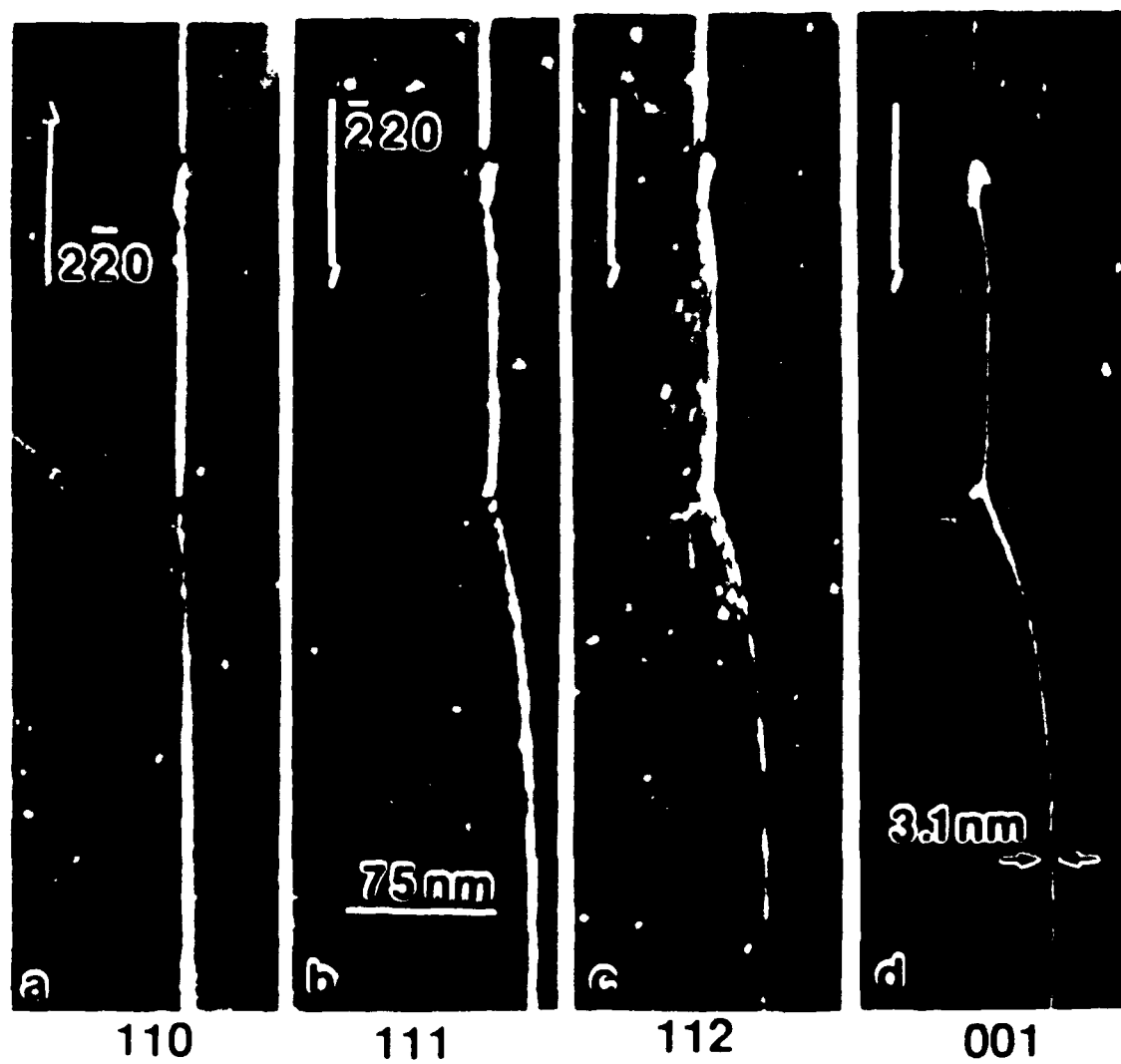
Fig. 4.51 Weak-beam images of dislocation and mixed-character segment bowed in (001) plane; alloy V 214, ±g-4g($2\bar{2}0$), deformed at 24 °C.

133

illustrate that the trace-analysis technique clearly reveals such dislocation activity. Figure 4.52 gives another example of the extremely straight K-W configurations in alloy V 214. Figures 4.53 and 4.54 are examples from alloy V 241 showing the extremely straight K-W configurations characteristic of the alloys exhibiting athermal CRSS-versus-temperature behavior at low temperatures. A long dislocation line, dissociated in the (111) plane, is shown in Fig. 4.55.

While the straightness and uniformity of the K-W configurations were characteristic of alloys deformed in the athermal regime (Region I of Fig. 1.2), the frequency of their occurrence was low. The wavy, tangled dipoles and isolated mixed-character dislocations (as shown for the binary alloys in Fig. 4.10) made up the greatest percentage of dislocations present after deformation in the athermal regime. As with the Ni-rich alloys, end segments with near-edge character in either (111) or cross-slipped into ($1\bar{1}1$) could be made to move in the foil by converging the illumination. Such observations indicate very low lattice-friction stress for the edge components.

4.4.2 DISLOCATIONS IN ALLOY Sn 214

As in the case of the Al-rich binary alloy, the alloy having the highest Sn content, Sn 214, exhibited an increased CRSS over the stoichiometric binary compound down to liquid-nitrogen temperature. Along with significant strengthening, the dislocation structure revealed significant differences from the "athermal" alloys. The bright-field TEM image of Fig. 4.56 shows a dominance of extended screw dislocations with macrokinks, aligned along <$10\bar{1}$> and indicated by C. As with the low-concentration Sn alloy, the field of view is spotted with fine elongated loop debris (at A in Fig. 4.56), which often extends from edge components of large loops and from the macrokink segments (indicated by B). With the two-beam imaging vector chosen perpendicular to the extended screw lines (new area
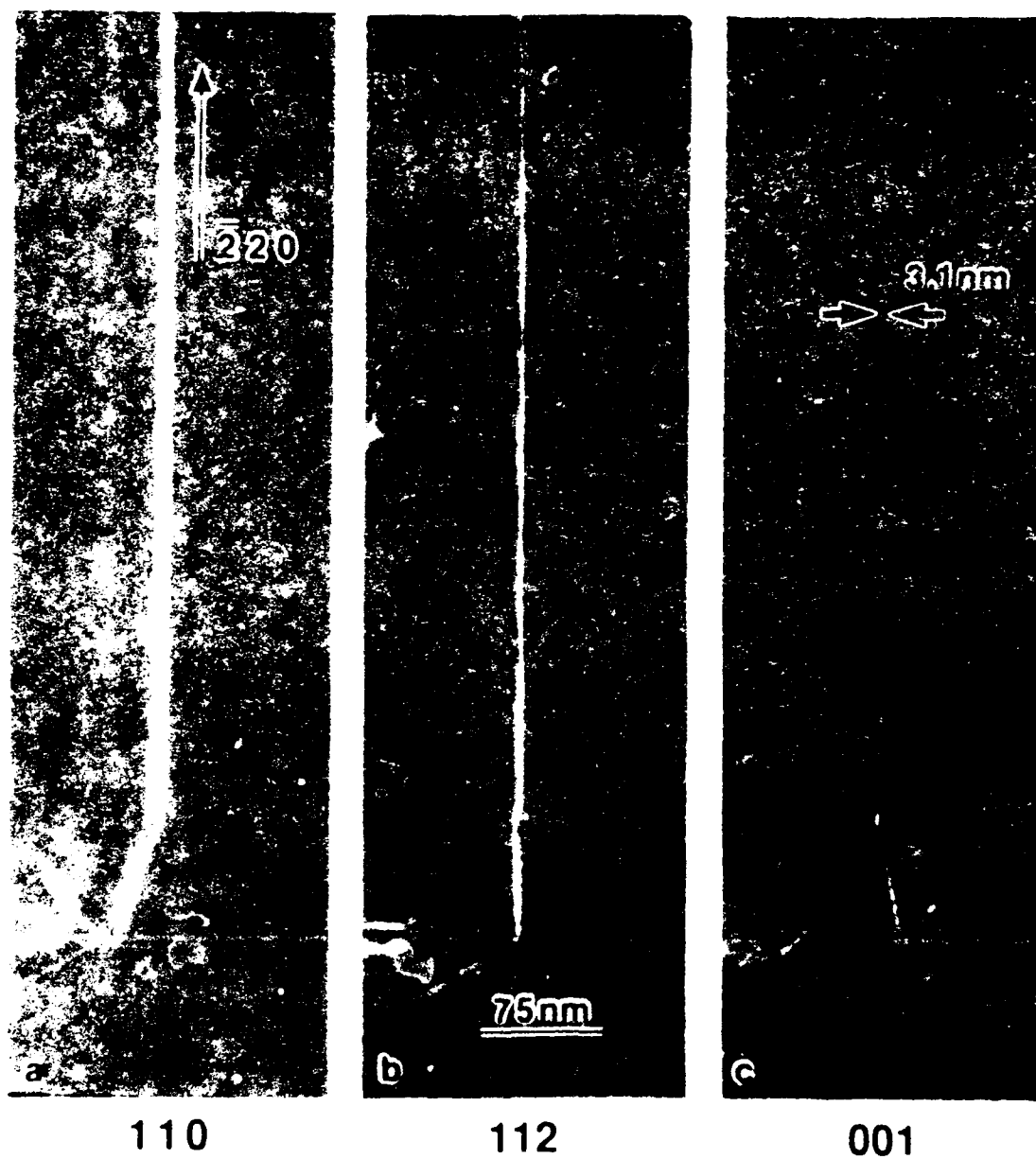
Fig. 4.52   Weak-beam dark-field images of screw dislocation in Kear-Wilsdorf
configuration; alloy V214, g-4g($\overline{2}$20), deformed at 24 °C.

135
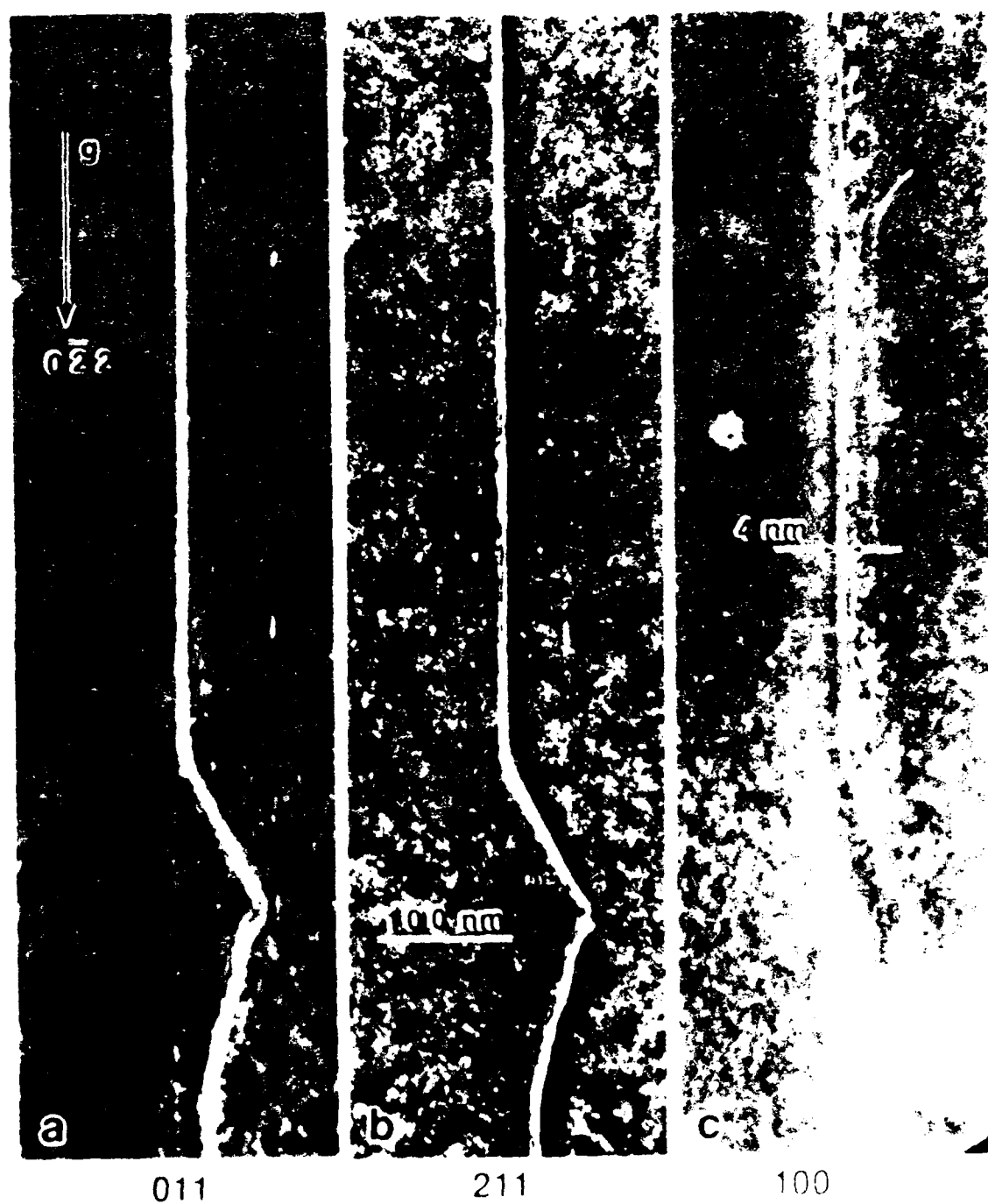
Fig. 4.53 Weak-beam images of screw dislocation with macrokink segments; alloy V
241, $\pm g$-4g(0$\bar{2}$2), deformed at 24 °C.
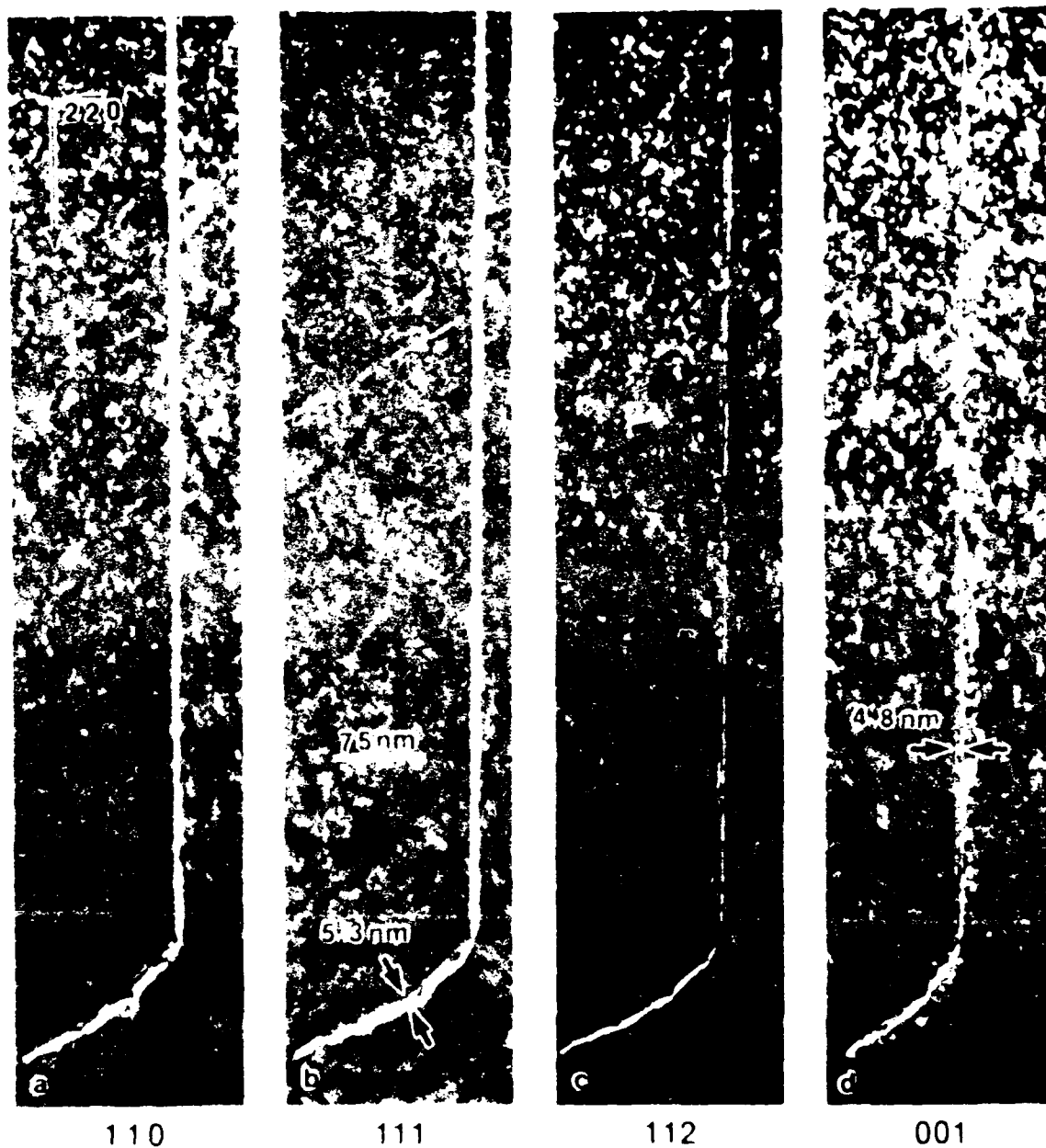
Fig. 4.54 Weak-beam dark-field images of long, straight screw dislocation in alloy V 241
after deformation at 24 °C; g-4g(2$\bar{2}$0). Straight segment is dissociated in (001)
while curved end segment is dissociated in ($\bar{1}$11).

137
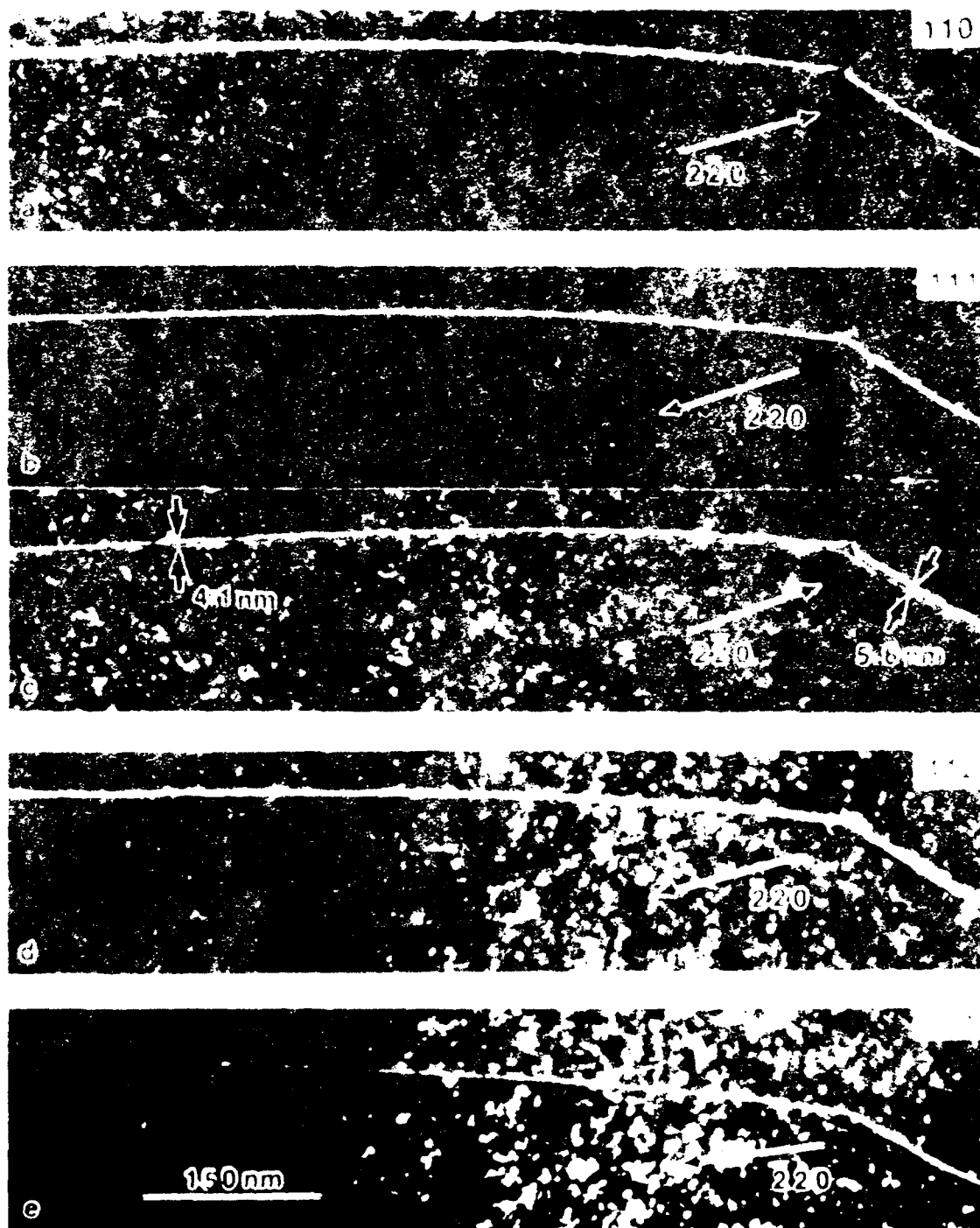
Fig. 4.55   Weak-beam images of long curved dislocation line dissociated in (111); alloy
V 241, ±g-4g($\bar{2}$20), after 24 °C deformation.

Fig. 4.56 Bright-field image of alloy Sn 214 deformed at 24 °C; B[121]. Isolated stacking fault dipole loops at A, dipole loops dragging from macrokinks at B, and kinked Kear-Wilsdorf dislocations at C. Note that Kear-Wilsdorf screw dislocations dominate the dislocation structure.

in Fig. 4.57), the loops exhibit similar contrast to that in alloy Sn 241, which is shown in Fig. 4.43(a). The Burgers vectors of the loops were analyzed and shown to be $a_0/3[11\bar{2}]$. Figures 4.58 and 4.59 show detailed bright-field and weak-beam dark-field images, respectively, of $a_0/3[11\bar{2}]$ loop formation from near-edge $a_0[10\bar{1}]$ dislocations (indicated by open arrows in Figs. 4.58(b), 4.58(d), and 4.59) and from an $a_0[10\bar{1}]$ K-W dipole loop (left-most solid arrows in Fig. 4.58, upper solid arrow in Fig. 4.59). The dragging out of a SISF dipole loop from a gliding superdislocation (such as the configuration described above) has been considered for Ni_3Ga, under the approximation of isotropic elasticity, by Suzuki et al.[108] Their analysis yields the following expression for the SISF energy as a function of the loop width and the CRSS:

$$\gamma_{SISF} = \frac{2\mu b'^2}{r} + \tau b' \qquad [4.5]$$

where b' is the magnitude of an $a_0/3[11\bar{2}]$ Burgers vector, and r is the distance between the long parallel sides of the loop. For alloy Sn 214, b' = 0.291 nm, μ = 70 GPa, and τ = 130 MPa at room temperature. The maximum observed loop width is 40 nm, which yields a SISF energy of 330 mJm^{-2}. Such a value is unrealistically high, suggesting that a more thorough analysis is required.

Examination of the fine structure of the screw-dislocation cores revealed many microkinks along the dislocation lines such as those in the Al-rich binary alloy. As shown in Figs. 4.60 through 4.62, long, straight segments now have aspect ratios of less than 15:1, as opposed to those of greater than 100:1 in the "athermal" alloys. The aspect ratio is limited by constrictions, microkinks, and macrokinks. As with the high-Al alloy, these features can best be observed by sighting along the dislocation line from an angle nearly parallel to the page. Some of the fine structure of SISF loops may be seen at the open arrows in
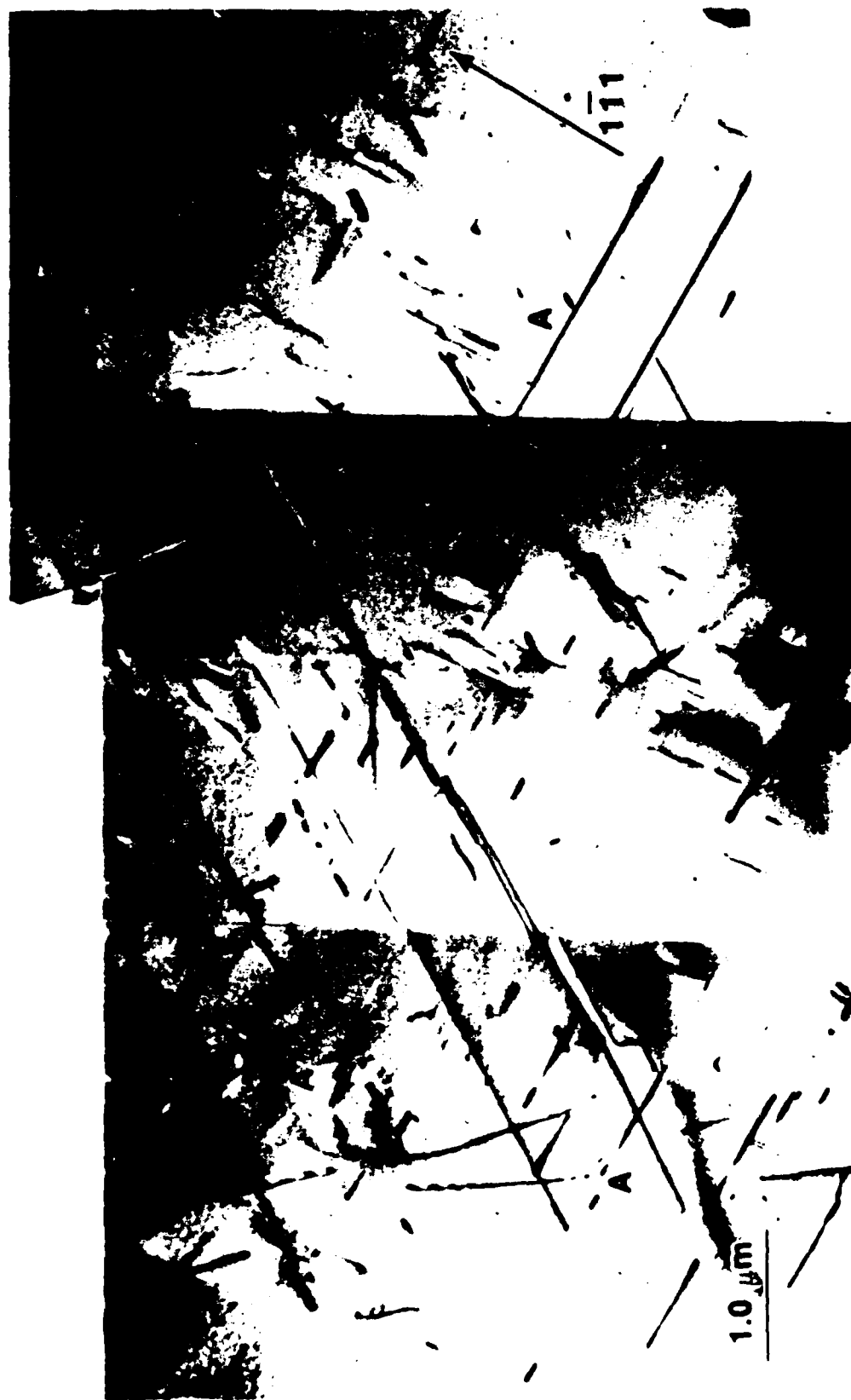
Fig. 4.57 Bright-field general-view image of alloy Sn 214 after room-temperature deformation; **B**[121], **g** chosen such that dislocations with **b** = $a_o/2[10\bar{1}]$ are invisible.

Fig. 4.58 Bright-field ±g image pairs of dislocations with **b** = a$_0$/3[11$\bar{2}$] forming from a$_0$/2[10$\bar{1}$] edge segments; alloy Sn 214, deformed at 24 °C. Note that dissociation event is just starting at open arrows, while stacking fault loop has a small extension at solid arrows.

142
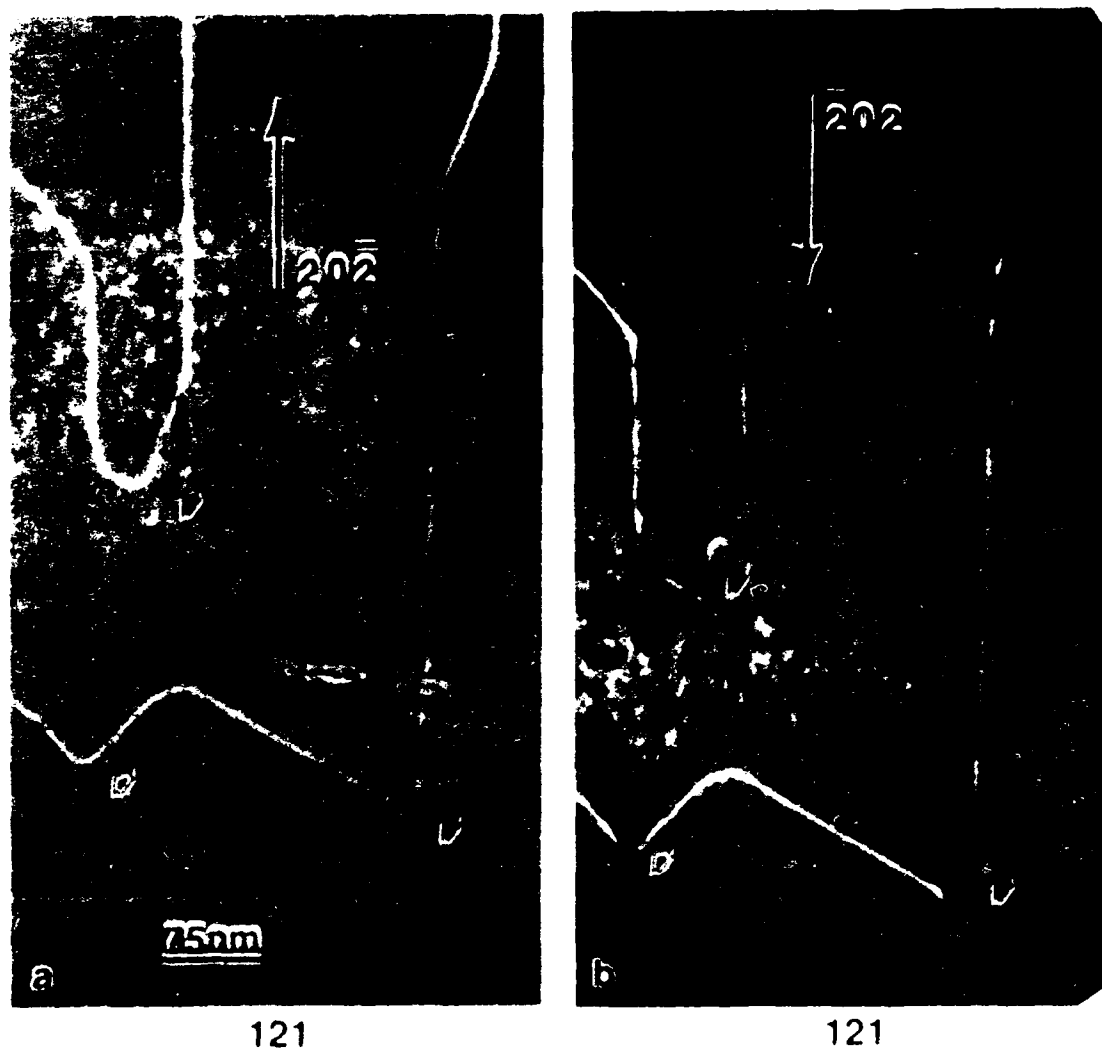
Fig. 4.59 Weak-beam images of area in Fig. 4.58. Dissociation is clearly resolved at solid arrows, but pinning event is not resolved (note open arrows).

Fig. 4.60 Weak-beam images of Kear-Wilsdorf screw dislocation in alloy Sn 214
deformed at 24 °C; **g**-4g(2̄2̄0̄ · a) dissociated pair viewed edge-on, b)
macrokink segments split in (111), c) pair viewed with **B**[112], and d) straight
segments dissociated in (001). Note periodic constrictions on dislocation line.

144

Fig. 4.61 Weak-beam images of Kear-Wilsdorf screw dislocation in alloy Sn 214 deformed at 24 °C; **g**-4**g**(022); a) dissociated pair viewed edge-on, with stacking fault loop extending from macrokink at open arrow, b) macrokink segments split in (111), c) pair viewed with **B**|211|, and d) straight segments dissociated in ((001). Note the fine structure of the dislocation loop at open arrow in d).

145

Fig. 4.62 Weak-beam images of screw dislocation in alloy Sn 214 after deformation at 24 °C; **g**-4**g**(0$\bar{2}$2). Microkinks may be observed by sighting along dislocation line, nearly parallel to the page.

146

Figs. 4.61(a) and 4.61(d). The overall line appearance is straighter than in alloy Al 270; however, the frequency of microkinking is approximately equivalent.

4.4.3 DETERMINATION OF TERNARY-ALLOY APB ENERGIES

The superpartial dislocation dissociation distances have been measured and tabulated for the ternary alloys in Appendix D. The dissociation distance on the {111} plane has been plotted as a function of dislocation character in Figs. 4.63 through 4.66. Values shown are for samples deformed at room temperature. The average spacing of pure-screw dislocations dissociated in the cube cross-slip plane is indicated on the y-axis for each alloy.

The data from the tables of Appendix D have been used to compute the average APB energy for the {111}and {010} planes as a function of composition. Equation [4.3] was used to convert the dissociation-distance data to APB energy. Again, the elastic-energy coefficient computed for Ni_3Al at room temperature by Yoo[59] has been used in this analysis, without any correction being made for the variation in the elastic constants (C_{ij}'s) with composition. As with the binary alloys, the Burgers vectors have been corrected for compositional variation using the data of Ochiai *et al.*[106] Table 4.2 contains the measured average APB energies for the {111}- and the {010}-planes (γ_{111} and γ_{010}, respectively) and the APB-energy ratio, $\gamma_{111} / \gamma_{010}$, for each ternary alloy.

147
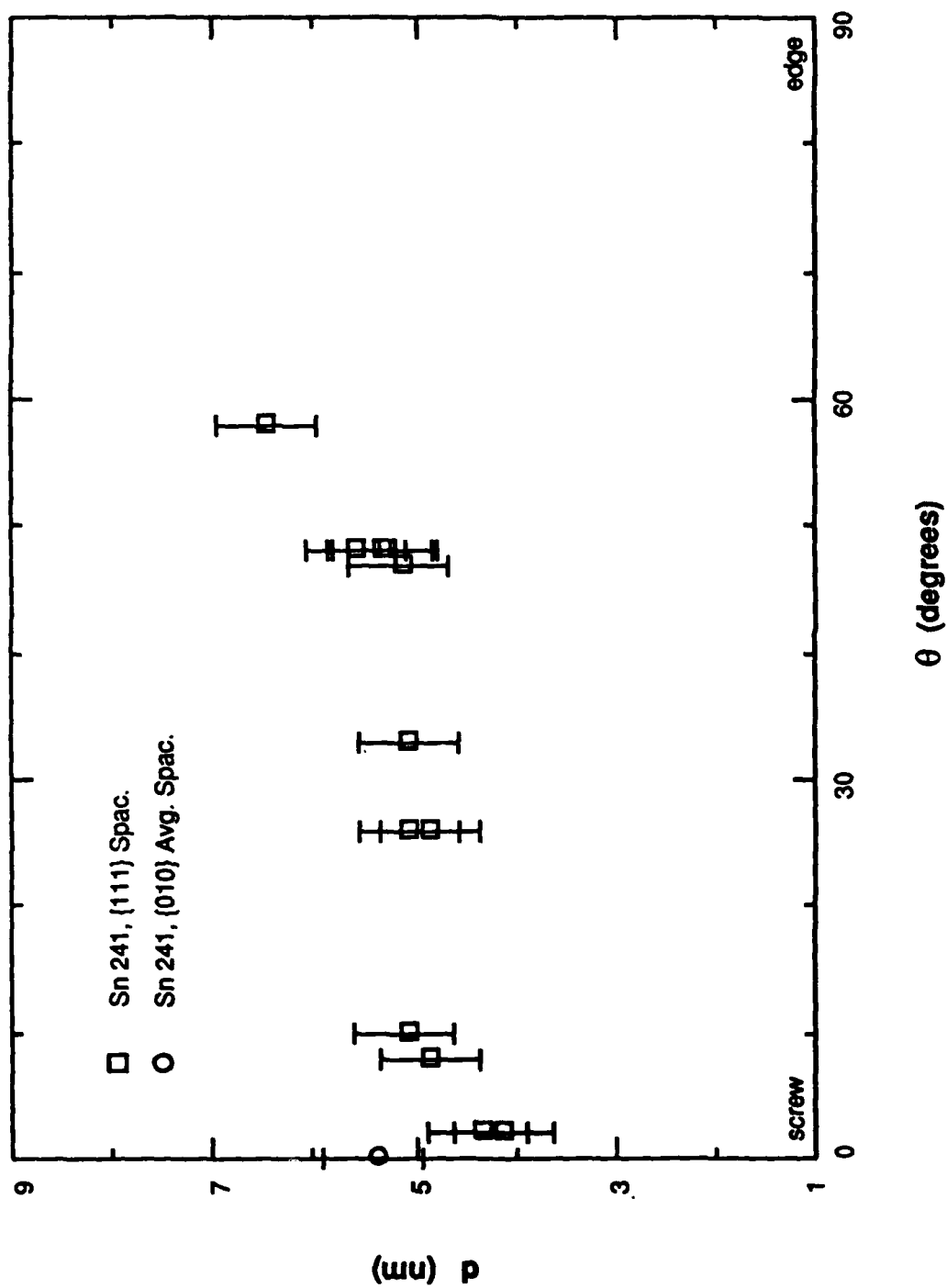
Fig. 4.63 Dissociation distance versus dislocation character, Sn 241, deformed at 24°C.

148
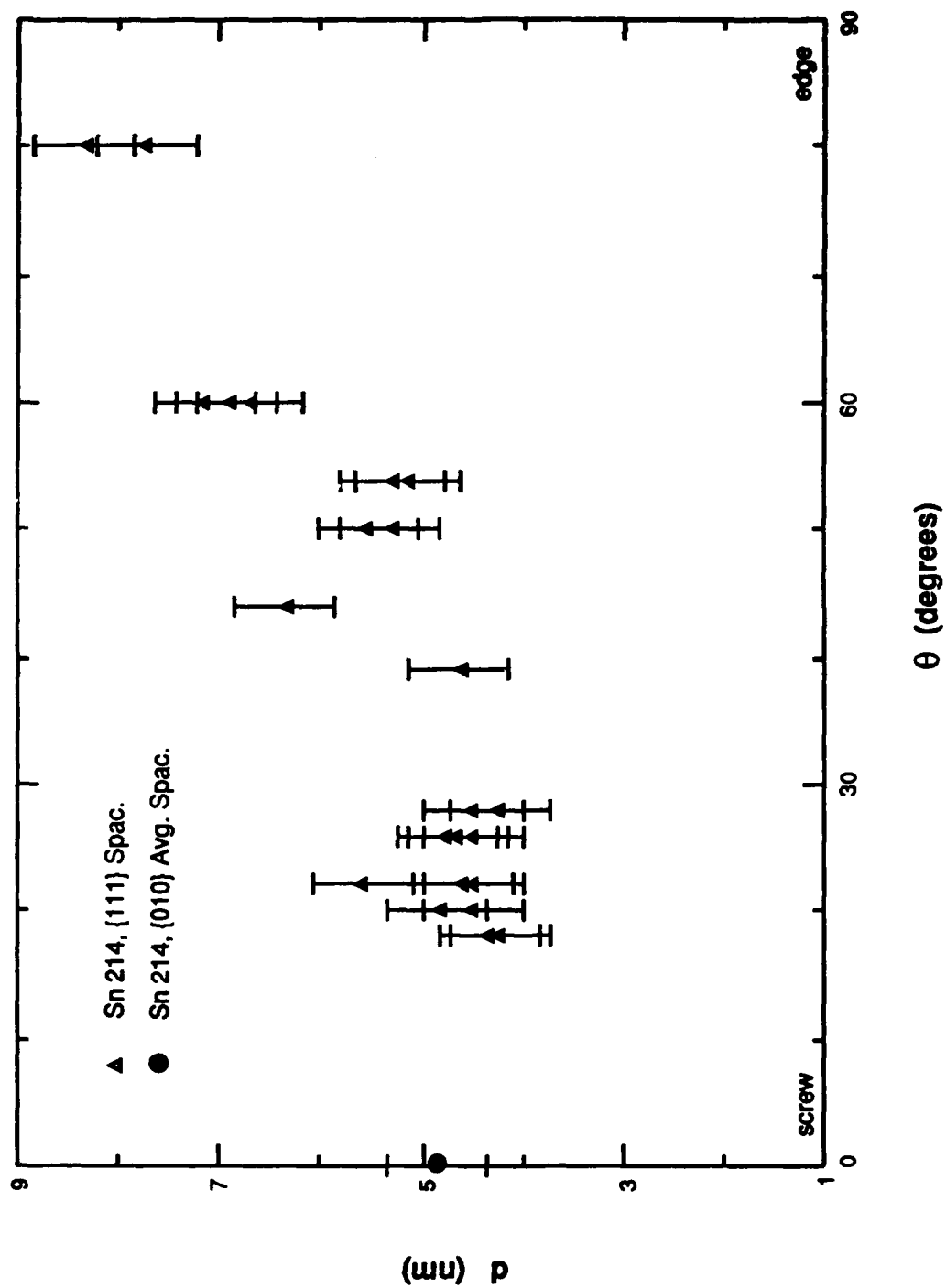
Fig. 4.64 Dissociation distance versus dislocation character, Sn 214, deformed at 24 °C.

149
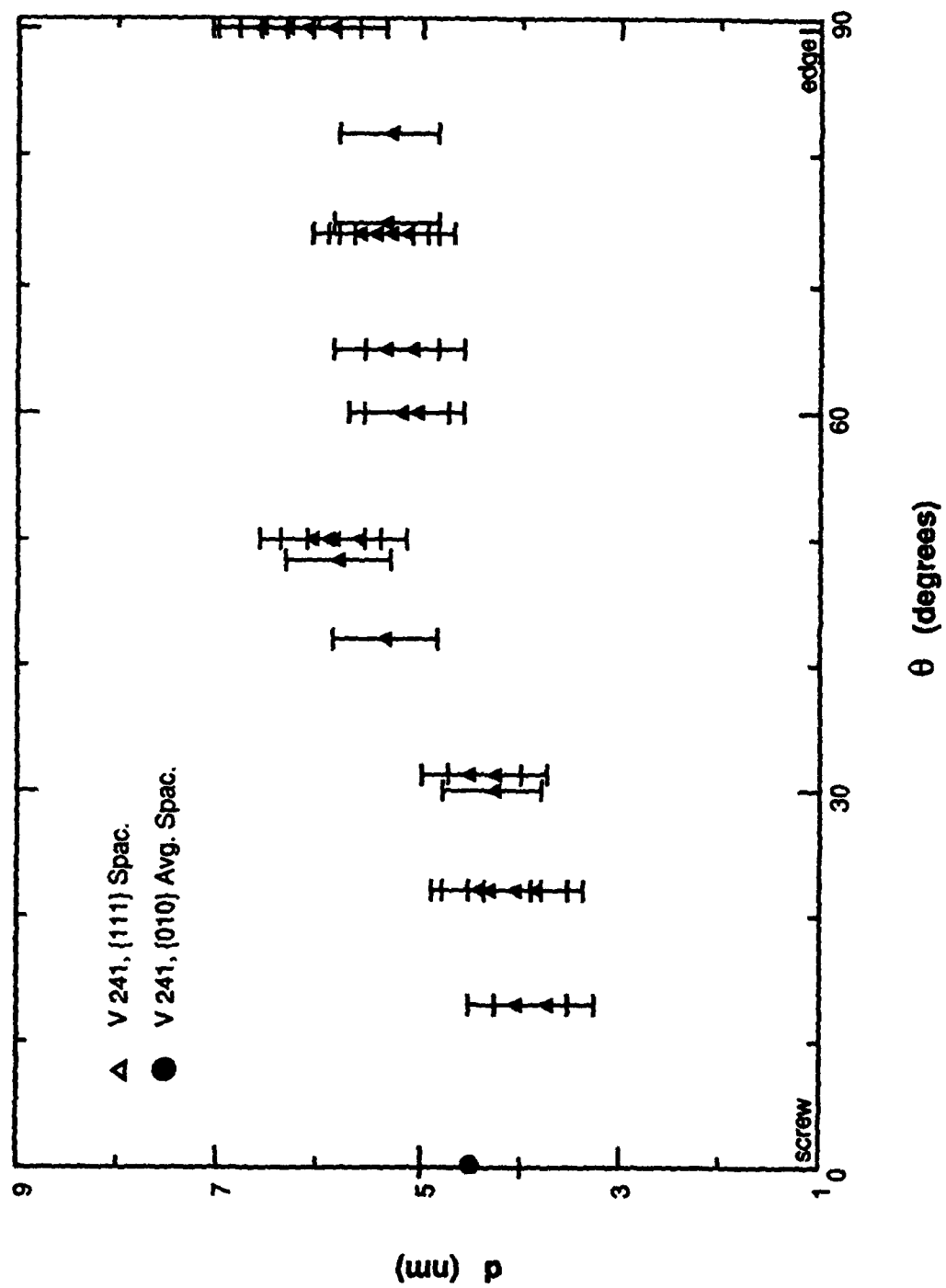
Fig. 4.65 Dissociation distance versus dislocation character; V 241, deformed at 24C.

150
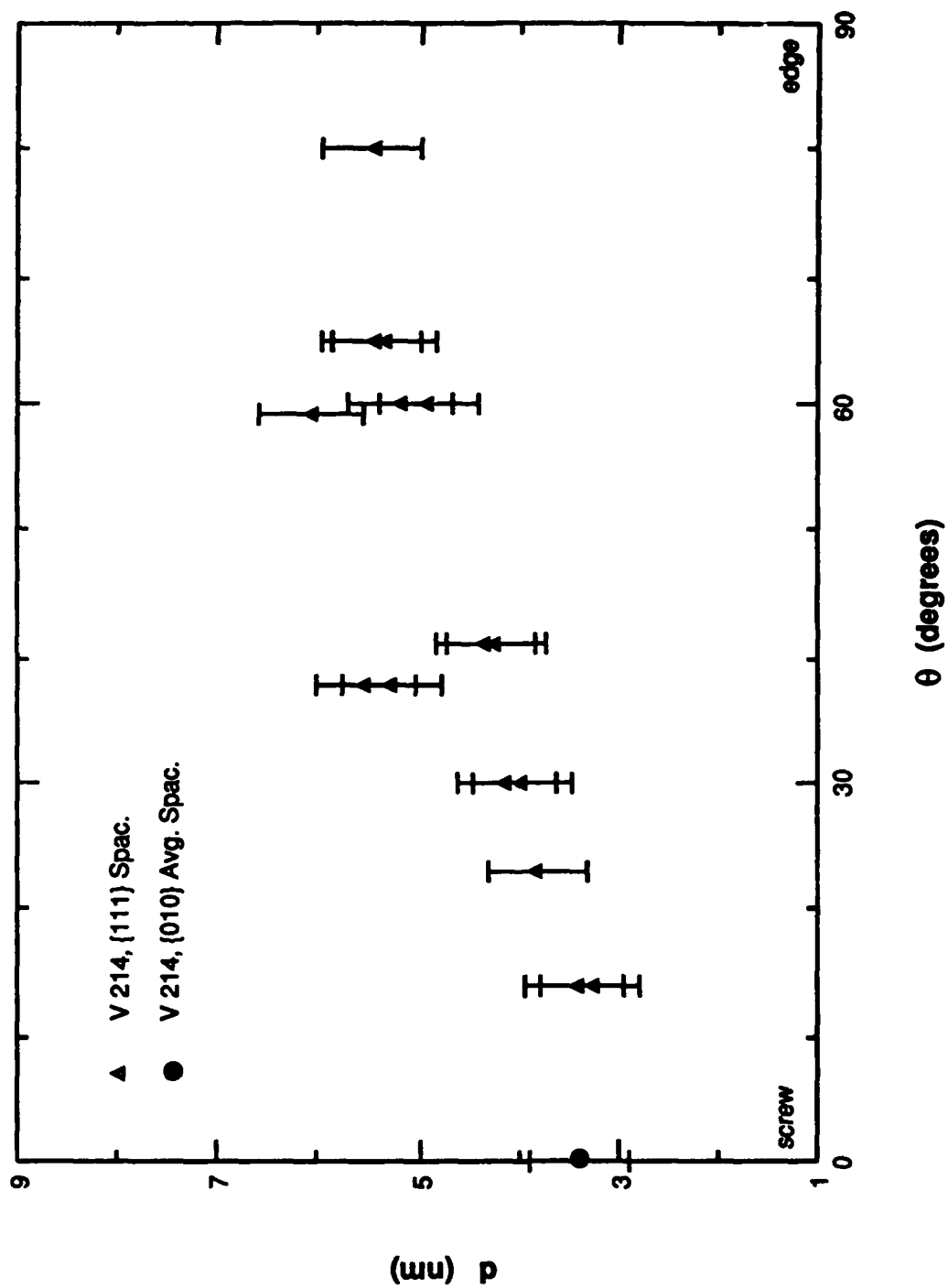
Fig. 4.66 Dissociation distance versus dislocation character; V 214, deformed at 24 °C.

151

Table 4.2 Antiphase Boundary Energies for Ternary Ni_3Al Alloys

Alloy	Composition (a/o)	γ_{010} (mJm^{-2})	γ_{111} (mJm^{-2})	$\gamma_{111}/\gamma_{010}$
Sn 241	Ni-24.1Al-0.9Sn	129 ± 12	166 ± 18	1.29
Sn 214	Ni-21.1Al-3.7Sn	146 ± 15	174 ± 20	1.19
V 241	Ni-23.4Al-1.0V	155 ± 17	192 ± 26	1.24
V 214	Ni-20.8Al-4.0V	201 ± 32	198 ± 32	0.98

The results show that increasing the Sn concentration has very little effect upon the APB energy for {111} planes relative to the values in the binary alloys (changes are within the experimental uncertainty), while the {010}-plane energy is raised, which *decreases* the APB-energy anisotropy. This result is contrary to the expected tendency for Sn to stabilize the DO_{19} structure within the simple view of that structure as a periodically faulted $L1_2$ structure. The effects of V upon the fault energies are potent. A small addition of V (alloy V 241) raises both the {111}- and {010}-plane energies sharply, but the {010}-plane energy rises more rapidly than that for the {111} plane, resulting in a decreasing anisotropy ratio. For an even greater V addition (alloy V 214), the {010}-plane energy is raised to a level nearly equal to that for the {111} plane, again contrary to the concept of periodic faulting. The *APB anisotropy ratio decreases for all solute additions and concentrations studied*, relative to the Ni-rich material; conversely, only the Ni-rich material exhibits an increasing anisotropy ratio relative to the nominally stoichiometric (by considering Al plus "X") compound.

CHAPTER 5

DISCUSSION

The experiments described herein were aimed at establishing the role of substitutional solutes within the current theory for anomalous flow behavior of Ni_3Al alloys. The findings are discussed under two general topics. First those results are treated which contribute to the TEM basis for understanding the mechanism of anomalous flow behavior in Ll_2 compounds. These data are interpreted along with other recent TEM results reviewed in Chapter 2. For purposes of this discussion, the findings from the binary alloys are critical. Next, the effects of ternary solute additions are discussed within the framework of proposed models for flow behavior and the concept of phase stability.

5.1 TEMPERATURE DEPENDENCE OF FLOW STRESS

5.1.1 MECHANICAL-BEHAVIOR PHENOMENOLOGY

The binary-alloy mechanical-property data presented in Chapter 4 are consistent with the results of previous investigations on Ni_3Al alloys[36,37,80] where direct comparisons can be made. The two critical defining features of the flow-stress anomaly, namely, a flow stress which begins to increase at modest temperatures and is reversible with temperature change, were clearly identified and verified in single crystals oriented near the [001] direction. The derivative property, $d\sigma/d\epsilon$, was shown to "lead" the flow-stress response by exhibiting a positive slope at -196 °C (no athermal regime) and by showing a well-defined peak at temperatures below the peak temperature for the flow stress. The anomalous temperature dependence of this property was also shown to be reversible with

temperature change, a point which is commonly overlooked and is critical for proper interpretation of the dislocation structures observed in the materials.

The same flow-stress-versus-temperature features were present with changes in composition on both sides of the stoichiometric composition; however, the magnitude of the flow stress varied asymmetrically about the stoichiometric composition. As shown in Chapter 2, Noguchi *et al.*[77] first demonstrated this fact in polycrystalline material; but the data presented in the present study show the asymmetry *to be more pronounced than in polycrystals and to diminish at high temperature.* The fact that Ni-rich deviations from the stoichiometric composition strengthen the alloy at low temperatures and weaken it at higher temperatures is interpreted as an indication that diffusive effects on the mechanism governing the flow stress become important at modest temperatures and decrease the effectiveness of cross-slip "barriers" in providing a drag stress on dislocations. Also, the possibility exists that excess Ni decreases the CSF energy, resulting in increased activation energy for obstacle formation. Ternary alloys exhibit the same flow-stress and work-hardening features, suggesting that solute additions primarily affect the thermally activated processes governing flow, a point treated in further detail in Section 5.2.

5.1.2 INTERPRETATION OF DISLOCATION STRUCTURES

Since 1984, several research efforts have been devoted to the establishment of a TEM-based description of the flow-stress anomaly in Ni_3Al. The findings and their interpretation have been cited in the summary of Chapter 2. Among these findings, climb-dissociation events,[68,69] slip by SISF-coupled dislocations,[59] cube glide,[72,74,75] superkinks,[73-75] lattice friction,[76] and mobility of edge dislocations[74] have been proposed as critical mechanisms for governing flow stress in Ni_3Al-based alloys. The present results introduce several possibilities for reinterpretation of the results of the most

154

recent studies and certain deficiencies in some of the views expressed therein. The literature results are reinterpreted, by subject, in the following discussion.

5.1.2.1 Climb Dissociation of Dislocation Cores

The present TEM studies were carried out on alloys deformed in both the athermal temperature regime (Region I) and the low-temperature end of the anomalous regime (Region II), both well below the expected temperature range over which diffusion-controlled events are important. The critical aspects of the anomalous flow behavior were observed in the alloys in Region II; that is, the mechanism of anomalous flow was found to be operative, independent of diffusive processes in this temperature range, and to be the principal influence on flow stress. Additionally, climb-dissociated $a_0<110>$ dislocation segments were not observed, even after static annealing of crystals deformed at low temperature. Veyssière has argued that the influence of climb-dissociated cores may be important at higher temperatures or late in Region II.[68,69,109] However, as is the case with K-W locks (to be discussed later), the frequency of these events and the length scale of their occurrence are inconsistent with a reversible mechanism which could occur at rates sufficiently fast to affect yielding (i.e., rates comparable to the dislocation free-flight velocity). Further, such diffusion-controlled events must give rise to a strain-rate-dependent flow stress, a feature which is absent in Region II.[41,110,111] In fact, the best definition of Region III is the temperature range over which strain-rate effects become important in determining the CRSS. At such temperatures, other dislocation mechanisms such as cube slip and APB dragging are likely to be equally important to climb-dissociation events. *Clearly, these events cannot be important in governing the flow stress in Region II.*

5.1.2.2 SISF-Coupled Dislocations

The role of <u>dissociated</u> SISF-coupled dislocations ($a_0/3<11\bar{2}>$ type) in governing flow stress is a subject which has received inadequate treatment to date. As mentioned in Chapter 2, these dislocations—although often observed in deformed polycrystals—are assumed, without basis, to be unimportant to flow-stress behavior. In the present studies, SISF-coupled-core dissociations of the type depicted in Fig. 2.1c were not found, but the flow-stress anomaly was observed. Other TEM investigations of deformed single-crystal Ni_3Al alloys[41,43,63,72,74] do not report SISF-coupled dislocations, even when samples of other orientations in the stereographic triangle are strained. The present study suggests that SISF dissociations may be an artifact of thin-foil handling or deformation (see Appendix C). This result implies that the state of stress (which may be different in polycrystalline material) and/or the strain rate may govern the dynamic events of dislocation nucleation and core dissociation. Given that the flow-stress anomaly exists without SISF dissociations, previous investigators have properly concluded that the role of these dissociations in governing the flow-stress anomaly must be negligible.

Dipole loops bounding SISF faults have also been observed in other deformation studies. For alloy Al 270 (Subsection 4.2.3), their density in the deformation structure increased as the temperature of deformation and flow stress decreased. One may readily conclude from this observation that the formation of these dislocations has little effect upon the mechanism governing the flow-stress anomaly. These dislocations are apparently sessile (remained upon annealing of alloy Sn 241) and must, therefore, contribute to the rate of formation and storage of dislocation debris. Such obstacles are likely to have the greatest influence on Stage III work hardening where they must be defeated if deformation is to continue. A mechanism by which these loops undergo sessile-to-glissile transforma-

156

tions with reversal of temperature is not apparent; therefore, they are likely to have little influence on the Stage II hardening behavior.

5.1.2.3 Kinks and Glide on the Cube Cross-Slip Plane

The results of the present study confirmed the anomalous flow behavior but did not, in general, reveal bowed dislocations on the cube cross-slip plane. For alloy Al 270 deformed at -196 °C, even the characteristic "sessile" screw dislocations were few in number. In the athermal flow-stress regime (Region I), very few screw dislocations were observed, suggesting that their mobility is high and that no preference exists for the screw orientation. The few screw dislocations in the K-W configuration were very long and straight and had a uniformly large dissociation distance, all indicative of their being formed by "cross-slip" of the leading screw partial of an expanding $a_0<10\bar{1}>$ loop in the primary octahedral plane. This view is further supported by the dislocation structure observed in the crystal of alloy Al 230 which was pre-strained at -196 °C, annealed at 600 °C, and re-strained at -196 °C. Most of the dislocations observed in this crystal were in the K-W configuration, even though the contributions from thermal activation were minimal during the deformation process.

The observations described above suggest that following initial formation events, the K-W configuration extends by glide of the closing $a_0/2<10\bar{1}>$ edge partial on the cube plane, as shown schematically in Fig. 5.1 and originally suggested by Kear.[39] As the temperature of deformation is raised or, equivalently, if a stronger alloy is examined at the same temperature (such as alloy Al 270 or Sn 214), glide of the edge segment closing the APB on the cube plane (see Fig. 5.1) is periodically inhibited by some currently unknown process. This results in the formation of a macrokink along the K-W line as the $a_0<10\bar{1}>$ loop continues to expand in the octahedral plane. Many of the junctions between the K-W and macrokink segments appear as constrictions of the dislocation line, while others have

157
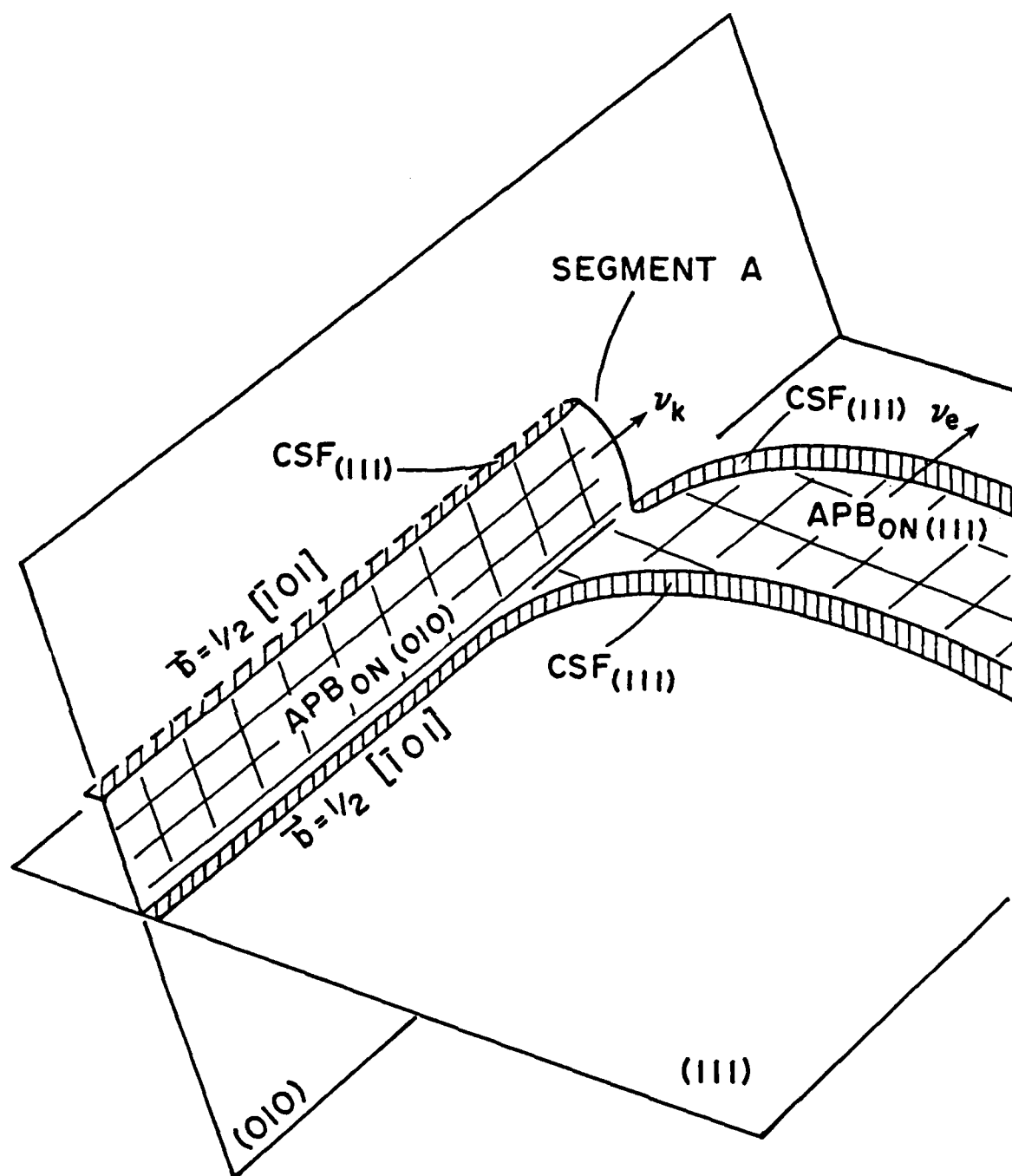
Fig. 5.1 Schematic diagram of Kear-Wilsdorf lock formation by cross-slip of expanding loop on (111). $a_0/2[10\bar{1}]$ edge segment on (010) at A may be periodically inhibited from gliding at same rate ($v_k \neq v_e$) as the edge segment on (111). When this occurs, macrokink is formed on Kear-Wilsdorf line.

158

no specific detail associated with them. The observations reported here suggest that the mechanism governing periodic impedment of lateral APB extension on the cube plane must take place on the same scale as the superlattice-partial-dislocation-core width (i.e., less than 1.0 nm) since these events are not directly observed. To date, the core structure of an $a_0/2<10\bar{1}>$ edge dislocation on the {010} plane has not been explored. A collective view of the weak-beam images shown in Chapter 4, coupled with similar observations too numerous to be included here, indicates that the frequency of macrokink occurrence varies directly with the strength of the alloy at a given temperature; however, the length of an individual macrokink in the (111) plane varies inversely with the strength of the alloy (i.e., strong alloys tend to exhibit many short macrokinks while the athermal alloys exhibit a few long ones). The strongest alloys also exhibited more microkinking (kinks having widths much less than the APB width).

The defining features of a K-W configuration should be pointed out here. A K-W "lock" consists of a screw dislocation with the two $a_0/2<10\bar{1}>$ superlattice partials being separated on the cube cross-slip plane at a distance near the equilibrium distance for that plane (i.e., core-dissociation widths on the order of several nm). These large dissociation distances exist even at room temperature and below. Such a dissociation distance would have an enormous activation enthalpy (compared to kT at room temperature) if it were to occur by a single glide/cross-slip event. Alternatively, the initial events that form these configurations are likely to be statistical in nature. Several successive lower-energy events such as the successive formation of microkinks (treated later as "Escaig" events) are likely to be required for forming the actual K-W configuration observed "postmortem." Elastic repulsion between the two superpartial dislocations provides a strong biasing of the statistical process until the equilibrium dissociation distance can be achieved. This implies that many unobserved events take place before a K-W lock becomes stabilized and extended.

159

Alloy Al 270 exhibited the following important features: i) significant strengthening over that in the Ni-rich alloys at low temperature, ii) no athermal behavior, iii) a dislocation structure after -196 °C deformation which was related to the typical structure of the athermal regime, iv) a higher work-hardening rate than that in the Ni-rich alloys, and v) a rate of change of the work-hardening rate with temperature, $d\theta_{II}/dT$, equal to that for the Ni-rich alloys; these features imply that the mechanisms governing flow are common to binary alloys and that K-W "locking" is a negligible feature when considering yield behavior. The K-W lock is important only in work hardening, as Kear originally suggested.[38,39] Flow stress is apparently governed by the effectiveness of the lattice intrinsic drag stress acting on new or mobile dislocation lines (that is, by the rate of obstacle formation and/or annihilation) and is comparatively unaffected by the debris content in the material at low strains. Additionally, the work-hardening rate must be governed by the net rate of debris accumulation (not the amount of debris present) since both low flow stress and low work-hardening rate are recoverable at low temperatures after high-temperature pre-straining. The pre-straining experiments showed the effect of the total debris content of the alloy upon flow to be comparatively small (as expected); however, this effect, as strong as it is in disordered metals, is negligible when compared to the potency of the thermally activated intrinsic-drag event in these alloys. This view of yielding contends that K-W "locks" as observed in the TEM are a statistical artifact of deformation and, as discussed below, are not "locks" at all. Additionally, this view of yield behavior and the results from this study provide a clear means of interpreting the following observations of glide on the cube planes reported in the recent literature.

Korner[72] and Mills et al.[74] have observed segmented dislocation loops on the (010) plane after deformation of Ni_3(Al,Ti) and Ni_3(Al,Ta) single crystals. Both studies examined crystals which were oriented near the $<\bar{1}23>$ compression axis and had a significant resolved stress on both the primary cube-slip and the cube cross-slip systems.

These investigators proposed that under the action of the Peach-Koehler force, cross-slipped (K-W) screw dislocations bow out on the cube planes with increasing frequency as the temperature is increased. Korner has argued, as did Thornton et al.,[41] that the bowed-out segments act as forest-debris obstacles to glide on the octahedral planes. While it is clear that such a mechanism could contribute to the work-hardening rate, no mechanism has been proposed to date by which such a process would be thermally reversible. A reversibility mechanism must be introduced before the presence of the debris itself can be considered to govern flow. The forest debris shown to exist from the segments bowed out on the (010) plane in Korner's study is clearly not reversible since it is observed after testing. As yet, no model has proposed a mechanism which provides variability to the strength of forest obstacles (to the ability to defeate forest dislocations) required for recovery of flow stress at low temperatures. For this reason alone, static debris-based models must be discounted.

Mills et al.[74] and Veyssière[75] have introduced a concept based upon the view proposed earlier by Sun and Hazzledine[73] in which "superkink" segments on K-W lines (the macrokinks described in Chapter 4) are inhibited during glide on the octahedral plane by bowing segments of K-W dislocations on the cube cross-slip plane during deformation in Region II (Region III in the paper by Mills et al.[74]). Sun and Hazzledine suggested that prior to the formation of bowed segments on the cube cross-slip plane, macrokinks are free to glide on the octahedral plane, indicating that K-W "locks" are not locks at all. This concept, introduced by Sun and Hazzledine and projected by Mills et al., is consistent with the concept of flow presented in the current study, which contends that a K-W dislocation is simply a screw line which is forced to move through the lattice at a lower rate for a given applied stress, since only restricted segments of the line (both macrokinks and microkinks) are mobile over a given time interval. Within this concept, the velocity of these dislocations may be treated as the velocity for screw dislocations in bcc metals which must move by

161

thermal activation of double-kink segments. *Kear-Wilsdorf segments must likewise move by thermally activated microkinks after the macrokink segments have been exhausted* in a local region. Veyssière has schematically illustrated the bowing process on the cube cross-slip plane in the diagram in Fig. 5.2 and suggested that such a mechanism becomes more potent as the temperature is increased since bowing becomes more extensive. The macrokink segments may overcome the bowed-out obstacles; however in so doing, the segments work against the Peach-Koehler force acting on the segment in the cube cross-slip plane. More extensive bowing reduces the ability of the macrokink segment gliding on (111) to defeat the obstacle.

Within the concept of yielding and flow proposed above, the mechanism suggested by Mills *et al.* and Veyssière can be interpreted as a provision for a reversible work-hardening rate. These investigators argued that the frequency of forming bowed segments and the extent of these on the cube cross-slip plane are temperature dependent since cube-plane glide is easier at higher temperatures. Given such a temperature dependence, lowering the temperature reduces the rate of formation and the effectiveness of cube-plane-glide obstacles and, thereby, maintains the mobility of new macrokink segments as they are formed on K-W lines at low temperature. However, such dislocation bowing in the cube cross-slip plane cannot account for the anomalous flow-stress behavior. The scale on which cube-plane glide is observed and described in studies by Mills *et al.* and Veyssière is significantly larger than the resolution of weak-beam microscopy; therefore, either such events, if operative, should have been observed in the present study or the flow-stress anomaly should not have been observed. Additionally, any such event is contingent upon the formation of a K-W configuration, which very likely does not occur with the same frequency with which dislocations are nucleated and propagated through the lattice. Cube-plane obstacles bowing on a smaller scale (less the 1 nm) are more readily defeated (and formed) by thermal activation in the temperature regime of interest and simply provide

162
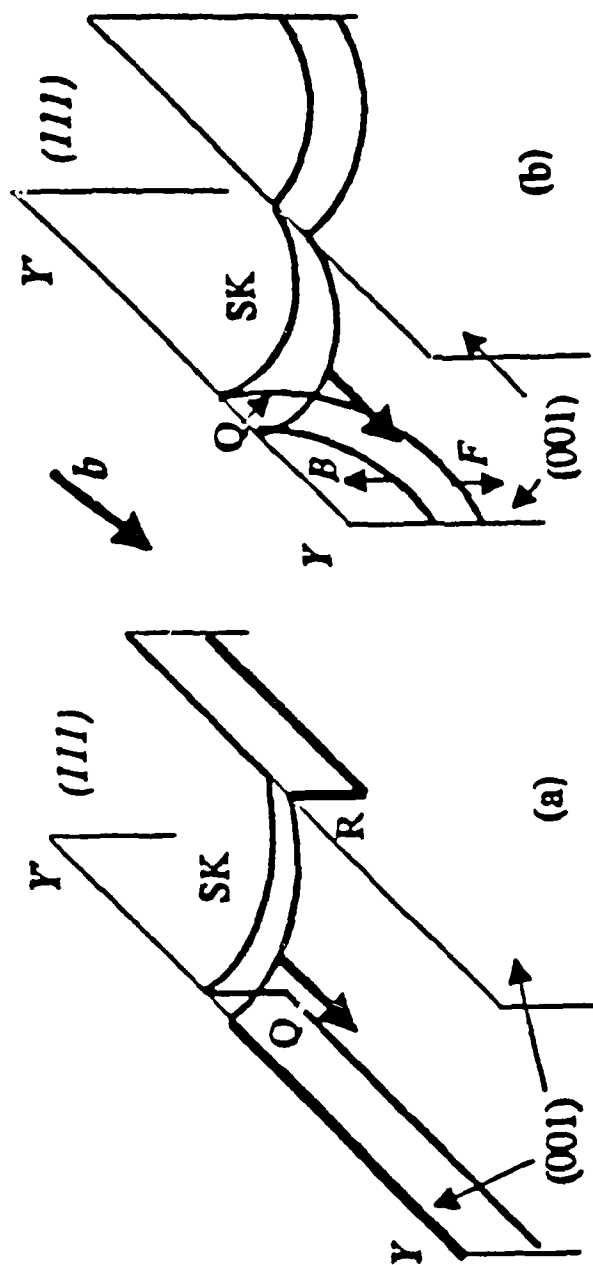
Fig. 5.2   Schematic illustration of pinning of macrokink segments by bowing out of Kear-Wilsdorf screw dislocation on cube cross-slip plane. Diagram here is by Veyssière.[75] Original concept is from Thornton, et al.[41] A similar view has recently been suggested by Mills, et al.[74]

another means of describing the cross-slip-pinning event formalized in the PP&V model. The microkinks observed in these studies (dislocation-line roughness in the strong alloys) may have some frequency of occurrence as small bowed segments on the cube plane but, in general, are not resolved by weak-beam TEM.

5.1.2.4 Lattice Friction

In the discussion thus far, the structure of superlattice partial dislocation cores has not been addressed. Yet events taking place on the expected size scale of the superpartial core width (CSF width) are the only events having expected activation energies which are sufficiently low to permit operation in the temperature regime demonstrated to be important for these materials (-196 to 600 °C). The experimental results presented in Chapter 4 point to the existence of a critical mechanism controlling the flow-stress variation with temperature which operates on an atomic scale (below the resolution of weak-beam TEM).

As reviewed in Chapter 2, Caillard et al.[76] have reintroduced a concept discussed by Copley and Kear[37] which contends that the lattice resistance to slip (friction stress) increases with temperature. Caillard et al. suggest that the specific mechanism of increasing lattice resistance is a "continuous increase in the amount of energy required to recombine a superpartial core spread out of its glide plane," which is interpreted here as a decrease in the CSF energy (increasing CSF width) with increasing temperature. Thermal activation contributes to the defeat of such obstacles; however, its ability to do so is diminished as the temperature increases. The concept of increased lattice friction was introduced by Copley and Kear; however, they argued that the mechanism was the reverse of the mechanism of Caillard et al.; that is, in the Copley and Kear concept, the lattice-friction stress increases with an increase in CSF energy (decrease in the superpartial core width) as expected from a simple Peierls model (core width model) for the source of lattice friction.

164

While the model of Caillard *et al.* cannot be directly refuted or supported by the present results, the following critical discussion is offered. Their model amounts to an inverse of the cross-slip-pinning model if the critical event (namely, core transformation from a sessile to a glissile configuration) alone is considered. The difference between their model and the cross-slip-pinning model lies in the mechanism of increased glide resistance. In the cross-slip-pinning model, the increased resistance to glide originates with the enhanced frequency of forming local (envisaged here as being < 3b in length) obstacles to glide as temperature is increased. The effectiveness of a given obstacle at a given temperature is not specifically addressed. The lattice-friction model suggests that the obstacles to glide are not local (>>3b in length) but that the initial event associated with their defeat must be local if thermal activation is to control the defeating process. This view presents several difficulties. The extended superpartial-core concept introduces the question of how the obstacles are formed. If the CSF energy decreases with increased temperature, then the glissile-to-sessile transformation must occur with increasing difficulty, as suggested for the sessile-to-glissile transformation. The CSF energy directly influences the activation barrier in both directions of the superpartial-core transformation path. One may argue that new dislocation line created during deformation by expansion of nucleated loops would be subjected to increasing difficulty for transformation to a sessile-core configuration. From this line of reasoning, it should follow that increasing the temperature of deformation should increase the planarity of cores and, thereby, decrease the flow stress at high temperature once the microstrain regime has been exhausted. Consequently, an expanded superlattice-partial core width at high temperature cannot be the mechanism of increased lattice friction.

The Copley and Kear concept of a decreased superpartial-core width creates similar difficulties. As pointed out and first demonstrated by Thornton *et al.*[41] and verified by Mulford and Pope,[43] the flow stress in the microstrain regime (<10^{-5}) is athermal over the

165

entire range of Region II. This critical feature is inconsistent with a static Peierls treatment or lattice-friction model of the flow stress. The Peierls model does not take into account the strain dependence.

Caillard *et al.* have not provided evidence to support the expected core-width increase with temperature required by their model. They have argued that the unlocking event takes place over the entire length of the dislocation line "instantaneously." Such an event is more likely to be a consequence of the thin-foil geometry used in their deformation studies and the expected rapid velocity associated with kink propagation along a dislocation line. Atomic relaxations at free surfaces have a high probability of diminishing the activation barrier or incubation time for the nucleation of thermal kinks.

Finally, Caillard *et al.* unnecessarily introduced their lattice-friction model based on their incorrect interpretation of the cross-slip-pinning model. Neither the T&K[44] nor the PP&V[56] interpretation of the cross-slip-pinning concept specifically states that "irreversible" locking is required or, in fact, that it occurs. Irreversibility is implicit in the formalism introduced by the T&K model and its foundation in the dynamics of dislocation glide; however, the requirement for irreversibility is a kinetic one only. The local obstacles need only have a lifetime comparable to the time required to defeat them by the Friedel break-away process analyzed by T&K. Consequently, debris accumulation does not occur at a rate comparable to obstacle formation. The principal mechanism governing debris accumulation is the full K-W event rather than the local subset event of double-kink formation on the cube plane. The PP&V model for the cross-slip driving force and activation enthalpy does not preclude this concept and has directly adopted the dynamic break-away concept of T&K. In principle, breaking away from local obstacles (as specifically described by the Friedel process) is not required for achieving anomalous flow-stress behavior; rather the obsticles themselves (even long obsticles) may decay, releasing the dislocation or reducing the drag stress. In either case, the net result (and only

requirement for controlling flow) is a dynamic mechanism for achieving a backstress on dislocation sources.

5.1.2.5 Edge-Dislocation Glide

Implicit in the concept of macrokinks (superkinks) introduced by Sun and Hazzledine[73] and explicitly stated in the treatment by Mills *et al.*[74] is the issue of edge-dislocation mobility on both the primary octahedral and cube cross-slip planes. The observations reported in Chapter 4 contain several instances of local locking and/or dissociation events occurring on dislocation segments having edge or mixed character in the primary glide plane. The discussion above indicated that the mobility of the $a_0/2<10\bar{1}>$ edge or mixed dislocation in the cube cross-slip plane controls the aspect ratio of K-W configurations and the frequency of macrokinking. Hazzledine[112] has considered possible Lomer-Cottrell type reactions of the edge superlattice partial on the cube plane as a pinning mechanism for these dislocations. However, the discussion provided above, coupled with the observations of dislocation structures reported herein, indicates that edge-dislocation mobility can be an important factor in determining only the work-hardening rate (not the yield stress) in Region II.

In summary, numerous recent TEM observations have added to the data base of detailed dislocation events occurring during deformation of Ni_3Al alloys in Region II. However, primarily due to the size scale (> 1.0 nm) and apparent irreversibility of the events described in those studies, such events must be considered mechanistic contributions to the work-hardening behavior. The results of the present investigation have corroborated many of the observations recently reported in the literature; however, a detailed interrogation of these events suggests that the cross-slip-pinning model maintains significant merit. The discrepancies between the current findings and the details of this model are discussed below.

167

5.1.3 CROSS-SLIP-PINNING MODEL

In Chapter 2 details of the thermally activated pinning model given by Takeuchi and Kuramoto[44] and by Paidar, Pope, and Vitek[56] for the mechanism of Region II behavior were reviewed. Figure 2.2 provides a convenient pictorial representation of the sequence of events occurring during thermal activation of a local obstacle, as described in the PP&V model. Collectively, the steps have been referred to as an Escaig event, after the Escaig cross-slip model,[53,54] even though a "true" Escaig event (the event for which Escaig has analyzed the energetics) involves cross-slip onto the $(1\bar{1}1)$ plane after a point constriction or constricted node is formed in the (111) plane (as depicted for Ni_3Al in Fig. 5.3). The two critical material parameters providing the driving force and activation barrier for such events in Ni_3Al are the APB energy ratio $(\gamma_{111}/\gamma_{010})$ and the CSF energy, respectively. The formalism for the activation enthalpy given by the PP&V model requires that the APB energy ratio have a magnitude which is greater than $\sqrt{3}$ or 1.73. Clearly, the values for the APB energy ratio determined in the current study and shown in Tables 4.1 and 4.2 fall far short of this value, suggesting an inadequate driving force for cross-slip pinning. In fact, one of the strongest alloys (Al 270) and one of the weakest (V 214) in this study had nearly equivalent, low APB-energy ratios. The activation barriers, or CSF energies, were not directly measured in the present study since weak-beam imaging is inadequate (both by theoretical development and by resolution) for making such observations.

The discrepancies between the results of the present investigation and the T&K / PP&V model of the driving force for "cross-slip" pinning are not completely debilitating to the cross-slip-pinning concept if the recent theoretical treatments by Yoo[57-59] are considered. Using the single-crystal elastic constants measured by Kayser and Stassis[83] and the solution for the anisotropic-elastic interaction between superlattice partials given by Stroh,[61] Yoo has shown that the out-of-plane interaction force (torque) acting on pure-screw $a_0/2<10\bar{1}>$ superlattice partials has a magnitude which is 62% of the radial or in-
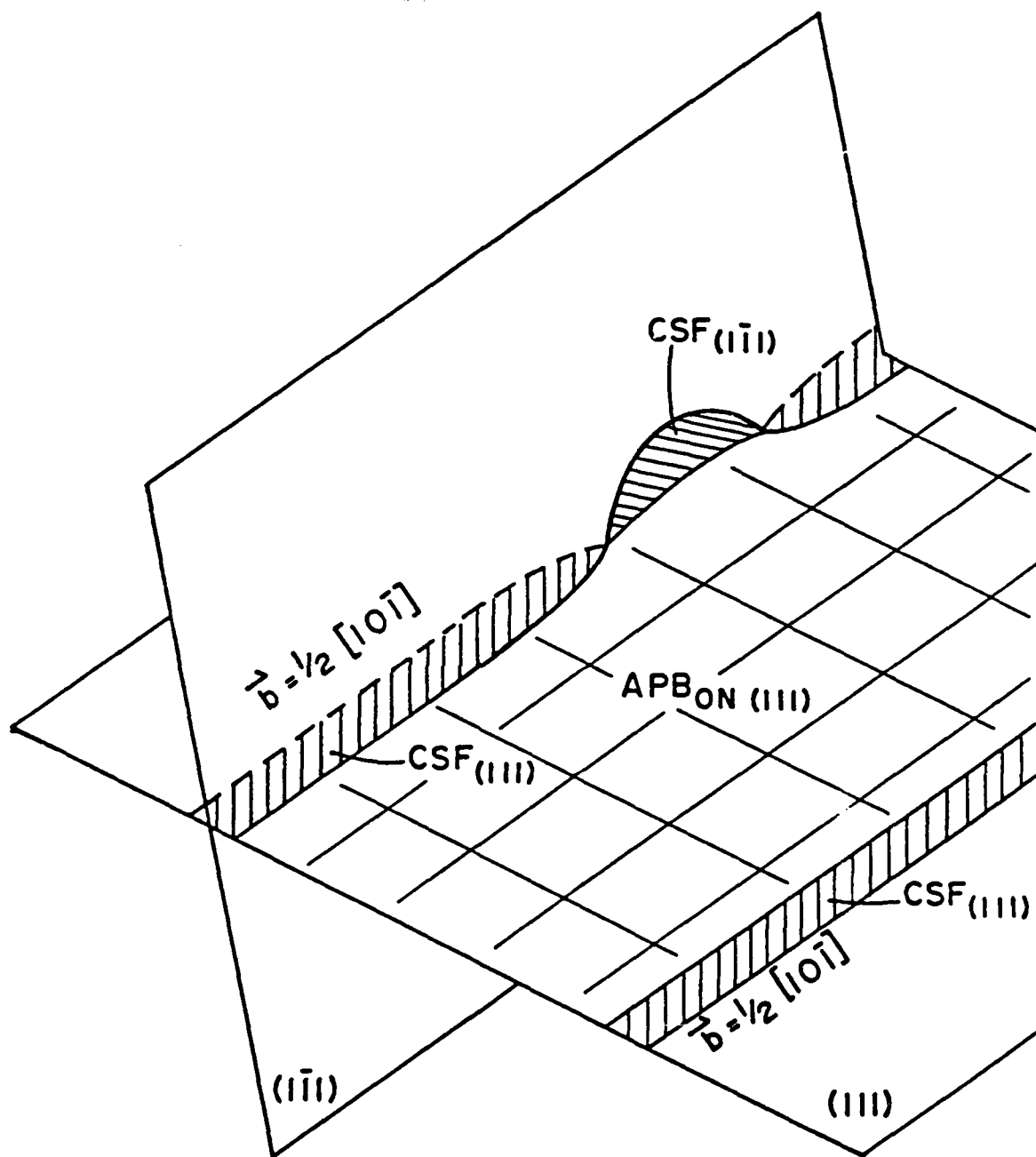
Fig. 5.3   Schematic illustration of Escaig-type core-transformation of leading
CSF-coupled dislocation onto ($1\bar{1}1$). Note CSF width is small by
comparison to the APB width.

169

plane interaction force. This force tends to spread the dislocations on a plane other than the primary slip plane. Yoo has suggested further that the dimensionless driving-force term given by PP&V (Eq. [2.7]) should be modified by an elastic torque term, yield the new driving force

$$\Delta E = \frac{\gamma_{111}}{\sqrt{3}} (1 + f_{111}\sqrt{2}) - \gamma_{010} + \tau_{010}b \qquad [5.1]$$

where τ_{010} is the resolved stress on the (010) plane and f_{111} is given by

$$f(\theta) = \frac{(A - 1)\sin 2\theta}{2(A\cos^2\theta + \sin^2\theta)} \qquad [5.2]$$

where $f(\theta) = f_{111}$ for $\theta = 54.74$ degrees (the angle between the {111} and {010} planes) and A is the Zener anisotropy ratio of the elastic constants. The elastic term $f(\theta)$ comes directly from the elastic-interaction force analysis given by Stroh.

Using Eq. [5.2] within the PP&V model, the new critical condition for the dimensionless driving force for cross-slip becomes

$$(1 + f_{111}\sqrt{2}) \frac{\gamma_{111}}{\gamma_{010}} > \sqrt{3} \qquad [5.3]$$

For stoichiometric Ni$_3$Al, $f_{111} = 0.62$ at room temperature, which yields the critical condition for cross-slip

$$1.877 \frac{\gamma_{111}}{\gamma_{010}} > \sqrt{3} \qquad [5.4]$$

The APB-energy-ratio data provided in Tables 4.1 and 4.2 indicate an adequate driving force to promote cross-slip onto (010) in Ni$_3$Al within the T&K / PP&V / Yoo cross-slip-

170

pinning model. More important, however, is the fact that the magnitude of the driving force does not change significantly with alloy chemistry, as does the mechanical behavior. *Consequently, the most important factor in differentiating the behavior of the alloys within the current cross-slip-pinning model is the effect of composition upon the activation barrier, or the ability to form a constriction on a CSF-coupled dislocation pair* (which could not be determined in the present study). This implies that factors other than the APB-energy anisotropy and elastic-interaction torque on dislocations are important in the control of yielding.

The energetics and kinetics of the Escaig cross-slip event, either onto the (010) plane as in the PP&V model or directly onto the ($1\bar{1}1$) plane as proposed for cross-slip in fcc metals in Escaig's original analysis,[53,54] must be considered as major factors which control the yield stress. The choice of either cross-slip plane, (010) or ($1\bar{1}1$), would provide an instantaneous drag stress on the screw dislocations gliding in the (111) plane if the leading or trailing CSF-coupled dislocation pair experiences the Escaig cross-slip event. As discussed above, each cross-slip or obstacle-formation event is required to have only a short "pinning" life (time), provided their frequency of occurrence is sufficient to alter the net velocity of the screw-dislocation lines (and, hence, for the yield stress to increase). *Also noteworthy are the results discussed above from Caillard et al. which are interpreted* here as an indication that the lateral velocity of expansion of such Escaig-event segments along the dislocation line is quite rapid (i.e., the observed core transformations were reported by Caillard *et al.* to occur instantaneously over the entire length of the dislocation line).

Escaig provided an analysis for cross slipping from (111) to ($1\bar{1}1$) on a larger length scale wherein the driving force for cross-slip was given by the resolved stress acting on the cross-slip plane. The event requires a large activation energy in ordinary metals due to the order-of-magnitude greater separation distance between Shockley partials in Cu, for

171

example, than that found in Ni$_3$Al. Assuming that the Escaig analysis can be applied for events occurring on a scale of < 1.0 nm, then the APB-energy anisotropy may not be relevant to an understanding of the yield behavior of Ni$_3$Al but rather may significantly affect the work-hardening rate by governing the tendency for K-W lock formation. The resolved shear stress provides a driving force for cross-slip into (010) just as it does for cross-slip into ($1\bar{1}1$) in the Escaig model. While the Escaig process has not yet been treated quantitatively for Ni$_3$Al, one can envision such a process providing the same violation of Schmid's law and tension-compression asymmetry as the current cross-slip model. Clearly, the effects of compositional variation and applied stress on the behavior of Shockley-partial-dislocation pairs bounding the CSFs are critical areas requiring further analysis. However, it is unlikely that the behavior of dislocations separated on this scale (< 1.0 nm) can be understood and treated from elastic theory alone.

An additional point which should be stressed from the isotropic-elastic analysis given by Flinn[31] and verified by Paidar[32] is that the anisotropy of the APB energy with respect to the screw-dislocation line direction is given by the relation

$$\gamma(\theta) = \gamma_{010} + \sqrt{\frac{3}{2}}(\gamma_{111} - \gamma_{010}) \sin(\theta) \qquad [5.5]$$

where θ is the angle between the {010} plane and the plane of the APB in the <$10\bar{1}$> zone. As the APB energy ratio $\gamma_{111}/\gamma_{010}$ approaches unity, there is no longer a preferred plane for the APB of the screw dislocation. Preference for a given plane originates primarily from the anisotropic elastic component of the forces on a dislocation pair and the response of the dislocation pair to an applied stress. For a pair of a$_0$/2<$10\bar{1}$> screw dislocations, the interaction torque due to elastic anisotropy goes to zero for the APB split on the (010) plane; but the resolved shear stress will, in general, have components in other planes in the zone of the dislocation line.

5.2 EFFECT OF SUBSTITUTIONAL SOLUTES

5.2.1 CLASSICAL SOLID-SOLUTION STRENGTHENING

The discussion in Chapter 2 indicated that the domain of applicability for the concepts of classical solid-solution-strengthening theory was the temperature range over which the alloys exhibited "athermal" or slightly decreasing yield strength with increasing temperature. From the CRSS data given in Appendix A, it is apparent that only the Ni-rich binary alloys and the V-containing ternary alloys can be considered to exhibit "classical" behavior. However, examination of the work-hardening behavior shows that none of the alloys exhibit a decreasing work-hardening rate from -196 °C to 24 °C, suggesting that even the "athermal" alloys are experiencing the effects of the thermally activated process for anomalous flow. Clearly, if an effect of classical elastic solute-dislocation interactions is to be observed and analyzed, alloys must be examined under conditions where temperatures are lower and experimental uncertainties fewer than in the present study. For temperatures greater than room temperature, the experimental data suggest that classical effects are negligible.

5.2.2 PHASE-STABILITY MODELS

The phase-stability rules of Suzuki *et al.*[23] were employed at the inception of this investigation. Two ternary elements, V and Sn, which were expected to have differing chemical behavior were chosen as solute additions. Both elements were expected to alter the anomalous flow behavior by destabilization of the $L1_2$ structure toward another long-period superlattice structure. The V addition was expected to lower the {010}-plane APB energy (increase the APB-energy anisotropy) by destabilizing the structure relative to the DO_{22} structure and, thereby, strengthen the alloy. Although Sn additions increased both

173

the electron-to-atom ratio (e/a) and atom-size-misfit parameter (ΔR), these additions were expected to lower the stacking-fault energy (including the CSF energy, on the basis that it is proportional to the sum of the SISF and {111}-plane APB energies) which would destabilize the compound relative to the DO_{19} structure, resulting in a strength decrease. The effect of Sn additions on the APB-energy anisotropy ratio could not be anticipated.

From the results reported in Chapter 4, these concepts must be re-evaluated. The solute additions (with the exception of excess Ni additions) examined in the present study decreased or held constant the APB-energy ratio relative to that for the stoichiometric compound. Although a concomitant decrease in strength should have been observed, this was not the case. Such an observation is diametrically opposed to the second conclusion drawn by Suzuki *et al.* and stated in Chapter 2. Although both solute types raised the e/a, V additions produced a greater change than Sn additions but had a less potent effect upon strength. This occurrence is at odds with the third conclusion of Suzuki *et al.* stated in Chapter 2. Clearly, the defining parameters regarding phase stability must be quantified in terms of fault energies before definitive, direct correlations can be made. Perhaps the most important inference from the fault-energy data in Chapter 4 is that the view of long-period superlattice structures being simple cubic structures having periodic, low-energy faults is not well founded. From the fault energies reported for the V-containing alloys, one may assume that the DO_{22} structure is an $L1_2$ structure having periodic APBs which align along the c-axis due to their high energy. That is, a structural change occurs which allows the bond configurations associated with an APB to be aligned along a single axis of symmetry and reduce the energy of the system, rather than arranged equally about three equivalent-symmetry axes in the $L1_2$ structure. For such concepts further investigation is clearly required before a definitive conclusion can be drawn.

5.2.3 CROSS-SLIP PINNING AND SUBSTITUTIONAL SOLUTES

The results for both binary and ternary alloys provided in Chapter 4 are consistent with the concept of yield and the mechanism for anomalous flow described above. Within this concept the role of substitutional solutes is to affect directly the ease with which a constricted-core configuration can be formed on an $a_0/2<10\bar{1}>$ superlattice partial dislocation and be stabilized in a transformed or cross-slipped configuration on the (010) or $(1\bar{1}1)$ plane. The specific mechanism governing this could not be elucidated from the results of the present experimental effort; further theoretical treatment is required. The most obvious means by which such core-transformation events can be enhanced or retarded is through a solute effect on the CSF energy. However, it is unlikely that this is the only means of influencing core-transformation events. Nearly every substitutional solute (with the possible exception of Cr and Fe) which has been added to Ni_3Al has been observed to strengthen the alloy and affect the anomalous flow response.[84] While it is possible that all solutes increase the CSF energy and reduce the activation barrier to core transformation, it is also possible that other mechanisms are in operation. For example, solutes may cluster or act individually to create local deviations in the mean potential field of the lattice which could either statistically enhance (retard) the core-transformation events or alter their lifetimes.

5.3 SUMMARY

Results from a TEM-based study the effect of varying the Ni/Al ratio in binary Ni_3Al and the effect of two ternary substitutional solutes on the flow behavior of Ni_3Al-based alloys have been discussed. The study was focused on the response of single-crystal alloys to low-temperature deformation; changes which develop in the dislocation structure

(during the transition from athermal flow-stress behavior to anomalous behavior) were examined under conditions which minimized the influence from thermally induced recovery. Classical elastic effects on strengthening were expected to be most evident at low-temperature; however, such effects were not evident. The APB-energy-anisotropy ratio was quantified as a function of chemistry change in order to interpret the results within the framework of current models for the driving force for thermally activated cross-slip in Ni_3Al.

Contrary to the findings of recent studies reported in the literature, the TEM results reported here (from both binary and ternary alloys) do not indicate a significant influence from K-W dislocations bowing on the cube cross-slip plane. The major experimental variable influencing these results was the use of cube-oriented crystals for the present study as opposed to the use of samples oriented near the $<\bar{1}23>$ direction for the literature studies. The alloys employed in this study exhibited an anomalous temperature-dependent flow-stress response in the cube orientation. Furthermore, the TEM investigations provided strong evidence that flow stress is controlled on a dimensional scale which is below the resolution of the weak-beam TEM technique. Based on these findings a concept for the mechanism of anomalous flow-stress increase with temperature has been suggested, which is consistent with earlier models proposed by T&K and PP&V. This concept also suggests that K-W dislocation configurations are affiliated with the strain-hardening rate rather than the yield stress (if, in fact, these two events can be separated).

The measured values for the APB-energy-anisotropy ratio indicate that these faults are universally less anisotropic than required for cross-slip pinning within the PP&V model. However, due to the contributions from elastic interactions between superlattice-partial dislocations, a sufficient driving force for cross-slip onto the cube planes is always present. The lack of significant variability in the APB-anisotropy ratio with composition (even though significant changes in mechanical behavior are observed) is an indication that

176

the primary influence of solute additions to Ni_3Al arises from variation of the activation barrier to cross-slip events. Within this concept, the dynamic influence of cross-slip onto the $(1\bar{1}1)$ plane must be considered along with cross-slip onto the (010) plane.

CHAPTER 6

CONCLUSIONS

1.   The CRSS and Stage II work-hardening rate of binary and ternary Ni_3Al-alloy single crystals suggests that the mechanism of anomalous flow behavior controls the flow stress for Ni- and Al-rich deviations from the stoichiometric composition and in ternary alloys. Both the CRSS and the work-hardening rate are controlled by a mechanism which varies reversibly with temperature. This mechanism dominates flow behavior in Region II, mitigating the influence of elastic solute-dislocation interactions. Changes in the Ni/Al ratio and ternary-element concentration are equivalent to changes in temperature within Region II.

2.   Weak-beam TEM examination of materials deformed at low temperatures revealed that screw dislocations having the Kear-Wilsdorf configuration exhibit an increased frequency of kinking (both microkinking and macrokinking) with increasing strength of the alloy. Kear-Wilsdorf configurations were characteristically straight in Region I (athermal alloys) and could be formed at -196 °C by straining, annealing, and re-straining, which suggests that these configurations form by glide of closing-edge segments on {010} planes (see Fig. 5.1). Both the existence of kink segments and observations of moving-edge segments suggest that Kear-Wilsdorf configurations are mobile. Kear-Wilsdorf configurations are a statistical artifact of deformation in Region II and contribute to the flow stress through their effect on the work-hardening rate.

3.   Bowing of Kear-Wilsdorf configurations on the cube planes was observed only rarely and has no significant effect on yield behavior. Likewise, the dislocation debris formed by such configurations does not significantly influence the anomalous flow-stress

178

behavior. Such debris is not expected to provide a thermally reversible mechanism for controlling flow stress.

4.   Static-lattice-friction (e.g. Peierls) models cannot describe the anomalous flow-stress behavior since such models do not take into account the strain dependence (absence of the anomaly in the microstrain regime) of flow stress. Such models introduced for Ni_3Al alloys lack self-consistency.

5.   Weak-beam TEM examination of dissociated-dislocation cores failed to provide evidence for general immobilization of edge dislocations.

6.   Yield behavior in Ni_3Al-based alloys is governed by the dynamics of screw-dislocation glide and the formation (annihilation) rate of kinetic barriers to glide. Both the measured apparent thermal-activation enthalpy and the dislocation structures observed suggest that flow is governed by events which occur on a dimensional scale of < 1.0 nm. Thermally activated dislocation-core transformations (cross-slip) via an Escaig-type process offer the most complete and self-consistent route by which the phenomenology of flow in these alloys can be rationalized. Further attempts to understand yield behavior must consider transformations into both the {010} and {1$\overline{1}$1} planes.

7.   Measurements of the APB-energy-anisotropy ratio, the driving force for cross-slip within the PP&V model, as a function of alloy composition suggest that this driving force is nominally invariant and that no correlation exists between this ratio and the CRSS. Anisotropic-elastic interactions between screw dislocations dominate the driving force for cross-slip onto {010} planes; however, literature data suggests that this effect is also insensitive to composition. These results suggest that variations in alloy composition principally affect the activation barrier to core transformation. The specific mechanism could not be deduced from weak-beam observations. These results further suggest that

179

core transformations of CSF-coupled dislocations from {111} into {1$\bar{1}$1} planes play an important role in yield behavior independent of transformations into {010} planes.

8. The alloys examined exhibited a positive variation in the Stage II work-hardening rate with increasing temperature in Regions I and II, suggesting that the mechanism for anomalous flow is operative at temperatures as low as -196 °C. Such behavior is inconsistent with the classical view of solute-dislocation interactions in disordered materials. This result, along with the measured flow stress-temperature data, suggests that solid-solution hardening by elastic effects is of secondary importance in Region II. The data from the present study neither span a sufficiently low temperature range nor are sufficiently sensitive that the influence of such effects in the athermal regime can be discerned.

9. No clear correlation among the APB energy variation with composition, the anticipated stability of the $L1_2$ structure, and the flow-stress-versus-temperature behavior could be established. Structural-stability concepts for describing the influence of solutes upon flow behavior must be quantitativly defined before their utility can be established.

CHAPTER 7

SUGGESTIONS FOR FUTURE RESEARCH

The present study has brought to light a number of aspects of flow behavior in Ni_3Al and other intermetallic compounds which merit further study. Some of these are discussed below, with no particular attention being paid to their importance.

1. The findings and interpretations of the present study have hinged heavily upon the assumption that the principal mechanism governing flow in Region II is constant over the entire temperature regime. This study specifically addressed the behavior in the low-temperature-transition regime between Region I and Region II behavior. The findings reported here form a foundation from which features occurring in the dislocation structure can be predicted. Alloys which exhibit athermal low-temperature behavior and are deformed at temperatures below the onset of Region III behavior (in the range 300 to 500 °C) should reveal features on the dislocations which are similar to those observed in alloys Al 270 and Sn 214. Several observations reported here were anticipated from the flow curves and from prior examination of alloys having similar flow curves before the actual observations were made. Several other ternary-alloy additions representing both the high-strength and the athermal alloy groups should be examined in order to corroborate the present findings.

2. Despite extensive studies of Ni_3Al-alloy single-crystal deformation which have been reported in the literature, Stage I work-hardening behavior as a function of temperature has not been investigated. The single-crystal studies reported to date have been significantly influenced by specimen end constraints in both tension and compression tests. Investigations designed to maximize the easy-glide regime could provide useful information

181

for determining the relative importance of {010}- and {1$\bar{1}$1}-plane core transformations. A relevant question is whether easy-glide can be sustained in the presence of {1$\bar{1}$1} plane core transformations and Kear-Wilsdorf "locking."

3.   Careful studies of the strain-rate dependence of flow behavior are warranted. The studies reported in the literature have been restricted to a narrow strain-rate range and, in particular, have been limited to low maximum strain rates. The processes suggested to govern yield in Ni_3Al are expected to occur on time scales which are several orders of magnitude smaller than those for dislocation multiplication at typical strain rates below 10^{-3}/s. Significantly higher strain rates may be required before these processes can be avoided. High-frequency internal-friction measurements should provide useful insight into the kinetics of core-transformation processes.

4.   The present weak-beam TEM study was limited by a lack of sufficient resolution for quantifying the core structure of superlattice-partial dislocations. The detailed structure of these dislocations must be quantified as a function of composition by atomic resolution microscopy. A critical part of such studies is computer simulation (using interatomic-force models) of the expected structure of these dislocations in thin-foil sections; since surface relaxation has a high probability of influencing the observed dissociation distances. High-resolution-TEM methods and atomic-simulation methods should provide direct information concerning the structure of $a_0/2<10\bar{1}>$ edge dislocations lying on {010} planes. As suggested in this dissertation, the mobility of these dislocations is expected to control the frequency of macrokinking and the mobility of Kear-Wilsdorf configurations.

5.   Perhaps the most critical area for further study is that of deriving a new analytical description of flow behavior for anomalous compounds. The view of yielding presented in this study suggests that glide is inhibited by kinetic barriers. Details of these barriers, such as the mean lifetime and length, should be explored analytically. It is unlikely that the

simple concept of localized dislocation pinning (as depicted in the T&K model) is accurate, given the expected velocities of kink propagation (see Appendix E). Before such aspects can be quantified, the Escaig analysis must be re-examined, with particular attention being payed to the question of relevance of the model on the dimensional scale of the CSF. The PP&V analysis has been surprisingly effective in describing flow-stress behavior despite their lack of treatment of this point.

6.   The results of the present study provide a basis for examining yield behavior in compounds having other crystal structures. The compound TiAl exhibits a similar, but less severe, anomalous flow-stress response. Currently, the mechanism governing this behavior is speculative at best. The behavior of this and other compounds must be explored within the core-transformation-pinning concept.

CHAPTER 8

REFERENCES

1. J.H. Westbrook: in *Ordered Alloys, Physical Metallurgy and Structural Applications*, Kear et al Clatiors, Baton Rough, 1970, pp. 1-24.

2. T.E. O'Connell: in *Application of Titanium Aluminide Products*, Interim Report, September 1979, Air Force Contract No. F33615-78-C-5144.

3. H.A. Lipsitt: in *High-Temperature Ordered Intermetallic Alloys*, C.C. Koch, C.T. Liu, and N.S. Stoloff, eds., Mater. Res. Soc. Proc., vol. 39, Pittsburgh, 1985, pp. 351-64.

4. K. Aoki and O. Izumi: *J. Japan. Inst. Met.*, 1979, vol. 43, pp. 1190-96.

5. D.P. Pope and S. S. Ezz: *International Metals Reviews*, 1984, vol. 29, pp. 136-67.

6. *Structural Uses for Ductile Ordered Alloys*, National Materials Advisory Bd., National Research Council, DARPA, Report No. NMAB-419.1984.

7. N.S. Stolloff: *International Metals Reviews*, 1989, vol. 34, in press.

8. R.L. Fleischer, D.M. Dimiduk and H.A. Lipsitt: *Annual Reviews of Materials Science*, 1989, pp. 231-63, in press.

9. M.J. Richards and J.W. Cahn: *Acta Metall.*, 1971, vol. 18, pp. 1263-77.

10. M. Hansen and K. Anderko: *Constitution of Binary Alloys*, McGraw-Hill Publishing Company, 1958, p. 119.

11. D.P. Pope and J.L. Garin: *J. Appl. Crystall.*, 1977, vol. 10, pp. 14-17.

12. K. Aoki and O. Izumi: Phys. *Status Solidi (a)*, 1975, vol.32a, pp. 657-64.

13. F.J. Bremer, M.Beyss, E. Karthaus, A. Hellwig, T. Schober, J.M. Welter, and H. Wenzl: *Jol. Crystal Growth*, 1988, vol. 87, pp. 185-92.

14. D.M. Wee and T. Suzuki: *Trans. Japan Inst. Met.*, 1979, vol. 20, pp. 634-46.

15. D.M. Wee, O. Noguchi, Y. Oya, and T. Suzuki: *Trans. Japan Inst. Met.*, 1980, vol. 21, pp. 237-47.

16. M.H. Yoo, J.A. Horton, and C.T. Liu: *Acta Metall.*, 1988, vol. 36, pp. 2935-46.

17. S. Ezz, D.P. Pope, and V. Paidar: *Acta Metall.*, 1982, vol. 30, pp. 921-26.

18. R.L. Fleischer: in *The Strengthening of Metals*, D. Peckner ed., Reinhold, London, 1964, pp. 93-140.

19. R. Labusch: *Phys. Stat. Sol.*, 1970, vol. 41, pp. 659-69.

20. F.R.N. Nabarro: *Phil. Mag.*, 1977, vol. 35, pp. 613-622.

21. P. Haasen: in *Fundamental Aspects of Structural Alloy Design*, R.I. Jaffee, and B. A. Wilcox, eds. Plenum, 1977, pp. 3-25.

22. U. F. Kocks: *Metall. Trans. A*, 1985, vol. 16A, pp. 2109-29.

23. T. Suzuki, Y. Oya, and S. Ochiai: *Metall. Trans. A*, 1984, vol. 15A, pp. 173-81

24. Kear, A.F. Giamei, J.M. Silcock, and R.K. Ham: *Scripta Metall.*, 1968, vol. 2, pp. 287-94.

25. B.H. Kear, A.F. Giamei, G.R. Leverant, and J.M. Oblak: *Scripta Metall.*, 1969, vol. 3, pp. 455-60.

26. B.H. Kear, A.F. Giamei, G.R. Leverant, and J.M. Oblak: *Scripta Metall.*, 1969, vol. 3, pp. 123-30.

27. B.H. Kear, G.R. Leverant, and J.M. Objak: *Trans. ASM*, 1969, vol. 62, pp. 639-50.

28. M. Yamaguchi, V. Vitek, and D.P. Pope: *Phil. Mag. A*, 1981, vol. 43, pp. 1027-44.

29. M. Yamaguchi, V. Paidar, D.P. Pope, and V. Vitek: *Phil. Mag. A*, 1982, vol. 45, pp. 867-82.

30. V. Paidar, M. Yamaguchi, D.P. Pope, and V. Vitek: *Phil. Mag. A*, 1982, vol. 45, pp. 883-94.

31. P. Flinn: *Trans. TMS-AIME*, 1960, vol. 218, pp. 145-54.

32. V. Paidar: *Acta Metall.*, 1985, vol. 33, pp. 1803-11.

33. P. Beauchamp, J. Douin, and P. Veyssiere: *Phil. Mag. A*, 1987, vol. 55, pp. 565-82.

34. J. Douin, P. Beauchamp, and P. Veyssière: *Phil. Mag. A*, 1988, vol. 58, pp. 923- 35.

35. R.G. Davies and N.S. Stoloff: *Trans. TMS-AIME*, 1965, vol. 233, pp. 714-19.

36. R.G. Davies and N. S. Stoloff: *Phil. Mag.*, 1965, vol. 12, pp. 297- 304.

37. S.M. Copley and B. H. Kear: *Trans. TMS-AIME*, 1967, vol. 239, pp. 977-84.

38. B.H. Kear and H.G.F. Wilsdorf: *Trans. TMS-AIME*, 1962, vol. 224, pp. 382-86.

39. B.H. Kear: *Acta Metall.*, 1964, vol. 12, pp. 555-69.

40. B.H. Kear and M.F. Hornbecker: *Trans. ASM*, 1966, vol. 59, pp. 155-61.

41. P.H. Thornton, R.G. Davies, and T.L. Johnston: *Metall. Trans.*, 1970, vol. 1, pp. 207-18.

42. P.H. Thornton: *Metall. Trans.*, 1970, vol. 3, pp. 291-300.

43. R.A. Mulford and D.P. Pope: *Acta Metall.*, 1973, vol. 21, pp.1375-80.

44. S. Takeuchi and Kuramoto: *Acta Metall.*, 1973, vol. 21, pp. 415-24.

45. J. Friedel: *Electron Microscopy and Strength of Crystals*, G. Thomas and J. Washburn eds., Interscience, New York, 1963, pp. 605-49.

46. J.P. Hirth and J. Lothe: *Theory of Dislocations*, 2nd. ed., John-Whiley & Sons, Inc., New York, 1982, pp. 591-94.

47. R.J. Taunt and B. Ralph: *Phil. Mag.*, 1974, vol. 30, pp. 1379-94.

48. N. Baluc, H.P. Karnthaler, and M.J. Mills: *Inst. Phys. Conf. Ser. No. 93*, 1988, vol. 2, pp. 463-64.

49. C. Lall, S. Chin, and D.P. Pope: *Metall. Trans A*, 1979, vol. 10A, pp. 1323-32.

50. A.N. Stroh: *Proc. Phys. Soc. B*, 1954, vol. 67, pp. 427-36.

51. A.N. Stroh: *Phil Mag.*, 1956, vol. 1, pp. 489-502.

52. J. Friedel: *Dislocations*, Pergamon Press, Oxford, 1964, pp. 161-66.

53. B. Escaig: *Jol. de Physique*, 1968, vol. 29, pp. 225-39.

54. B. Escaig: *Dislocation Dynamics*, A.R. Rosenfield, G.T. Hahn, A.L. Bement Jr., and R.I. Jaffee, eds., McGraw Hill, New York, 1968, pp. 655-77.

55. J. Bonneville and B. Escaig: *Acta Metall.*, 1979, vol. 27, pp. 1477-86.

56. V. Paidar, D.P. Pope, and V. Vitek: *Acta. Metall.*, 1984, vol. 32, pp. 435-48.

57. M.H. Yoo: *Scripta Metall.*, 1986, vol. 20, pp. 915-20.

58. M.H. Yoo: *High Temperature Ordered Intermetallic Alloys II*, N.S. Stoloff, C.C. Kock, C. T. Liu, and O. Izumi, eds., Materials Research Society Symposia Proceedings, Materials Research Society, Pittsburgh, vol. 81, 1987, pp.207-12.

59. M.H. Yoo: *Acta Metall.*, 1987, vol. 35, pp. 1559-69.

60. A.J.E. Foreman: *Acta Metall.*, 1955, vol. 3, pp. 322-30.

61. A.N. Stroh: *Phil. Mag.*, 1958, vol. 3, pp. 625-46.

62. A.F. Giamei, J.M. Oblak, B.H. Kear, and W.H. Rand: *Proc. 29th Annual Meeting of Electron Microscopy Society of America*, C.J. Arceneaux, ed., Claitor's, Baton Rouge, 1971, pp. 112-13.

63. A.E. Staton-Bevan and R.D. Rawlings: *Phil. Mag.*, 1975, vol. 32, pp. 787-800.

64. T. Saburi, T. Hamana, S. Nenno, and H-R. Pak: *Jap. Jol. Appl. Phys.*, 1977, vol. 16, pp. 267-72.

65. A. Baldan: *Phys. Stat. Sol. (a)*, 1983, vol. 75, pp. 441-49.

66. I. Baker and E.M. Schulson: *Phys. Stat. Sol. (a)*, 1984, vol. 85, pp. 481-90.

67. J.M. Oblak and W.H. Rand: *Proc. 32nd Annual Meeting of Electron Microscopy Society of America*, C.J. Arceneaux, ed., Claitor's, Baton Rouge, 1974, pp. 502-03.

68. P. Veyssière, D.L. Guan, and J. Rabier: *Phil. Mag. A*, 1984, vol. 49, pp. 45-54.

69. P. Veyssière: *Phil. Mag. A*, 1984, vol. 50, pp. 189-203.

70. P. Veyssiere, J. Douin, and P. Beauchamp: *Phil. Mag. A*, 1985, vol. 51, pp. 469-83.

71. J. Douin, P. Veyssiere, and P. Beauchamp: *Phil. Mag. A*, 1986, vol. 54, pp. 375-93.

72. A. Korner: *Phil. Mag. A*, 1988, vol. 58, pp. 507-22.

73. Y.Q. Sun and P.M. Hazzledıne: *Phil. Mag. A*, 1988, vol. 58, pp. 603-18.

74. M.J. Mills, N. Baluc, and H.P. Karnthaler: *High Temperature Ordered Intermetallic Alloys III*, C.C. Kock, C.T. Liu, N.S. Stoloff, and A.I. Taub, eds., Materials Research Society Symposium Proceedings, Pittsburgh, PA, vol. 133, 1989, in press.

75. P. Veyssière: *High Temperature Ordered Intermetallic Alloys III*, C.C. Kock, C.T. Liu, N.S. Stoloff, and A.I. Taub, eds., Materials Research Society Symposium Proceedings, Pittsburgh, PA, vol. 133, 1989, in press.

76. D. Caillard, N. Clement, A. Couret, P. Lours, and A. Coujou: *Phil. Mag. Letters*, 1988, vol. 58, pp. 263-69.

77. O. Noguchi, Y. Oya, and T. Suzuki: *Metall. Trans A*, 1981, vol. 12A, pp. 1647-53.

78. R.W. Guard and J.H. Westbrook: *Trans. TMS-AIME*, 1959, vol. 215, pp. 807-14.

79. J.A. Lopez and G.F. Hancock: *Phys. Stat. Sol. (a)*, 1970, vol. 2, pp. 469-74.

80. L.R. Curwick: PhD. Thesis, Univ. of Minnnesota, 1972.

81. K. Ono and R. Stern: *Trans. TMS- AIME*, 1969, vol. 245, pp. 171 -72.

82. R.W. Dickson, J.B. Wachtman, and S.M. Copley: *J. Appl. Phys.*,1969, vol. 40, pp. 2276-79.

83. F.X. Kayser and C. Stassis: *Phys. Stat. Sol. (a)*, 1981, vol. 64, pp. 335-42.

84. R.D. Rawlings and A. Staton-Bevan: *J. Mat. Sci.*, 1975, vol. 10, pp. 505-14.

85. K. Aoki and O. Izumi: *J. Jap. Inst. Met.*, 1975, vol. 39, pp. 1282-89.

86. K. Aoki and O. Izumi: *Phys. Stat. Sol.(a)*, 1976, vol. 38, pp. 587-94.

87. T. Suzuki, Y. Oya and D.M. Wee: *Acta Metall.*, 1980, vol. 28, pp. 301-10.

88. M. Yodogawa, D.M. Wee, Y. Oga, and T. Suzuki: *Scripta Metall.*, 1980, vol. 14, pp. 849-54.

89. D.M. Wee and T. Suzuki: *Trans. Jap. Inst. Met.*, 1981, vol. 22, pp. 163-72.

90. T. Suzuki and Y. Oya: *J. Mat. Sci.*, 1981, vol. 16, pp. 2737-44.

91. S. Ochiai, Y. C. and T. Suzuki: *Acta Metall.*, 1984, vol. 32, pp. 289-98.

92. S.J. Liang and D.P. Pope: *Acta. Metall.*, 1977, vol, 25, pp. 485-93.

93. P.C. Clapp and S.C. Moss: *Phys. Rev.*, 1966, vol. 142, pp. 418-27.

94. P.C. Clapp and S.C. Moss: *Phys. Rev.*, 1968, vol. 171, pp. 754-63.

95. S.C. Moss and P.C. Clapp: *Phys. Rev.*, 1968, vol. 171, pp. 764-77.

96. M. Morinaga: *Acta Metall.*, 1977, vol. 25, pp.957-62.

97. A.J. Freeman, C.L. Fu, and J.I. Lee: in preparation.

98. C.C. Law, D.M. Shah, and J. Lin: *Fundamental Understanding of the Intrinsic Ductility in Nickel-Base $L1_2$ Type Alloys*, Final Report, June 1988, Air Force Contract No.F49620-86-C-0033.

99. M.M. Janssen: *Met. Trans.*, 1973, vol. 4, pp. 1623-33.

100. D.J.H. Cockayne, I.L.F. Ray, and M.J. Whelan: *Phil. Mag.*, 1969, vol. 20, pp. 1265-70.

101. D.J.H. Cockayne: *Z. Naturforsch.*, 1972, vol. 27a, pp. 452-460.

102. J.P. Riviere and J. Cadoz: *J. Microsc. Spectrosc. Electron*, 1982, vol. 7, pp. 183-212.

103. D.E. Laughlin: Private Communication.

104. J.P. Hirth and J. Lothe: *Theory of Dislocations*, 2nd. ed. John-Whiley & Sons, Inc., New York, 1982, pp. 423-63.

105. M.J. Marcinkowski: *Treatise On Materials Science and Technology*, H. Herman, ed., Academic Press, New York, 1974, pp.181-287.

106. S. Ochiai, Y. Mishima, and T. Suzuki: *Bull Prec. Machin. Electron. Res. Lab. (T.I.T.)*, 1984, vol. 53, pp.15-28.

107. H.-R. Pak, T. Saburi, and S. Nenno: *Scripta. Metall.*, 1976, vol. 10, pp.1081-85.

108. K. Suzuki, M. Ichihara, and S. Takeuchi: *Acta Metall.*, 1979, vol. 27, pp. 193-200.

109. P. Veyssière: *Revue Phys. Appl.*, 1988, vol. 23, pp. 431-43.

110. J.K. Tien, S. Eng, and J.M. Sanchez: *High Temperature Ordered Intermetallic Alloys II*, ed. N.S. Stoloff, Pittsburgh, Mat. Res. Soc., 1987, pp. 183-93.

111. T. Suzuki, Y. Mishima, and S Miura: *Trans. Iron Steel Inst. Jpn.*, 1989, vol. 29, pp.1-23.

112. P. Hazzledine: *High Temperature Ordered Intermetallic Alloys III*, C.C. Kock, C.T. Liu, N.S. Stoloff, and A.I. Taub, eds., Materials Research Society Symposium Proceedings, Pittsburgh, PA, vol. 133, 1989, in press.

APPENDIX A

COMPRESSION TEST PARAMETERS AND RESULTS

The tables in this appendix contain specific experimental parameters and test results for each specimen examined in the present study. Each table is divided into two major parts, with all results for a single alloy being contained on one page. The alloy identification, heat-treatment condition, and analyzed composition are contained in each table heading. The upper part of the table provides the mechanical-testing results, with the test temperature being given in the left-most column and the specimen-identification number along the top. The matrix is filled out with the test results paired as the 0.2 % resolved shear stress (CRSS) and the Stage II work-hardening rate (ds/de), both given in MPa units. The lower section lists the individual specimen parameters prior to testing; these are: i) total nominal plastic strain, Ep, (in %) for isothermal specimens only; ii) specimen dimensions, Lo x Do x Do, in mm units; iii) specimen aspect ratio, L/D; iv) initial cross-sectional area, Ao, in mm^2; v) three Schmid factors for the slip systems listed; vi) the Schmid factor ratio

$$N = m(010)[\bar{1}01] / m(111)[\bar{1}01]$$

and vii) the Schmid factor ratio

$$Q = m(111)[1\bar{2}1] / m(111)[\bar{1}01]$$

The specimen identification numbers are along the top. For alloy Al 240, three cylindrical specimens were sectioned from crystal 2 and tested. These specimens have indentification numbers ending with -2R1, -2R2, and -2R3.

190

Al 230 1200°C /120hr /FC

0.2%RSS MPa / ds/de MPa Microprobe: 22.9 a/o Al Analytical: 23.1 a/o Al

Temp °C/K	Al 230 1	Al 230 2	Al 230 3	Al 230 4	Al 230 5	Al 230 6	Al 230 7	Al 230 9	Al 230 10	Al 230 11	AVERAGE
-197/77	-----	-----	-----	-----	-----	-----	-----	-----	32.0	-----	32.0
									780.0		780.0
24/297	34.0	< 0.2%	35.0	53 +	-----	-----	-----	-----	-----	32.0	33.5
	1323.0	Strain	1464.0	1818 +	1856*	-----	-----	-----	-----	1256.0	1348.0
200/473	Cut for	Cut for	Cut for	+ Retested	42.0	-----	Cut for	Specimen	Tested at	41.0	41.5
	TEM	TEM	TEM	after	1797.0		TEM	Bent	-196°	2204.0	2000.0
400/673			700°C/	600°C	81.0	-----	As	During	Annealed	80.0	80.5
			1hr./WQ	Test	4858*		Annealed	-196°C	at 600°C	3519.0	3519.0
600/873			Post Test	163.0	158.0	156.0	1200°C/	Testing	Retested	161.0	159.5
				5192.0	4961.0	5396*	100hr.	Cut for	at -196°C	5099.0	5084.0
700/973				-----	220.0	-----	-----	TEM	Cut for	217.0	218.5
					4871*	-----		-----	TEM	3692.0	3692.0
800/1073					272.0	298.0			-----	-----	285.0
					2967.0	4016*			-----	2967.0	2967.0

* Insufficient Strain / Value not Averaged

	Al 230 1	Al 230 2	Al 230 3	Al 230 4	Al 230 5	Al 230 6	Al 230 7	Al 230 9	Al 230 10	Al 230 11
Ep (%Egr.)	0.930	0.140	0.570	-----	-----	-----	-----	-----	-----	-----
Lo (mm)	12.500	14.700	17.540	12.970	12.690	9.030	-----	12.700	11.700	11.940
Do (mm)	5.140	5.170	5.080	5.190	4.340	2.880	-----	4.950	5.000	4.040
Do (mm)	5.140	5.090	5.090	5.020	4.380	2.910	-----	4.950	5.050	4.140
L/D	2.430	2.870	3.450	2.540	2.910	3.120	-----	2.570	2.330	2.920
Ao (mm**2)	26.390	26.270	25.740	26.060	19.030	8.390	-----	24.503	25.230	16.710
m(111)[-101]	0.429	0.415	0.438	0.415	0.425	0.441	-----	0.425	0.433	0.445
m(010)[-101]	0.038	0.013	0.057	0.013	0.031	0.063	-----	0.031	0.038	0.078
m(111)[1-21]	0.214	0.215	0.201	0.215	0.220	0.202	-----	0.216	0.213	0.177
N	0.088	0.031	0.129	0.031	0.073	0.142	-----	0.074	0.088	0.175
Q	0.498	0.518	0.459	0.518	0.518	0.458	-----	0.508	0.492	0.397

Al 234   AR   (1300°C/1hr)   0.2%RSS MPa   Microprobe: 23.3 a/o Al
                                  ds/de MPa   Analytical: 23.4 a/o Al

Temp °C/K	Al 234 1	Al 234 2	Al 234 3	Al 234 4	Al 234 5			AVERAGE
-197/77	-----	34.0	31.0	32.0	-----			32.3
		842.0	700.0	1120.0				887.0
24/297	31.0	35.0	32.0	32.0	31.0			32.2
	828.0	1297.0	1159.0	1001.0	771.0			1011.0
200/473	-----	43.0	45.0	44.0	-----			44.0
		2546.0	2463.0	2601.0				2537.0
400/673	-----	87.0	94.0	91.0	-----			90.7
		4796.0	3850.0	3968.0				4205.0
600/873	-----	176.0	182.0	179.0	-----			179.0
		5210.0	4411.0	4333.0				4651.0
700/973	-----	233.0	233.0	236.0	-----			234.0
		3767.0	3105.0	4043.0				3638.0
800/1073	-----	-----	-----	-----	-----			-----

	Al 234 1	Al 234 2	Al 234 3	Al 234 4	Al 234 5
Ep (%Egr.)	0.982	-----	-----	-----	0.803
Lo (mm)	11.130	13.070	11.760	11.510	12.340
Do (mm)	3.910	4.170	3.880	3.960	3.990
Do (mm)	3.880	3.890	3.870	4.050	3.970
L/D	2.850	3.250	3.040	2.880	3.100
Ao (mm**2)	15.200	16.200	14.990	16.030	15.820
m(111)[-101]	0.444	0.440	0.442	0.434	0.426
m(010)[-101]	0.062	0.057	0.056	0.038	0.044
m(111)[1-21]	0.206	0.201	0.209	0.214	0.207
N	0.140	0.130	0.127	0.088	0.103
Q	0.464	0.457	0.473	0.493	0.486

Al 240-1 1200°C/100hr/FC
Al 240-2 1200°C/100hr/FC

0.2%RSS MPa
ds/de MPa

Microprobe: 24.2 a/o Al
Analytical: 24.3 a/o Al

(For each temperature the first sub-row is **0.2%RSS MPa** and the second sub-row is **ds/de MPa**.)

Temp °C/K	Al240-1 1	Al240-1 2	Al240-1 3	Al240-2 4	Al240-2 6	Al240-2 9	240-2R1	240-2R2	240-2R3	240-1 AVERAGE	240-2 AVERAGE
-197/77	-----	-----	-----	30.6	28.1	26.6	26.3	33.8+	-----	-----	28.4
	-----	-----	-----	631.0	719.0	734.0	2461*	982.0	-----	-----	695.0
24/297	26.0	25.0	-----	31.5	29.1	28.6	30.8	+ Spec.	33.5	25.3	29.7
	1115.0	1598.0	-----	1020.0	947.0	1094.0	1080.0	was	807.0	1176.0	1020.0
200/473	56 *	43.0	Cut for	44.0	42.0	42.0	-----	Bicrystal	-----	43.0	42.7
	2105.0	1801.0	TEM	2766 *	2613 *	2373.0	-----	Not	-----	1953.0	2373.0
400/673	92.0	89.0	-----	92 (84)†	107 (83)†	97.0	-----	Averaged	-----	90.5	98.7
	4520.0	5210.0	-----	6636.0	8852.0	7718.0	-----		-----	4865.0	7735.0
600/873	187.0	183.0	-----	197.0	-----	201.0				185.0	199.0
	4568.0	5147.0	-----	5977.0	-----	4799.0				4858.0	5388.0
700/973	247.0	245.0	-----	-----	-----	-----				246.0	-----
	3471.0	4037.0	-----	-----	-----	-----				3754.0	-----
800/1073	-----	303.0	-----	-----	-----	-----				303.0	-----
	2836.0	2836.0	-----	-----	-----	-----				2836.0	-----

† Easy Glide
* Insufficient Strain / Value not Averaged

Ep (%Egr.)	Al240-1 1	Al240-1 2	Al240-1 3	Al240-2 4	Al240-2 6	Al240-2 9	240-2R1	240-2R2	240-2R3
Ep (%Egr.)	-----	-----	1.630	-----	-----	-----	-----	-----	-----
Lo (mm)	10.250	10.150	10.000	12.070	13.110	14.240	11.087	11.275	12.383
Do (mm)	3.710	3.580	3.620	4.830	4.790	4.920	4.394	4.432	4.534
Do (mm)	3.610	3.660	3.660	4.570	4.670	4.870	-----	-----	-----
L/D	2.800	2.780	2.740	2.570	2.770	2.910	2.930	2.970	2.730
Ao (mm**2)	13.420	13.350	13.290	22.080	22.370	23.950	15.168	15.432	16.142
m(111)[-101]	0.433	0.431	0.429	0.469	0.464	0.469	0.465	0.465	0.465
m(010)[-101]	0.025	0.044	0.037	0.115	0.093	0.113	0.117	0.117	0.117
m(111)[1-21]	0.223	0.215	0.217	0.160	0.185	0.167	0.171	0.171	0.171
N	0.058	0.102	0.086	0.245	0.200	0.241	0.252	0.252	0.252
Q	0.515	0.499	0.506	0.341	0.399	0.356	0.367	0.367	0.367

Al 270 1100°C/100hr/FC
Samples contain NiAl dendrite cores

0.2%RSS MPa
ds/de MPa

Microprobe: 25.9 a/o Al (matrix only)
Analytical: 26.4 a/o Al

Temp °C/K	Al 270 1	Al 270 2	Al 270 3	Al 270 4	Al 270 5	Al 270 6	Al 270 7	Al 270 8	Al 270 9	Al 270 10	AVERAGE
-197/77	----	----	----	----	----	60.0	57.0	57.0	----	59.6	58.4
						1152.0	1309.0	1423.0		1416.0	1325.0
24/297	96 *	89 *	94 *	98 *	88 *	88.0	82.0	89.0	85.0		86.0
	----	1684 *	4816 *	3961 *	4589 *	----	3548.0	2450.0	2147.0		2715.0
200/473			Cut for TEM			143.0	132.0	146.0			140.0
						----	3145.0	3923.0			3534.0
400/673				228 *		231.0	220.0	232.0	Cut for TEM	Cut for TEM	228.0
				3298 *		----	----	----			----
600/873				377 *		381.0	362.0	373.0			372.0
				5134 *		6262.0	5467.0	6591.0			6107.0
700/973						462.0	434.0	446.0			447.0
						Kinked	Kinked	Kinked			----
800/1073											----
											----

* L/D low / Insufficient strain / Value not averaged

	Al 270 1	Al 270 2	Al 270 3	Al 270 4	Al 270 5	Al 270 6	Al 270 7	Al 270 8	Al 270 9	Al 270 10
Ep (%Egr.)	----	1.09 - 1.5	0.510	----	0.680	----	----	----	1.010	1.023
Lo (mm)	7.930	8.410	10.010	10.790	11.130	12.470	11.840	13.270	12.310	12.910
Do (mm)	4.980	5.590	4.880	5.250	4.910	4.870	4.950	4.860	4.870	4.850
Do (mm)	5.100	4.710	4.980	4.910	4.810	4.840	4.870	4.900	4.910	4.880
L/D	1.570	1.640	2.030	2.130	2.290	2.570	2.420	2.720	2.520	2.650
Ao (mm**2)	25.420	25.810	23.870	25.760	23.610	23.570	24.100	23.810	23.930	23.670
m(111)[-101]	----	0.425	0.422	0.434	0.418	0.465	0.480	0.463	0.443	0.452
m(010)[-101]		0.038	0.013	0.050	0.019	0.099	0.129	0.092	0.063	0.088
m(111)[1-21]	0.206	0.206	0.227	0.212	0.225	0.182	0.163	0.189	0.202	0.185
N	#VALUE!	0.089	0.031	0.115	0.045	0.213	0.269	0.199	0.142	0.195
Q	#VALUE!	0.485	0.538	0.488	0.538	0.391	0.340	0.408	0.456	0.409

194

Sn 241   1250°C/100hr/FC

0.2%RSS MPa
ds/de MPa

Microprobe: 24.1 a/o Al - 0.9 a/o Sn
Analytical: 22.9 a/o Al - 1.1 a/o Sn

Temp °C/K	Sn 241 1	Sn 241 2	Sn 241 3	Sn 241 4	Sn 241 5	Sn 241 6	Sn 241 7	Sn 241 8	AVERAGE
-197/77	-----	-----	-----	34.0	-----	-----	-----	42†	34.0
	-----	-----	-----	645.0	-----	-----	-----	2870†	645.0
24/297	56°	40.0	43.0	-----	40.0	41.0	42.0	†Bicrystal	41.2
	2548°	1461.0	1405.0	-----	1910.0	1653.0	2530 *	Values	1607.0
200/473	°Sample	Cut for	Cut for	-----	96.0	90.0	-----	Not	93.0
	Not	TEM	TEM	-----	3477.0	4960 *	-----	Averaged	3477.0
400/673	Annealed	TEM	700°C/	-----	-----	176.0	-----		176.0
	Values		1hr./WQ	-----	-----	5148.0	-----		5148.0
600/873	Not		Post Test	-----	272.0	272.0	276.0		273.0
	Averaged			-----	5148.0	4777.0	5698.0		5208.0
700/973				-----	340.0	-----	352.0		345.0
	-----	-----	-----	-----	Kinked	-----	Kinked		-----
800/1073	-----	-----	-----	-----					-----
									-----

* Insufficient Strain / Value not Averaged

	Sn 241 1	Sn 241 2	Sn 241 3	Sn 241 4	Sn 241 5	Sn 241 6	Sn 241 7	Sn 241 8
Ep (%Egr.)	0.880	1.210	0.870	0.490	-----	-----	-----	0.650
Lo (mm)	12.140	11.910	12.210	11.970	11.350	12.490	9.080	11.650
Do (mm)	5.020	4.330	4.440	4.150	4.270	4.120	4.140	3.950
Do (mm)	5.120	4.250	4.370	4.350	4.280	4.110	4.190	4.000
L/D	2.420	2.850	2.800	2.820	2.650	3.030	2.180	2.930
Ao (mm**2)	25.350	18.000	19.030	18.050	18.260	16.970	17.350	15.810
m(111)[-101]	0.419	0.427	0.422	0.418	0.426	0.431	0.429	0.418
m(010)[-101]	0.031	0.038	0.038	0.025	0.031	0.038	0.031	0.019
m(111)[1-21]	0.220	0.213	0.213	0.223	0.216	0.214	0.220	0.221
N	0.074	0.089	0.090	0.060	0.073	0.088	0.072	0.045
Q	0.525	0.499	0.505	0.533	0.507	0.497	0.513	0.529

195

Sn 214   1180°C/100hr/FC
Sn 214-SH   Ni3Sn Dispersoid

Microprobe: 21.1 a/o Al - 3.7 a/o Sn
Analytical: 21.0 a/o Al - 3.9 a/o Sn
Microprobe -SH: 21.8 a/o Al - 3.2 a/o Sn (matrix only)

0.2%RSS MPa
ds/de MPa

Temp °C/K	Sn 214 1	-SH 2	-SH 3	-SH 4	Sn 214 5	Sn 214 6	Sn 214 7	Sn 214 8	Sn 214 9	-SH AVG.	AVERAGE
-197/77	86.0	-----	-----	-----	-----	-----	-----	91.0	88.0	-----	88.3
	919.0	-----	-----	-----	-----	-----	-----	1331.0	268†		1125.0
24/297	-----	106.0	109.0	109.0	141.0	137.0	132.0	142.0	-----	108.0	138.0
		5220.0	5387.0	4558.0	2917 *	1853.0	2089.0	2474.0			2139.0
200/473	-----	164.0	-----	-----	218.0	-----	-----	214.0	207.0	164.0	213.0
		4464.0			1959 *			3117.0	3443.0		3280.0
400/673	-----	272.0	-----	-----	317.0 *	Cut for TEM	-----	306.0	313.0 *	272.0	312.0
		3961.0			1167 *			3423.0	2037 *		3423.0
600/873	-----	403.0	-----	-----	434.0	-----	-----	394°	429.0	403.0	431.0
		5981.0			Kinked			°Bending	2037 *		-----
700/973	-----	438.0	-----	-----	-----	-----	-----	403°	494.0	438.0	494.0
		Kinked						°Bending			-----
800/1073	-----	-----	-----	-----	-----	-----	-----	-----	-----	-----	-----

† Easy Glide
* Insufficient Strain Value not Averaged

	Sn 214 1	-SH 2	-SH 3	-SH 4	Sn 214 5	Sn 214 6	Sn 214 7	Sn 214 8	Sn 214 9
Ep (%Egr.)	0.620	-----	0.320	0.420	-----	0.920	1.010	-----	-----
Lo (mm)	12.790	13.800	13.820	13.990	11.380	11.910	12.330	13.170	13.020
Do (mm)	5.180	5.250	5.180	4.880	4.640	4.560	3.580	3.930	4.920
Do (mm)	4.890	4.910	4.690	5.270	4.610	4.530	3.770	3.890	4.930
L/D	2.540	2.720	2.800	2.760	2.460	2.620	3.360	3.370	2.640
Ao (mm**2)	25.300	25.740	24.300	25.610	21.370	20.670	13.490	15.300	24.270
m(111)[-101]	0.449	0.437	0.445	0.443	0.446	0.444	0.440	0.438	0.432
m(010)[-101]	0.070	0.050	0.069	0.064	0.065	0.063	0.057	0.038	0.038
m(111)[1-21]	0.183	0.204	0.199	0.194	0.183	0.202	0.201	0.214	0.214
N	0.156	0.114	0.155	0.144	0.146	0.142	0.130	0.087	0.088
Q	0.408	0.467	0.447	0.438	0.410	0.455	0.457	0.489	0.495

V 241   1200°C/100hr/FC   0.2%RSS MPa   Microprobe: 23.4 a/o Al - 1.0 a/o V
                                   ds/de MPa   Analytical: 23.0 a/o Al - 0.8 a/o V

Temp °C/K	V 241 1	V 241 2	V 241 3	V 241 4	V 241 5	AVERAGE
-197/77	-----	20.3	20.5	21.1	20.8	20.7
	-----	786.0	976.0	585.0	248*	782.0
24/297	24.1	-----	Smashed	28.9	28.2	27.1
	836.0	-----	-----	1346.0	1274.0	1152.0
200/473	-----	-----	70.1*	62.6	59.0	60.8
	Cut for	-----	3618*	2966.0	2370.0	2668.0
400/673	TEM	-----	-----	159.0	155.0	157.0
	-----	-----	-----	4994*	3416.0	3416.0
600/873	-----	-----	-----	293.0	293.0	293.0
	-----	-----	-----	3705*	3045.0	3045.0
700/973	-----	-----	-----	372.0	368.0	370.0
	-----	-----	-----	Kinked	Kinked	-----
800/1073	-----	-----	-----	-----	-----	-----
	-----	-----	-----	-----	-----	-----

* Insufficient Strain / Value not Averaged

	V 241 1	V 241 2	V 241 3	V 241 4	V 241 5
Ep (%Egr.)	0.948	0.550	-----	-----	-----
Lo (mm)	12.590	12.890	12.450	12.550	12.570
Do (mm)	4.850	4.890	4.530	4.470	4.470
Do (mm)	5.050	4.580	4.440	4.470	4.510
L/D	2.540	2.730	2.780	2.810	2.800
Ao (mm**2)	24.510	22.370	20.080	19.990	20.170
m(111)[-101]	0.431	0.437	0.429	0.433	0.433
m(010)[-101]	0.051	0.051	0.039	0.052	0.045
m(111)[1-21]	0.204	0.196	0.202	0.188	0.199
N	0.118	0.117	0.091	0.120	0.104
Q	0.473	0.449	0.471	0.434	0.460

V 214 1200°C/100hr/FC 0.2%RSS MPa Microprobe: 20.8 a/o Al - 4.0 a/o V
ds/de MPa Analytical: 21.4 a/o Al - 2.9 a/o V

Temp °C/K	V 214 1	V 214 2	V 214 3	V 214 4	V 214 5	AVERAGE
-197/77	25.2	25.7	26.3	27.0	-----	26.0
	-----	450.0	590.0	614.0	-----	551.0
24/297	34.6	34.2	39 +	41 +	-----	34.4
	1873.0	1505.0	2288 +	2687 +	-----	1689.0
200/473	86.2	-----		93.5	-----	89.8
	7897*	Cut for		3104.0	-----	3104.0
400/673	183.0*	TEM	187.0	185.0	-----	185.0
	3358*		2400.0	3279.0	-----	2839.0
600/873	296.0	-----	-----	300.0	296.0	297.6
	2997.0	-----	-----	2652.0	3788*	2824.0
700/973	363.0	-----	-----	-----	343.0	353.0
	2575.0	-----	-----		5311*	2575.0
800/1073	-----	-----	-----	-----	-----	-----

* Insufficient Strain / Value not Averaged
+ Test Temperature 305K

	V 214 1	V 214 2	V 214 3	V 214 4	V 214 5
Ep (%Egr.)	-----	1.390	-----	-----	-----
Lo (mm)	11.630	11.700	8.620	8.938	6.985
Do (mm)	3.960	3.950	2.943	2.941	2.914
Do (mm)	3.890	3.940	2.858	2.989	2.969
L/D	2.960	2.960	2.970	3.010	2.370
Ao (mm**2)	15.440	15.570	8.412	8.793	8.651
m(111)[-101]	0.438	0.432	0.432	0.441	0.446
m(010)[-101]	0.072	0.045	0.045	0.064	0.074
m(111)[1-21]	0.178	0.199	0.203	0.194	0.204
N	0.164	0.104	0.103	0.145	0.166
Q	0.406	0.461	0.469	0.440	0.457

+ Test Temperature 305K

APPENDIX B

COMPRESSION SPECIMEN ORIENTATIONS

Specimen ID	Angles (Deg.) [-100]	[010]	[001]
Al 230 1	89.0	87.0	3.0
Al 230 2	88.0	89.0	4.0
Al 230 3	88.5	85.5	4.5
Al 230 4	88.0	89.0	4.0
Al 230 5	89.5	87.5	2.0
Al 230 6	89.0	85.0	5.0
Al 230 7	-----	-----	-----
Al 230 9	89.0	87.5	5.0
Al 230 10	89.0	87.0	5.5
Al 230 11	86.5	84.0	6.5
Al 234 1	89.5	85.0	5.0
Al 234 2	88.5	85.5	4.5
Al 234 3	89.5	85.5	4.0
Al 234 4	89.0	87.0	3.0
Al 234 5	88.5	86.5	4.0
Al 240-1 1	89.5	88.0	2.5
Al 240-1 2	89.5	86.5	4.0
Al 240-1 3	89.5	87.0	3.0
Al 240-2 4	87.0	81.0	9.5
Al 240-2 6	89.0	82.5	7.5
Al 240-2 9	88.0	81.0	9.0
Al 240-2R 1	89.0	80.5	9.5
Al 240-2R 2	89.0	80.5	9.5
Al 240-2R 3	89.0	80.5	9.5
Al 270 1	-----	-----	-----
Al 270 2	88.0	87.0	4.0
Al 270 3	89.5	89.0	2.0
Al 270 4	89.5	86.0	4.0
Al 270 5	89.5	88.5	1.5
Al 270 6	89.0	82.0	8.0
Al 270 7	89.0	79.5	10.5
Al 270 8	89.5	82.5	7.5
Al 270 9	89.0	85.0	5.5
Al 270 10	88.5	83.0	7.0

Specimen ID	Angles (Deg.)		
	[-100]	[010]	[001]
Sn 241 1	89.5	87.5	3.0
Sn 241 2	89.0	87.0	3.5
Sn 241 3	89.0	87.0	3.0
Sn 241 4	89.5	88.0	2.0
Sn 241 5	89.0	87.5	2.5
Sn 241 6	89.0	87.0	3.0
Sn 241 7	87.5	89.5	3.0
Sn 241 8	89.0	88.5	1.5
Sn 214 1	87.0	84.5	6.0
Sn 214-SH 2	88.5	86.0	4.5
Sn 214-SH 3	89.0	84.5	5.0
Sn 214-SH 4	88.0	85.0	5.5
Sn 214 5	86.5	85.0	6.0
Sn 214 6	89.0	85.0	5.0
Sn 214 7	88.5	85.5	5.0
Sn 214 8	89.0	87.0	2.5
Sn 214 9	89.0	87.0	3.0
V 241 1	88.5	86.0	4.5
V 241 2	87.5	86.0	4.5
V 241 3	87.5	87.0	4.0
V 241 4	86.5	86.0	5.5
V 241 5	87.5	86.5	4.0
V 214 1	86.0	84.5	6.5
V 214 2	87.5	86.5	3.0
V 214 3	88.0	87.0	6.5
V 214 4	88.0	85.0	9.5
V 214 5	90.0	84.0	6.0

APPENDIX C

ANALYSIS OF SLIP TRACES IN DAMAGED THIN FOILS

In Chapter 3, a unique deformation substructure which is believed to be an artifact of deformation of thin-foil samples was reported to exist when either very thin specimen blanks were used in foil preparation or thin-foil samples were damaged after thinning. A similar thin-foil artifact was reported to occur in "cracked" specimens of polycrystalline Ni_3Al according to Veyssière et al.[1]; however, no specific details were provided. As shown in Fig. C.1, extended stacking-fault coupled dislocations were found in alloy Sn 241 which was deformed at room temperature, annealed at 700 °C for 1 hour and water quenched. The photomicrogragh in Fig. C.1(a) is from a sample prepared using a 0.2 mm thick specimen blank, thinned by hand grinding on 600 grit emery paper prior to electropolishing. The photo in Fig. C.1(b) shows the $a_0<110>$-type dislocations of both edge and screw character (points A and B, respectively) which were the the overwhelming feature in all of the alloys examined in this study. This sample was prepared from the same crystal of alloy Sn 241 (heat treated after testing) as the sample in Fig. C.1(a); however, a 0.3 mm-thick specimen blank was used.

Extended stacking-fault-coupled dislocations were also found in thin foil specimens which were damaged in handling, even though thick specimen blanks were used for thin-foil preparation. Figure C.2 shows several slip traces lying on ($1\bar{1}1$) in a region of a thin foil of alloy Al 230 which was damaged with tweezers [damage point shown below the open arrow in Fig. C.2(a)] after being thinned by electropolishing. Following the line of the slip traces toward the edge of the thin foil (upper right of Figure) reveals an off-set or slip step at the edge of the foil [solid arrow in Figs. C.2(a) and C.2(b)]. A detailed

201
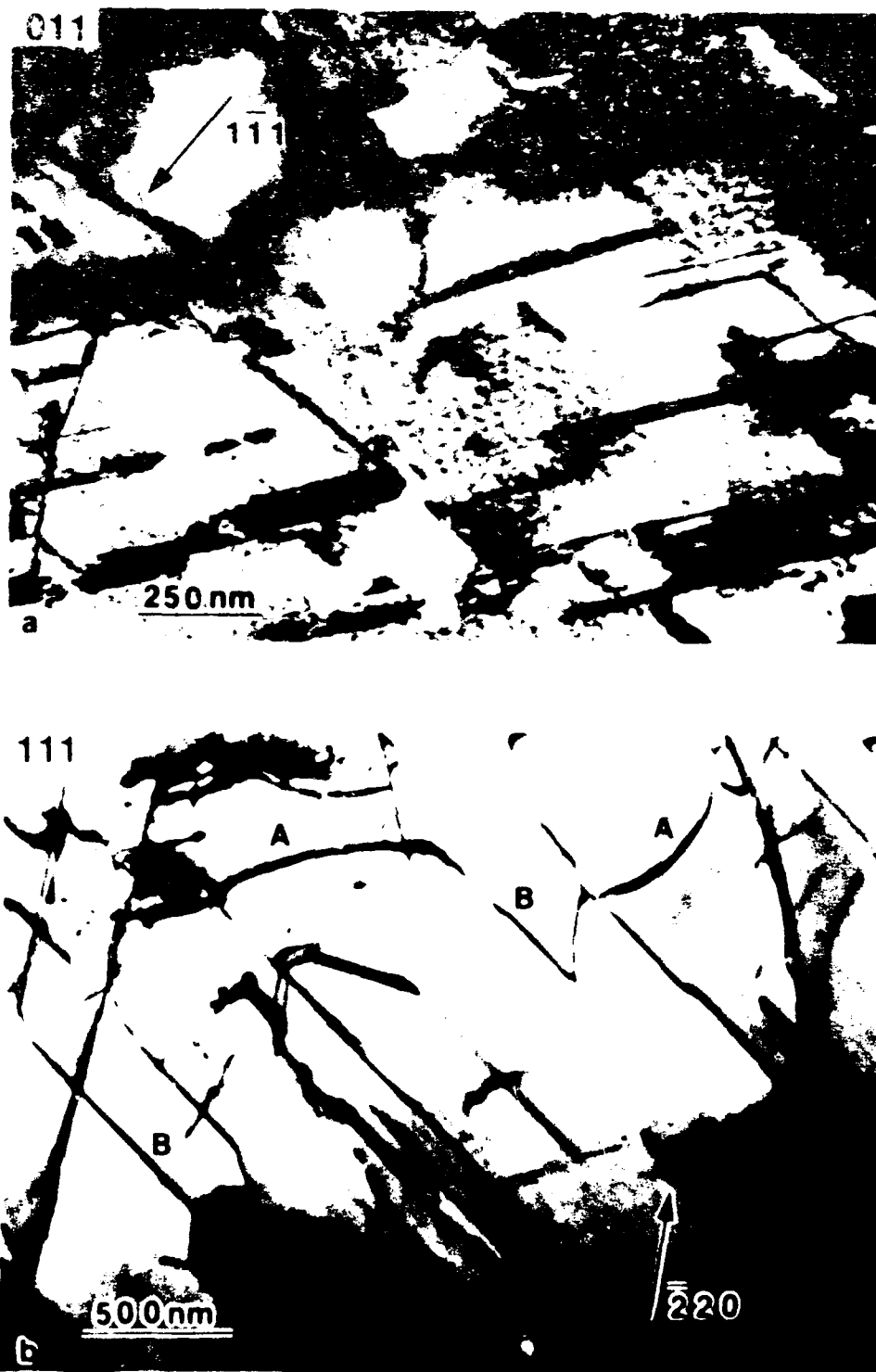
Fig. C.1 Bright-field images from alloy Sn 241 deformed at 24 °C, annealed at 700 °C, and water quenched; a) foil prepared from 0.2 mm thick blank; extended pairs of $\mathbf{b} = a_0/3<11\bar{2}>$ dislocations visible; and b) foil prepared from 0.3 mm thick blank; $\pm a_0<10\bar{1}>$dislocations visible, edge components, A, and straight screw components B.

202

Fig. C.2 Bright-field images from alloy Al 230 deformed at 24 °C, annealed at 700 °C, and water quenched, foil damaged by handling; a) pairs of $\mathbf{b} = a_0/3<11\bar{2}>$ dislocations extending from damaged area below open arrow, slip step at solid arrow; and b) same area, $(1\bar{1}1)$ slip planes viewed edge-on.

analysis was performed on the dislocations within several slip bands having a higher dislocation density due to their being located in thicker regions of the foil. One portion of a slip band which was analyzed is shown at low magnification in Fig. C.3(a). Dislocations with Burgers vectors equal to $\pm a_0[10\bar{1}]$ are invisible in this image. The slip band is viewed edge-on at higher magnification in Fig. C.3(b), revealing that the slip plane is $(1\bar{1}1)$. The Burgers vectors of the dissociated dislocations are given by the analysis presented in Figs. C.3(b) through C.3(d) and C.4. Two types of near edge $a_0<110>$ dislocations were observed. The majority of the dislocations in the slip band were invisible for $\pm g(020)$ [Figs. C.4(c) and C.4(d)] and for $\pm g(1\bar{3}1)$ (not shown), indicating that their Burgers vector is $a_0[10\bar{1}]$. These are dislocations having the same contrast as the one indicated by the curved arrow in Figs. C.3 and C.4. The dislocation indicated by the pair of large arrows in each photo is invisible for $\pm g(002)$ [Figs. C.3(c) and C.3(d)] and $\pm g(\bar{1}11)$ (not shown), suggesting a Burgers vector of $a_0[110]$.

In Figs. C.3(c) and C.3(d), fault-coupled dissociated dislocations can be clearly observed. The stacking faults exhibit symmetric fringe contrast at the intersections with the foil surfaces. Further, the fault fringes are invisible for two beam images formed with $\pm g(022)$ (Fig. C.4), $g(20\bar{2})$ and $g(\bar{1}31)$, indicating that the fault vector is $\pm a_0/3(1\bar{1}1)$. When viewed by centered dark-field imaging, with the deviation parameter, s, set equal to zero, one of the outer finges appeared as a bright fringe, and the direction of g pointed toward the light fringe. For the partial dislocation indicated by the pair of arrowheads in Figs. C.3 and C.4, the characteristic contrast features for $a_0/3<121>$-type partial dislocations are observed[2]. For $g(002)$, $g(00\bar{2})$, $g(0\bar{2}0)$, and $g(020)$ [Figs. C.3(c) and C.3(d) and Figs. C.4(c) and C.4(d)] the partial is alternatively invisible and visible, with the partial exhibiting the characteristic white fringe of $g \cdot b = +4/3$ for $g(0\bar{2}0)$. The partial is visible for $\pm g(022)$ in Figs C.4(a) and C.4(b). This contrast behavior indicates that the partial has a Burgers vector of $a_0/3[\bar{1}\,\bar{2}\,\bar{1}]$. The partial dislocations indicated by the pairs of

204
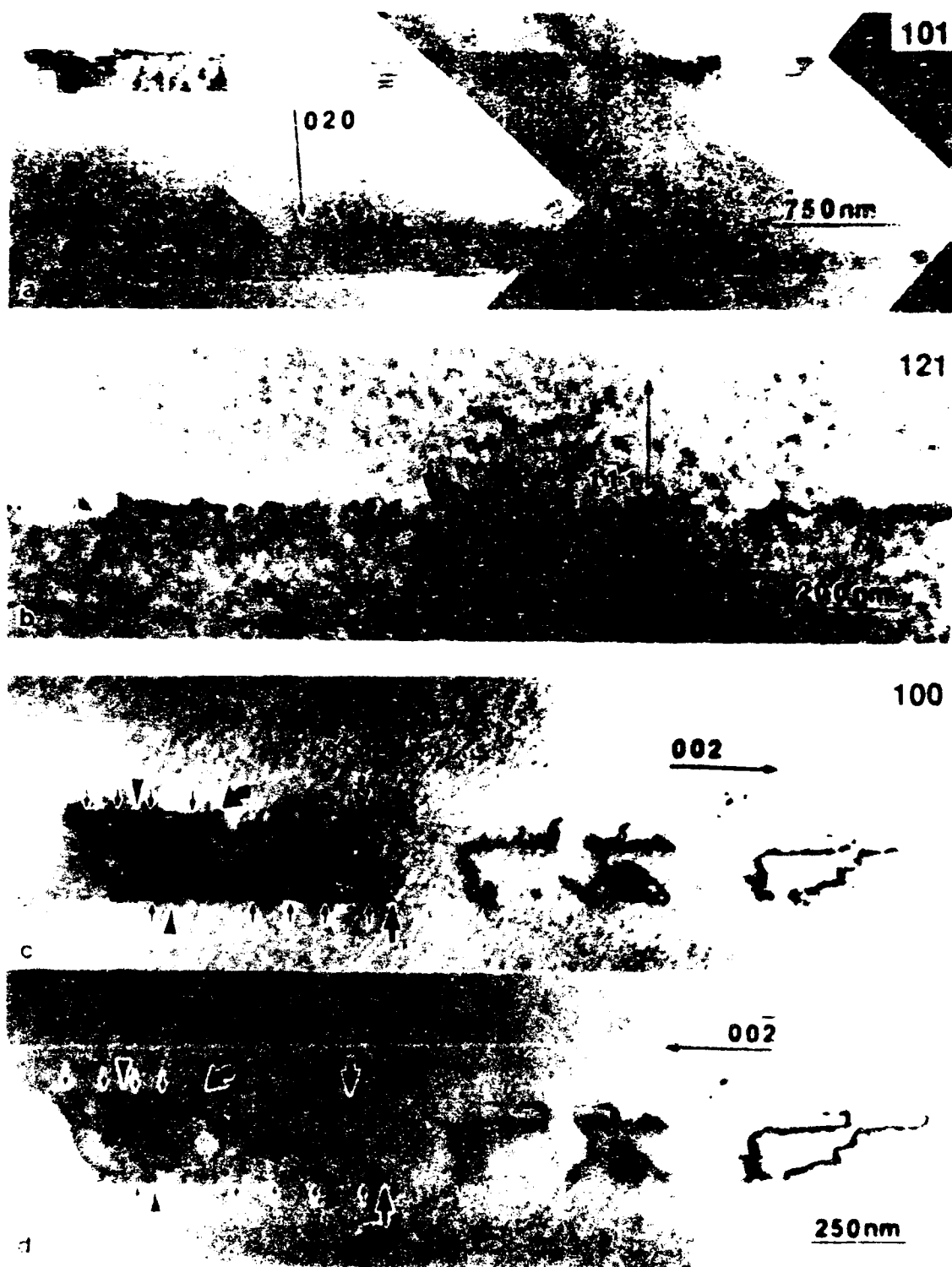
Fig. C.3 Bright-field images from alloy Al230 deformed at 24 °C, annealed at 700 °C,
and water quenched; a) low magnification view of slip bands; b) slip band on
$(1\bar{1}1)$ viewed edge-on; c) and d) dislocations with $\mathbf{b} = a_0[110]$ invisible at large
arrows, $\mathbf{b} = a_0[10\bar{1}]$ at curved arrows, $\mathbf{b} = a_0/3[\bar{1}\,\bar{2}\,\bar{1}\,]$ invisible at arrow heads
in c), visible at arrow heads in d), and $\mathbf{b} = a_0/3[\bar{2}\,\bar{1}\,1]$ visible at small arrows in
c), invisible at small arrows in d).

205
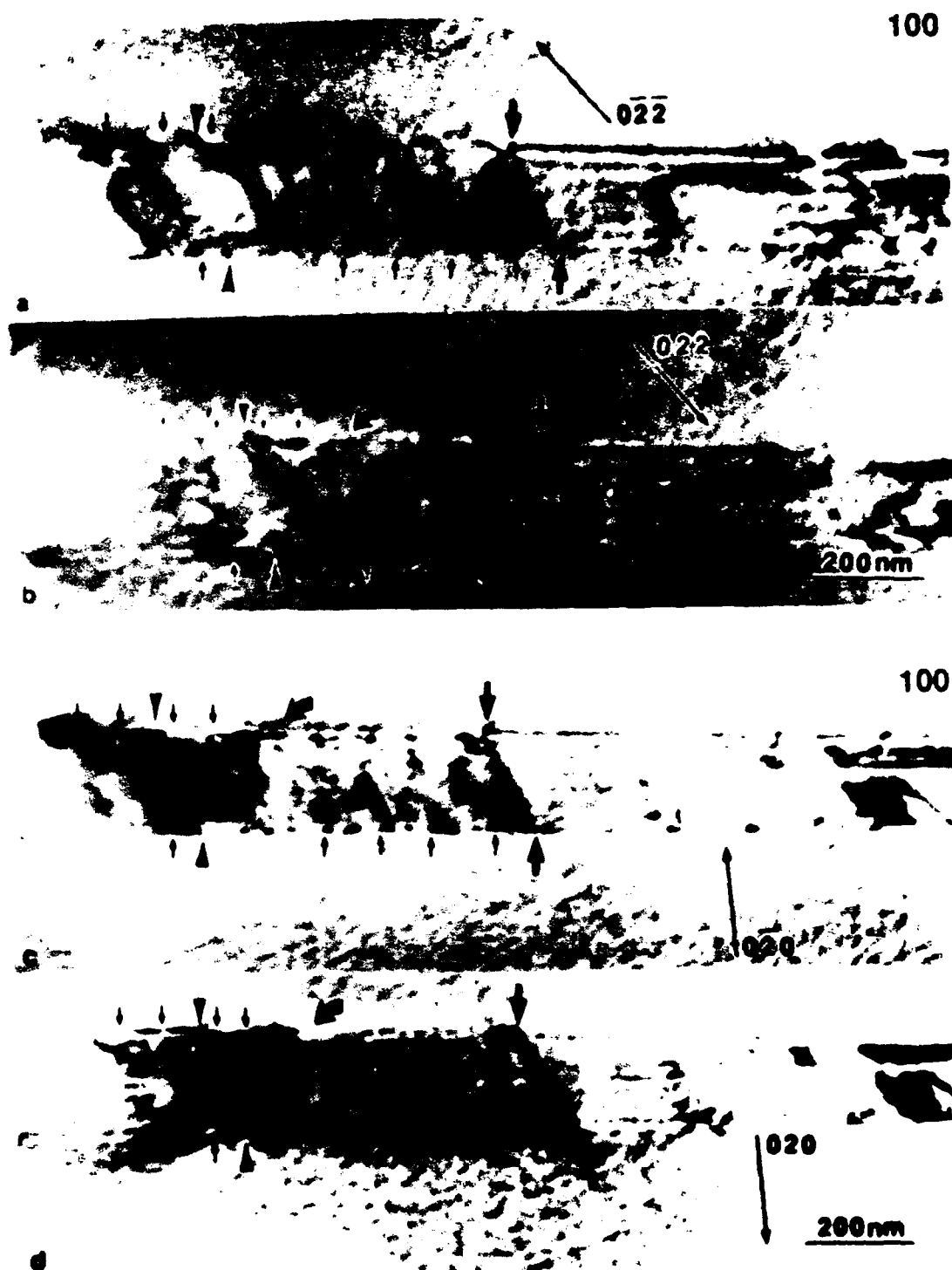
Fig. C.4 Bright-field images from alloy Al230 deformed at 24 °C, annealed at 700 °C, and water quenched; a) and b) $b = a_0/3[\bar{2}\,\bar{1}\,1]$ partials invisible at small arrows, $b = a_0[110]$, $b = a_0[10\bar{1}]$, and $b = a_0/3[\bar{1}\,\bar{2}\,\bar{1}]$ dislocations visible; c) $b = a_0/3[\bar{1}\,\bar{2}\,\bar{1}]$ dislocation shows white fringe at arrow heads, $b = a_0[10\bar{1}]$ dislocations invisible; and d) dislocations with $b = a_0/3[\bar{2}\,\bar{1}\,1]$ invisible at small arrows

206

smallest arrows in Figs. C.3 and C.4 exhibit similar contrast to that of the $a_0/3<121>$-type partials identified above; however, the values of $g \cdot b$ are $+2/3$, $-2/3$, $+2/3$, and $-2/3$ for Figs. C.3(c) and C.3(d) and Figs. C.4(c) and C.4(d), respectively. These partials are invisible for $\pm g(022)$ in Figs. C.4(a) and C.4(b). Therefore, these partials have a Burgers vector of $a_0/3[\bar{2}\,\bar{1}\,1]$. Collectively, the analysis shows that superlattice intrinsic stacking faults (SISF's) are formed by dislocation reactions of the following type:

$$a_0[\bar{1}\,0\,1] \rightarrow a_0/3[\bar{2}\,1\,1] + a_0/3[\bar{1}\,\bar{1}\,2] \qquad [C.1]$$
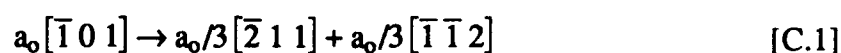
Finally, note that the dislocations indicated by the small arrow pairs throughout these figures often exhibit the dissociation reaction starting at the surfaces of the thin foil. Such artifacts occurring due to relaxations in thin foils have been analyzed by Hazzledine et al.[3] These investigators have suggested that the reactions occur spontaneously in thin foils, where elastic interactions between the dislocation and the surface-image stress tend to cause the dislocations to rotate toward the screw orientation. However, the dissociations observed here and under similar conditions, as reported by Barker et al.,[4,5] do not always have their origin or widest extension at the free surfaces and, therefore, may be an artifact of the *in situ* nature of the deformation or of reactions between dislocations in densely populated slip bands such as these.

1. P. Veyssière, J. Douin, and P. Beauchamp: *Phil. Mag.A*, 1985, vol. 51, pp. 469-83.

2. B.H. Kear, G.R. Leverant, and J.M. Objak: *Trans. ASM*, 1969, vol. 62, pp. 639-50.

3. P.M. Hazzledine, H.P. Karnthaler, and E. Wintner: *Phil. Mag.*, 1975, vol. 32, pp. 81-97.

4. I. Baker, E.M. Schulson, and J.A. Horton: *Acta Metall.*, 1987, vol. 35, pp. 1533-41.

5. I. Baker, J. A. Horton, and E.M. Schulson: *Phil. Mag. Ltr.*, 1987, vol. 55, pp. 3-6.

APPENDIX D

DISSOCIATION DISTANCES AND APB ENERGIES

The tables in this appendix give the individual dislocation dissociation distances used to construct the graphs in Chapter 4. The alloy identification number, a value for the elastic-energy coefficient for the screw orientation (K_s), and the magnitude of the $a_0/2[101]$ Burgers vector can be found in the header on each page. These values were used to convert the dissociation distances recorded on that page to APB energies. The columns on the left-hand side of the table contain the plate serial numbers from which a particular set of measurements were made. The original plate magnification is given in the column marked "Magnification" along with the magnification factor (Å/mm) for the photographic prints used. The dissociation distances measured from the photographic prints are given, *in mm* units, for spacings on both the cube planes (d[010]) and the octahedral planes (d[111]) in the columns labeled "Measurement." The "Angle Theta" is measured between the line direction **u** and the Burgers vector for dislocations dissociated in the (111) plane. Screw dislocations lying in (010) are listed as Theta = 0 deg. Actual dislocation spacings are contained (in Å units) in the columns labeled "Spacing."

The value for K(theta) shown in the table was determined by fitting the following elliptical function to the inverse Wulff plots for the elastic-energy coefficients given by Yoo:[59]

$$K(\theta) = K_s \left[\left(\frac{a^2 b^2}{a^2 \sin^2 \theta + b^2 \cos^2 \theta} \right)^{\frac{1}{2}} \right]^{-1}$$

where a = 0.608 and b = 1.0 for Ni_3Al at room temperature. Using these values for K(θ), the APB energies were computed from anisotropic elasticity as described in Chapter 4.

208

ALLOY: Al230
DEFORMATION TEMPERATURE: 297 K
HEAT TREATMENT: None

Ks (GPa) = 68.47
b (Å) = 2.522

PLATE SERIES NUMBERS				Magnification		Measurement		Angle Theta	Spacing (Å)		Modulus K(theta)	APB Energy (mJm-1)	
Beam Directions				plate (K)	print (Å/mm)	d[010] (mm)	d[111] (mm)	(deg.)	[010]	[111]	(GPa)	[010]	[111]
<101>	<111>	<121>	<010>										
5495	5492	----	5485/5488	46.0	82.6	0.75	----	0	62.0	----	68.47	111.8	----
5495	5492	----	5485/88	46.0	82.6	0.85	----	0	70.2	----	68.47	98.7	----
5495	5492	----	5485/88	46.0	82.6	0.85	----	0	70.2	----	68.47	98.7	----
5495	5492	----	5485/88	46.0	82.6	0.90	----	0	74.3	----	68.47	93.2	----
5495	5492	----	5485/88	46.0	82.6	0.77	----	0	63.6	----	68.47	108.9	----
5495	5492	----	5485/88	46.0	82.6	----	0.51	15	----	42.1	72.27	----	173.6
----	6394	----	----	77.0	45.7	----	1.60	90	----	73.1	112.62	----	155.8
----	6394	----	----	77.0	45.7	----	1.45	80	----	66.3	111.54	----	170.3
----	6394	----	----	77.0	45.7	----	1.35	61	----	61.7	103.94	----	170.5
5533	5523	5527	5530	62.0	40.7	1.60	----	0	65.1	----	68.47	106.4	----
5533	5523	5527	5530	62.0	40.7	----	1.13	16	----	46.0	72.77	----	160.1
5533	5523	5527	5530	62.0	40.7	----	1.25	42	----	50.9	90.92	----	180.8
5447	5470	----	5458	62.0	58.8	1.20	----	0	70.6	----	68.47	98.2	----
5496	5491	----	5487	62.0	54.9	1.25	----	0	68.6	----	68.47	101.0	----
5496	5491	----	5487	46.0	54.9	1.12	----	0	61.5	----	68.47	112.7	----
5496	5491	----	5487	46.0	54.9	1.15	----	0	63.1	----	68.47	109.7	----
5496	5491	----	5487	46.0	54.9	----	0.75	19	----	41.2	74.40	----	182.8
5496	5491	----	5487	46.0	54.9	----	0.90	18	----	49.4	73.83	----	151.2
5496	5491	----	5487	46.0	54.9	----	0.80	13	----	43.9	71.36	----	164.4
5496	5491	----	5487	46.0	54.9	----	1.10	61	----	60.4	103.94	----	174.2
5496	5491	----	5487	46.0	54.9	----	0.95	41	----	52.2	90.16	----	174.9
5496	5491	----	5487	46.0	54.9	----	0.77	22	----	42.3	76.22	----	182.5
5447	5470	----	5458	62.0	58.8	1.20	----	0	70.6	----	68.47	98.2	
5447	5470	----	5458	62.0	58.8	1.12	----	0	65.9	----	68.47	105.2	--
5447	5470	----	5458	62.0	58.8	----	0.80	15	----	47.0	72.27	----	155.?

ALLOY: AI 230
DEFORMATION TEMPERATURE: 297 K
HEAT TREATMENT: 700°C/1hr/WQ Post Deformation

Ks (GPa) = 57.00
b (Å) = 2.522

PLATE SERIES NUMBERS				Magnification		Measurement		Angle Theta (deg.)	Spacing (Å)		Modulus K(theta) (GPa)	APB Energy (mJm-1)	
Beam Directions				plate (K)	print (Å/mm)	d[010] (mm)	d[111] (mm)		[010]	[111]		[010]	[111]
<101>	<111>	<121>	<010>										
8106	8120	---	8117	77.0	52.4	1.27	---	0	66.5	---	57.00	86.7	---
8106	8120	---	8117	77.0	52.4	1.21	---	0	63.4	---	57.00	91.0	---
8106	8120	---	8117	77.0	52.4	1.38	---	0	72.3	---	57.00	79.8	---
8106	8120	---	8117	77.0	52.4	1.16	---	0	60.8	---	57.00	94.9	---
8106	8120	---	8117	77.0	52.4	---	1.10	14	---	57.6	60.20	---	105.7
8106	8120	---	8117	77.0	52.4	---	1.00	31	---	52.4	70.35	---	135.9
8103	8121	---	8114	77.0	52.4	---	0.95	24	---	49.8	65.65	---	133.4
8103	8121	---	8114	77.0	52.4	---	1.30	48	---	68.1	82.39	---	122.4
8103	8121	---	8114	77.0	52.4	---	1.30	48	---	68.1	82.39	---	122.4
8103	8121	---	8114	77.0	52.4	---	1.00	21	---	52.4	63.81	---	123.2
8103	8121	---	8114	77.0	52.4	---	1.35	58	---	70.7	88.65	---	126.8
8103	8121	---	8114	77.0	52.4	---	1.22	39	---	63.9	76.07	---	120.4
8104	8122/23	---	8116	77.0	52.4	1.10	---	0	57.6	---	57.00	100.1	---
35649	37124	37116	35640	50.0	200.0	0.34	---	0	68.0	---	57.00	84.8	---
35649	37124	37116	35640	50.0	200.0	0.27	---	0	54.0	---	57.00	106.8	---
8249/53	8259	---	8258/55	77.0	46.1	---	1.20	18	---	55.3	62.14		113.7

ALLOY: Al240
DEFORMATION TEMPERATURE: 297 K
HEAT TREATMENT: None

Ks (GPa) = 68.47
b (Å) = 2.524

| PLATE SERIES NUMBERS Beam Directions | | | | Magnification | | Measurement | | Angle Theta | Spacing (Å) | | Modulus K(theta) | APB Energy (mJm-1) | |
<101>	<111>	<121>	<010>	plate (K)	print (Å/mm)	d[010] (mm)	d[111] (mm)	(deg.)	[010]	[111]	(GPa)	[010]	[111]
8829	8826	8825	8820	77.0	44.1	1.28	----	0	56.4	----	68.47	123.0	----
8829	8826	8825	8820	77.0	44.1	1.33	----	0	58.7	----	68.47	118.4	----
8829	8826	8825	8820	77.0	44.1	1.33	----	0	58.7	----	68.47	118.4	----
8829	8826	8825	8820	77.0	44.1	1.28	----	0	56.4	----	68.47	123.0	----
8829	8826	8825	8820	77.0	44.1	----	1.30	48	----	57.3	95.41	----	168.8
8829	8826	8825	8820	77.0	44.1	----	1.20	26	----	52.9	78.89	----	151.2
8829	8826	8825	8820	77.0	44.1	----	1.35	48	----	59.5	95.41	----	162.5
8829	8826	8825	8820	77.0	44.1	----	1.15	26	----	50.7	78.89	----	157.8
8829	8826	8825	8820	77.0	44.1	----	1.10	35	----	48.5	85.55	----	178.9
8829	8826	8825	8820	77.0	44.1	----	1.50	62	----	66.2	104.50	----	160.2
9101	9087	9012	9002	77.0	45.4	1.25	----	0	56.8	----	68.47	122.4	----
9101	9087	9012	9002	77.0	45.4	1.30	----	0	59.0	----	68.47	117.7	----
9101	9087	9012	9002	77.0	45.4	1.30	----	0	59.0	----	68.47	117.7	----
9101	9087	9012	9002	77.0	45.4	1.35	----	0	61.3	----	68.47	113.3	----
9101	9087	9012	9002	77.0	45.4	1.30	----	0	59.0	----	68.47	117.7	----
9108	9093/88	9016/45	9004/05	77.0	45.7	1.25	----	0	57.1	----	68.47	121.6	----
9108	9093/88	9016/45	9004/05	77.0	45.7	1.27	----	0	58.0	----	68.47	119.7	----
9108	9093/88	9016/45	9004/05	77.0	45.7	1.25	----	0	57.1	----	68.47	121.6	----
9108	9093/88	9016/45	9004/05	77.0	45.7	1.15	----	0	52.6	----	68.47	132.1	----
9108	9093/88	9016/45	9004/05	77.0	45.7	1.12	----	0	51.2	----	68.47	135.7	----
9108	9093/88	9016/45	9004/05	77.0	45.3	----	0.95	12	----	43.0	70.95	----	167.2
9108	9093/88	9016/45	9004/05	77.0	45.3	----	0.98	12	----	44.4	70.95	----	162.1
9108	9093/88	9016/45	9004/05	77.0	45.3	----	1.00	22	----	45.3	76.22	----	170.7
9108	9093/88	9016/45	9004/05	77.0	45.3	----	1.10	22	----	49.8	76.22	----	155.1
9108	9093/88	9016/45	9004/05	77.0	45.3	----	1.00	12	----	45.3	70.95	----	158.8

ALLOY: Al 270
DEFORMATION TEMPERATURE: 297 K
HEAT TREATMENT: None

Ks (GPa) = 68.47
b (Å) = 2.528

| PLATE SERIES NUMBERS Beam Directions | | | | Magnification | | Measurement | | Angle Theta | Spacing (Å) | | Modulus K(theta) | APB Energy (mJm-1) | |
<101>	<111>	<121>	<010>	plate (K)	print (Å/mm)	d[010] (mm)	d[111] (mm)	(deg.)	{010}	{111}	(GPa)	[010]	[111]
0620	0653	0644	0639	77.0	52.5	0.80	----	0	42.0	----	68.47	165.8	----
0620	0653	0644	0639	77.0	52.5	0.75	----	0	39.4	----	68.47	176.8	----
0620	0653	0644	0639	77.0	52.5	0.75	----	0	39.4	----	68.47	176.8	----
0620	0653	0644	0639	77.0	52.5	0.78	----	0	41.0	----	68.47	170.0	----
0620	0653	0644	0639	77.0	52.5	0.75	----	0	39.4	----	68.47	176.8	----
----	0657	----	0625	77.0	51.4	0.70	----	0	36.0	----	68.47	193.5	----
----	0657	----	0625	77.0	51.4	0.70	----	0	36.0	----	68.47	193.5	----
----	0657	----	0625	77.0	51.4	0.78	----	0	40.1	----	68.47	173.7	----
----	0657	----	0625	77.0	51.4	0.72	----	0	37.0	----	68.47	188.1	----
----	0657	----	0625	77.0	51.6	----	0.80	26	----	41.3	78.89	----	194.3
----	0657	----	0625	77.0	51.6	----	0.78	26	----	40.2	78.89	----	199.3
----	0657	----	0625	77.0	51.6	----	0.75	20	----	38.7	74.99	----	197.0
----	0657	----	0625	77.0	51.6	----	0.70	20	----	36.1	74.99	----	211.1
----	0657	----	0625	77.0	51.6	----	0.65	3	----	33.5	68.63	----	208.1
----	0657	----	0625	77.0	51.6	----	0.75	18	----	38.7	73.83	----	194.0
----	0657	----	0625	77.0	51.6	----	0.70	18	----	36.1	73.83	----	207.9
0612	0662/61	----	0630	77.0	53.1	----	0.80	32	----	42.5	83.26	----	199.3
0612	0662/61	----	0630	77.0	53.1	----	0.85	32	----	45.1	83.26	----	187.6
0612	0662/61	----	0630	77.0	53.1	----	0.95	38	----	50.4	87.85	----	177.1
0616	0687/88	----	0634	77.0	53.1	----	1.10	54	----	58.4	99.60	----	173.4
0616	0687/88	----	0634	77.0	53.1	----	0.90	32	----	47.8	83.26	----	177.2
0616	0687/88	----	0634	77.0	53.1	----	0.85	32	----	45.1	83.26	----	187.6
0607	0685	0677	0638	77.0	51.2	0.90	----	0	46.1	----	68.47	151.1	----
0607	0685	0677	0638	77.0	51.2	0.85	----	0	43.5	----	68.47	160.0	----
0607	0685	0677	0638	77.0	51.2	0.85	----	0	43.5	----	68.47	160.0	----

ALLOY: Al 270 (cont.)
DEFORMATION TEMPERATURE: 297 K
HEAT TREATMENT: None

Ks (GPa) =   68.47
b (Å) =   2.528

| PLATE SERIES NUMBERS Beam Directions | | | | Magnification | | Measurement | | Angle Theta | Spacing (Å) | | Modulus K(theta) | APB Energy (mJm-1) | |
<101>	<111>	<121>	<010>	plate (K)	print (Å/mm)	d[010] (mm)	d[111] (mm)	(deg.)	[010]	[111]	(GPa)	[010]	[111]
0607	0685	0677	0638	77.0	51.2	0.80	----	0	41.0	----	68.47	170.0	----
0607	0685	0677	0638	77.0	51.2	0.82	----	0	42.0	----	68.47	165.8	----
0607	0685	0677	0638	77.0	51.2	0.78	----	0	39.9	----	68.47	174.3	----
0607	0685	0677	0638	77.0	51.2	----	1.02	60	----	52.2	103.36	----	201.3
0607	0685	0677	0638	77.0	51.2	----	1.00	60	----	51.2	103.36	----	205.3
0617	0659	----	0628/36	77.0	52.9	----	0.95	42	----	50.3	90.92	----	184.0
0617	0659	----	0628/36	77.0	52.9	----	0.90	42	----	47.6	90.92	----	194.2
0617	0659	----	0628/36	77.0	52.9	----	0.95	44	----	50.3	92.44	----	187.1
0617	0659	----	0628/36	77.0	52.9	----	0.95	44	----	50.3	92.44	----	187.1
0617	0659	----	0628/36	77.0	52.9	----	1.10	54	----	58.2	99.60	----	174.1
0617	0659	----	0628/36	77.0	52.9	----	1.07	54	----	56.6	99.60	----	178.9
0617	0659	----	0628/36	77.0	52.9	----	1.15	74	----	60.8	109.89	----	183.7
0617	0659	----	0628/36	77.0	52.9	----	1.20	74	----	63.5	109.89	----	176.0
0617	0659	----	0628/36	77.0	52.9	----	0.80	4	----	42.3	68.75	----	165.2
0617	0659	----	0628/36	77.0	52.7	0.85	----	0	44.8	----	68.47	155.4	----
0617	0659	----	0628/36	77.0	52.9	----	0.78	22	----	41.3	76.22	----	187.8
0617	0659	----	0628/36	77.0	52.9	----	0.75	22	----	39.7	76.22	----	195.4
0617	0659	----	0628/36	77.0	52.9	----	0.88	40	----	46.6	89.39	----	195.3
0617	0659	----	0628/36	77.0	52.9	----	0.86	40	----	45.5	89.39	----	199.8
0617	0659	----	0628/36	77.0	52.9	----	0.82	40	----	43.4	89.39	----	209.6
0725	0737	0708	0713	77.0	51.1	----	0.90	11	----	46.0	70.56	----	156.0
0725	0737	0708	0713	77.0	51.1	----	1.00	60	----	51.1	103.36	----	205.7
0725	0737	0708	0713	77.0	51.1	----	1.00	60	----	51.1	103.36	----	205.7
0725	0737	0708	0713	77.0	51.1	----	0.82	25	----	41.9	78.20	----	189.8
0725	0737	0708	0713	77.0	51.1	0.95	----	0	48.5	----	68.47	143.4	----

213

ALLOY: Sn 241
DEFORMATION TEMPERATURE: 297 K
HEAT TREATMENT: None

Ks (GPa) = 68.47
b (Å) = 2.531

PLATE SERIES NUMBERS				Magnification		Measurement		Angle Theta (deg.)	Spacing (Å)		Modulus K(theta) (GPa)	APB Energy (mJm-1)	
Beam Directions				plate (K)	print (Å/mm)	d[010] (mm)	d[111] (mm)		[010]	[111]		[010]	[111]
<101>	<111>	<121>	<010>										
7015	7013	7034	7023	77.0	48.5	----	0.90	2	----	43.7	68.54	----	160.1
7015	7013	7034	7023	77.0	48.5	----	0.85	2	----	41.2	68.54	----	169.5
7015	7013	7034	7023	77.0	48.5	----	1.10	48	----	53.4	95.41	----	182.3
7015	7013	7034	7023	77.0	48.5	----	1.06	47	----	51.4	94.68	----	187.7
7015	7013	7034	7023	77.0	48.5	----	1.05	10	----	50.9	70.21	----	140.5
7015	7013	7034	7023	77.0	48.5	----	1.00	8	----	48.5	69.59	----	146.3
7017	7036	7029	7019	62.0	58.8	0.85	----	0	50.0	----	68.47	139.6	----
7017	7036	7029	7019	62.0	58.8	0.90	----	0	52.9	----	68.47	131.9	----
7017	7036	7029	7019	62.0	58.8	----	0.90	48	----	52.9	95.41	----	183.8
7017	7036	7029	7019	62.0	58.8	----	0.95	48	----	55.9	95.41	----	174.1
7017	7036	7029	7019	62.0	58.8	----	1.10	58	----	64.7	102.16	----	161.0
7017	7036	7029	7019	62.0	58.8	----	1.10	58	----	64.7	102.16	----	161.0
8887	8878/79	----	8891	77.0	44.1	1.20	----	0	52.9	----	68.47	131.9	----
8887	8878/79	----	8891	77.0	44.1	1.25	----	0	55.1	----	68.47	126.6	----
8887	8878/79	----	8891	77.0	44.1	1.25	----	0	55.1	----	68.47	126.6	----
8887	8878/79	----	8891	77.0	44.1	----	1.15	26	----	50.7	78.89	----	158.6
8887	8878/79	----	8891	77.0	44.1	----	1.10	26	----	48.5	78.89	----	165.8
8887	8878/79	----	8891	77.0	44.1	----	1.15	33	----	50.7	84.02	----	168.9
8887	8878/79	----	8891	77.0	44.1	----	1.15	33	----	50.7	84.02	----	168.9
----	----	----	8898	77.0	44.1	1.20	----	0	52.9	----	68.47	131.9	----
----	----	----	8898	77.0	44.1	1.25	----	0	55.1	----	68.47	126.6	----
----	----	----	8898	77.0	44.1	1.24	----	1	54.7	----	68.49	127.7	----
----	----	----	8898	77.0	44.1	1.35	----	0	59.5	----	68.47	117.2	----
----	----	----	8898	77.0	44.1	1.20	----	0	52.9	----	68.47	131.9	----

ALLOY: Sn 214
DEFORMATION TEMPERATURE: 297 K
HEAT TREATMENT: None

Ks (GPa) = 68.47
b (Å) = 2.546

PLATE SERIES NUMBERS Beam Directions				Magnification		Measurement		Angle Theta	Spacing (Å)		Modulus K(theta)	APB Energy (mJm-1)	
<101>	<111>	<121>	<010>	plate (K)	print (Å/mm)	d[010] (mm)	d[111] (mm)	(deg.)	[010]	[111]	(GPa)	[010]	[111]
5958	5948	-----	5934	77.0	50.8	1.00	-----	0	50.8	-----	68.47	139.0	-----
5955	5947	7421	5939	77.0	50.8	1.10	-----	0	55.9	-----	68.47	126.4	-----
-----	7398	7433	-----	77.0	50.8	-----	0.95	20	-----	48.3	74.99	-----	160.3
-----	7398	7433	-----	77.0	50.8	-----	1.25	44	-----	63.5	92.44	-----	150.2
-----	7398	7433	-----	77.0	50.8	-----	1.10	22	-----	55.9	76.22	-----	140.7
0984	0963	0973	0967	77.0	52.9	0.87	-----	0	46.0	-----	68.47	153.5	-----
0984	0963	0973	0967	77.0	52.9	0.90	-----	0	47.6	-----	68.47	148.4	-----
0984	0963	0973	0967	77.0	52.9	0.90	-----	0	47.6	-----	68.47	148.4	-----
0984	0963	0973	0967	77.0	52.9	0.87	-----	0	46.0	-----	68.47	153.5	-----
0984	0963	0973	0967	77.0	52.9	0.85	-----	0	45.0	-----	68.47	157.1	-----
0984	0963	0973	0967	77.0	52.8	-----	0.80	28	-----	42.2	80.31	-----	196.1
0984	0963	0973	0967	77.0	52.8	-----	0.85	28	-----	44.9	80.31	-----	184.6
0984	0963	0973	0967	77.0	52.8	-----	0.85	26	-----	44.9	78.89	-----	181.3
0984	0963	0973	0967	77.0	52.8	-----	0.88	26	-----	46.5	78.89	-----	175.2
0984	0963	0973	0967	77.0	52.8	-----	0.85	20	-----	44.9	74.99	-----	172.4
0983	0979	0975	0968	77.0	52.5	0.88	-----	0	46.2	-----	68.47	152.9	-----
0983	0979	0975	0968	77.0	52.5	0.85	-----	0	44.6	-----	68.47	158.3	-----
0983	0979	0975	0968	77.0	52.5	0.87	-----	0	45.7	-----	68.47	154.6	-----
0983	0979	0975	0968	77.0	52.5	0.85	-----	0	44.6	-----	68.47	158.3	-----
0983	0979	0975	0968	77.0	52.9	-----	0.87	22	-----	46.0	76.22	-----	170.8
0983	0979	0975	0968	77.0	52.9	-----	0.85	22	-----	45.0	76.22	-----	174.9
0983	0979	0975	0968	77.0	52.9	-----	0.97	54	-----	51.3	99.60	-----	200.2
0983	0979	0975	0968	77.0	52.9	-----	1.00	54	-----	52.9	99.60	-----	194.2
0983	0979	0975	0968	77.0	52.9	-----	0.80	18	-----	42.3	73.83	-----	180.0
0983	0979	0975	0968	77.0	52.9	-----	0.82	18	-----	43.4	73.83	-----	175.6

ALLOY: Sn 214 (cont.)
DEFORMATION TEMPERATURE: 297 K
HEAT TREATMENT: None

Ks (GPa) = 68.47
b (Å) = 2.5459

PLATE SERIES NUMBERS Beam Directions				Magnification		Measurement		Angle	Spacing (Å)		Modulus	APB Energy (mJm-1)	
<101>	<111>	<121>	<010>	plate (K)	print (Å/mm)	d[010] (mm)	d[111] (mm)	Theta (deg.)	[010]	[111]	K(theta) (GPa)	[010]	[111]
----	0962	----	0970	77.0	52.9	1.02	----	0	54.0	----	68.47	130.9	----
----	0962	----	0970	77.0	52.9	0.95	----	0	50.3	----	68.47	140.5	----
----	0962	----	0970	77.0	52.9	1.00	----	0	52.9	----	68.47	133.5	----
----	0962	----	0970	77.0	52.9	0.90	----	0	47.6	----	68.47	148.4	----
----	0962	----	0970	77.0	52.9	1.00	----	0	52.9	----	68.47	133.5	----
----	7398	7433	----	120.0	30.9	----	2.50	80	----	77.2	111.54	----	149.1
----	7398	7433	----	120.0	30.9	----	2.70	80	----	83.3	111.54	----	138.1
----	7398	7433	----	77.0	46.2	----	1.45	60	----	67.0	103.36	----	159.2
----	7398	7433	----	77.0	46.2	----	1.55	60	----	71.6	103.36	----	149.0
----	7398	7433	----	77.0	46.2	----	1.50	60	----	69.3	103.36	----	153.9
----	7398	7433	----	77.0	46.2	----	1.15	50	----	53.1	96.85	----	188.1
----	7398	7433	----	77.0	46.2	----	1.20	50	----	55.4	96.85	----	180.3
----	7398	7433	----	77.0	46.2	----	1.15	50	----	53.1	96.85	----	188.1
----	7398	7433	----	77.0	46.2	----	1.00	39	----	46.2	88.62	----	198.0
----	7398	7433	----	77.0	46.2	----	1.00	39	----	46.2	88.62	----	198.0
0982	0964	0974	0965	77.0	52.5	0.95	----	0	49.9	----	68.47	141.6	----
0982	0964	0974	0965	77.0	52.5	0.85	----	0	44.6	----	68.47	158.3	----
0982	0964	0974	0965	77.0	52.5	0.92	----	0	48.3	----	68.47	146.2	----
0955	0961	0972	0969	77.0	52.9	0.98	----	0	51.8	----	68.47	136.2	----
0955	0961	0972	0969	77.0	52.9	0.95	----	0	50.3	----	68.47	140.5	----
0955	0961	0972	0969	77.0	52.9	0.92	----	0	48.7	----	68.47	145.1	----
0955	0961	0972	0969	77.0	52.9	0.90	----	0	47.6	----	68.47	148.4	----
0955	0961	0972	0969	77.0	52.7	----	0.85	26	----	44.8	78.89	----	181.7
0955	0961	0972	0969	77.0	52.7	----	0.90	26	----	47.4	78.89	----	171.6
0955	0961	0972	0969	77.0	52.7	----	0.80	28	----	42.2	80.31	----	196.5

ALLOY: V 241
DEFORMATION TEMPERATURE: 297 K
HEAT TREATMENT: None

Ks (GPa) = 68.47
b (Å) = 2.525

PLATE SERIES NUMBERS	Beam Directions			Magnification		Measurement		Angle Theta (deg.)	Spacing (Å)		Modulus K(theta) (GPa)	APB Energy (mJm-1)	
<101>	<111>	<121>	<010>	plate (K)	print (Å/mm)	d[010] (mm)	d[111] (mm)		[010]	[111]		[010]	[111]
0063	----	0076	0080	77.0	53.1	0.80	----	0	42.5	----	68.47	163.6	----
0063	----	0076	0080	77.0	53.1	0.80	----	0	42.5	----	68.47	163.6	----
0063	----	0076	0080	77.0	53.1	0.82	----	0	43.5	----	68.47	159.6	----
0063	----	0076	0080	77.0	53.4	----	0.79	31	----	42.2	82.51	----	198.5
0063	----	0076	0080	77.0	53.4	----	0.79	31	----	42.2	82.51	----	198.5
0063	----	007?	0080	77.0	53.4	----	0.84	31	----	44.9	82.51	----	186.7
0029	0031/40	0034	0037	77.0	53.4	----	0.72	22	----	38.4	76.22	----	201.2
0029	0031/40	0034	0037	77.0	53.4	----	0.75	22	----	40.1	76.22	----	193.2
0029	0031/40	0034	0037	77.0	53.4	----	0.75	13	----	40.1	71.36	----	180.9
0029	0031/40	0034	0037	77.0	53.4	----	0.70	13	----	37.4	71.36	----	193.8
0029	0031/40	0034	0037	77.0	53.4	----	0.80	22	----	42.7	76.22	----	181.1
0029	0031/40	0034	0037	77.0	53.4	----	0.82	22	----	43.8	76.22	----	176.7
0029	0031/40	0034	0037	77.0	53.4	----	1.10	50	----	58.7	96.85	----	167.4
0029	0031/40	0034	0037	77.0	53.4	----	1.05	50	----	56.1	96.85	----	175.3
0029	0031/40	0034	0037	77.0	53.4	----	1.00	42	----	53.4	90.92	----	172.8
0029	0031/40	0034	0037	77.0	53.4	----	1.00	42	----	53.4	90.92	----	172.8
0043/62	0045	0074	0077	77.0	53.4	0.90	----	0	48.1	----	68.47	144.6	----
0043/62	0045	0074	0077	77.0	53.4	0.90	----	0	48.1	----	68.47	144.6	----
0043/62	0045	0074	0077	77.0	53.4	0.80	----	0	42.7	----	68.47	162.7	----
0043/62	0045	0074	0077	77.0	53.4	0.85	----	0	45.4	----	68.47	153.1	----
0043/62	0045	0074	0077	77.0	53.4	0.85	----	0	45.4	----	68.47	153.1	----
0043/62	0045	0074	0077	77.0	53.4	0.90	----	0	48.1	----	68.47	144.6	----
0043/62	0045	0074	0077	77.0	53.4	0.80	----	0	42.7	----	68.47	162.7	----
0043/62	0045	0074	0077	77.0	53.4	0.85	----	0	45.4	----	68.47	153.1	----
0043/62	0045	0074	0077	77.0	53.4	0.90	----	0	48.1	----	68.47	144.6	----

ALLOY: V 241 (cont.)
DEFORMATION TEMPERATURE: 297 K
HEAT TREATMENT: None

Ks (GPa) =   68.47
b (Å) =   2.525

| PLATE SERIES NUMBERS Beam Directions | | | | Magnification | | Measurement | | Angle Theta (deg.) | Spacing (Å) | | Modulus K(theta) (GPa) | APB Energy (mJm-1) | |
<101>	<111>	<121>	<010>	plate (K)	print (Å/mm)	d[010] (mm)	d[111] (mm)		[010]	[111]		[010]	[111]
0096	0092	0094	----	78.0	53.4	----	1.00	75	----	53.4	110.21	----	209.5
0096	0092	0094	----	78.0	53.4	----	1.00	75	----	53.4	110.21	----	209.5
0096	0092	0094	----	78.0	53.4	----	0.95	65	----	50.7	106.09	----	212.3
0096	0092	0094	----	78.0	53.4	----	1.00	65	----	53.4	106.09	----	201.7
0096	0088	0094	----	78.0	53.1	----	1.05	74	----	55.8	109.89	----	200.0
0096	0088	0094	----	78.0	53.1	----	1.00	74	----	53.1	109.89	----	210.1
0096	0088	0094	----	78.0	53.1	----	0.97	74	----	51.5	109.89	----	216.5
0096	0088	0094	----	78.0	53.1	----	1.02	74	----	54.2	109.89	----	205.9
0096	0088	0094	----	78.0	53.1	----	1.00	74	----	53.1	109.89	----	210.1
0022	0015	0012	0007	78.0	53.1	----	1.10	90	----	58.4	112.62	----	195.7
0022	0015	0012	0007	78.0	53.1	----	1.15	90	----	61.1	112.62	----	187.2
0022	0015	0012	0007	78.0	53.1	----	1.00	82	----	53.1	111.93	----	214.0
0022	0015	0012	0007	78.0	53.1	----	1.00	82	----	53.1	111.93	----	214.0
0043/62	0045	0074	0077	78.0	53.1	----	0.98	60	----	52.0	103.36	----	201.6
0043/62	0045	0074	0077	78.0	53.1	----	0.95	60	----	50.4	103.36	----	208.0
0043/62	0045	0074	0077	78.0	53.1	----	0.80	30	----	42.5	81.77	----	195.4
----	0706/04	----	----	78.0	52.6	----	1.25	90	----	65.8	112.62	----	173.9
----	0706/04	----	----	78.0	52.6	----	1.20	90	----	63.1	112.62	----	181.1
----	0706/04	----	----	78.0	52.6	----	1.20	90	----	63.1	112.62	----	181.1
----	0706/04	----	----	78.0	52.8	----	1.15	50	----	60.7	96.85	----	161.9
----	0706/04	----	----	78.0	52.8	----	1.12	50	----	59.1	96.85	----	166.2
----	0706/04	----	----	78.0	52.8	----	1.10	48	----	58.1	95.41	----	166.7
0929	0926	0934	0729	78.0	52.8	0.83	----	0	43.8	----	68.47	158.6	----
0929	0926	0934	0729	78.0	52.8	0.81	----	0	42.8	----	68.47	162.5	----
0929	0926	0934	0729	78.0	52.8	0.86	----	0	45.4	----	68.47	153.1	----

ALLOY: V 214
DEFORMATION TEMPERATURE: 297 K
HEAT TREATMENT: None

Ks (GPa) =   68.47
b (Å) =   2.524

PLATE SERIES NUMBERS				Magnification		Measurement		Angle Theta (deg.)	Spacing (Å)		Modulus K(theta) (GPa)	APB Energy (mJm-1)	
Beam Directions				plate (K)	print (Å/mm)	d[010] (mm)	d[111] (mm)		[010]	[111]		[010]	[111]
<101>	<111>	<121>	<010>										
----	0802	----	----	78.0	54.5	----	1.00	65	----	54.5	106.09	----	197.4
----	0802	----	----	78.0	54.5	----	0.98	65	----	53.4	106.09	----	201.4
----	0802	----	----	78.0	54.5	----	0.90	60	----	49.1	103.36	----	213.7
----	0802	----	----	78.0	54.5	----	0.95	60	----	51.8	103.36	----	202.4
----	0802	----	----	78.0	54.5	----	1.00	80	----	54.5	111.54	----	207.5
0835	0849	0845	0840	78.0	54.3	0.65	----	0	35.3	----	68.47	196.7	----
0835	0849	0845	0840	78.0	54.3	0.68	----	0	36.9	----	68.47	188.0	----
0835	0849	0845	0840	78.0	54.3	0.70	----	0	38.0	----	68.47	182.7	----
0835	0849	0845	0840	78.0	54.3	0.65	----	0	35.3	----	68.47	196.7	----
0835	0849	0845	0840	78.0	54.3	0.60	----	0	32.6	----	68.47	213.1	----
0835	0849	0845	0840	78.0	54.3	0.62	----	0	33.7	----	68.47	206.2	----
0835	0849	0845	0840*	78.0	54.3	0.75	----	22	40.7	----	76.22	189.8	----
0835	0849	0845	0840*	78.0	54.3	0.80	----	22	43.4	----	76.22	177.9	----
0835	0849	0845	0840*	78.0	54.3	0.80	----	22	43.4	----	76.22	177.9	----
0831/27	0814	0820	0817	78.0	54.0	0.63	----	0	34.0	----	68.47	204.1	----
0831/27	0814	0820	0817	78.0	54.0	0.65	----	0	35.1	----	68.47	197.8	----
0831/27	0814	0820	0817	78.0	54.0	0.69	----	0	37.3	----	68.47	186.3	----
0831/27	0814	0820	0817	78.0	54.0	0.63	----	0	34.0	----	68.47	204.1	----
0831/27	0814	0820	0817*	78.0	54.0	0.69	----	5	37.3	----	68.91	187.5	----
0831/27	0814	0820	0817*	78.0	54.0	0.70	----	5	37.8	----	68.91	184.9	----
1029	1033	1036/35	1040/39	78.0	52.2	0.58	----	0	30.3	----	68.47	229.3	----
1029	1033	1036/35	1040/39	78.0	52.2	0.61	----	0	31.8	----	68.47	218.0	----
1029	1033	1036/35	1040/39	78.0	52.2	0.60	----	0	31.3	----	68.47	221.7	----
1029	1033	1036/35	1040/39	78.0	52.2	0.57	----	0	29.8	----	68.47	233.3	----
1029	1033	1036/35	1040/39	78.0	52.2	0.61	----	0	31.8	----	68.47	218.0	----

ALLOY: V 214 (cont.)
DEFORMATION TEMPERATURE: 297 K
HEAT TREATMENT: None

Ks (GPa) = 68.47
b (Å) = 2.524

PLATE SERIES NUMBERS Beam Directions				Magnification		Measurement		Angle Theta (deg.)	Spacing (Å)		Modulus K(theta) (GPa)	APB Energy (mJm-1)	
<101>	<111>	<121>	<010>	plate (K)	print (Å/mm)	d[010] (mm)	d[111] (mm)		[010]	[111]		[010]	[111]
1022	1015	1018	1016	78.0	52.8	-----	1.00	38	-----	52.8	87.85	-----	168.7
1022	1015	1018	1016	78.0	52.8	-----	1.00	38	-----	52.8	87.85	-----	168.7
1022	1015	1018	1016	78.0	52.8	-----	1.05	38	-----	55.4	87.85	-----	160.7
1022	1015	1018	1016	78.0	52.8	-----	0.75	30	-----	39.6	81.77	-----	209.4
1022	1015	1018	1016	78.0	52.8	-----	0.78	30	-----	41.2	81.77	-----	201.3
1022	1015	1018	1016	78.0	52.8	-----	0.78	30	-----	41.2	81.77	-----	201.3
1022	1015	1018	1016	78.0	52.8	-----	0.65	14	-----	34.3	71.81	-----	212.1
1022	1015	1018	1016	78.0	52.8	-----	0.62	14	-----	32.7	71.81	-----	222.4
1022	1015	1018	1016	78.0	52.8	-----	0.72	23	-----	38.0	76.87	-----	205.0
1022	1015	1018	1016	78.0	52.8	-----	0.80	41	-----	42.2	90.16	-----	216.4
1022	1015	1018	1016	78.0	52.8	-----	0.82	41	-----	43.3	90.16	-----	211.2
1022	1015	1018	1016	78.0	52.8	-----	1.15	59	-----	60.7	102.77	-----	171.6
1028	1032	1034	1037/38	78.0	52.5	0.65	-----	0	34.1	-----	68.47	203.5	-----
1028	1032	1034	1037/38	78.0	52.5	0.62	-----	0	32.6	-----	68.47	213.3	-----
1028	1032	1034	1037/38	78.0	52.5	0.65	-----	0	34.1	-----	68.47	203.5	-----
1028	1032	1034	1037/38	78.0	52.5	0.67	-----	0	35.2	-----	68.47	197.4	-----
1028	1032	1034	1037/38	78.0	52.5	0.67	-----	0	35.2	-----	68.47	197.4	-----

ON APB DRAGGING AND APB-ENERGY ANISOTROPY IN BINARY Ni₃Al

ABSTRACT

Recent weak-beam electron microscopy studies of Ni₃Al provided evidence indicating that glide of Kear-Wilsdorf locked dislocation segments may occur on {111} planes, accompanied by APB dragging, during deformation at high temperature. A direct implication of those studies is that a mechanism other than the onset of {010} slip may be important in controlling the peak in yield strength in Ni₃Al. The present weak-beam investigations of Ni₃Al have centered on the possibility that such configurations result from thermally induced dislocation kink and jog activity rather than the APB-dragging mechanism previously proposed.

INTRODUCTION

Theoretical descriptions of mechanisms governing the anomalous temperature dependence of flow stress in Ni₃Al alloys have evolved over the last twenty-eight years [1-8]. Aspects of this theory have been supported by transmission-electron-microscopy (TEM) investigations of the deformation substructure in both polycrystalline and single-crystal materials [2,3,9-22]. Mulford and Pope [10] provided the first microscopic evidence indicating that at any temperature the microyield behavior of Ni₃Al is dominated by the nucleation and mobility of edge dislocations. They further suggested, as did others before them, that with increasing deformation temperature screw dislocations, immobilized by Kear-Wilsdorf (K-W) lock formation, dominate the flow stress. Staton-Bevan and Rawlings [11] added further support to this view through TEM investigations of the deformation substructure in single crystals deformed at temperatures from

166 to 775 K. Recently, Veyssière, et al., [16,17] provided microscopic evidence of dislocations exhibiting climb or non-conservative dissociations, proposed by Flinn [1], after high-temperature deformation. All of these investigations agree on the dominance of "sessile" screw-dislocation configurations (known as Kear-Wilsdorf locks [2]) after deformation in the regime of increasing flow stress with temperature.

Veyssière, et al., [22] recently reported observations of a_o<110>-type superdislocations dissociated in an {001} plane, and yet, bowed or curved in the {111} glide plane. They concluded that such configurations arise from portions of dislocations which have formed K-W locks, with their adjoining antiphase boundary (APB) on the {001} plane, experiencing further glide in the {111} plane accompanied by dragging their out-of-plane APB. Veyssière, et al., argued further that this process occurred by local "atomic interchanges" roughly perpendicular to the dislocation line. They regarded this observation as an indication of higher than expected mobility and "flexibility" of the APB, and hence, of K-W locks, on the glide plane. A direct implication of this result is that a mechanism other than the onset of {010} slip may be important in controlling the yield-strength peak in Ni_3Al. The present investigations have centered on the possibility that such configurations are thermally induced by kink and jog activity rather than the APB-dragging mechanism proposed by Veyssière, et al.

EXPERIMENTAL

For the present studies, cast binary-alloy single-crystals, having an analysed composition of 22.9 a/o Al - 77.1 a/o Ni, were homogenized at 1500 K for 100 h and slow cooled. Compression specimens, approximately 5 x 5 x 15 mm, with an axial orientation within 6° of [001], were sectioned from the crystals by electrodischarge machining and electropolished then annealed at 1300 K for 1 h prior to testing. Compression tests were

carried out at 300 K at an initial strain rate of 1.7 x 10^{-4}/sec, to a maximum plastic strain from 0.7 to 1.3 %.

Compressed samples were oriented parallel to the primary slip plane by two-surface slip-trace analysis and sectioned into 0.5 mm thick slices. Thin-foil specimens were prepared from the slices by twin-jet electropolishing in a solution of 2 % perchloric acid in butoxy ethanol at 260 K and 75 to 80 V. The deformation substructure was characterized using a JEOL 2000FX microscope, operating at 200 kV, and both bright-field and weak-beam dark-field imaging. Trace analysis was performed by using weak-beam conditions (g-ng{202}, with n = 3.5 to 5) and tilting about an axis parallel to the dislocation-line direction, **u**, in order to determine the dissociation plane of superlattice dislocations. Dislocation types were identified by standard two-beam dynamical imaging using ±g conditions to identify dipole-dislocation lines. The standard g·b = 0 and g·(bxu) = 0 invisibility conditions were employed for determining dislocation Burgers vectors. Magnifications were held constant for all beam directions by imaging at fixed, calibrated lens currents and focusing the image by adjusting the specimen height. Dislocation lines were photographed at direct magnifications ranging from 5 to 8 x 10^4. The specimen-conditions examined were: i) as homogenized, ii) deformed at 300 K, and iii) deformed at 300 K, followed by annealing at 975 K for 1 h and water quenching. The dissociation distance of superlattice partial dislocations, was determined by calibrating 2 to 4X enlarged photographs of dislocation lines (recorded under g·b = 2 weak-beam conditions) and viewing them with a ruled, 7X magnifying loupe. The measured distances between positions of maximum intensity of partial dislocations were used as the dissociation distance for calculating APB energies.

r˙

RESULTS

The homogenized material was examined on the {111} planes to determine if long, straight, dissociated $a_0<101>$ screw segments existed on the slip planes as grown-in artifacts prior to deformation. Virtually no dislocations existed in the field of view of the foils. Some low-angle boundaries, characterized by well-developed dislocation networks, were observed. The possibility of some grown-in, non-conservative configurations cannot be ruled out; however, we conclude from these observations, that the dislocation structures observed after deformation are due to the deformation process itself.

Material deformed at 300 K showed the wavy superdislocation structure in Fig. E.1, where the dislocation lines are curved or bowed in the (111) glide plane. Determination of the dislocation Burgers vectors showed that most dislocations were edge- or mixed-type pairs with $b = a_0<101>$, and many superdislocation dipoles were observed. Weak-beam imaging studies showed that the nearly-straight segments of nominally screw orientation consist of long, straight segments of perfect screw orientation and large kinked segments of mixed character. Figure E.2 shows weak-beam images and trace analysis of these dislocation lines revealing that the longer screw segments are dissociated on {010} planes, while the shorter kink segments of mixed character (> 5° deviation from pure screw) are dissociated on {111} planes. The kink segments are curved or kinked in the (111) glide plane and a local constriction of the dissociated line occurs at the junction of the kink segment with the pure-screw segments, maintaining "conservative" APB or glide dissociations.

Nearly all dislocation lines had their end segments in a near-edge orientation curving toward and intersecting the foil surface. On occasion, near-edge end segments could be made to move in the foil by converging the electron beam. Estimates based on the lengths of these moving segments suggest that the lattice resistance to their motion is on the
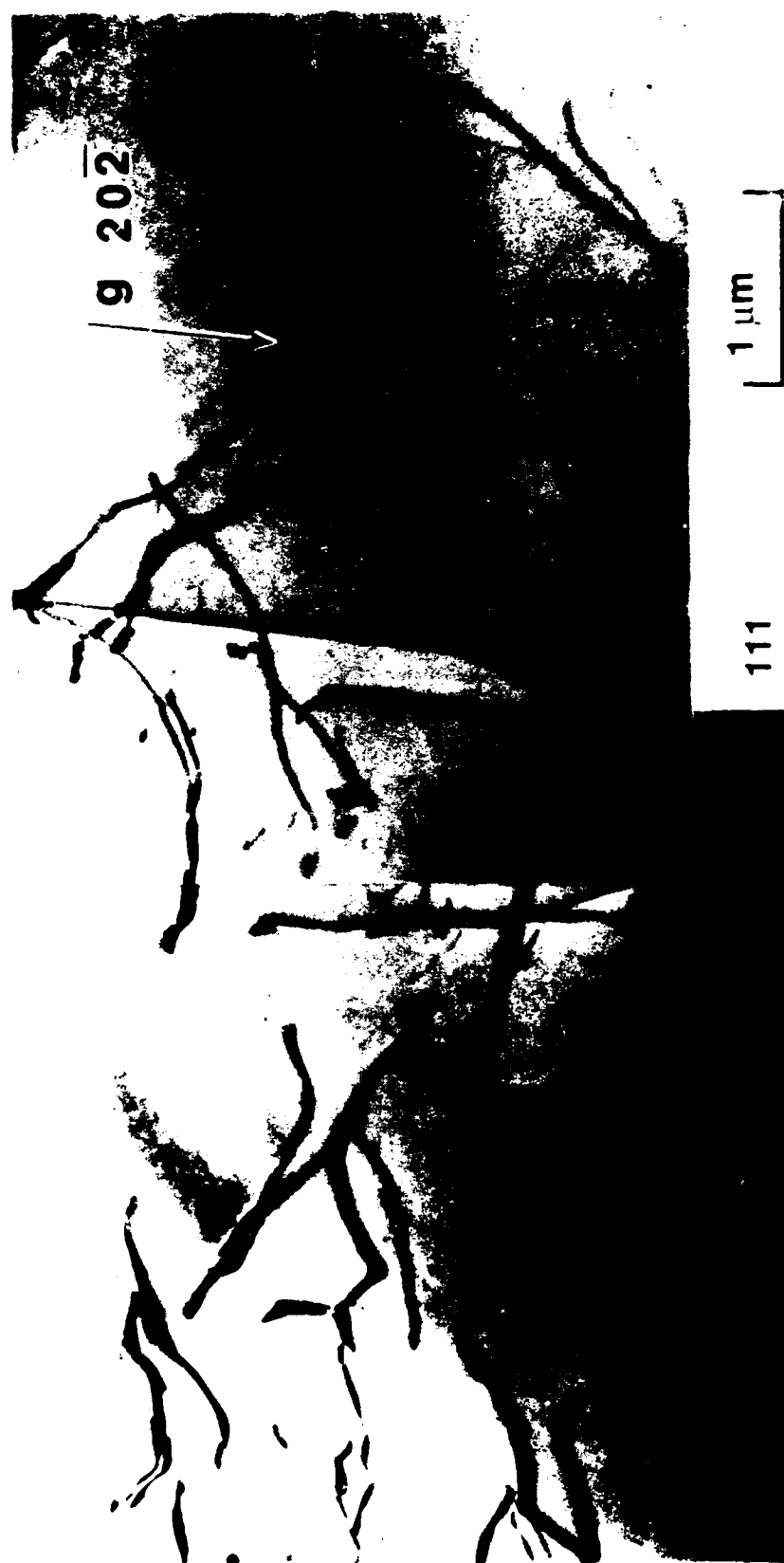
224

Fig. E.1   Bright-field, B[111]; wavy superdislocation dipoles primarily of mixed character.

Fig. E.2   Weak-beam dark-field, g-3.5g{202}; as deformed at 300 K; a) B[101],
b) B[111], and c) B[010].

226

order of 20 MPa. Pure-screw segments dissociated on a {111} plane could not be located in the foil. This result suggests that the driving force for dislocation dissociation on {010} planes is very high, even at room temperature, and that segments which achieve the near-screw orientation will dissociate on the cube planes. The small angular deviation of long, straight segments away from pure-screw orientation, reported in other studies after high-temperature deformation [16-20], was not observed here after room-temperature deformation.

The plot in Fig. E.3 shows the variation in dissociation distance, as a function of deviation angle from the pure-screw orientation, for kink-segments dissociated in the (111) plane. A value for the dissociation distance of pure-screw segments on the (010) plane is also shown. The following standard relationship was used for converting the measured dislocation spacings to APB energies:

$$\gamma = K(\theta) \, b^2 / 2 \, \pi \, d \qquad (1)$$

where γ is the APB energy, $K(\theta)$ the orientation dependent elastic-energy coefficient, b the Burgers-vector magnitude, and d the measured dissociation distance. The anisotropic-elastic-energy coefficients, given by Yoo [23], were used to convert these measured super-partial spacings to APB energy for both the {111} and {010} planes. The measured dislocation spacings were used directly with no correction for actual dislocation position relative to the weak-beam image. A value of 169 ± 17 mJm^{-2} was obtained for the {111}-plane APB energy and a value of 104 ± 11 mJm^{-2} for the {010}-plane APB energy.

Annealing after room temperature deformation revealed a slightly different dislocation structure. Screw segments were observed with greater frequency. The long segments having curves or kinks were shown to remain bowed or kinked in the (111) glide plane. Weak-beam examination revealed that the screw parts remained dissociated in the (010)
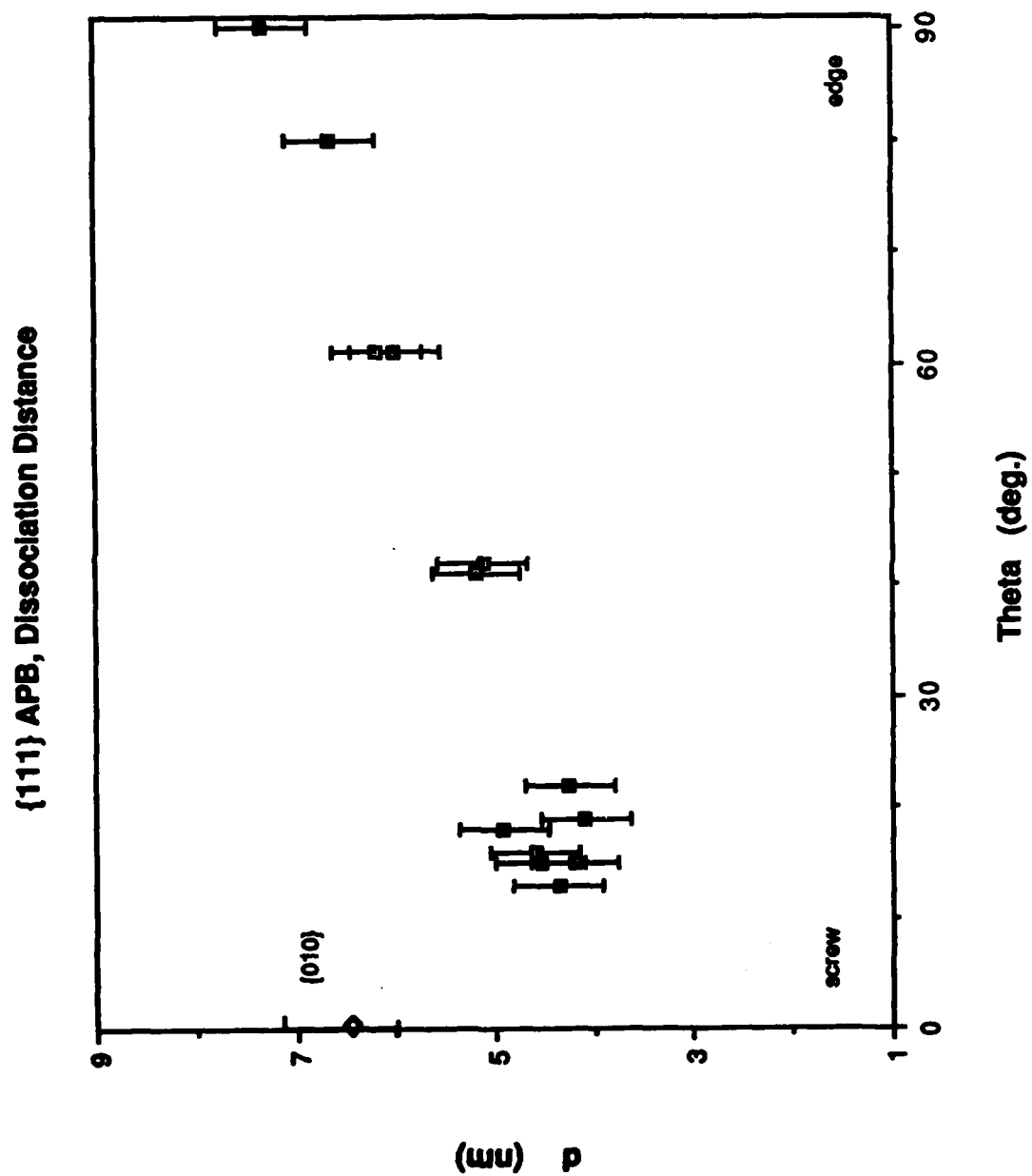
Fig. E.3 Dissociation distance vs. character for $a_0/2<101>$ dislocations and {111} APB.

plane, while the kink segments remained dissociated in the (111) plane. In several instances the kink segments dissociated over larger distances in the (111) plane and took on the serrated or roughened appearance as shown in Fig. E.4.

DISCUSSION

These results are consistent with several previous deformation studies in Ni_3Al. The homogenized materials are expected to have very low dislocation contents and observations made on the general deformation structure, agree with those of previous investigations of the low-temperature deformation behavior of Ni_3Al alloys [9-13]. The values of the {010} ABP energy reported above are consistent with previous measurements (90 ± 5 mJm^{-2}) for near-stoichiometric Ni_3Al deformed at high temperature, and the range of error overlaps the previously reported range [17-20]. However, a significant difference exists between the value of {111} ABP energy reported here and the previously-determined value (111 ± 15 mJm^{-2}). This variation may be attributable to the differences in composition or deformation-temperatures used in these studies. We have considered that our measurement could be affected by local stresses in the foil which may not be relaxed at low temperature; however, a consistent value for the {111} plane APB energy was obtained regardless of the line direction or character of the dislocation. As reported above, the lattice friction for near-edge dislocations or kinks, was estimated to be very low. In most cases, the separation distance in the {111} plane was measured on the same dislocation lines which gave a value for the {010} plane-dissociation distance consistent with previous measurements. One would expect the pure-screw segments to experience a much higher glide barrier than the edge or mixed segments due to core relaxations, and therefore, would expect greater variation in those measurements. However, little variation was actually observed.
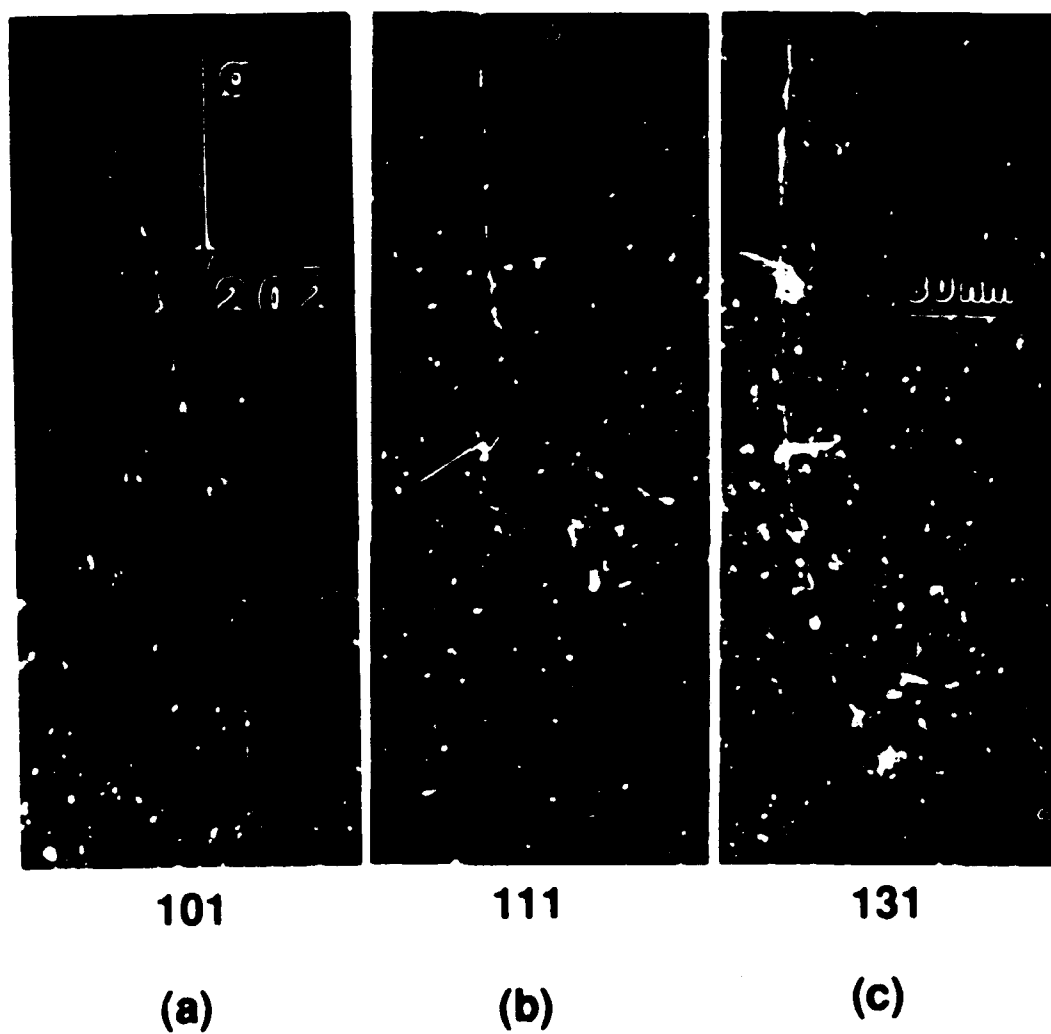
229

Fig. E.4   Weak-beam dark-field, g-4g{202}; deformed at 300 K + 975 K / 1h / WQ;
a) B[101], b) B[111], roughened APB at arrow, and c) B[131].

We have considered the explanation given by Veyssière, et al., (glide coupled with stress-assisted APB dragging) for the occurrence of the non-conservative dislocation segments after high-temperature deformation [22]. In the present study, stress-assisted APB dragging could not occur and, therefore, the thermal effects of APB energy and elastic anisotropy were directly studied. One would expect to observe similar non-conservative dislocation configurations due to migration of thermally activated kinks and jogs, driven by the anisotropic APB energy and anisotropic elastic driving forces.

Flinn provided the first analysis suggesting that all $L1_2$ compounds have anisotropic APB energies within the quasi-chemical model of ordering [1]. Paidar extended this analysis to include second-near-neighbor bonds and non-conservative APB of two types [24]. The Paidar analysis suggests that several low-energy planes can exist with non-conservative APB. Based on these analyses, a non-mechanistic, intrinsic thermodynamic driving force exists acting to transform glide-dissociated superdislocations of screw type into the K-W configuration. A similar driving force exists (over and above any elastic driving forces) tending to transform the conservative kink segments, of mixed character, into jogs with non-conservative APB. The energy difference between the initial and final configurations is the driving force. A first-order estimate of this driving force is given by the difference in APB energy between the glide plane and the plane, (hkl), containing the lower-energy APB in the final configuration. This is a force per-unit-length yielding an out-of-plane stress, σ, given by the effective line tension divided by the Burgers vector, or

$$\sigma = (\gamma_{111} - \gamma_{hkl}) / b \qquad (2)$$

Here, γ_{hkl}, is for any APB plane having a lower APB energy than (111) within the Flinn or Paidar analyses. For previous measurements of the APB-energy anisotropy [20], and from those made here, σ ranges from 80 to 240 MPa. One may anticipate that these driving

231

forces would be high enough to transform glide-dissociated kinks on the {111} planes to climb-dissociated jogs. Dissociations of this nature could exist in combination with conservative dissociations of various lengths, form atomically faceted, dissociated jogs which could appear to lie on any plane. Diffusion and thermally activated kink and jog formation are sufficient mechanisms for such tranformations.

The diffusion distances required to form non-conservative configurations by thermal-kink and-jog migration are approximately equal to the measured separation of the partials (~ 6 nm). Using a simple square-root-of-time dependence for the diffusion distance at 975 K and measured self-diffusion data [25], one estimates that the dissociation distance can be achieved in about one second. The stresses estimated from Eq. (2) and elastic interaction stresses would act to shorten this diffusion time. Lateral kink and jog migration along the dislocation line could either enhance or limit the transformation process. The rate for kink migration may be estimated from the kink diffusivity and the local forces acting to propagate the kink [26], assuming that the thermal-migration rate is not significantly altered by the kink lying out of the glide plane in {010}. The lateral velocity of a thermal kink, v, is given by

$$v = \upsilon \, a_o^2 \exp(-\Delta H_m/kT) \, (\sigma b w/kT) \tag{3}$$

where υ is an attempt frequency for atom jumping [on the order of the Debye frequency (10^{12}/sec.)]; a_o the lattice parameter; ΔH_m the activation energy for kink migration; σ the local stress acting to move the kink; b the length of the partial-dislocation Burgers vector; w the kink width on {010}; and k and T are the Boltzmann constant and the absolute temperature, respectively. For Ni_3Al, $a_o = 0.3566$ nm, b = 0.252 nm, and w has been estimated from the theory of Paidar, et al., to be about 3b or 0.75 nm. In most metals ΔH_m is less than kT even near absolute zero [26]. Here the activation enthalpy for kink diffusion, ΔH_m, may be higher since the kinks lie out of the glide plane. Nonetheless, the activation

enthalpy for motion must be significantly less than that for kink formation and less than the activation enthalpy which has been measured for the anomalous flow stress in Ni_3Al (0.1 to 0.3 eV) [4,7]. Values in the range 0.01 to 0.05 eV would be conservative estimates. Using these values in Eq. (3), the thermal-kink velocity can be estimated for assumed local stress at 975 K. Such stresses would be expected from elastic interactions between dislocations. Estimates from Eq. (3) suggest that kink velocities on the order of 1 m/sec could be attained with only 1 MPa local stress acting to propagate the kink. Clearly, this velocity would allow for kink-migration distances well in excess of the dislocation line-lengths observed here, during the annealing time used for these studies. From these estimates, it is apparent that the diffusive spreading of the APB in the {010} or jog plane, or the diffusive propagation of jog segments, would be the rate-limiting step in forming non-conservative configurations by thermal activation. The present results show that in spite of the anticipated high driving force to transform conservative {111} APB to {010} and non-conservative APB at high temperature, this process does not readily occur, and in some cases, the APB tends to spread on the {111} plane upon annealing above the temperature of peak flow stress. This result suggests that the {111} APB energy decreases at high temperature and implies that the result of Veyssière, et al., is not due to thermally activated motion of kinks and jogs.

SUMMARY

The dissociation of a_0<101> superlattice dislocations was examined in single-crystal Ni_3Al deformed at room temperature. Weak-beam kinematical imaging, coupled with trace analysis, was used to determine the APB anisotropy. The determined values of {111} APB energy are 52 % greater than those previously reported [20], and the measured ratio of {111} APB energy to {010} APB energy was found to be 1.62.

Estimates of the atomic mobility and the driving forces for forming non-conservative configurations of mixed character, without an applied stress, suggested that such core transformations should occur. Dislocations were observed to increase their dissociation distance on the {111} plane in an irregular form after annealing samples deformed at room temperature. The presence of these configurations suggests that the actual driving force is not high in the absence of an applied stress. Stress-assisted APB dragging, as observed by Veyssière, et al., may be important in controlling the yield strength peak.

REFERENCES

1. P.A. Flinn, Trans. AIME. 218, 145 (1960).

2. B.H. Kear and H.G.F. Wilsdorf, Trans. AIME. 224, 382 (1962).

3. P.H. Thornton, R.V. Davies, & T.L. Johnston, Metall. Trans. 1A, 27 (1970).

4. S. Takeuchi and E. Kuramoto, Acta Metall. 21, 415 (1973).

5. S.-J. Liang and D.P. Pope, Acta Metall. 25, 485 (1977).

6. C. Lall, S. Chin, and D.P. Pope, Metall. Trans. 10A, 1323 (1979).

7. V. Paidar, D.P. Pope, and V. Vitek, Acta Metall. 32, 435 (1984).

8. M.H. Yoo, J.A. Horton, and C.T. Liu, Acta Metall. 36, 2935 (1988).

9. B.H. Kear and M.F. Hornbecker, Trans. ASM, 59, 155 (1966).

10. R.A. Mulford and D.P. Pope, Acta Metall. 21, 1375 (1973).

11. A.E. Staton-Bevan and R.D. Rawlings, Phil. Mag. 32, 787 (1975).

12 T. Saburi, T. Hamana, S. Nenno, and H-R. Pak, Jap. J. Appl. Phys. 16, 267 (1977).

13. I. Baker and E.M. Schulson, Phys. Stat. Sol. (a), 89, 163 (1985).

14. I. Baker, E.M. Schulson, and J.A. Horton, Acta Metall. 35, 1533 (1987).

15. I. Baker, J.A. Horton, and E.M. Schulson, Phil. Mag. Lett. 55, 3 (1987).

16. P. Veyssière, D.L. Guan, and J. Rabier, Phil. Mag. A, 49, 45 (1984).

17. P. Veyssière, Phil. Mag. A, 50, 189 (1984).

18. P. Veyssière, J. Douin, and P. Beauchamp, Phil. Mag. A, 51, 469 (1985).

19. P. Veyssière and J. Douin, Phil. Mag. A, 51, L1 (1985).

20. J. Douin, P. Veyssière, and P. Beauchamp, Phil. Mag. A., 54, 375 (1986).

21. W. Yan, I.P. Jones and R.E. Smallman, Scripta Metall. 21, 1511 (1987).

22. P. Veyssière, J.A. Horton, M.H. Yoo, and C.T. Liu, Phil. Mag. Lett. 56, 17 (1988).

23. M.H. Yoo, Acta Metall. 35, 1559 (1987).

24. V. Paidar, Acta Metall. 33, 1803 (1985).

25. M.M.P. Janssen, Metal. Trans. 4, 1623 (1973).

26. J.P. Hirth and J. Lothe, Theory of Dislocations, 2nd ed. (John-Wiley & Sons, Inc., New York, 1982) p. 533.